

UNIVERSITÉ DU QUÉBEC À RIMOUSKI

**PHOTOPRODUCTION DE MONOXYDE DE CARBONE
DANS LES ÉCOSYSTÈMES MARINS: PARTICULES
CONTRE SOLUTÉS**

Thèse présentée

dans le cadre du programme de doctorat en Océanographie
en vue de l'obtention du grade de philosophiae doctor

PAR
Guisheng Song

Octobre 2013

UNIVERSITÉ DU QUÉBEC À RIMOUSKI
Service de la bibliothèque

Avertissement

La diffusion de ce mémoire ou de cette thèse se fait dans le respect des droits de son auteur, qui a signé le formulaire « *Autorisation de reproduire et de diffuser un rapport, un mémoire ou une thèse* ». En signant ce formulaire, l'auteur concède à l'Université du Québec à Rimouski une licence non exclusive d'utilisation et de publication de la totalité ou d'une partie importante de son travail de recherche pour des fins pédagogiques et non commerciales. Plus précisément, l'auteur autorise l'Université du Québec à Rimouski à reproduire, diffuser, prêter, distribuer ou vendre des copies de son travail de recherche à des fins non commerciales sur quelque support que ce soit, y compris l'Internet. Cette licence et cette autorisation n'entraînent pas une renonciation de la part de l'auteur à ses droits moraux ni à ses droits de propriété intellectuelle. Sauf entente contraire, l'auteur conserve la liberté de diffuser et de commercialiser ou non ce travail dont il possède un exemplaire.

UNIVERSITÉ DU QUÉBEC À RIMOUSKI

**CARBON MONOXIDE (CO) PHOTOPRODUCTION IN
MARINE ECOSYSTEMS: PARTICLES VERSUS SOLUTES**

A dissertation

submitted in partial fulfillment of the requirements

for the Doctor of Philosophy Degree in Oceanography

BY

Guisheng Song

October 2013

Composition du jury:

Jean-Pierre Gagné, président du jury, Université du Québec à Rimouski

Huixiang Xie, directeur de recherche, Université du Québec à Rimouski

Simon Bélanger, codirecteur de recherche, Université du Québec à Rimouski

**David J. Kieber, examinateur externe, State University of New York College of
Environmental Science and Forestry**

**Michael G. Scarratt, examinateur externe, Maurice Lamontagne Institute, Fisheries
and Oceans Canada**

Dépôt initial le 15-08-2013

Dépôt final le 22-10-2013

REMERCIEMENTS

Je tiens à remercier mon directeur de thèse, le Dr Huixiang Xie, pour son soutien et ses conseils. Au cours de mes études supérieures dans les 4 dernières années, il m'a beaucoup appris sur la science et sur la vie, et m'a aidé à grandir et devenir un scientifique en océanographie. Ses encouragements et conseils sont précieux pour ma future carrière.

Je remercie également tous les membres de mon comité pour leur soutien, leurs conseils tout au long de ce projet: Simon Bélanger (co-directeur) a fait un travail exemplaire dans la détermination des spectres d'absorption de particules (également Thomas Jaegler) et la modélisation de l'irradiance solaire et le taux de photoproduction de CO à partir de la CDOM et des particules sur la base des données de couleur de l'océan, Michel Gosselin et Michael Scarratt m'ont aidé dans l'incubation d'algues de glace. En outre, ils m'ont beaucoup aidé dans le traitement des données, la composition et la présentation du rapport et mes publications.

J'apprécie grandement le Dr David J. Kieber (SUNY-ESF) de m'avoir reçu en tant qu'étudiant-invité dans son laboratoire et pour son aide lors des croisières dans l'estuaire du Delaware (avec Sara Button, John Richardson et James Werner). Je suis reconnaissant à Connie Lovejoy (Université Laval) et Andrew R. Juhl (Columbia University) d'avoir fourni des cultures d'algues de glace. Je tiens à remercier les populations concernées dans mon travail, sans qui je n'aurais pu terminer ce projet avec succès. Je tiens à remercier Souad Annane, Pascal Rioux, Karine Lemarchand, Eva Alou-Font et Jean-Pierre Gagné d'avoir fourni des instruments et leur assistance lors de l'incubation de la culture, Mélanie Simard pour la chlorophylle et l'analyse du COD, les scientifiques, les collègues, CJ Mundy et Jens K. Ehn d'avoir fourni des données pour mes publications, Edouard Leymarie d'avoir lancé la simulation Mont-Carlo, et les capitaines et membres d'équipage de l' NGCC Amundsen et RV Sharp pour leur coopération au cours des études sur le terrain. Enfin, je suis

reconnaissant pour tout le monde (Cyril Aubry, Xiaomeng Wang, Abderrahmane Taalba et Liming Qi) dans notre groupe et tout le monde dans mon bureau de me tenir compagnie ici.

Ce travail a été financé par des subventions en sciences naturelles et en génie du Canada (CRSNG) et de l'Année canadienne polaire internationale (API) du bureau du programme fédéral. J'ai a été soutenu par une bourse de doctorat de Recherche pour étudiants étrangers du Fonds québécois de la recherche sur la nature et les technologies (FQRNT) et une bourse d'études supérieures ISMER.

ACKNOWLEDGMENTS

I would like to thank my supervisor, Dr. Huixiang Xie, for his support and guidance. During my graduate studies in the past four years, he taught me a lot in science and life, and helped me to grow up and become a scientist in Oceanography. His encouragement and guidance is invaluable for my future career.

I also thank all the members of my committee for their support, advice throughout this project: Simon Bélanger (co-supervisor) did a lot work in determining the absorbance spectra of particles (with his student, Thomas Jaegler) and modeling solar irradiance and CO photoproduction rate from both CDOM and particles based on the ocean color data; Michel Gosselin and Michael Scarratt helped me in the ice algae incubation. Also they helped me a lot in processing the data, composing and presenting the report and my publications.

I greatly appreciate Dr. David J. Kieber (SUNY-ESF) for inviting me as a guest student in his lab and his help during the cruises in the Delaware Estuary (along with Sara Button, John Richardson and James Werner). I am grateful to Connie Lovejoy (University Laval) and Andrew R. Juhl (Columbia University) for providing ice algal cultures. I would like to thank the peoples involved in my work, and I will not finish the project successfully without their assistance: I would thank Souad Annane, Pascal Rioux, Karine Lemarchand, Eva Alou-Font, Jean-Pierre Gagné, Émilien Pelletier, Gustavo A. Ferreyra and Thomas Pollet for providing instruments, lab space and their assistance, Mélanie Simard for chlorophyll *a* and DOC analysis, Claude Belzile for biomass analysis, Mathieu Babin for extracting the compounds, James Caveen for technical assistance in modeling, C. J. Mundy for providing data for my publications, Edouard Leymarie for running the Mont-Carlo simulation, and the captains and crew of the *CCGS Amundsen* and *R.V. Sharp* for their cooperation during the field studies. At last, I am grateful to everyone in our group (Cyril

Aubry, Xiaomeng Wang, Abderrahmane Taalba and Liming Qi) and everyone in my office for making me comfortable to stay here.

This work was supported by grants from the Natural Sciences and Engineering Research Council of Canada (NSERC) and Canadian International Polar Year (IPY) federal program office. I received a bourse de doctorat de recherche pour étudiants étrangers from the Fonds Québécois de la recherche sur la nature et les technologies (FQRNT) and an ISMER graduate fellowship.

RÉSUMÉ

Le monoxyde de carbone (CO) joue un rôle important dans le cycle du carbone organique marin et dans la chimie atmosphérique. L'océan est reconnu depuis longtemps comme la principale source de CO dans l'atmosphère. Dans la couche supérieure de l'océan, le CO est produit principalement à partir de la photodégradation de la matière organique dissoute chromophorique (CDOM). Cependant, des données récentes suggèrent que la photolyse de la matière organique particulaire (POM) peut également produire une quantité importante de CO dans la colonne d'eau. Pour comprendre la contribution de la POM à la photoproduction de CO et, par conséquent, évaluer l'importance de la photodégradation de la POM dans le cycle du carbone marin, ce travail a permis, pour la première fois, de quantifier le rendement apparent quantique de la photoproduction de CO (AQY CO) à partir de la POM et du CDOM dans des écosystèmes aquatiques de climat froid (c.-à-d., le sud-est de la mer de Beaufort) et tempéré (c.-à-d., la baie du Delaware). La variation spatio-temporelle du CO dans la glace de mer de première année, un autre écosystème important de l'Arctique, a également été évaluée. En outre, les spectres AQY CO de la POM et du CDOM provenant de cultures d'algues de glace ont été déterminés. La contribution de la POM et du CDOM à la photoproduction de CO à la base de la glace de mer a également été estimée.

La concentration de CO a fluctué de façon irrégulière dans la couche superficielle de la glace de mer. À la base de la glace, elle a toutefois suivi la concentration des algues, avec de faibles valeurs au début de la période d'accumulation des algues, un fort enrichissement pendant l'efflorescence et la période post-efflorescence, et un appauvrissement de nouveau pendant la fonte de la banquise. Les profils verticaux montrent une diminution de la concentration en CO de la surface vers la base de la glace

au début du printemps et ces profils sont variables pendant la saison de fonte. En présence de fortes biomasses algales à la base de la glace à la mi-printemps, le CO a été fortement enrichi à la base de la glace ($82,9 \pm 84 \text{ nmol L}^{-1}$) par rapport à la surface ($16,8 \pm 7 \text{ nmol L}^{-1}$). De plus, la banquise côtière contenait des teneurs en CO supérieures à celles de la glace dérivante. La concentration moyenne de CO dans la glace de mer pendant la campagne d'échantillonnage a été de $13,9 \pm 10 \mu\text{mol m}^{-2}$ et la production nette de CO pendant le bloom d'algues de glace a été évaluée à $13,2 \mu\text{mol m}^{-2}$. La glace de mer est reconnue comme une source importante de CO atmosphérique et elle pourrait contribuer à un flux annuel vers l'atmosphère de 7.4×10^7 moles de CO dans la zone d'étude.

Généralement, les AQYs CO des particules et du CDOM diminuent avec l'augmentation de la longueur d'onde, mais la forme du spectre dans le visible, en ce qui concerne les particules était supérieure et plus plate. Cette caractéristique a donné lieu à une production de CO par la lumière visible disproportionnellement élevée pour les particules. Ainsi, le ratio entre la photoproduction de CO par les particules et celle par le CDOM augmente avec la profondeur dans la zone euphotique et dans la glace de mer. Plus précisément, les spectres AQY CO des particules provenant de cultures d'algues de glace en phases de croissance exponentielles et sénescentes ont été plus élevés que ceux du CDOM des cultures, en particulier aux longues longueurs d'onde. Contrairement au CDOM, il y avait une photoproduction de CO substantielle à partir des particules aux longueurs d'ondes $> 600 \text{ nm}$. Étant donné que le flux de photons du rayonnement solaire atteignant la couche inférieure de la glace de mer est largement dominé par la lumière visible, notamment sous un couvert de neige, on s'attend à ce que la POM joue un rôle plus important que celui de la matière organique dissoute (DOM) dans l'accumulation de CO durant le bloom d'algues de glace. Toutefois, nous estimons que la contribution relative de la DOM à l'accumulation du CO dans la glace augmente avec la progression de la fonte de la neige et de la glace.

Dans le sud-est de la mer de Beaufort, l'AQY CO des particules a augmenté de l'estuaire et du plateau vers le bassin, tandis que celui du CDOM a suivi une tendance inverse. L'eau provenant du maximum profond de chlorophylle (DCM) a révélé des

dominée par le rayonnement ultraviolet (UV, 290-400 nm) alors que la lumière UV et visible a joué un rôle à peu près égal dans la production de CO à partir des particules.

Dans l'estuaire du Delaware, les valeurs du AQY CO ont été déterminées sur des échantillons d'eau de mer filtrée sur membranes de 0,2, 10 et 20 μm de porosité, afin d'évaluer l'effet de la taille de la matière organique sur l'efficacité de photoproduction de CO. En raison des propriétés distinctes de la matière organique le long de l'estuaire, la forme des spectres du CO AQY du CDOM et des particules a moins varié que celle obtenue lors d'études précédentes. Par conséquent, la lumière visible plutôt que l'UV a été le principal responsable de la photoproduction de CO à partir, à la fois, des particules et du CDOM dans la colonne d'eau. Les particules et le CDOM au milieu de la zone de turbidité maximum ont été plus photoréactifs que leurs homologues provenant de la terre ferme, en raison de la floculation, de l'adsorption et/ou de la désorption aux endroits où il y avait suffisamment de mélange de l'eau douce avec l'eau salée. Aucune différence significative dans la photoréactivité des particules en termes de production de CO n'a été trouvée entre les deux fractions de taille des particules le long de l'estuaire.

Selon notre modèle, la contribution des particules à la photoproduction totale de CO serait supérieure à 84% à la base de la glace de mer, de 12-32% en eau libre dans le secteur sud-est de la mer de Beaufort et de 29-77% dans l'estuaire du Delaware. En outre, la contribution des particules de petite taille ($<10 \mu\text{m}$) à la photoproduction totale de CO basée sur l'ensemble des particules a été plus grande dans l'estuaire du Delaware, car cette fraction de taille est la composante dominante des particules chromophoriques. Cette étude présente de nouvelles preuves que la photochimie des particules joue un rôle important dans le cycle du carbone océanique et des gaz traces, en particulier dans les eaux estuariennes et côtières et dans la glace de mer, des milieux où la photochimie des particules pourrait dépasser celle du CDOM.

Mot clés : monoxyde de carbone, photoproduction, le rendement apparent quantique, CDOM, les particules, la glace de mer, la mer de Beaufort, l'estuaire du Delaware

ABSTRACT

Carbon monoxide (CO) plays an important role in marine organic carbon cycle and in atmospheric chemistry. The ocean has long been recognized as an important source of atmospheric CO. In the upper ocean, CO is produced primarily from photodegradation of chromophoric dissolved organic matter (CDOM). However, recent evidence suggests that photolysis of particulate organic matter (POM) can also produce a significant amount of CO in the water column. To understand the contribution of POM to CO photoproduction and hence assess the importance of POM photodegradation to marine carbon cycling, this work for the first time quantified the spectrally resolved apparent quantum yields (AQYs) of CO photoproduction from POM, as well as from CDOM in cold (southeastern (SE) Beaufort Sea) and warm aquatic ecosystems (Delaware Bay). The spatiotemporal variation of CO concentration ([CO]) in first-year sea ice in the SE Beaufort Sea was also examined. CO AQY spectra of POM and CDOM harvested from ice algal cultures were determined to model the contributions of POM and CDOM to CO photoproduction in bottom sea ice.

[CO] fluctuated irregularly in surface ice but followed the biomass of ice algae in bottom ice, i.e. low at the start of ice algal accumulation, highly enriched during the peak-bloom and early post-bloom, and depleted again during sea ice melt. Vertical profile of CO typically decreased downward in early spring and was variable in the melting season. In the presence of high bottom ice algal biomass in mid-spring, CO was highly enriched in the bottom ($82.9 \pm 84 \text{ nmol L}^{-1}$) relative to the surface (CO: $16.8 \pm 7 \text{ nmol L}^{-1}$). Furthermore, landfast ice contained higher levels of CO than drifting ice. Cruise-mean CO inventory in sea ice was $13.9 \pm 10 \text{ } \mu\text{mol m}^{-2}$, and the net production of CO during the ice algal bloom was assessed to be $13.2 \text{ } \mu\text{mol m}^{-2}$. Sea ice is recognized as an important

source of atmospheric CO and might contribute 7.4×10^7 moles of CO a⁻¹ to the atmosphere in the study area.

Generally, CO AQYs of both particles and CDOM decreased with wavelength but the spectral shape of the particulate AQY was flatter in the visible regime. This feature resulted in a disproportionately higher visible light-driven CO production by particles, thereby increasing the ratio of particle- to CDOM-based CO photoproduction with depth in the euphotic zone and in sea ice. Specifically, CO AQY spectra of particles collected from ice algal cultures at the exponential and senescent phases were higher than the corresponding CDOM samples, particularly at long wavelengths. Unlike CDOM, at $\lambda > 600$ nm, there was prolific CO photoproduction from particles collected from ice algal cultures. Given that the photon flux of solar radiation reaching the bottom sea ice is overwhelmingly dominated by the visible regime, particularly under snow cover, POM is expected to play a far more important role than DOM in contributing to the CO accumulation during the ice algal bloom. The relative contribution from DOM, however, is estimated to increase with the progression of snow and ice melting.

In the SE Beaufort Sea, CO AQY of particles augmented from the estuary and shelf to the basin while that of CDOM trended inversely. Water from the deep chlorophyll maximum (DCM) layer revealed higher CO AQYs than did surface water for both particles and CDOM. CO AQY of particles exceeded that of CDOM on the shelf and in the basin but the sequence inversed in the estuary. In terms of depth-integrated production in the euphotic zone, CO formation from CDOM was dominated by the ultraviolet (UV, 290-400 nm) radiation whereas UV and visible light played roughly equal roles in CO production from particles.

In the Delaware Estuary, CO AQYs in 0.2-, 10- and 20- μ m filtered water samples were determined, to evaluate the size effect of organic matter on CO photoproduction efficiency. Owing to the distinct properties of organic matter along the estuary, the spectral shape of CO AQY of CDOM and particles were flatter than those in previous studies, and hence visible light, rather than UV, were the main contributor to CO photoproduction from both

particles and CDOM in the water column. Both particles and CDOM in the mid-TMZ were more photoreactive than their counterparts from land, due mainly to flocculation, adsorption and/or desorption during intense mixing of fresh water with saline seawater. No significant difference in particle photoreactivity in terms of CO production was found between the two size fractions of particles along the estuary.

Modeled CO photoproduction indicated that particles could contribute more than 84% in bottom sea ice, 12-32% in open water in the SE Beaufort Sea and 29%-77% in the Delaware Estuary to total CO photoproduction. Furthermore, small-sized particles ($< 10 \mu\text{m}$) accounted for more of particle-based CO photoproduction in the Delaware Estuary, since this size fraction is the dominant component of chromophoric particles. This study provides novel evidence that particle photochemistry is an important term in marine carbon and trace gas cycling, especially in estuarine and coastal waters and sea ice, where particle photochemistry may exceed that of CDOM.

Keywords: carbon monoxide, photoproduction, apparent quantum yield, CDOM, particles, sea ice, Beaufort Sea, Delaware Estuary

TABLE DES MATIÈRES

| | |
|--|--------|
| REMERCIEMENTS | IX |
| ACKNOWLEDGMENTS | XI |
| RÉSUMÉ | XIII |
| ABSTRACT..... | XVII |
| TABLE DES MATIÈRES..... | XXI |
| Liste des tableaux..... | XXV |
| Liste des figures | XXVII |
| Liste des abréviations | XXXI |
| Liste des symboles..... | XXXIII |
| CHAPITRE 1 INTRODUCTION | 1 |
| 1.1 PHOTOCIMIE DE LA MATIÈRE ORGANIQUE MARINE..... | 1 |
| 1.2 CYCLE BIOGÉOCHIMIQUE DU CO DANS L'OCÉAN | 3 |
| 1.3 MOTIVATIONS..... | 4 |
| 1.4 OBJECTIFS..... | 6 |
| CHAPITRE 2 VARIATIONS SPATIOTEMPORELLE DU CARBONE ORGANIQUE DISSOUS ET MONOXYDE DE CARBONE DANS LA GLACE DE MER DE PREMIERE ANNEE DANS L'OUEST DE L'ARCTIQUE CANIDIEN | 15 |
| RÉSUMÉ..... | 16 |
| ABSTRACT | 16 |
| 2.1 INTRODUCTION | 17 |
| 2.2 METHODS..... | 19 |
| 2.2.1 METEOROLOGY AND HYDROLOGY | 19 |

| | | |
|-------|--|-----------|
| 2.2.2 | CHLOROPHYLL <i>A</i> | 20 |
| 2.2.3 | DOC AND CO | 23 |
| 2.3 | RESULTS | 24 |
| 2.3.1 | GENERAL METEOROLOGICAL AND HYDROLOGICAL PROPERTIES..... | 24 |
| 2.3.2 | CHLOROPHYLL <i>A</i> , DOC, AND CO IN SURFACE AND BOTTOM SEA ICE..... | 28 |
| 2.3.3 | VERTICAL DISTRIBUTIONS OF CHL <i>A</i> , DOC, AND CO..... | 33 |
| 2.3.4 | VERTICAL DISTRIBUTIONS OF CHL <i>A</i> , DOC, AND CO..... | 36 |
| 2.4 | DISCUSSION | 38 |
| 2.4.1 | COMPARISON WITH PREVIOUS STUDIES..... | 38 |
| 2.4.2 | FACTORS CONTROLLING [DOC] AND [CO] IN SEA ICE..... | 39 |
| 2.4.3 | NET PRODUCTION OF DOC AND CO..... | 42 |
| 2.4.4 | CONTRIBUTION OF SEA ICE TO ATMOSPHERIC CO | 44 |
| 2.5 | SUMMARY AND CONCLUSIONS..... | 46 |
| | ACKNOWLEDGMENTS..... | 47 |
| | | |
| | CHAPITRE 3 PHOTOPRODUCTION DE MONOXYDE DE CARBONE A PARTIR DE MATIERES ORGANIQUES PARTICULAIRE ET DISSOUTE DANS LES CULTURES D'ALGUES DE GLACE..... | 49 |
| | RÉSUMÉ | 50 |
| | ABSTRACT..... | 50 |
| 3.1 | INTRODUCTION..... | 51 |
| 3.2 | METHODS | 53 |
| 3.2.1 | ICE ALGAL CULTURE INCUBATIONS | 53 |
| 3.2.2 | SAMPLE COLLECTION..... | 56 |
| 3.2.3 | IRRADIATION | 58 |
| 3.2.4 | SAMPLE ANALYSES | 59 |
| 3.2.5 | RETRIEVAL OF CO AQY..... | 61 |
| 3.3 | RESULTS | 63 |
| 3.3.1 | GENERAL CHEMICAL, BIOLOGICAL AND OPTICAL PROPERTIES | 63 |
| 3.3.2 | CONTROLS AND LINEARITY OF CO PHOTOPRODUCTION FROM PARTICLES. | 68 |

| | |
|---|-----------|
| 3.3.3 CO AQY SPECTRA..... | 70 |
| 3.3.4 Φ AND PHOTOREACTIVITY..... | 71 |
| 3.4 DISCUSSION..... | 77 |
| 3.4.1 COMPARE Φ_A WITH PREVIOUS STUDIES | 77 |
| 3.4.2 ACTION SPECTRA OF CO PHOTOPRODUCTION IN BOTTOM SEA ICE..... | 79 |
| 3.5 SUMMARY | 84 |
| ACKNOWLEDGMENTS | 85 |
| CHAPITRE 4 L'EFFICACITE SPECTRALE DE LA PHOTOPRODUCTION DE MONOXYDE DE CARBONE (CO) DANS L'ARCTIQUE CANADIEN DE L'OUEST: PARTICULES CONTRE SOLUTES | 87 |
| RÉSUMÉ..... | 88 |
| ABSTRACT | 89 |
| 4.1 INTRODUCTION | 91 |
| 4.2 METHODS..... | 93 |
| 4.2.1 STUDY AREA | 93 |
| 4.2.2 SAMPLING..... | 97 |
| 4.2.3 IRRADIATION..... | 100 |
| 4.2.4 ANALYSES..... | 101 |
| 4.2.5 RETRIEVAL OF CO AQY | 103 |
| 4.3 RESULTS AND DISCUSSION | 106 |
| 4.3.1 GENERAL PHYSICAL, BIOLOGICAL, AND CHEMICAL SETTINGS | 106 |
| 4.3.2 CO AQY SPECTRA..... | 109 |
| 4.3.3 PHOTOREACTIVITY OF CDOM AND PARTICLES..... | 116 |
| 4.3.4 ACTION SPECTRA OF CO PHOTOPRODUCTION | 118 |
| 4.3.5 MODELING CO PHOTOPRODUCTION..... | 123 |
| 4.4 SUMMARY | 129 |
| ACKNOWLEDGMENTS | 129 |

| | |
|--|------------|
| CHAPITRE 5 PHOTOPRODUCTION DE MONOXYDE DE CARBONE (CO) A PARTIR DE DIFFERENTES CLASSES DE TAILLE DE MATIERE ORGANIQUE DANS L'ESTUAIRE DU DELAWARE SOUS DES CONDITIONS HYDRO-BIOLOGIQUES CONTRASTEES | 131 |
| RÉSUMÉ | 132 |
| ABSTRACT..... | 133 |
| 5.1 INTRODUCTION..... | 134 |
| 5.2 METHODS | 135 |
| 5.2.1 STUDY SITE | 135 |
| 5.2.2 SAMPLING | 137 |
| 5.2.3 IRRADIATION | 142 |
| 5.2.4 DETERMINATION OF ABSORPTION SPECTRA OF CDOM AND PARTICLES... | 143 |
| 5.2.5 RETRIEVAL OF CO AQY SPECTRA | 145 |
| 5.3 RESULTS | 147 |
| 5.3.1 GENERAL HYDROLOGICAL, BIOLOGICAL AND METEOROLOGICAL CONDITIONS | 147 |
| 5.3.2 ABSORPTION COEFFICIENT OF CDOM..... | 148 |
| 5.3.3 ABSORPTION COEFFICIENT OF PARTICLES | 152 |
| 5.3.4 ABSORPTION COEFFICIENT OF PARTICLES | 154 |
| 5.3.5 Φ AND PHOTOREACTIVITY | 161 |
| 5.3.6 ACTION SPECTRA OF CO PHOTOPRODUCTION..... | 164 |
| 5.3.7 MODELING CO PHOTOPRODUCTION | 167 |
| 5.4 SUMMARY | 172 |
| ACKNOWLEDGMENTS..... | 173 |
| CHAPITRE 7 SOMMAIRE ET CONCLUSIONS | 175 |
| ANNEX 1..... | 181 |
| ANNEX 2..... | 189 |
| RÉFÉRENCES BIBLIOGRAPHIQUES..... | 193 |

LISTE DES TABLEAUX

| | |
|---|-----|
| Table 2-1 Sampling dates, locations and corresponding sea ice conditions..... | 22 |
| Table 2-2 Results of linear least-squares regression analysis between DOC, CO and Chl <i>a</i> in the bottom 10-cm sea ice layer..... | 32 |
| Table 2-3 Comparison of depth-integrated (i.e., column burden) and depth-weighted concentrations of Chl <i>a</i> , DOC, and CO between drifting and landfast sea ice and among different Chl <i>a</i> phases..... | 37 |
| Table 3-1 Information of selected ice algae and the incubation conditions..... | 55 |
| Table 3-2 Biological and optical properties of the particle samples..... | 65 |
| Table 3-3 Chemical and optical properties of the 0.2- μm filtered samples..... | 66 |
| Table 3-4 Fitted parameters of Eq. (3-4) for CDOM and Eq. (3-5) for particle samples, along with Φ_{330} and $\bar{\Phi}$ | 73 |
| Table 4-1 Sampling information along with salinity and water temperature..... | 99 |
| Table 4-2 Means and ranges of salinity, temperature, [Chl <i>a</i>], $a_{cdom,412}$, $a_{p,412}$, and $a_{phy,412}$: $a_{p,412}$ | 108 |
| Table 4-3 Fitted parameters for filtered (CDOM) and unfiltered (CDOM plus particles) samples, along with Φ_{330} and $\bar{\Phi}$ for CDOM, CDOM plus particles, and particles.... | 110 |

| | |
|--|-----|
| Table 4-4. Arithmetic means (\pm s.d.) of P_0 , P_{col} , ΣP_{col} , and $a_{p,412}:a_{cdom,412}$ in August 2009 based on individual stations within each sub-region..... | 127 |
| Table 4-5. $P_{cdom,col}$, $P_{p,col}$ ($\mu\text{mol m}^{-2} \text{d}^{-1}$), and $P_{p,col}:P_{cdom,col}$ based on ocean color data from remote sensing..... | 128 |
| Table 5-1 Station coordinates, sampling dates along with salinity, temperature, total water depth, Chl a and attenuation coefficient (k_d)..... | 139 |
| Table 5-2 Fitted parameters for function $\Phi_\lambda = m_1 \times \exp(m_2 \times (\lambda - 290))$ for 0.2-, 10- and 20- μm filtered water samples and the values of Φ_{330} and $\bar{\Phi}$ | 152 |
| Table 5-3 Modeled CO photoproduction rates at the surface (P_0) and in the water column (P_{col}) at each station in August and November..... | 170 |
| Table 5-4 Comparison of the contributions of particles to total CO photoproduction at the surface and in the water column with the values in other regions..... | 171 |

LISTE DES FIGURES

| | |
|---|----|
| Fig. 1-1 The identified sources and sinks of CO in the ocean..... | 8 |
| Fig. 2-1 Map of sea ice sampling stations..... | 21 |
| Fig. 2-2 Spatiotemporal variations of (a) daily averaged shortwave, and photosynthetic active radiation (PAR), (b) daily averaged air temperature, (c) sea ice temperature, and (d) bulk sea ice salinity from 17 March to 6 July 2008..... | 26 |
| Fig. 2-3 Depth profiles of sea ice salinity and temperature..... | 27 |
| Fig. 2-4 Spatiotemporal variations of (a) chlorophyll <i>a</i> (Chl <i>a</i>), (b) dissolved organic carbon (DOC), (c) carbon monoxide (CO) concentrations in surface and bottom sea ice layers from 17 March to 6 July 2008..... | 31 |
| Fig. 2-5 Depth profiles of sea ice chlorophyll <i>a</i> (Chl <i>a</i>), dissolved organic carbon (DOC), carbon monoxide (CO) concentrations..... | 35 |
| Fig. 3-1 Flow-chart of the main procedures of sample collection and processing..... | 57 |
| Fig. 3-2 Examples of absorption spectra of particles and CDOM..... | 67 |
| Fig. 3-3 Examples of [CO] along with irradiation time under full spectrum (A) and with dark incubation time (B)..... | 69 |
| Fig. 3-4 Example of CO photoproduction from CDOM and particles as a function of the nominal 50% cutoff wavelength..... | 74 |
| Fig. 3-5 Spectra of $\Phi_{cdom,\lambda}$ and $\Phi_{p,\lambda}$ as a function of wavelength..... | 75 |

| | |
|---|-----|
| Fig. 3-6 Lower and upper limits of $\Phi_{cdom,\lambda}$ of each culture | 76 |
| Fig. 3-7 Comparison of Φ_{λ} obtained in this study with previous studies..... | 78 |
| Fig. 3-8 Transmittance of landfast sea ice measured at the depth of 10 cm from the ice-water interface in Franklin Bay (southeastern Beaufort Sea) (A), the calculated solar irradiance ($\text{mol m}^{-2} \text{h}^{-1}$) at this depth (B) and the action spectra of CO photoproduction ($\text{mol CO m}^{-2} \text{h}^{-1}$) from CDOM and particles for <i>P. taeniata</i> at the 10-cm interface from the bottom (surface action spectra) (C) and in the bottom 10 cm layer (depth-integrated action spectra) (D)..... | 82 |
| Fig. 3-9 Relative contributions of particles and CDOM to total CO photoproduction in the bottom 10 cm first-year sea ice under different snow cover conditions..... | 83 |
| Fig. 4-1 Sampling map..... | 96 |
| Fig. 4-2 Typical $\Phi_{cdom,\lambda}$, $\Phi_{p,\lambda}$, and $\Phi_{t,\lambda}$ spectra from the Mackenzie River estuary (Sta. 697), Mackenzie Shelf (Sta. 280), and Canada Basin (Sta. 345 and 430)..... | 112 |
| Fig. 4-3 Comparison of mean $\bar{\Phi}$ of particles and CDOM and the ratio of the two among the three sub-regions..... | 113 |
| Fig. 4-4 Relationships between $\bar{\Phi}_{cdom}$ and $a_{cdom,412}$ (A) and between $\bar{\Phi}_p$ and $a_{p,412}$ (B)..... | 115 |
| Fig. 4-5. Modeled surface spectral solar irradiance (A), a_{cdom} and a_p (B), surface CO action spectra (C and D) and depth-integrated CO action spectra (E and F)..... | 121 |
| Fig. 4-6. Modeled vertical profiles of normalized solar irradiance (A), CO photoproduction rate ($\text{mol CO m}^{-3} \text{h}^{-1}$) from CDOM (B) and particles (C), the contribution of visible to full-spectrum CO photoproduction (D), and the ratio of full-spectrum particle-based to CDOM-based CO photoproduction (E) at Sta. 430..... | 122 |

| | |
|---|-----|
| Fig. 5-1 Map of sampling stations for the two cruises..... | 141 |
| Fig. 5-2 Measured $a_{cdom,412}$ and ideal two end-member conservative mixing lines of August cruise (A) and November cruise (B)..... | 150 |
| Fig. 5-3 Actual $S_{275,295}$ and ideal two end-member conservative mixing lines of August cruise (A) and November cruise (B)..... | 151 |
| Fig. 5-4 The distributions of $a_{p,412}$ of different sizes (<20 μm , <10 μm and 10-20 μm) along with salinity for August cruise (A) and November cruise (B)..... | 153 |
| Fig. 5-5 $\Phi_{cdom,\lambda}$, $\Phi_{<10,\lambda}$ and $\Phi_{<20,\lambda}$ spectra for August cruise (A) and November cruise (B) and seasonal comparison of $\Phi_{cdom,\lambda}$ (C), $\Phi_{<10,\lambda}$ and $\Phi_{<20,\lambda}$ (D)..... | 159 |
| Fig. 5-6 Comparison $\Phi_{cdom,\lambda}$ (A) and $\Phi_{<20,\lambda}$ (B) spectra in this study with $\Phi_{cdom,\lambda}$ and $\Phi_{t,\lambda}$ spectra published in other studies..... | 160 |
| Fig. 5-7 $\bar{\Phi}_{cdom}$, $\Phi_{<10,\lambda}$ and $\Phi_{<20,\lambda}$ at each station for August cruise (A) and November cruise (B)..... | 163 |
| Fig. 5-8 Surface CO action spectra for August (A) and November (B), and depth-integrated CO action spectra for August (C) and November (D)..... | 166 |

LISTE DES ABRÉVIATIONS

| | |
|------------------|---|
| AQY | apparent quantum yield |
| ASW | artificial seawater |
| CB | Canada Basin |
| Chl <i>a</i> | chlorophyll <i>a</i> |
| CO | carbon monoxide |
| CO ₂ | carbon dioxide |
| DCM | deep chlorophyll maximum |
| DMS | dimethylsulfide |
| DOC | dissolved organic carbon |
| DOM | dissolved organic matter |
| HCP | high chlorophyll phase |
| LCP | low chlorophyll phase |
| MRE | Mackenzie River estuary |
| MS | Mackenzie Shelf |
| N ₂ O | nitrous oxide |
| NIAA | natural ice algal assemblage |
| SGT-E | salinity gradient transect-east channel |
| SGT-W | salinity gradient transect-west channel |

| | |
|--------|-------------------------------------|
| OCIO | chlorine dioxide |
| OCS | carbonyl sulfide |
| OM | organic matter |
| PAR | photosynthetically active radiation |
| POC | particulate organic carbon |
| POM | particulate organic matter |
| SPM | suspended particulate matter |
| TMZ | turbidity maxima zone |
| UV/UVR | ultraviolet radiation (290- 400 nm) |
| UVA | ultraviolet-A (320- 400 nm) |
| UVB | ultraviolet-B (290- 320 nm) |

LISTE DES SYMBOLES

| Symbol | Meaning | Unit |
|-----------------|---|----------|
| a | absorption coefficient | m^{-1} |
| a_{cdom} | absorption coefficient of CDOM | m^{-1} |
| a'_{cdom} | absorption coefficient of CDOM contained in ASW | m^{-1} |
| a_i | absorption coefficient of pure ice | m^{-1} |
| a_{nap} | absorption coefficient of non-algal particles | m^{-1} |
| $a_{nap,10}$ | absorption coefficient of non-algal particles with the size of $< 10 \mu m$ | m^{-1} |
| $a_{nap,10-20}$ | absorption coefficient of non-algal particles with the size between $10-20 \mu m$ | m^{-1} |
| $a_{nap<20}$ | absorption coefficient of non-algal particles with the size of $< 20 \mu m$ | m^{-1} |
| a_p | absorption coefficient of particles | m^{-1} |
| $a_{p<10}$ | absorption coefficient of particles with the size of $< 10 \mu m$ | m^{-1} |
| $a_{p,10-20}$ | absorption coefficient of particles with the size between $10-20 \mu m$ | m^{-1} |
| $a_{p<20}$ | absorption coefficient of particles with the size of $< 20 \mu m$ | m^{-1} |
| a_{phy} | absorption coefficient of phytoplanktonic pigments | m^{-1} |

| | | |
|------------------------|---|------------------------|
| $a_{phy<10}$ | absorption coefficient of phytoplanktonic pigments with the size of $< 10 \mu\text{m}$ | m^{-1} |
| $a_{phy,10-20}$ | absorption coefficient of phytoplanktonic pigments with the size between $10\text{-}20 \mu\text{m}$ | m^{-1} |
| $a_{phy<20}$ | absorption coefficient of phytoplanktonic pigments with the size of $< 20 \mu\text{m}$ | m^{-1} |
| a_t | absorption coefficient of the sum of a_{cdom} , a_p , and a_w | m^{-1} |
| a_w | absorption coefficient of pure water | m^{-1} |
| A | clearance area of filters for retaining particles | m^2 |
| bb_m | particle backscattering coefficient | m^{-1} |
| β | path length amplification factor | unitless |
| B_f | brine volume fraction | unitless |
| c | volume attenuation coefficient | m^{-1} |
| $[\text{Chl } a]_{cb}$ | column burden of chlorophyll a | mg m^{-2} |
| $[\text{Chl } a]_{dw}$ | depth-weighted concentration of chlorophyll a | $\mu\text{g L}^{-1}$ |
| $[\text{CO}]_{cb}$ | column burden of CO | $\mu\text{mol m}^{-2}$ |
| $[\text{CO}]_{dw}$ | depth-weighted concentration of CO | nmol L^{-1} |
| $[\text{DOC}]_{cb}$ | column burden of CO | g C m^{-2} |
| $[\text{DOC}]_{dw}$ | depth-weighted concentration of DOC | mg C L^{-1} |
| k_d | diffuse attenuation coefficient | m^{-1} |
| λ | wavelength | nm |
| L | light path length of irradiation cells | m |
| OD | optical density | unitless |

| | | |
|---------------------|---|---|
| OD_{blank} | optical density of blank GF/F filter | unitless |
| OD_{cdom} | optical density of CDOM | unitless |
| OD_f | optical density of particles | unitless |
| P_0 | modeled CO photoproduction rate at the surface | $\mu\text{mol CO m}^{-3} \text{d}^{-1}$ |
| $P_{cdom,0}$ | modeled CO photoproduction rate at the surface from CDOM | $\mu\text{mol CO m}^{-3} \text{d}^{-1}$ |
| $P_{<10,0}$ | modeled CO photoproduction rate at the surface for 10 μm filtered samples | $\mu\text{mol CO m}^{-3} \text{d}^{-1}$ |
| $P_{<20,0}$ | modeled CO photoproduction rate at the surface for 20 μm filtered samples | $\mu\text{mol CO m}^{-3} \text{d}^{-1}$ |
| $P_{p,0}$ | CO photoproduction rate at the surface from particles | $\mu\text{mol CO m}^{-3} \text{d}^{-1}$ |
| P_z | modeled CO photoproduction rate at depth z | $\mu\text{mol CO m}^{-3} \text{d}^{-1}$ |
| P_{col} | depth-integrated CO photoproduction rate in the euphotic zone | $\mu\text{mol CO m}^{-2} \text{d}^{-1}$ |
| $P_{cdom,col}$ | depth-integrated CO photoproduction rate in the euphotic zone from CDOM | $\mu\text{mol CO m}^{-2} \text{d}^{-1}$ |
| $P_{<10,col}$ | depth-integrated CO photoproduction rate in the euphotic zone for 10 μm filtered samples | $\mu\text{mol CO m}^{-2} \text{d}^{-1}$ |
| $P_{<20,col}$ | depth-integrated CO photoproduction rate in the euphotic zone for 20 μm filtered samples | $\mu\text{mol CO m}^{-2} \text{d}^{-1}$ |
| $P_{p,col}$ | depth-integrated CO photoproduction rate in the euphotic zone from particles | $\mu\text{mol CO m}^{-2} \text{d}^{-1}$ |
| $\sum P_{col}$ | area-integrated CO photoproduction in the euphotic zone | $\text{mol CO m}^{-2} \text{d}^{-1}$ |
| $\sum P_{cdom,col}$ | area-integrated CO photoproduction in the euphotic zone from CDOM | $\text{mol CO m}^{-2} \text{d}^{-1}$ |

| | | |
|---------------------|---|--|
| $\sum P_{p, col}$ | area-integrated CO photoproduction in the euphotic zone from particles | mol CO m ⁻² d ⁻¹ |
| Φ | CO apparent quantum yield (AQY) | mol CO (mol photons) ⁻¹ |
| Φ_{cdom} | AQY from CDOM | mol CO (mol photons) ⁻¹ |
| $\Phi_{<10}$ | AQY for 10 μ m filtered samples | mol CO (mol photons) ⁻¹ |
| $\Phi_{<20}$ | AQY for 20 μ m filtered samples | mol CO (mol photons) ⁻¹ |
| Φ_p | AQY from particles | mol CO (mol photons) ⁻¹ |
| Φ_t | AQY from CDOM plus particles | mol CO (mol photons) ⁻¹ |
| $\bar{\Phi}$ | solar irradiance spectrum-weighted mean Φ (290-600 nm) | mol CO (mol photons) ⁻¹ |
| $\bar{\Phi}_{cdom}$ | solar irradiance spectrum-weighted mean Φ (290-600 nm) for CDOM | mol CO (mol photons) ⁻¹ |
| $\bar{\Phi}_{<10}$ | solar irradiance spectrum-weighted mean Φ (290-600 nm) for 10 μ m filtered samples | mol CO (mol photons) ⁻¹ |
| $\bar{\Phi}_{<20}$ | solar irradiance spectrum-weighted mean Φ (290-600 nm) for 20 μ m filtered samples | mol CO (mol photons) ⁻¹ |
| $\bar{\Phi}_p$ | solar irradiance spectrum-weighted mean Φ (290-600 nm) for particles | mol CO (mol photons) ⁻¹ |
| $\bar{\Phi}_t$ | solar irradiance spectrum-weighted mean Φ (290-600 nm) for CDOM plus particles | mol CO (mol photons) ⁻¹ |
| Q | photon flux just below the upper surface of the vials | mol photons m ⁻² s ⁻¹ nm ⁻¹ |
| Q_a | photons absorbed by CDOM, or CDOM plus particles | mol photons m ⁻² s ⁻¹ nm ⁻¹ |
| Q_0 | modeled surface solar photon fluxes | mol photons m ⁻² h ⁻¹ nm ⁻¹ |
| $Q_{0.}$ | scalar photon flux just beneath the sea surface | mol photons m ⁻² d ⁻¹ nm ⁻¹ |
| $Q_{d0.}$ | downwelling photon flux just beneath the sea surface | mol photons m ⁻² d ⁻¹ nm ⁻¹ |

| | | |
|---------------|---|--|
| Q_z | photon flux at depth z (m) | mol photons $\text{m}^{-2} \text{d}^{-1} \text{nm}^{-1}$ |
| S | cross-section of the irradiation cells | m^2 |
| $S_{275-295}$ | the spectral slope of CDOM in the wavelength interval of 275-295 nm | nm^{-1} |
| V | filtered volume of seawater through GF/F filters | m^3 |
| A_0 | surface CO action spectrum | mol CO $\text{m}^{-3} \text{h}^{-1} \text{nm}^{-1}$ |
| $A_{cdm,0}$ | surface CO action spectrum of CDOM | mol CO $\text{m}^{-2} \text{h}^{-1} \text{nm}^{-1}$ |
| $A_{p,0}$ | surface CO action spectrum of particles | mol CO $\text{m}^{-2} \text{h}^{-1} \text{nm}^{-1}$ |
| A_z | CO action spectrum at depth z | mol CO $\text{m}^{-2} \text{h}^{-1} \text{nm}^{-1}$ |
| A_{col} | depth-integrated CO action spectrum | mol CO $\text{m}^{-2} \text{h}^{-1} \text{nm}^{-1}$ |
| $A_{cdm,col}$ | depth-integrated CO action spectrum of CDOM | mol CO $\text{m}^{-2} \text{h}^{-1} \text{nm}^{-1}$ |
| $A_{p,col}$ | depth-integrated CO action spectrum of particles | mol CO $\text{m}^{-2} \text{h}^{-1} \text{nm}^{-1}$ |

CHAPITRE 1

INTRODUCTION

1.1 PHOTOCHEMIE DE LA MATIÈRE ORGANIQUE MARINE

Globalement, chaque année, les rivières transportent environ $0,4 \times 10^{15}$ g C de la matière organique (OM) (c'est-à-dire la matière organique dissoute (DOM) plus la matière organique particulaire (POM)) à l'océan (Hedges et al., 1997). Cependant, moins de la moitié des apports fluviaux de la OM (principalement POM) est enfouie dans les sédiments marins et seule une petite fraction de la MO dans l'océan ouvert est d'origine terrestre. Par ailleurs, seulement $\sim 0,4\%$ de la production primaire mondiale annuelle (PP) peut être en fin de compte retenu dans les eaux profondes (Hedges, 2002). La majorité de la MO est reminéralisée en dioxyde de carbone (CO_2) durant le transport (OM terrestre) et après avoir été produite (OM marine). Des études récentes apportent de plus en plus de preuves que la phototransformation (Mopper et Kieber, 2002; Zafiriou, 2002) et la consommation microbienne (Moran et al, 2000; Vähätalo et Wetzel, 2004; Benner et Kaiser, 2010) sont principalement responsables de la perte en OM dans les écosystèmes aquatiques.

Au cours des dernières décennies, beaucoup d'attention a été accordée à la photochimie de la fraction chromophorique de la DOM (CDOM) (Mopper et Kieber, 2002; Zafiriou, 2002; Zepp, 2003), puisque le CDOM est un important absorbeur du rayonnement ultraviolet (UV) et visible dans les eaux naturelles (Blough et al., 1993; Nelson et al., 1998; Siegel et al., 2002). Écologiquement parlant, l'absorption de la lumière par la CDOM, d'une part, protège les organismes marins contre les rayons UV nocifs (Schindler et al., 1996; Williamson et al., 1999) alors que, d'autre part, elle limite la production primaire en captant une partie du rayonnement actif pour photosynthèse (PAR, 400-700 nm) (Le Fouest et al., 2010; Mei et al., 2010). La diminution de l'absorbance du CDOM (c.-à-d le

photoblanchiment) après photo-oxydation dans la couche supérieure des océans augmente la pénétration du rayonnement UV et la disponibilité en PAR dans la colonne d'eau, ce qui affecte l'écologie marine (Zepp, 2003). Biogéochimiquement, la photochimie du CDOM peut directement reminéraliser la DOM en CO_2 et en monoxyde de carbone (CO) (Miller et Zepp, 1995), et elle peut transformer le carbone organique dissous (DOC) réfractaire en substrats biolabiles (Kieber et al., 1989; Miller et al., 2002) ou vice versa (Kieber et al., 1997; Benner et Biddanda, 1998). Ce processus peut également affecter le cycle de l'azote marin en transformant l'azote organique dissous (DON) réfractaire en azote inorganique biodisponible (par exemple ammonium, nitrite) (Bushaw et al., 1996; Vähätalo et Zepp, 2005; Xie et al., 2012) et par une demande accrue des bactéries pour les nutriments inorganiques (Smith et Benner, 2005). En outre, la photochimie du CDOM modifie la toxicité et la biodisponibilité de certains métaux, tels que le fer et le cuivre, et par conséquent leur sort et leur transport (Miller et al., 1995; Voelker et Sedlak, 1995; Voelker et al., 2000). Certains biomarqueurs importants, tels que la lignine et les acides aminés, peuvent être dégradés photochimiquement (Opsahl et Benner, 1998; Benner et Kaiser, 2010). Pendant la photodégradation du CDOM, des composés oxygénés très réactifs environnementalement et biologiquement (par exemple, $\text{HO}\cdot$, O_2^- , et H_2O_2) sont formés (Zafiriou et al., 1984; Blough et Zepp, 1995), et influent sur divers processus biologiques et chimiques dans l'eau de surface éclairée par le soleil. De plus, les processus photochimiques impliquant le CDOM produisent (par exemple, monoxyde de carbone (CO) et sulfure de carbonyle (COS)) ou décomposent (par exemple sulfure de diméthyle (DMS)) certains gaz en traces actifs dans l'atmosphère qui affectent la composition chimique de l'atmosphère et le bilan radiatif de la terre (Thompson, 1992; Brimblecombe, 2003).

En contraste avec les énormes efforts et le progrès réalisés dans la photochimie du CDOM, beaucoup moins d'attention a été accordée à la photodégradation de la POM. La similitude entre les spectres d'absorption de la POM et du CDOM (Kirk, 1980) suggère toutefois que la POM pourrait subir des processus photochimiques analogues à ceux qui affectent la DOM. Par ailleurs, la photochimie de la POM pourrait être plus efficace grâce à

l'enrichissement de substrats organiques et/ou de métaux photoréactifs (par exemple Fe, Cu et Mn) dans des micro-environnements localisés sur ou à l'intérieur des particules (Zafiriou, 2002), comme le suggèrent par des études sur la photodégradation de chlorophylles et de lipides insaturés de phytoplancton (par exemple SooHoo et Kiefer, 1982; Nelson, 1993; Rontani, 2001). Les premières études ont montré que l'irradiation de détritiques de certaines plantes vasculaires produit du CO (Tarr et al., 1995) et de CO₂ (Anesio et al., 1999a) et libère du DOC (Anesio et al., 1999b). Plus récemment, quelques études ont rapporté d'importantes pertes de carbone organique particulaire (POC) et des productions de DOC, CO₂, DON, et de CDOM issues de l'irradiation contrôlée des remises en suspension des sédiments fluviaux et côtiers (Kieber et al., 2006 ; Riggsbee et al., 2008; Pisani et al., 2011; Shank et al., 2011; Estapà et al., 2012a). Des résultats similaires ont été rapportés pour les détritiques de la flagellés verts *Tetraselmis sp.*, avec la découverte additionnelle d'une production photochimique d'ammonium (c.-à-d. une <<photoammonification>>) (Mayer et al., 2009; Estapà et Mayer, 2010). Ces découvertes récentes ont stimulé le débat sur l'importance de savoir si la photodégradation de la DOM peut effectivement affecter la matière organique et les cycles des éléments dans les écosystèmes des rivières et des océans (Kieber et al., 2006; Xie et Zafiriou, 2009; Pisani et al., 2011; Estapà et al., 2012a). Par ailleurs, il est important de comparer quantitativement la photochimie de la POM avec celle de la DOM, puisque les études précédentes évaluant les flux des principaux photoproduits (par exemple DIC, CO, NH₄⁺) ont généralement ignoré la contribution de la POM (Bélanger et al., 2006; Xie et Zafiriou, 2009; Xie et al., 2012).

1.2 CYCLE BIOGÉOCHIMIQUE DU CO DANS L'OcéAN

Le CO est le principal puits de radicaux d'hydroxyde troposphériques (OH[•]) et il réduit ainsi la capacité oxydante de l'atmosphère et agit comme un gaz à effet de serre indirect dans l'atmosphère (Thompson, 1992). L'océan a longtemps été reconnu comme une source de CO atmosphérique (Conrad et Seiler, 1980). Dans l'océan supérieur, le CO est produit

principalement par photolyse du CDOM (Conrad et Seiler, 1980; Zafiriou et al., 2003; Stubbins et al., 2006a; Xie et al., 2009a). En outre, le CO peut également être produit par la dégradation thermique de la DOM (également appelée production foncée) (Xie et al., 2005; Zhang et al., 2008; Zhang et Xie, 2012). Certains organismes marins peuvent aussi produire du CO par processus biologiques (King et al., 2001; Gros et al., 2009), même si cela reste toutefois à confirmer. Dans la couche supérieure des océans, la consommation microbienne et l'échange air-mer sont les principaux puits de CO, et une petite partie du CO peut être transférée dans l'océan profond par le mélange vertical (Kettle, 2005). Les sources et les puits de CO actuellement connus dans l'océan sont présentés dans la figure. 1-1. Le cycle biogéochimique du CO des océans est important parce que 1) le CO est sans doute le sous-produit issu de la photodégradation du CDOM qui est mesurable avec le plus d'exactitude et le photoproduit inorganique le plus abondant après le CO₂, 2) le CO peut être utilisé comme un proxy d'autres photoproduits qui sont plus difficiles à mesurer, comme le CO₂ (Miller et Zepp, 1995; Mopper et Kieber, 2000) et la DOM biolabile (Miller et al., 2002), 3) le CO est une source d'énergie et carbone pour certains microbes marins (King et Weber, 2007; Moran et Miller, 2007), 4) le CO est une espèce utile pour évaluer la cinétique de consommation microbienne des solutés dilués dans les eaux marines (Xie et al., 2009b), et 5) le CO est un excellent traceur pour modéliser les interactions dans la dynamique de mélange, l'optique, la photochimie, la biologie et les échanges gazeux air-mer dans la partie supérieure de l'océan (Doney et al., 1995; Kettle, 2005).

1.3 MOTIVATIONS

La photoproduction de CO à partir du CDOM a été largement étudiée dans différents écosystèmes aquatiques au cours des dernières décennies, y compris les lacs (Bourbonnière et al., 1997), les estuaires (Law et al., 2002; Zhang et al., 2006; Stubbins et al., 2011), les eaux côtières (Day et Faloona, 2009; Xie et al., 2009a), et l'océan ouvert (Zafiriou et al., 2003; Stubbins et al., 2006a). Des données récentes suggèrent que la photolyse de la POM,

comme le CDOM, peut également produire une quantité importante de CO (Xie et Zafiriou, 2009; Stubbins et al, 2011). Toutefois, Xie et Zafiriou (2009) n'ont rapporté que les résultats préliminaires (c.-à-d la contribution globale des particules à la photoproduction totale de CO) pour un nombre limité d'échantillons, tandis que Stubbins et al. (2011) ont estimé la photoproduction potentielle de CO à partir des particules dans l'estuaire de la Tyne en supposant que l'efficacité spectrale (c.-à-d le rendement quantique apparent, AQY¹) de la photoproduction de CO à partir de particules était la même que celle du CDOM. Par conséquent, les résultats obtenus par ces études sont insuffisants pour les extrapoler à de plus grandes échelles spatiales et temporelles.

Pour mieux comprendre la contribution des particules dans la photoproduction de CO et donc l'implication de la photochimie des particules du cycle du carbone marin, d'autres études sont nécessaires pour élucider 1) les spectres AQY de CO des particules sur de grandes échelles spatiales et temporelles; 2) l'effet des propriétés des particules, comme l'historique de lumière, l'origine (terrestre contre marine), la variabilité (les cellules vivantes versus les détritiques) et la taille des particules, sur les spectres AQY de CO; 3) les facteurs environnementaux influençant la photoproduction de CO à partir des particules, tels que la salinité, le pH et la température de l'eau.

Par ailleurs, une enquête préliminaire sur le terrain a révélé que le CO est enrichi dans la couche inférieure de la banquise arctique de première année au cours de la prolifération d'algues de glace et suggère que la photo-oxydation du CDOM pourrait être un contributeur majeur à l'accumulation de CO observée dans la glace de l'Arctique (Xie et Gosselin, 2005). Cependant, des mesures de terrain sur des échelles de temps et d'espace plus larges sont nécessaires pour mieux comprendre la variabilité saisonnière et spatiale de la distribution du CO dans la glace de mer et pour mieux contraindre son origine. En effet, je fais l'hypothèse que les particules contribuent à l'enrichissement du CO à la base de la

¹ CO AQY est défini comme le nombre de moles de CO produites par mole de photons absorbés par un ensemble donné de matériaux absorbant la lumière à longueur d'onde λ .

glace de mer par les processus photochimiques et biologiques, en tenant compte des mêmes procédés dans l'eau de mer (Xie et Zafiriou 2009; Gros et al, 2009.). En particulier, il faut évaluer l'importance relative des particules pour la photoproduction totale de CO à la base de la glace de mer, surtout pendant la prolifération d'algues de glace.

1.4 OBJECTIFS

Utilisant le CO comme proxy du processus de photodégradation du CDOM, l'objectif global de ce projet est de mieux comprendre l'importance relative des particules et la photochimie de CDOM dans divers écosystèmes marins. L'objectif sera atteint par les objectifs spécifiques suivants:

- 1) Examiner la variation spatiotemporelle de CO dans les glaces de mer de première année dans le sud-est (SE) de la mer de Beaufort, et évaluer la production nette de CO dans la glace de mer pendant l'efflorescence des l'algues de glace;
- 2) Déterminer les spectres AQY de CO à partir du CDOM et les particules récoltées sur les cultures d'algues de glace dans les phases croissantes (exponentielles et décroissantes) et modéliser l'importance relative des particules et du CDOM dans la photoproduction de CO dans la glace de mer de fond au cours des efflorescences d'algues de glace;
- 3) Déterminer les spectres AQY de CO à partir du CDOM et des particules dans l'eau de mer en surface et au maximum profond de chlorophylle (DCM) dans le SE de la mer de Beaufort;
- 4) Déterminer les spectres AQY de CO du CDOM et les particules fractionnées par taille dans l'estuaire du Delaware;

- 5) Modéliser la contribution relative des particules et du CDOM à la photoproduction totale de CO dans la colonne d'eau de mer du SE de la mer de Beaufort et dans l'estuaire du Delaware.

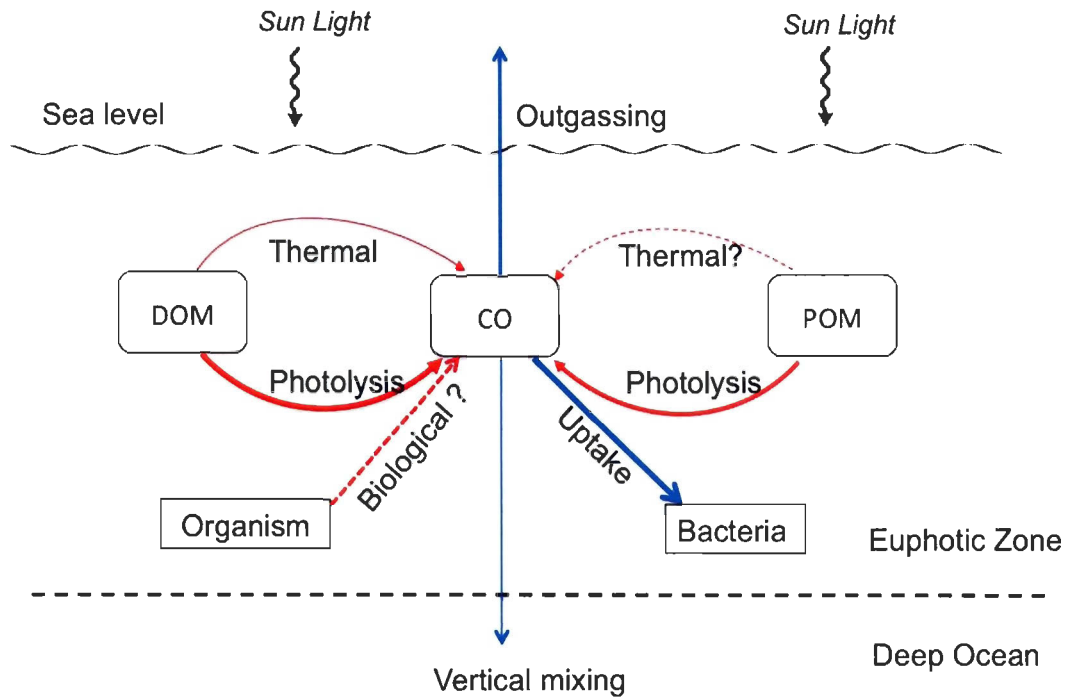


Fig. 1-1 Known sources and sinks of CO in the ocean. Red arrows denote sources, blue arrows denote sinks, and the size of arrows represents the relative strength of the sources or sinks. “?” denotes the pathway needs to be further confirmed.

Introduction

1.1 Photochemistry of marine organic matter

Globally, the rivers transport approximately 0.4×10^{15} g C of organic matter (OM) (i.e. dissolved organic matter (DOM) plus particulate organic matter (POM)) to the ocean per year (Hedges et al., 1997). However, less than half of the riverine input of OM (mainly POM) is buried in marine sediment and only a small fraction of OM in the open ocean is of terrestrial origin. Furthermore, 0.2×10^{15} g C a⁻¹, only ~ 0.4% of the yearly global primary production (PP) can be ultimately sequestered to the deep ocean (Hedges, 2002). The majority of OM is remineralized to carbon dioxide (CO₂) during transport (terrestrial OM) and after being produced (marine OM). Recent studies provide growing evidence that phototransformation (Mopper and Kieber, 2002; Zafiriou, 2002) and microbial consumption (Moran et al., 2000; Vähätalo and Wetzel, 2004; Benner and Kaiser, 2010) are mainly responsible for the loss of terrestrial and marine OM.

During the past decades, much attention has been paid to chromophoric DOM (CDOM) photochemistry (Mopper and Kieber, 2002; Zafiriou, 2002; Zepp, 2003), since CDOM is an important light absorber at both the ultraviolet (UV) and visible wavelengths in natural waters (Blough et al., 1993; Nelson et al., 1998; Siegel et al., 2002). Ecologically, the absorption of light by CDOM, on one hand, protects marine organisms against deleterious UV radiation (Schindler et al., 1996; Williamson et al., 1999) while, on the other hand, it curbs primary production if the availability of photosynthetically active radiation (PAR, 400-700 nm) limits photosynthesis (Le Fouest et al., 2010; Mei et al., 2010). The decrease in CDOM absorbance (i.e. photobleaching) after photooxidation in the upper ocean increases the penetration of UV radiation and the availability of PAR in the water column, thereby affecting marine ecology (Zepp, 2003). Biogeochemically, CDOM photochemistry can directly remineralize DOM to CO₂ and carbon monoxide (CO) (Miller and Zepp, 1995), and convert refractory dissolved organic carbon (DOC) to bio-labile substrates

(Kieber et al., 1989; Miller et al., 2002) or vice versa (Kieber et al., 1997; Benner and Biddanda, 1998). This process can also affect marine nitrogen cycling by transforming refractory dissolved organic nitrogen (DON) to bio-available inorganic nitrogen (e.g. ammonium, nitrite) (Bushaw et al., 1996; Vähätalo and Zepp, 2005; Xie et al., 2012) and through enhanced bacterial demand for inorganic nutrients (Smith and Benner, 2005). Furthermore, CDOM photochemistry alters the toxicity and bioavailability of certain metals, such as Fe and Cu, and hence their fate and transport (Miller et al., 1995; Voelker and Sedlak, 1995; Voelker et al., 2000). Some important biomarkers, such as lignin and amino acids, can be degraded photochemically (Opsahl and Benner, 1998; Benner and Kaiser, 2010). During CDOM photodegradation, environmentally and biologically reactive oxygen species (e.g. $\text{HO}\cdot$, O_2^- , and H_2O_2) are formed (Zafiriou et al., 1984; Blough and Zepp, 1995), which influence various biological and chemical processes in the sunlit surface water. In addition, CDOM photoprocesses produce (e.g. carbon monoxide (CO) and carbonyl sulfide (OCS)) or decompose (e.g. dimethyl sulfide (DMS)) certain atmospherically active trace gases that affect the chemical composition of the atmosphere and the Earth's radiative balance (Thompson, 1992; Brimblecombe, 2003).

In contrast to the enormous efforts and progress made in CDOM photochemistry, much less attention has been paid to POM photodegradation. The similarity in the absorption spectrum between POM and CDOM (Kirk, 1980), however, suggests that POM may undergo photochemical processes analogous to those of CDOM. Besides, POM photochemistry could be more efficient due to enrichment of organic substrates and/or photoreactive metals (e.g. Fe, Cu, Mn) in localized microenvironments on or within particles (Zafiriou, 2002), as suggested by studies on photodegradation of chlorophylls and unsaturated lipids of phytoplankton (e.g. SooHoo and Kiefer, 1982; Nelson, 1993; Rontani, 2001). Early studies have demonstrated that irradiation of detritus of certain vascular plants produces CO (Tarr et al., 1995) and CO_2 (Anesio et al., 1999a) and releases DOC (Anesio et al., 1999b). More recently, a few groups have reported significant losses of particulate organic carbon (POC) and productions of DOC, CO_2 , DON, and CDOM from controlled

irradiation of resuspensions of river and coastal sediments (Kieber et al., 2006; Riggsbee et al., 2008; Pisani et al., 2011; Shank et al., 2011; Estapa et al., 2012a). Similar results have been reported for the detritus of green flagellate *Tetraselmis sp.*, with an added finding of ammonium production (i.e. photoammonification) (Mayer et al., 2009; Estapa and Mayer, 2010). These recent findings have stimulated discussion on whether POM photodegradation can effectively affect organic matter and elemental cycles in river and oceanic ecosystems (Kieber et al., 2006; Xie and Zafiriou, 2009; Pisani et al., 2011; Estapa et al., 2012a). Moreover, it is important to quantitatively compare POM with DOM photochemistry, since previous studies assessing fluxes of major photoproducts (e.g. DIC, CO, NH_4^+) usually ignored the POM contribution (Bélanger et al., 2006; Xie et Zafiriou, 2009; Xie et al., 2012).

1.2 Biogeochemical cycling of CO in the ocean

CO is the main sink of tropospheric hydroxide radicals (OH^*) and hence reduces the oxidizing capacity of the atmosphere and acts as an indirect greenhouse gas in the atmosphere (Thompson, 1992). The ocean has long been recognized as a source of atmospheric CO (Conrad and Seiler, 1980). In the upper ocean, CO is produced primarily via photolysis of CDOM (Conrad and Seiler, 1980; Zafiriou et al., 2003; Stubbins et al., 2006a; Xie et al., 2009a). In addition, CO can also be produced by thermal degradation of DOM (also called dark production) (Xie et al., 2005; Zhang et al., 2008; Zhang and Xie, 2012). Certain marine organisms may also produce CO by biological processes (King et al., 2001; Gros et al., 2009), however, this pathway needs to be further confirmed. In the upper ocean, microbial uptake and air-sea exchange are the main sinks of CO, and a small portion of CO can be transferred into the deep ocean by vertical mixing (Kettle, 2005). The currently known sources and sinks of CO in the ocean are shown in Fig. 1-1. The biogeochemical cycle of oceanic CO is important because 1) CO is arguably the most reliably measured and the second most abundant inorganic carbon photoproduct of CDOM (only after CO_2), 2) CO can be used as a proxy of other major but more-difficult-to-

measure CDOM photoproducts, such as CO₂ (Miller and Zepp, 1995; Mopper and Kieber, 2000) and bio-labile DOC (Miller et al., 2002), 3) CO is a potential energy and carbon source of certain marine microbes (King and Weber, 2007; Moran and Miller, 2007), 4) CO is a useful species for probing microbial uptake kinetics of dilute solutes in marine waters (Xie et al., 2009b), and 5) CO is an excellent tracer for modeling the interactions among mixing dynamics, optics, photochemistry, biology, and air-sea gas exchange in the upper-ocean (Doney et al., 1995; Kettle, 2005).

1.3 Motivations

Previous studies mainly focused on CO photoproduction from CDOM in various aquatic ecosystems in the past decades, including lakes (Bourbonniere et al., 1997), estuaries (Law et al., 2002; Zhang et al., 2006; Stubbins et al., 2011), coastal waters (Day and Faloona, 2009; Xie et al., 2009a), and the open ocean (Zafiriou et al., 2003; Stubbins et al., 2006a). Recent evidence suggests that photolysis of POM, like CDOM, can also produce significant amount of CO (Xie and Zafiriou, 2009; Stubbins et al., 2011). However, Xie and Zafiriou (2009) only reported preliminary results (i.e. the overall contribution of particles to total CO photoproduction) with limited samples, while Stubbins et al. (2011) estimated the CO photoproduction from particles in the Tyne Estuary based on the assumption that the spectrally resolved efficiency (i.e. apparent quantum yield, AQY) of CO photoproduction from particles was the same as that of CDOM. Hence, the results obtained by these studies are inadequate to extrapolate to larger spatial and temporal scales.

To better understand the contribution of particles to CO photoproduction and hence the implication of particle photochemistry to marine carbon cycling, more studies are needed to elucidate 1) the CO AQY² spectra of particles on larger spatial and time scales; 2) the effect

²CO AQY is defined as the number of moles of CO produced per mole of photons absorbed by a given set of light-absorbing materials at wavelength λ

of particle properties, such as light history, origin (terrestrial vs. marine), viability (living cells vs. detritus) and particle size, on CO AQY spectra; and 3) the environmental factors influencing CO photoproduction from particles, such as water salinity, pH and temperature.

Moreover, a preliminary field survey revealed that CO is enriched in the bottom layer of Arctic first-year sea ice during ice algal blooms and suggested that CDOM photooxidation could be a major contributor to the CO accumulation observed (Xie and Gosselin, 2005). Field measurements on larger time and space scales are required to better understand the seasonal and spatial variability of the sea-ice [CO] distribution, to better constrain its source strength. In addition, particles may also be involved in the enrichment of CO in bottom sea ice by photochemical and biological processes, considering the same processes in seawater (Xie and Zafiriou, 2009; Gros et al., 2009). In particular, the relative importance of particles to total CO photoproduction in bottom sea ice, especially during ice algal blooms, needs to be assessed.

1.4 Objectives

Using CO as a targeted photoproduct, the overall goal of this project is to better understand the relative importance of particle and CDOM photochemistry in diverse marine ecosystems. The goal will be accomplished by the following specific objectives:

- 1) Investigate the spatiotemporal variation of CO in first-year sea ice in the southeastern (SE) Beaufort Sea and assess the net production of CO in sea ice during ice algal blooms;
- 2) Determine CO AQY spectra of both CDOM and particles harvested from ice algal cultures at exponential and senescent phases and model the relative importance of particles and CDOM in CO photoproduction in bottom sea ice during ice algal blooms;
- 3) Determine CO AQY spectra of both CDOM and particles in surface and deep chlorophyll maxima (DCM) seawater in the SE Beaufort Sea;

- 4) Determine CO AQY spectra of CDOM and size-fractionated particles in the Delaware Estuary;
- 5) Model the relative contribution of particles and CDOM to total CO photoproduction in the water column of the SE Beaufort Sea and Delaware estuary.

CHAPITRE 2
VARIATIONS SPATIOTEMPORELLE DU CARBONE ORGANIQUE DISSOUS
ET MONOXYDE DE CARBONE DANS LA GLACE DE MER DE PREMIÈRE
ANNÉE DANS L'OUEST DE L'ARCTIQUE CANIDIEN

SPATIOTEMPORAL VARIATIONS OF DISSOLVED ORGANIC CARBON
AND CARBON MONOXIDE IN FIRST-YEAR SEA ICE IN THE WESTERN
CANADIAN ARCTIC

Article Publié dans Journal of Geophysical Research

Song, G., H. Xie, C. Aubry, Y. Zhang, M. Gosselin, C. J. Mundy, B. Philippe, and T. N. Papakyriakou, 2011. Spatiotemporal variations of dissolved organic carbon and carbon monoxide in first-year sea ice in the western Canadian Arctic, *J. Geophys. Res.*, 116, C00G05, doi:10.1029/2010JC006867.

RÉSUMÉ

Nous avons suivi l'évolution spatiotemporelle du carbone organique dissous (DOC) et du monoxyde de carbone (CO) dans la glace de mer de première année dans l'ouest de l'Arctique Canadien en parallèle avec des variables météorologiques, hydrographiques et biologique entre la mi-mars et début juillet 2008. Les concentrations de DOC et de CO ont fluctué irrégulièrement dans la glace de surface, mais elles suivaient la concentration des algues de glace dans la glace de fond : faibles au début de l'accumulation d'algues de glace; fortes pendant le pic-floraison et le début de la post-floraison; de nouveau appauvries au cours de la fonte de la glace de mer. Les profils verticaux de DOC et de CO montraient une diminution avec la profondeur dans la glace au début du printemps, alors qu'ils ont été variables pour le reste de la saison. En présence de biomasse élevée d'algues de glace à la base du couvert de glace de mer à la mi-printemps, les concentrations de DOC et CO présentaient des valeurs élevées dans le fond (DOC: $563 \pm 434 \mu\text{mol L}^{-1}$; CO: $82,9 \pm 84 \text{ nmol L}^{-1}$) par rapport à la surface (DOC : $56 \pm 26 \mu\text{mol L}^{-1}$; CO: $16,8 \pm 7 \text{ nmol L}^{-1}$). La glace de rive contenait des niveaux plus élevés de DOC et de CO que la glace de dérive. L'inventaire moyen de DOC et de CO durant la campagne en mer dans la glace de mer étaient respectivement de $87 \pm 51 \text{ mmol m}^{-2}$ et de $13,9 \pm 10 \mu\text{mol m}^{-2}$. Les taux de productions netteregus de DOC et de CO liées à la prolifération d'algues de glace ont été estimés à 75 mmol m^{-2} et $13,2 \mu\text{mol m}^{-2}$ respectivement. La glace de mer dans la zone d'étude contribuerait à la hauteur de 7.4×10^7 moles de CO comme source vers l'atmosphère. Cette étude suggère que la glace de mer joue un rôle important dans le cycle du carbone organique et des gaz traces.

ABSTRACT

We monitored the spatiotemporal progression of dissolved organic carbon (DOC) and carbon monoxide (CO), along with general meteorological, hydrographic, and biological variables, in first-year sea ice in the western Canadian Arctic between mid-

March and early July 2008. DOC and CO concentrations fluctuated irregularly in surface ice, but followed the concentration of ice algae in bottom ice, i.e. low at the start of ice algal accumulation, highly enriched during the peak-bloom and early post-bloom, and depleted again during sea ice melt. Vertical profiles of DOC and CO typically decreased downward in early spring and were variable in the melting season. In the presence of high bottom ice algal biomass in mid-spring, DOC and CO exhibited high concentrations in the bottom (DOC: $563 \pm 434 \mu\text{mol L}^{-1}$; CO: $82.9 \pm 84 \text{ nmol L}^{-1}$) relative to the surface (DOC: $56 \pm 26 \mu\text{mol L}^{-1}$; CO: $16.8 \pm 7 \text{ nmol L}^{-1}$). Landfast ice contained higher levels of DOC and CO than drifting ice. Cruise-mean DOC and CO inventories in sea ice were $87 \pm 51 \text{ mmol m}^{-2}$ and $13.9 \pm 10 \mu\text{mol m}^{-2}$, respectively. Net productions of DOC and CO linked to the ice algal bloom were assessed to be 75 mmol m^{-2} and $13.2 \mu\text{mol m}^{-2}$. Sea ice in the study area was estimated to contribute 7.4×10^7 moles of CO a^{-1} to the atmosphere. This study suggests that sea ice plays important roles in the cycling of organic carbon and trace gases.

2.1 INTRODUCTION

Sea ice influences the carbon cycle in polar oceans through modulating the transmission of light available for sea ice and water column primary production and photooxidation and by providing a habitat for a variety of organisms. It has been estimated that ice algae contribute 3-25% of the total primary production in seasonally ice-covered Arctic seas (Legendre et al., 1992) and > 50% in the perennially ice-covered central Arctic Ocean (Gosselin et al., 1997). Biological processes involving ice algae produce dissolved organic carbon (DOC) and hence enrich it in bottom sea ice relative to underlying seawater (Bunch and Harland, 1990; Gosselin et al., 1997; Smith et al., 1997) despite exclusion of organic constituents during ice formation (Giannelli et al., 2001; Belzile et al., 2002; Amon, 2004). DOC production makes up ~40% of the total organic carbon fixation by ice algae (Gosselin et al., 1997; Smith et al., 1997), demonstrating that organic carbon production can be seriously underestimated if the dissolved fraction is ignored. Understanding the distribution of DOC in sea ice and its seasonal variability, which

remains poorly documented, is therefore critical for establishing links between DOC cycling and ecological functions of ice microorganisms.

In addition to its role in organic carbon cycling, sea ice is also involved in the production or destruction of certain climatically and biogeochemically reactive trace constituents. For example, carbon monoxide (CO) (Xie and Gosselin, 2005) and hydrogen peroxide (Klánová et al., 2003; King et al., 2005) are generated while chlorine dioxide (Pursell et al., 1995) and dimethylsulfide (Hellmer et al., 2006) are decomposed in sea ice. Both sea ice and open seas can release CO to the atmosphere where it regulates the oxidizing capacity and acts as an indirect greenhouse gas through its reaction with the hydroxyl radical (Watson et al., 1990; Thompson, 1992). As the second most abundant and most precisely measured carbon photoproduct in the ocean, CO plays a crucial role in chromophoric dissolved organic matter (CDOM) photochemistry (Miller and Zepp, 1995; Mopper and Kieber, 2000). CO also serves as potential carbon and energy sources for certain marine microbes (King and Weber, 2007; Moran and Miller, 2007). Its short turnover times (usually <1 d), mainly resulting from rapid microbial oxidation (Conrad et al., 1982; Zafiriou et al., 2003; Xie et al., 2005), make CO an excellent tracer for modeling upper-ocean mixing dynamics (Doney et al., 1995; Kettle, 2005). In spite of extensive CO surveys in open oceans (Conrad et al., 1982; Bates et al., 1995; Zafiriou et al., 2003, 2008; Stubbins et al., 2006b), information on CO in sea ice is scarce and incomplete. Swinnerton and Lamontagne (1974) briefly reported the observation of CO enrichment in Antarctic sea ice relative to open surface seawater. Xie and Gosselin (2005) collected a limited number of vertical profiles of CO concentration ([CO]) in landfast sea ice during the ice algal bloom season in Franklin Bay, western Canadian Arctic. [CO] profiles typically exhibit minima in the middle and increasing concentration towards the surface and bottom with particularly strong elevations at the bottom. Based on laboratory evidence, Xie and Gosselin (2005) suggested that this distribution was a function of CO photoproduction from CDOM in sea ice. However, these [CO] profiles were obtained over a narrow time span (11 d) and only at one site. Field measurements on larger time and space scales are required to

better understand the seasonal and spatial variability of sea ice [CO] distribution, to constrain its source strength, and to evaluate its flux to the overlying atmosphere.

Here we report measurements of DOC and CO concentrations in full-length sea ice cores collected in the western Canadian Arctic, covering both landfast and drifting ice and spanning from late winter to mid-summer. We assess the DOC and CO inventories and their net productions in sea ice and evaluate the contribution of sea ice to atmospheric CO. Results from this study improve our understanding of the roles of sea ice in marine organic carbon and trace gas cycling.

2.2 METHODS

2.2.1 Meteorology and hydrology

The field campaign was carried out in the southeastern Beaufort Sea, including the Amundsen Gulf, Prince of Wales Strait, the coastal shelf west of Banks Island, and M'Clure Strait, during the 2007-2008 International Polar Year–Circumpolar Flaw Lead (IPY–CFL) system study aboard the icebreaker CCGS *Amundsen* (Barber et al., 2010). A meteorological tower mounted at the bow of the CCGS *Amundsen* was used to monitor shortwave radiation (285-2800 nm, PSPTM, Eppley), photosynthetically active radiation (PAR, 400-700 nm, PARLiteTM, Kipp & Zonen), and air temperature (Vasaila HMP45C212, Campbell Scientific) at 1-min intervals.

All sea ice sampling was conducted on first-year drifting and landfast sea ice from 17 March to 6 July 2008 (Fig. 2-1). In the case of drifting ice, the ship drifted with the same ice floe for a certain period of time and then re-positioned to the next ice floe. Sampling usually started around 9 am and lasted for ~1 h. Some stations were sampled 2-4 times, often 3 d apart (Table 2-1). When on site, a moderate snow depth (typically < 5 cm; Table 2-1) was located. Numerous ice cores were extracted using a manually-operated MARK II

coring system (9 cm in diameter, Kovacs Enterprises). Following ice core extraction, the ice thickness and freeboard were measured. Sea ice temperature measurements were conducted on one of the ice cores immediately after extraction. Ice temperature was measured at 10 cm intervals using a handheld drill and a temperature sensor coupled with a stainless steel NTC food probe (IP65, Testo). The thermometer had a 0.001 reading resolution and an accuracy of $\pm 0.05^{\circ}\text{C}$. Thawed ice cores collected for CO and DOC analyses (section 2.2.3) were used to determine sea ice salinity profiles using a WTW 330i conductivity meter with an accuracy of $\pm 0.5\%$.

2.2.2 Chlorophyll *a*

At each sampling site, one of the extracted ice cores was used for determination of chlorophyll *a* concentration ([Chl *a*]). From the bottom upwards, the ice core was consecutively cut into 3, 7, and 10 cm thick ice sections followed by 20 cm thick sections until reaching the surface section, which was variable in thickness. The ice sections were immersed in 0.2 μm -filtered seawater and left in the dark within isothermal containers overnight (12-14 h) to melt. The addition of filtered seawater (~3:1 filtered seawater to ice melt dilution) was intended to reduce osmotic stress-induced artifacts (Garrison and Buck, 1986). Subsamples from the diluted meltwater were filtered onto duplicate GF/F filters (Whatman). The filters were then placed in 10 mL of 90% acetone in scintillation vials for at least 18 h in the dark at $\sim 4^{\circ}\text{C}$. The supernatant was measured for fluorescence, before and after acidification with 5% HCl, using a Turner Designs fluorometer (model 10-AU) according to the method of Parsons et al. (1984). [Chl *a*] was then calculated using the equation of Holm-Hansen et al. (1965) and corrected for filtered seawater dilution. The manufacturer-designated lower detection limit of the fluorometer is $0.025 \mu\text{g L}^{-1}$. Analytical variability for 122 duplicate GF/F filters as prepared above was evaluated; the average pairwise difference was 11%, suggesting a standard deviation of the means of 8%.

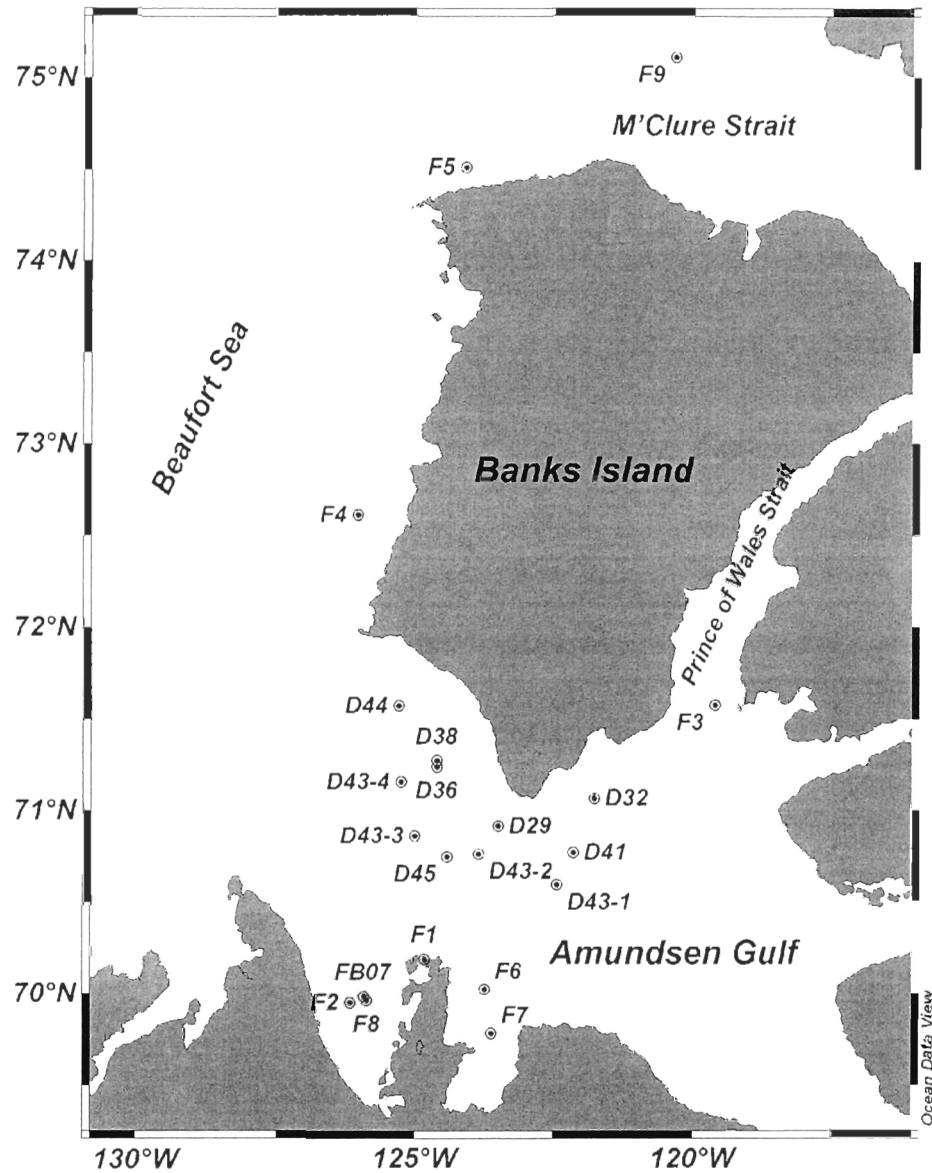


Fig. 2-1 Map of sea ice sampling stations. Station symbols starting with D signify drifting ice and F landfast ice. This map was constructed using the online software of Ocean Data View (R. Schlitzer, 2010, unpublished data, <http://odv.awi.de>).

Table 2-1. Sampling dates, locations and corresponding sea ice conditions.

| Date | Station | Coordinates | | Snow depth (cm) | Ice thickness (cm) | Freeboard (cm) |
|--------|---------|--------------|---------------|--------------------|-----------------------|-------------------|
| | | Latitude (N) | Longitude (W) | | | |
| 17 Mar | D29 | 70°54.6' | 123°30.0' | 4.0 | 135 | 13 |
| 22 Mar | D32 | 71°3.7' | 121°46.7' | 3.5 | 149 | 9 |
| 25 Mar | D33-1 | 71°3.8' | 121°47.2' | 3.5 | 145 | 10 |
| 28 Mar | D33-2 | 71°3.8' | 121°47.2' | 3.5 | 149 | 10 |
| 31 Mar | D33-3 | 71°3.8' | 121°47.2' | 4.0 | 154 | 14 |
| 6 Apr | D36-1 | 71°16.0' | 124°24.0' | 2.5 | 160 | 12 |
| 9 Apr | D36-2 | 71°14.0' | 124°36.0' | 1.0 | 72 | 6 |
| 11 Apr | D38 | 71°16.0' | 124°36.0' | 2.0 | 124 | 12 |
| 16 Apr | D41 | 70°46.0' | 122°9.0' | 4.5 | 131 | 11 |
| 26 Apr | D43-1 | 70°35.3' | 122°26.5' | 4.5 | 135 | 12 |
| 29 Apr | D43-2 | 70°45.5' | 123°51.4' | 4.5 | 135 | 11 |
| 2 May | D43-3 | 70°51.3' | 125°0.4' | 4.5 | 141 | 12 |
| 5 May | D43-4 | 71°9.1' | 125°15.2' | 5.0 | 137 | 10 |
| 8 May | F1-1 | 70°11.0' | 124°49.8' | 4.0 | 124 | 10 |
| 9 May | F1-2 | 70°11.0' | 124°49.8' | 3.5 | 122 | NA |
| 13 May | F2-1 | 69°56.8' | 126°10.3' | 10.0 | 170 | 12 |
| 16 May | F2-2 | 69°56.8' | 126°10.3' | 1.0 | 170 | 15 |
| 20 May | F3 | 71°34.4' | 119°36.4' | 5.0 | 132 | 10 |
| 24 May | F4 | 72°36.6' | 126°2.2' | 5.0 | 122 | 11 |
| 28 May | F5 | 74°30.7' | 124°5.9' | 3.0 | 185 | 14 |
| 30 May | D44 | 71°34.1' | 125°17.6' | 2.5 | 85 | 7 |
| 31 May | D45 | 70°44.5' | 124°25.1' | 3.0 | 96 | 7 |
| 2 Jun | F6 | 70°1.1' | 123°45.1' | 9.0 | 163 | 15 |
| 9 Jun | F7-1 | 69°46.6' | 123°37.9' | 5.0 | 134 | 8 |
| 12 Jun | F7-2 | 69°49.4' | 123°38.0' | 5.0 | 115 | NA |
| 16 Jun | F8 | 69°57.4' | 125°52.5' | 4.0 | 115 | 13 |
| 18 Jun | F7-3 | 69°48.9' | 123°39.0' | 0.0 | 110 | 20 |
| 21 Jun | FB07 | 69°58.7' | 125°55.4' | 5.0 | 120 | 15 |
| 6 Jul | F9 | 75°6.4' | 120°19.9' | 0.0 | 147 | 15 |

NA: data were not available.

2.2.3 DOC and CO

DOC and CO sampling protocols were modified from those of Xie and Gosselin (2005). Briefly, full-length ice cores were cut into 7-9 10 cm thick sections from different depths. The center of each ice section was taken out using a custom-built metal corer (4 cm in diameter, 10 cm in length) and immediately transferred into a 200 mL all-glass syringe (Perfektum®) having been pre-flushed with ambient air and fitted with a three-way nylon gas-tight valve. A known volume of ice plus ambient air was obtained by replacing the syringe's plunger to a pre-set marker. Ambient air was simultaneously collected in duplicate with 10 mL glass syringes (Perfektum®). Both ice and air sampling were performed under conditions that avoided direct sunlight and minimized the influence from the ship's exhaust. Samples were placed in the dark and immediately brought to the nearby ship-based laboratory. After being thawed in a bucket of tap water at room temperature (~20°C), ice samples were gently shaken for 5 min, which was found to be of sufficient duration for attaining gas-liquid equilibrium. The equilibrated headspace gas was transferred into a 5-mL glass syringe and analyzed for [CO] using a Reduction Gas Analyzer (RGA 3) (Xie et al., 2002). Air samples were analyzed by directly injecting the samples into the analyzer. [CO], reported here as per unit volume of meltwater, was calculated by correcting for [CO] in the ambient air. The lower detection limit was ca. 1 parts per billion by volume (ppbv) for air samples and better than 0.02 nmol L⁻¹ for aqueous samples (Xie et al., 2002). An estimate of analytical variability was made based on 138 duplicate injections of equilibrated headspace gas prepared from in situ ice samples. The average pairwise difference was 3%, suggesting a standard deviation of the means of 2%.

Immediately after the headspace gas transfer for [CO] measurement, the ice meltwater remaining in the 200 mL glass syringes was passed through 0.2 µm polyethersulfone membrane syringe filters (Whatman) and collected into 60 mL glass bottles (Qorpak®). The samples were transported under refrigeration and darkness to the land-based laboratory in Rimouski for determination of DOC concentration ([DOC]). Prior

to use, the syringe filters had been profusely rinsed with Nanopure water and the storage glass bottles were soaked with 10% HCl overnight and then thoroughly washed with Nanopure water. Control tests proved the filters and bottles to be free of DOC contamination. DOC samples were acidified to pH ~2 with 25% H₃PO₄ to remove the dissolved inorganic carbon and analyzed in triplicate using a Shimadzu TOC-5000A Total Carbon Analyzer calibrated with potassium biphthalate. The system was checked, at intervals of seven consecutive sample analyses, against Hansell's low-carbon ([DOC]: 1-2 $\mu\text{mol L}^{-1}$) and deep Sargasso Sea ([DOC]: 44-46 $\mu\text{mol L}^{-1}$) reference waters. The mean coefficient of variation of triplicate measurements was 4% (range: 0.2-13%).

2.3 RESULTS

2.3.1 General meteorological and hydrological properties

Over the sampling period, snow depth, ice thickness and ice freeboard ranged from 0-10 cm (mean: 4 cm), 72-185 cm (mean: 134 cm) and 6-20 cm (mean: 12 cm), respectively (Table 2-1). Daily-averaged incident shortwave radiation, PAR, and air temperature increased from ca. 160 to 330 W m^{-2} , from ca. 300 to 700 $\mu\text{mol photons m}^{-2} \text{s}^{-1}$, and from ca. -25 to 7°C, respectively (Fig. 2-2a, b). Sea ice temperature increased from -21.6 to -0.8°C in the top 10 cm and from -3.4 to -0.6°C in the bottom 10 cm, whereas bulk ice salinity in the corresponding layers decreased from 8.8 to 0.20 and 5.1 to 0.70 (Fig. 2-2c, d). From 13 May onward, sea ice started melting and salinity approached zero at certain stations in both the top and bottom layers (Fig. 2-2d) due apparently to nearly complete loss of brine. Imposed over the general trends of these variables were substantial fluctuations resulting from both temporal variation and spatial heterogeneity.

The temporal progression in sea ice temperature profiles was typical for the spring season. Temperature generally increased with depth prior to the start of the melting season

(Fig. 2-3a, b); after the melting set in, temperature at the surface began to climb and a C-shaped structure formed (Fig. 2-3c-e). C-shaped profiles dominated the ice salinity structure before substantial ice melt had occurred (Fig. 2-3a, b, d). Once ice melt commenced, bulk ice salinity rapidly decreased at the surface and bottom (Fig. 2-3c, e, f). These profiles were consistent with results from previous studies (Eicken, 2003; Toyota et al., 2007; Ehn et al., 2011).

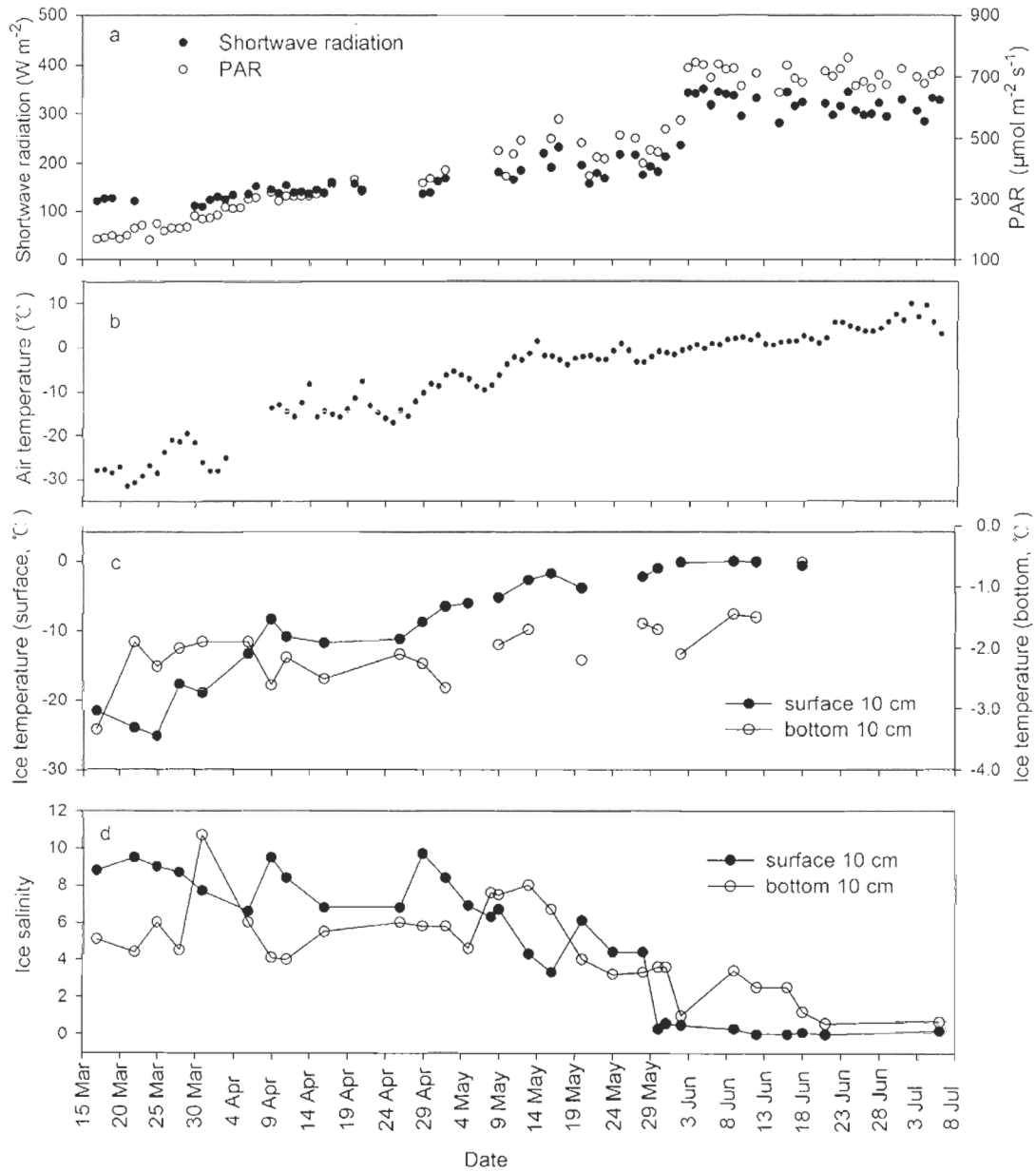


Fig. 2-2 Spatiotemporal variations of (a) daily averaged shortwave, and photosynthetic active radiation (PAR), (b) daily averaged air temperature, (c) sea ice temperature, and (d) bulk sea ice salinity from 17 March to 6 July 2008. See Table 2-1 for sampling stations corresponding to each sampling date.

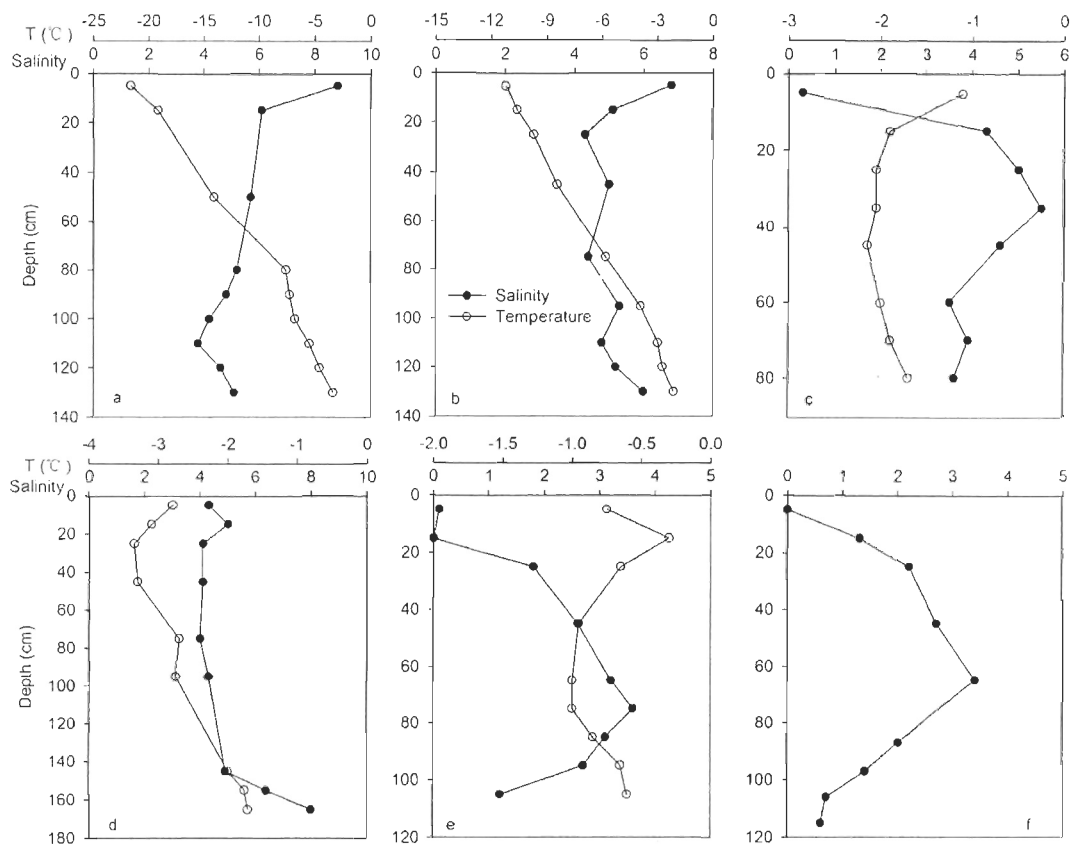


Fig. 2-3 Depth profiles of sea ice salinity and temperature: (a) D29 (17 March, LCP1), (b) D43-1 (26 April, HCP1), (c) D44 (30 May, LCP2), (d) F2 (13 May, HCP2), (e) F7 (18 June, LCP2), (f) FB07 (21 June, LCP2). Temperature data were not available for Stn FB07. Key: LCP1 = low Chl *a* phase 1; LCP2 = low Chl *a* phase 2; HCP1 = high Chl *a* phase 1; HCP2 = high Chl *a* phase 2. See definitions of these keys in the text.

2.3.2 Chlorophyll *a*, DOC, and CO in surface and bottom sea ice

[Chl *a*] in the surface sea ice layer remained low ($<1.0 \mu\text{g L}^{-1}$) over the entire sampling period except for two sharp peaks observed in landfast ice near the end of the study (Fig. 2-4a). In the lowermost 10 cm layer, [Chl *a*] gradually increased, peaked twice, and then rapidly decreased to relatively low values for the rest of the study. Based on the variability of [Chl *a*] in bottom ice, the data was grouped into the following periods: low Chl *a* phase 1 (LCPI, 17-31 March), high Chl *a* phase 1 (HCP1, 6 April-5 May), high Chl *a* phase 2 (HCP2, 8-16 May), and low Chl *a* phase 2 (LCP2, 20 May-6 July). LCPI was sampled exclusively on drifting ice and corresponded to the early stage of ice algal accumulation. HCP1 and HCP2 covered the peak bloom in drifting sea ice and the peak to post-bloom in landfast sea ice, respectively (Brown et al., 2010). LCP2 was mainly sampled on landfast sea ice (except Stn D44, 30 May) and matched the period of sea ice melt. The overall range of [Chl *a*] in the bottom layer was 1.1 (24 May, Stn F4) to 1570 $\mu\text{g L}^{-1}$ (13 May, Stn F2) with the average concentration for the two high Chl *a* phases (HCPs = HCP1 + HCP2; 561 $\mu\text{g L}^{-1}$) ~20 times that for the two low Chl *a* phases (LCPs = LCPI + LCP2; 27 $\mu\text{g L}^{-1}$). In the bottom layer of drifting ice, mean [Chl *a*] (\pm s.d.) was $54 \pm 43 \mu\text{g L}^{-1}$ for LCPI and $310 \pm 144 \mu\text{g L}^{-1}$ for HCP1. The only drifting ice station sampled in LCP2, Stn D44, showed that [Chl *a*] dropped to $58 \mu\text{g L}^{-1}$ during the melting season. In the bottom layer of landfast ice, mean [Chl *a*] was $1230 \pm 360 \mu\text{g L}^{-1}$ for HCP2 and $9 \pm 10 \mu\text{g L}^{-1}$ for LCP2. The mean bottom ice [Chl *a*] of landfast ice was approximately 4 times that of drifting ice for the high Chl *a* phase (HCP).

The general trend of [DOC] at the surface differed from that of [Chl *a*] (Fig. 2-4a, b). [DOC] often displayed small but significant variations, even at the same sites sampled over extended periods (e.g. Stn D43) (Fig. 4b). The peak at Stn F7 on 12 June ($264 \mu\text{mol L}^{-1}$) was the dominant feature at the surface. Bottom ice [DOC] was high during the HCPs and low during the LCPs, generally following that of the [Chl *a*]. An exception occurred at the early sampling stage (17 March-11 April) when [DOC] remained low and fairly constant despite a gradual increase in [Chl *a*]. Bottom ice [DOC] was linearly correlated with

[Chl *a*] during the HCPs but not during the LCPs (Table 2-2); surface ice [DOC] showed no significant correlation with [Chl *a*] during the entire sampling period ($p > 0.05$). The highest [DOC] ($1230 \mu\text{mol L}^{-1}$) occurred at Stn F2 on 16 May in landfast ice (Fig. 2-4b). Mean surface [DOC] in drifting ice varied little between LCP1 ($62 \pm 37 \mu\text{mol L}^{-1}$) and HCP1 ($58 \pm 30 \mu\text{mol L}^{-1}$) but decreased to $39 \pm 16 \mu\text{mol L}^{-1}$ in LCP2. Averaged bottom [DOC] in drifting ice was comparable between LCP1 ($49 \pm 16 \mu\text{mol L}^{-1}$) and LCP2 ($53 \pm 1.8 \mu\text{mol L}^{-1}$), but much lower than that of HCP1 ($307 \pm 247 \mu\text{mol L}^{-1}$). In landfast ice, mean [DOC] at the surface increased from $53 \pm 16 \mu\text{mol L}^{-1}$ in HCP2 to $80 \pm 69 \mu\text{mol L}^{-1}$ in LCP2 while at the bottom it was highly enriched during HCP2 ($1070 \pm 154 \mu\text{mol L}^{-1}$) relative to LCP2 ($55 \pm 25 \mu\text{mol L}^{-1}$). On average, bottom landfast ice contained >3 times DOC than bottom drifting ice during the HCPs (1070 vs. $307 \mu\text{mol L}^{-1}$).

[CO] in the upper 10 cm layer ranged from 0.57-30.0 nmol L⁻¹ (mean: 10.8 ± 8 nmol L⁻¹) (Fig. 2-4c) and was supersaturated relative to the atmosphere (~ 100 ppbv), consistent with previous findings (Xie and Gosselin, 2005). [CO] fluctuated, often erratically, over the entire sampling period, including those stations that were sampled multiple times (e.g. Stns D33 and D43) (Fig. 2-4c). However, a substantial [CO] drawdown was evident after 13 May, which coincided with the start of ice melt. [CO] distribution at the surface showed no similarity to those of [Chl *a*] and [DOC]. Bottom ice [CO] generally corresponded to [Chl *a*] and [DOC], showing peak concentrations during the HCPs. [CO] at the bottom increased slowly during LCP1, tracking the trend of [Chl *a*]. At the surface of drifting ice, mean [CO] was 10.7 ± 3 nmol L⁻¹ for LCP1, 16.4 ± 7 nmol L⁻¹ for HCP1, and 5.6 ± 5 nmol L⁻¹ for LCP2; mean values at the bottom were 3.2 ± 2 , 34.8 ± 26 , and 11.5 ± 2 nmol L⁻¹ for the corresponding Chl *a* phases. Mean surface [CO] in landfast ice decreased from 17.7 ± 8 nmol L⁻¹ in HCP2 to 4.7 ± 4 nmol L⁻¹ in LCP2. Similarly, mean bottom [CO] decreased from 179 ± 78 to 13.7 ± 10 nmol L⁻¹. The mean bottom ice [CO] of landfast ice was 5 times that of drifting ice (179 vs. 34.8 nmol L⁻¹) during the HCPs. Surface [CO] showed no significant relationship with [Chl *a*] and [DOC] ($p > 0.05$). However, bottom [CO] was linearly correlated with [Chl *a*] during the HCPs and LCP1, but not LCP2 (Table 2-2). Bottom ice [CO] was also significantly correlated with [DOC] during the HCPs. Partial

correlation analysis indicated that this relationship largely stemmed from the correspondence of [DOC] to [Chl *a*] (see above).

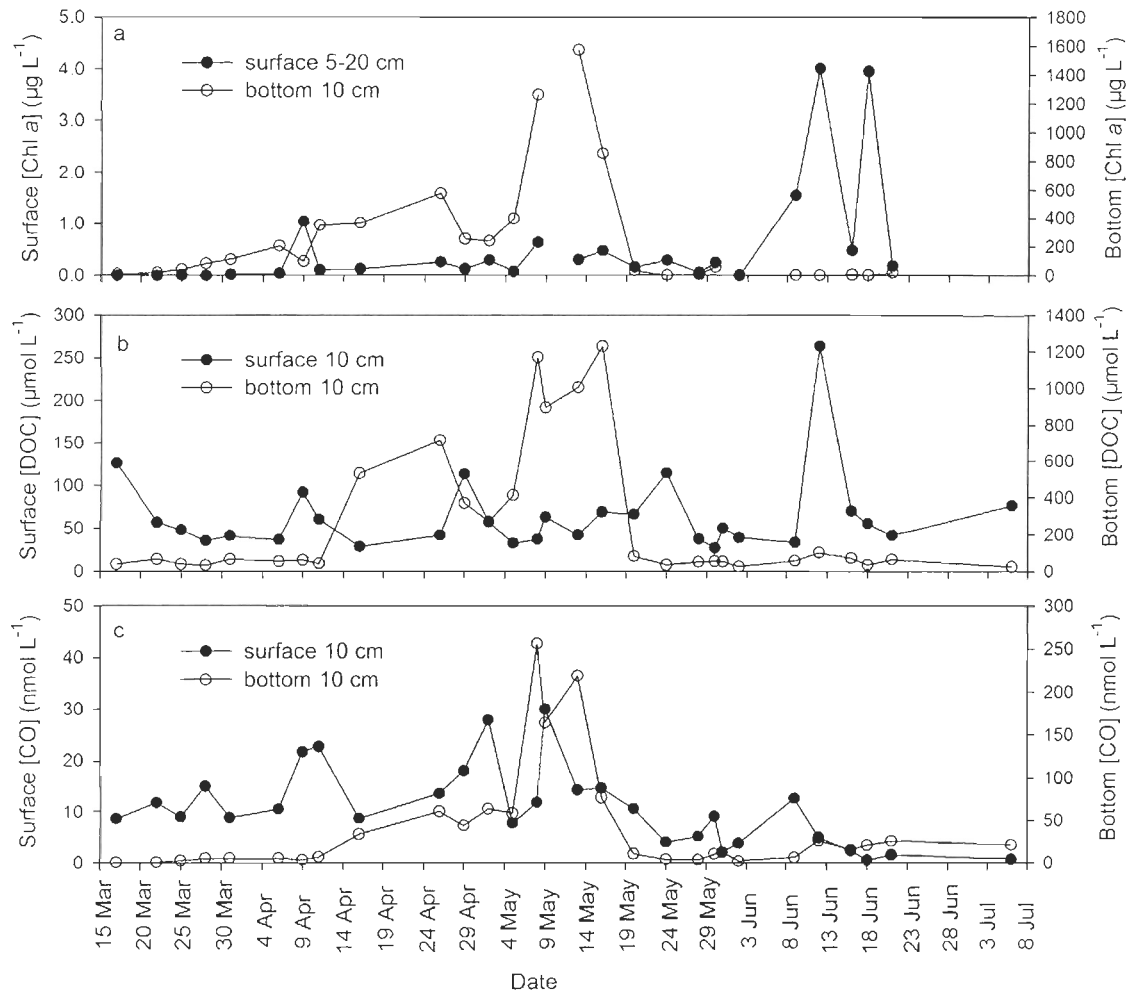


Fig. 2-4 Spatiotemporal variations of (a) chlorophyll *a* (Chl *a*), (b) dissolved organic carbon (DOC), (c) carbon monoxide (CO) concentrations in surface and bottom sea ice layers from 17 March to 6 July 2008. See Table 2-1 for sampling stations corresponding to each sampling date.

Table 2-2. Results of linear least-squares regression analysis between DOC, CO and Chl *a* in the bottom 10-cm sea ice layer^a.

| Chl <i>a</i> phase | R^2 | p | n |
|--------------------|--------|----------|----|
| DOC-Chl <i>a</i> | | | |
| LCPs | 0.036 | 0.95 | 15 |
| HCPs | 0.723 | < 0.001 | 11 |
| CO- Chl <i>a</i> | | | |
| LCP1 | 0.941 | < 0.01 | 5 |
| LCP2 | 0.0002 | 0.97 | 10 |
| HCPs | 0.846 | < 0.0001 | 11 |
| CO-DOC | | | |
| LCPs | 0.017 | 0.16 | 17 |
| HCPs | 0.640 | < 0.001 | 12 |

^aLCPs = low Chl *a* phases; HCPs = high Chl *a* phases; LCP1 = low Chl *a* phase 1; LCP2 = low Chl *a* phase 2. See definitions of these keys in the text.

2.3.3 Vertical distributions of Chl *a*, DOC, and CO

[Chl *a*] profiles in drifting ice were typically L-shaped during both low and high Chl *a* phases (Fig. 5a-c). Profiles in landfast ice were also L-shaped during HCP2 (Fig. 2-5d) but strayed from the L-shape and exhibited multiple peaks during LCP2 (Fig. 2-5e, f).

In contrast to [Chl *a*] profiles, [DOC] profiles during LCP1 showed decreasing [DOC] from the surface to the middle sections and less variation at deeper depths (Fig. 2-5a). [DOC] was $<131 \mu\text{mol L}^{-1}$ throughout the ice column. [DOC] during the HCPs remained low at the surface but was slightly elevated relative to the depths immediately below (Fig. 2-5b, d). The extreme DOC enrichment in bottom ice, however, obscured this character, resulting in an overall L-shaped distribution that paralleled that of [Chl *a*] (Fig. 2-5b, d). [DOC] in the lowermost 10 cm layer reached $>700 \mu\text{mol L}^{-1}$ in drifting ice (Fig. 2-5b) and $>1000 \mu\text{mol L}^{-1}$ in landfast ice (Fig. 5d). Note that DOC enrichment started at ~ 30 cm up from the bottom, but the strongest enrichment was within the lowermost section (Fig. 2-5b, d). During the melting season (LCP2), [DOC] vertical structures varied from station to station and often displayed zigzag patterns that were either alike (Fig. 2-5e) or dissimilar (Fig. 2-5c) to that of [Chl *a*]. The marked near-bottom peak at Stn FB07, matching no [Chl *a*] counterpart, was unique among all [DOC] profiles obtained (Fig. 2-5f).

Vertical profiles of [CO] during LCP1 generally mimicked those of [DOC] (Fig. 2-5a). During the HCPs, [CO] was slightly elevated within the surface ice, reached a minimum towards the middle, and increased rapidly at the bottom (Fig. 2-5b, d). Depth distributions in the melting season were less regular and variable from station to station. The [CO] profile at Stn D44 followed the [DOC] profile within the upper portion of the ice column but was opposite in the lower portion (Fig. 2-5c). [CO] at Stn F7 was lowest at the surface and moderately high and rather constant in the intermediate layer and then increased at the bottom, dissimilar to the [DOC] and [Chl *a*] profiles (Fig. 2-5e). Stn FB07 was characterized by a sharp [CO] peak near the bottom that paralleled the [DOC] spike

and displayed the greatest [CO] (762 nmol L^{-1}) observed in this study (Fig. 2-5f). These unusually high [CO] and [DOC] were excluded from the calculations of depth-integrated and -weighted concentrations of DOC and CO in section 2.3.4.

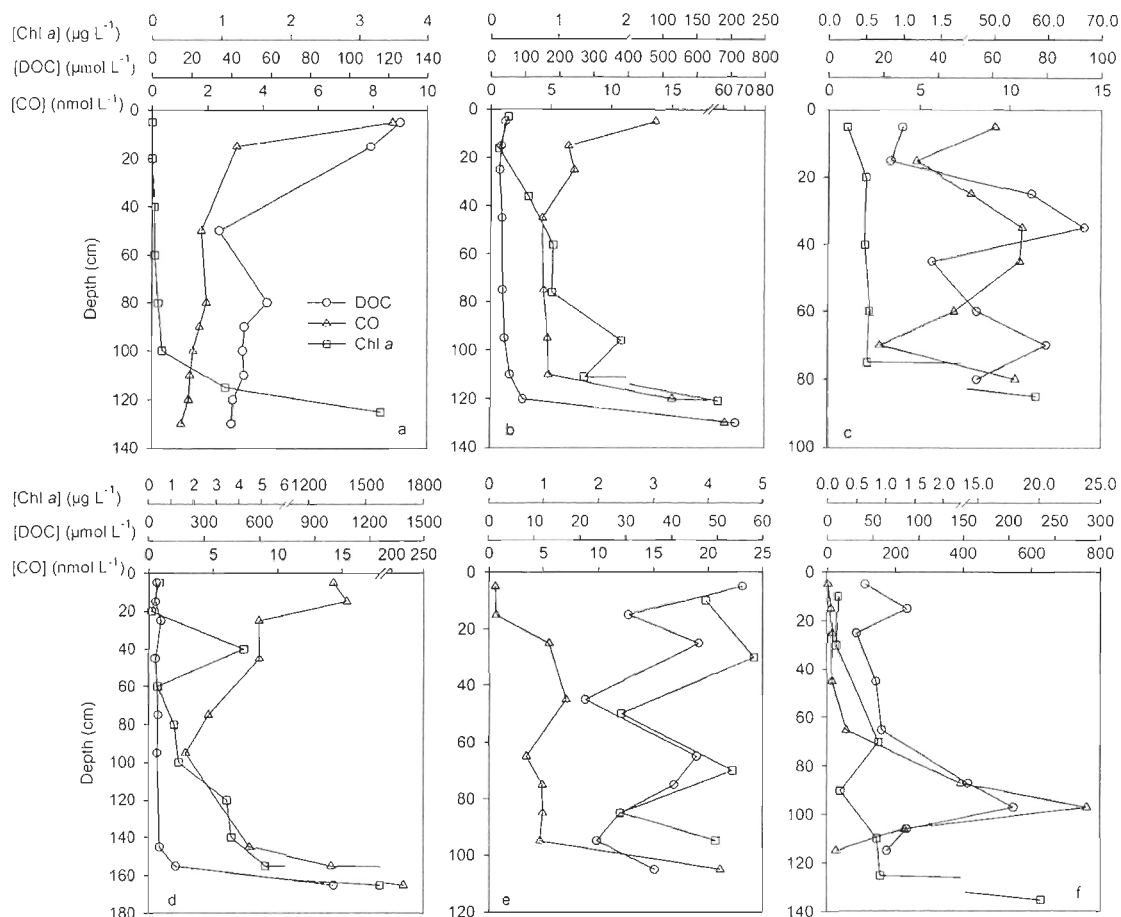


Fig. 2-5 Depth profiles of sea ice chlorophyll *a* (Chl *a*), dissolved organic carbon (DOC), carbon monoxide (CO) concentrations. (a) D29 (17 March, LCP1), (b) D43-1 (26 April, HCP1), (c) D44 (30 May, LCP2), (d) F2 (13 May, HCP2), (e) F7 (18 June, LCP2), (f) FB07 (21 June, LCP2). Keys and definitions of LCP1, LCP2, HCP1, and HCP2 are the same as those in Fig. 2-3.

2.3.4 Vertical distributions of Chl *a*, DOC, and CO

Depth-integrated concentrations, also referred to as column burdens (subscript cb), of Chl *a*, DOC, and CO for the entire ice core were obtained by the trapezoid method, assuming homogenous distributions of these variables within the top and bottom ice sections sampled. Depth-weighted concentrations (subscript dw) were derived by dividing column burdens by the total depth of the ice core. Table 2-3 summarizes the column burdens and depth-weighted concentrations. [Chl *a*]_{cb} and [Chl *a*]_{dw} ranged from 0.30 to 161 mg m⁻² (mean: 25 ± 7 mg m⁻²), and from 0.25 to 103 μg L⁻¹ (mean: 18 ± 6 μg L⁻¹), respectively. [Chl *a*]_{cb} in the HCP was 4.5 times that in LCP1 for drifting ice and 53 times that in LCP2 for landfast ice. [Chl *a*]_{dw} followed a similar trend with slightly different HCP-to-LCP ratios. [Chl *a*]_{cb} and [Chl *a*]_{dw} in landfast ice for HCP2 were approximately 5 and 4 times higher, respectively, than those in drifting ice for HCP1.

[DOC]_{cb} and [DOC]_{dw} spanned from 25 to 251 mmol m⁻² (mean: 87 ± 51 mmol m⁻²) and 23 to 148 μmol L⁻¹ (mean: 64 ± 33 μmol L⁻¹), respectively. In drifting ice, [DOC]_{cb} and [DOC]_{dw} in HCP1 were both ~40% higher than those in the LCPs (Table 2-3). In landfast ice, [DOC]_{cb} and [DOC]_{dw} in HCP2 were both more than twice those in LCP2. As expected, [DOC]_{cb} and [DOC]_{dw} in landfast ice were higher compared to those in drifting ice. The cruise-mean [DOC]_{cb} was 5.3% of the concurrently determined [DOC]_{cb} in the under-ice surface mixed layer (1.63 ± 0.6 mol m⁻²) that was 19 m deep on average (M. Gosselin, unpublished data, 2008).

[CO]_{cb} and [CO]_{dw} ranged from 3.2 to 41.2 μmol m⁻² (mean: 13.9 ± 10 μmol m⁻²) and 2.0 to 33.2 nmol L⁻¹ (mean: 10.6 ± 8 nmol L⁻¹), respectively. In drifting ice, both [CO]_{cb} and [CO]_{dw} in HCP1 were about twice those in LCP1 but the differences between HCP1 and LCP2 were smaller (Table 2-3). In landfast ice, [CO]_{cb} and [CO]_{dw} in HCP2 were 2.5 times greater than those in LCP2. [CO]_{cb} and [CO]_{dw} in landfast ice were about twice those in drifting ice.

Table 2-3. Comparison of depth-integrated (i.e., column burden) and depth-weighted concentrations of Chl *a*, DOC, and CO between drifting and landfast sea ice and among different Chl *a* phases^a.

| | Drifting Ice | | | Landfast Ice | |
|---|-------------------------|--------------------------|--------------------------|---------------------------|---------------------------|
| | LCPI | HCP1 | LCP2 ^b | HCP2 | LCP2 ^c |
| [Chl <i>a</i>] _{cb} (mg m ⁻²) | 1.4 – 12 (5.7 ± 4) | 10 – 44 (26 ± 13) | 6.2 | (87 – 161) (126 ± 37) | (0.30 – 4.3) (2.4 ± 2) |
| [Chl <i>a</i>] _{dw} (μg L ⁻¹) | 1.1 – 8.2 (4.0 ± 3) | 9.4 – 23 (21 ± 9) | 6.9 | 50 – 103 (82 ± 28) | 0.25 – 3.8 (1.9 ± 1) |
| [DOC] _{cb} (mmol m ⁻²) | 39 – 93 (62 ± 24) | 39 – 122 (78 ± 26) | 25 – 47 (36 ± 15) | 152 – 251 (188 ± 45) | 38 – 113 (74 ± 26) |
| [DOC] _{dw} (μmol L ⁻¹) | 26 – 62 (43 ± 17) | 43 – 91 (60 ± 16) | 26 – 55 (41 ± 21) | 110 – 148 (128 ± 15) | 23 – 97 (57 ± 23) |
| [CO] _{cb} (μmol m ⁻²) | 3.2 – 12.6 (5.7 ± 4) | 5.5 – 19.0 (11.3 ± 4) | 6.8 – 7.9 (7.3 ± 0.8) | 24.0 – 41.2 (33.4 ± 7) | 3.3 – 26.2 (13.4 ± 7) |
| [CO] _{dw} (nmol L ⁻¹) | 2.4 – 8.4 (3.9 ± 3) | 4.3 – 13.5 (8.7 ± 3) | 7.9 – 8.3 (8.1 ± 0.2) | 14.1 – 33.2 (23.8 ± 8) | 2.0 – 21.5 (10.5 ± 6) |

^aSubscript “cb” designates column burden and “dw” designates depth-weighted concentrations. Values are range and, in parentheses, mean ± s.d. Keys and definitions of LCPI, LCP2, HCP1, and HCP2 are the same as those in Fig. 2-3.

^b[Chl *a*] data were collected only at Stn D44 on 30 May, 2008.

^cStn FB07 is excluded for calculations of [DOC]_{cb}, [DOC]_{dw}, [CO]_{cb}, and [CO]_{dw}.

2.4 DISCUSSION

2.4.1 Comparison with previous studies

Published studies on DOC distributions in first-year sea ice are rare and exclusively focused on the lowermost 4 centimeters of landfast ice (Smith et al., 1997; Riedel et al., 2008). Our finding of co-variation between [DOC] and [Chl *a*] in the bottom layer is consistent with the previous studies. Our peak-bloom (HCP2) DOC concentrations ([DOC]s) in the bottom layer of the landfast sea ice in the western Canadian Arctic (893-1230 $\mu\text{mol L}^{-1}$) were lower than those in the Resolute area, eastern Canadian Arctic under thin snow cover (1000-3358 $\mu\text{mol L}^{-1}$) (Smith et al., 1997). This could be due partly to the higher ice algal biomass observed in the Resolute area ([Chl *a*]: 700-2480 $\mu\text{g L}^{-1}$) than in the present study ([Chl *a*]: 854-1260 $\mu\text{g L}^{-1}$). Furthermore, our thicker ice sampling layer (10 vs. 4 cm) should also substantially contributed to this difference, given that ice algae and DOC are enriched predominantly within the very thin bottom layer. Riedel et al. (2008) reported a mean [DOC] of $\sim 800 \mu\text{mol L}^{-1}$ in the bottom 4 centimeters of landfast sea ice in Franklin Bay, western Canadian Arctic under thin snow cover during the vernal ice algal bloom season. Corresponding mean [DOC] from our study, 1070 $\mu\text{mol L}^{-1}$, was higher even without taking into account the difference in the ice sampling thickness, in accordance with more abundant Chl *a* observed in the present study (854-1260 vs. $< 872 \mu\text{g L}^{-1}$).

Vertical CO profiles collected during the HCPs resembled those previously documented in Franklin Bay (Xie and Gosselin, 2005). However, in the present study, we observed a substantially higher mean [CO] in the bottom 10 cm layer (179 nmol L^{-1}) than the earlier study (81.4 nmol L^{-1} in the bottom 4 cm layer). Accordingly, the mean $[\text{CO}]_{\text{dw}}$ and $[\text{CO}]_{\text{cb}}$ from the present study, 23.8 nmol L^{-1} and 33.6 $\mu\text{mol m}^{-2}$, are greater than the values of 15.3 nmol L^{-1} and 29.4 $\mu\text{mol m}^{-2}$ reported by Xie and Gosselin (2005). The smaller difference in $[\text{CO}]_{\text{cb}}$ is due to thicker sea ice during the previous survey (mean ice thickness: 134 vs. 192 cm). The cruise-mean $[\text{CO}]_{\text{cb}}$ in sea ice is approximately 3 times and

21% of the CO inventories observed in the open water of the Amundsen Gulf in fall 2003 and late spring 2004, respectively (Xie et al., 2009a).

2.4.2 Factors controlling [DOC] and [CO] in sea ice

Significant relationships between [DOC] and [Chl *a*] (Table 2-2) suggested that primary production was the main control on DOC accumulation in bottom sea ice during the HCPs, in accordance with previous studies (Smith et al., 1997; Riedel et al., 2008), but not within the upper ice matrix and during the LCPs. Other processes influencing DOC distribution in sea ice include trapping of riverine and resuspended organic matter during ice formation (Rachold et al., 2004), aeolian organic matter deposition, chemical enrichment in the quasi-liquid layer at the surface (Grannas et al., 2007), brine drainage (Giannelli et al., 2001; Amon, 2004), and microbial (Amon et al., 2001) and photochemical remineralization (Belzile et al., 2000; Xie and Gosselin, 2005). Inclusion of resuspended or riverine organic matter into ice could be attributable to the marked near-bottom [DOC] peak observed at Stn FB07 (Fig. 2-5f). Similar CDOM peaks have been observed in Franklin Bay (Xie and Gosselin, 2005). Atmospheric deposition and organic matter accumulation in the quasi-liquid layer might be responsible for the frequent DOC enrichment at the surface (Fig. 2-5a, e). Brine drainage most likely resulted in the rapid [DOC] drawdown in bottom ice at the onset of ice melting (Figs. 2-4b and 5c, e, f). To further elucidate this point, we calculated brine volume fractions (B_f) according to Cox and Weeks (1983) and assumed that significant fluid transport occurs in first year sea ice at $B_f \geq 5\%$ (Golden et al., 1998). B_f in the top 10 cm increased by ca. 4 times from the pre-melting (before 13 May; $4.4\% \pm 2\%$) to the melting season (after 13 May; $16\% \pm 7\%$). Similarly, B_f within the interior ice increased by ca. 3 times from $4.4\% (\pm 3\%)$ to $13\% (\pm 6\%)$ over the same time of period. B_f in the bottom 10 cm ranged from 7.2% to 32% and on average was only moderately higher during the melting season ($18\% \pm 8\%$) than during the preceding period ($14\% \pm 7\%$). Bottom ice was thus permeable to fluids over the entire sampling

period while surface and interior ice were permeable only during the period of ice melt. Brine drainage, which requires compensation by melting in the upper layers (Tison et al., 2008), should thus take place primarily during the melting season when the entire ice column was fluid-permeable.

Notably, exchange of interior ice brine with the atmosphere and ocean can be impeded by the formation of superimposed ice as fresh ice melt comes in contact with interior ice temperature below its freezing temperature near the surface and bottom of the ice cover (Eicken, 1992; Ehn et al., 2011). This process has been suggested to be responsible for the development of a distinct interior ice community during advanced stages of ice melt (Mundy et al., 2011). This formation of superimposed ice contributes to the explanation of why vertical distributions of [DOC] during the melting season were more erratic than during the previous periods, particularly within the interior ice (Fig. 2-5c, e).

The significant relationships between [CO] and [Chl *a*] suggest that [CO] distribution in the bottom ice prior to the melting season was dictated by biological processes and chemical reactions involving algal particles and algae-derived DOM. Based on controlled laboratory experiments and field observations, Xie and Gosselin (2005) proposed that CO photoproduction from CDOM is the principal driving force creating the distinct sea-ice [CO] vertical structure during the ice algal bloom season: lowest near the middle, highly elevated at the bottom, and moderately enriched at the surface (Fig. 2-5b, d). Solar-simulated irradiations of sea ice and brine samples collected from the IPY-CFL project further confirmed the CDOM photochemical source (H. Xie, unpublished data, 2008). Moreover, Xie and Zafiriou (2009) discovered that photodegradation of particulate organic matter (POM) in seawater is also an important CO production pathway. A later study further suggests that marine POM is more efficient than marine CDOM at CO photoproduction, particularly at visible wavelengths (G. Song and H. Xie, unpublished data, 2009). As relatively more visible radiation reaches the bottom ice due to stronger reflection of UV radiation by snow and ice (Wiscombe and Warren, 1980; Winther et al.,

2004), this evidence is of great significance to the high Chl *a* phases when POM can be more abundant than DOM in the bottom ice (Smith et al., 1997; Riedel et al., 2008). Additionally, prolific oxygen production due to photosynthesis by ice algae (Gleitz et al., 1995; Delille et al., 2007) promotes CO photoproduction since high oxygen concentrations accelerate organic matter photooxidation (Gao and Zepp, 1998; Xie et al., 2004). If CDOM and POM photochemistry were the primary CO sources, then the pre-HCP [CO] in sea ice should decrease with depth as a consequence of progressive light attenuation through ice and of weak organic matter enrichment at the bottom, as was observed in the pre-HCP vertical CO profiles (Fig. 2-5a).

Besides photochemistry, organic matter thermal (dark) reactions also produce CO with its formation rate rising quickly above pH 8 (Zhang et al., 2008). Although low temperatures in sea ice are not favorable for dark CO production, the highly elevated levels of organic matter and pH (up to 10) (Gleitz et al., 1995) associated with the ice algal bloom suggest that this process can be potentially important to bottom ice CO production. Moreover, Gros et al. (2009) observed significant CO production in laboratory cultures of marine phytoplankton, particularly certain diatoms. The strong correlation between [CO] and [Chl *a*] found in the present study during the early stage of the ice algal accumulation (LCPI) offers circumstantial field evidence for this argument. Further investigations, particularly laboratory incubations, are needed to elucidate whether ice algae, among which diatoms often dominate in the Arctic first-year sea ice (Horner, 1985; Riedel et al., 2008; Róžańska et al., 2009), are important CO producers.

The nature of multiple formation pathways implies that CO production in sea ice commenced during freeze-up around mid-October of the preceding year and sustained all the way towards the end of the melting season in summer. The strength and mechanism of CO production, however, varied in response primarily to the seasonal periodicity of solar radiation. The production is expected to be moderate and mainly CDOM photochemistry-based in fall, minimal and virtually exclusively thermal reaction-induced in winter, and maximal and largely photochemically and biologically driven in spring and summer. The

continued increase in [CO] in the middle layer during the melting season (data not shown), where CO loss was weaker than at the upper and lower interfaces (see below), was indicative of continued CO production after the disappearance of the high ice algal biomass. Vanishing snow cover and thawing surface sea ice in the melting season allow more UV radiation to enter the ice, thereby facilitating CO photoproduction.

Loss of CO in sea ice results from microbial uptake, upward release into the atmosphere, and downward transport into the water column. Microbial CO uptake, though well-documented in various marine water bodies (Conrad et al., 1982; Tolli and Taylor, 2005; Xie et al., 2005, 2009a, b), has been little studied in sea ice. Limited published data suggests that this process in sea ice is relatively slow but significant with turnover times from ~10 d in the high-biomass bottom layer to several tens of days in the much less biologically active upper layer (Xie and Gosselin, 2005). Surface ice temperature was close to or above -10°C from 6 April onward (Fig. 2-2c), suggesting that the ice matrix was diffusive to gas transport (Gosink et al., 1976; Loose et al., 2009, 2011). The supersaturated state of CO (see section 2.4.2) hence led to an egress of this gas from ice to the atmosphere. Warmer surface ice temperatures during the melting season (range: -0.1 to -4°C ; mean: -1.5°C) greatly enhanced gas diffusion and brine movement (see above), thereby boosting ice-to-air gas exchange and lowering [CO] within the surface layer (Fig. 2-4c). Similar to DOC, the abrupt loss of CO at the start of ice melt in the bottom ice (Fig. 2-4c) most likely resulted from brine drainage and the irregularity of [CO] vertical distributions during the melting season, particularly within the interior ice (Fig. 2-5c, e), was plausibly linked to the formation of superimposed ice.

2.4.3 Net production of DOC and CO

Biological DOC production in the ice took place predominantly during the HCPs and within the lowermost 30-cm layer (see sections 2.4.2 and 2.4.3). Depth-integrated [DOC] in

that layer averaged over the HCP was $127 \pm 22 \text{ mmol m}^{-2}$ in landfast ice and $57 \pm 19 \text{ mmol m}^{-2}$ in drifting ice excluding data from 6-11 April when [DOC] remained low (Fig. 2-4b). Net biological DOC production was estimated as the difference between [DOC] in the HCP and that in LCP1, taking the mean depth-integrated [DOC] in the lowermost 30-cm layer for LCP1 ($13 \pm 5 \text{ mmol m}^{-2}$) as the background [DOC]. This gave a net DOC production of $114 \pm 22 \text{ mmol m}^{-2}$ in landfast ice and $44 \pm 19 \text{ mmol m}^{-2}$ in drifting ice. The net biological DOC production averaged for both the landfast and drifting ice ($75 \pm 29 \text{ mmol m}^{-2}$ or $1.9 \pm 0.7 \text{ mmol m}^{-2} \text{ d}^{-1}$ over a period of 40 d) is comparable to the ice algal DOC release rate in the Chukchi Sea ($1.6 \pm 2 \text{ mmol m}^{-2} \text{ d}^{-1}$) estimated by Gosselin et al. (1997) using deck incubations. Our value is also similar in magnitude to the annual ice algal primary production ($\sim 80 \text{ mmol m}^{-2} \text{ a}^{-1}$) modeled by Lavoie et al. (2009) for the Mackenzie Shelf and corresponds to 45-90% of the spring primary production of ice algae on the shelves of the Chukchi and Beaufort Seas ($83\text{-}167 \text{ mmol m}^{-2}$) (Gradinger, 2009). The majority of this newly produced DOC would be released into the water column during the melting season as inferred from the precipitous [DOC] drop at the onset of bottom ice melt in mid-May (Fig. 2-4b). Notably, the net DOC production estimated here omits any biological DOC formation occurring during the melting season and does not take into account DOC loss processes as elaborated above. Therefore, our estimate is believed to be conservative and thus underestimates the gross DOC production. In contrast, all our ice cores were taken under relatively low snow covers ($\leq 10 \text{ cm}$), which reportedly favor biological DOC production over higher snow covers (Riedel et al., 2008). This potentially leads to upward biases in our estimates. However, we note that snow depths of greater than 15 cm were not common during the present study, except near deformed ice (C.J. Mundy, unpublished data, 2008) and that maximum Chl *a* concentrations during HCP2 were observed under a medium snow cover (10-15 cm), reaching $>3000 \mu\text{g L}^{-1}$ (M. Gosselin, unpublished data, 2008).

Net production of CO in the bottom 30-cm layer during the HCPs, assessed with an approach similar to that for DOC, was $6.5 \pm 2 \mu\text{mol m}^{-2}$ in drifting ice, $21.5 \pm 9 \mu\text{mol m}^{-2}$ in landfast ice, and $13.2 \pm 9 \mu\text{mol m}^{-2}$ averaged for the two. For comparison, the parallel CO

net production in the whole ice column was 7.2, 27.5, and 15.3 $\mu\text{mol m}^{-2}$, respectively, demonstrating that CO production primarily took place within the bottom layer. Furthermore, we estimated the CO net production from the start of ice formation to the end of the HCPs as 11.3 $\mu\text{mol m}^{-2}$ in drifting ice, 33.4 $\mu\text{mol m}^{-2}$ in landfast ice, and 18.7 $\mu\text{mol m}^{-2}$ averaged for the two, assuming negligible inclusion of CO from seawater during ice formation (Xie and Gosselin, 2005). These estimates are only moderately higher than those for the HCPs due apparently to low CO production over the extended dark winter period. It is again noted that all above estimates were lower limits of the corresponding gross production rates since various loss processes were not taken into account.

2.4.4 Contribution of sea ice to atmospheric CO

As sea ice in our study area was supersaturated with CO, it acted as a source of CO to the atmosphere. Only the Amundsen Gulf was evaluated with regard to the CO flux to the atmosphere since the majority of the sampling stations were located in this region (Fig. 2-1). The CO flux can be roughly estimated by multiplying a sea-ice CO transfer velocity of 0.70 m d^{-1} (Xie and Gosselin, 2005) by the cruise-mean surface ice [CO] ($11.7 \pm 8 \text{ nmol L}^{-1}$) in the Amundsen Gulf. Here the sea-ice CO transfer velocity is based on the study by Fanning and Torres (1991) indicating that ice cover reduces the ^{222}Rn transfer velocity by ~80%. The resultant ice-to-air flux estimate was $8.2 \pm 5 \mu\text{mol m}^{-2} \text{ d}^{-1}$, which is 45% of the CO flux from the open seawater to the atmosphere in the Amundsen Gulf in spring 2004 (Xie et al., 2009a). This value translates to an annual area-integrated flux of 7.4×10^7 moles of CO in the Amundsen Gulf by applying it to the period from mid-March to mid-July and taking a mean sea ice area of $7.4 \times 10^4 \text{ km}^2$ (CIS, <http://ice-glaces.ec.gc.ca/IceGraph103/page1.jsf>). Therefore, the annual sea ice CO flux is >74% of that from the open water in the same region (Xie et al., 2009a). Note that the flux estimates made here omit the period from the start of ice formation (mid-October 2007) to mid-March 2008 over which sea ice [CO] is unknown. This underestimates the annual flux,

though fluxes during wintertime are likely low due to low CO production and low ice permeability. It must be mentioned that there could be potentially large uncertainties in our CO flux estimates associated with using a constant transfer velocity. Unlike air-sea gas exchange, which has been relatively well parameterized by wind speed (e.g. Wanninkhof, 1992), there are currently no acceptable parameterizations for air-sea ice gas exchange. Gas transfer through sea ice should be dominated by diffusive processes controlled by the porosity of sea ice (Gosink et al., 1976; Loose et al., 2011). As porosity is a function of sea ice temperature (Cox and Weeks, 1983), gas permeability is expected to change seasonally. A recent laboratory simulation study, conducted at ice surface temperatures of -4 to 12°C, observed significant gas diffusion but was unable to find a consistent relationship between gas diffusion and sea ice porosity within the porosity range encountered (0.061-0.079) (Loose et al., 2011). Therefore, our CO flux estimates represent a first-approximation and will likely need to be refined upon the advent of a quantitative understanding of gas transfer across the air-sea ice interface.

In addition to the direct emission of CO from ice, part of the CO released from ice into the water column is also exchanged to the atmosphere when the ice cover breaks up or through leads and polynyas. $[\text{CO}]_{\text{cb}}$ lacked a consistent drawdown during LCP2 (data not shown), implying that CO production during that time was no less than losses caused by melting, brine drainage, microbial uptake, and emission to air. The sea-ice CO stock in LCP2 ($12.3 \pm 7 \mu\text{mol m}^{-2}$) can, therefore, be considered the lower limit transferred to and trapped in surface seawater through melting. According to Xie et al. (2009a), microbial uptake and outgassing each accounts for half of the CO loss in the mixed layer of the Amundsen Gulf in spring. Consequently, 50% of the sea-ice CO released to the surface seawater ended up in the atmosphere, i.e. $6.2 \mu\text{mol m}^{-2}$ or 3.5×10^5 moles of CO, taking the mean sea ice area of $5.7 \times 10^4 \text{ km}^2$ during LCP2 (CIS, <http://ice-glaces.ec.gc.ca/IceGraph103/page1.jsf>). This represents only 0.5% of the direct ice-to-air flux assessed above.

2.5 SUMMARY AND CONCLUSIONS

[DOC] and [CO] in the bottom sea ice generally followed the progression of ice algal biomass (as inferred by [Chl *a*]) while no consistent trends existed at the surface. Both [DOC] and [CO] decreased from the surface to the bottom of the ice at the start of the study during the period of low sea ice [Chl *a*]. During the peak ice algal bloom, [DOC] and [CO] decreased towards the interior of the ice cover and were highly enriched at the bottom. During the period of ice melt, the vertical structure of [CO] usually differed from that of [DOC] and both displayed no consistent patterns. It is noteworthy that bottom landfast ice in the study area contained higher concentrations of DOC and CO than bottom drifting ice during the period of high ice algal biomass.

Biological production during the peak period of the ice algal bloom and brine drainage-linked loss in the melting season were the dominant factors controlling the evolution of [DOC] in the bottom sea ice. The spatiotemporal distributions of [CO] in sea ice was in accordance with an *in situ* CO production by photooxidation of both dissolved and particulate organic matter, though the possibility of direct biological CO production, particularly during the peak period of the ice algal bloom, could not be ruled out. CO loss appeared fastest in the melting season as rising temperatures accelerated brine drainage, microbial consumption, and outgassing.

While DOC stock in sea ice was much smaller than its counterpart in the underlying water column surface mixed layer, CO inventories in sea ice and sunlit ice-free waters were of the same magnitude. Biological DOC production constituted a significant part of the ice algal primary production. Net accumulations of both DOC and CO predominantly occurred within the bottom ice layer when ice algal biomass was at its maximum. It is suggested that sea ice is an important source of atmospheric CO with its source strength approaching that of the ice-free water in spring. If this preliminary evaluation of CO flux is confirmed in the future, then Arctic climate warming, which leads to a shrinking ice cover, is not expected to

substantially increase the CO flux to the atmosphere in spite of anticipated increases in the ice-free water area and water column CO production.

ACKNOWLEDGMENTS

We thank C. Nozais, S. Pineault, C. Lacoste, J. Ehn, R. Memorana, and many other colleagues for their help with sea ice coring; G. Carnat, J. Ehn, and others for sea ice temperature measurement; M. Simard for DOC analysis; and D. A. Hansell and W. Chen for providing the DOC certified reference materials. We appreciate the cooperation of the chief scientists, captains, and crews of the Circumpolar Flaw Lead (CFL) system study cruises. This study was supported by grants from the Canadian International Polar Year (IPY) federal program office and the Natural Sciences and Engineering Research Council of Canada (NSERC). GS and YZ were supported by graduate scholarships from HX's NSERC Discovery Grant, CFL, and the Institut des sciences de la mer de Rimouski (ISMER). CA was supported by funds from CFL and the IPY Arctic Surface Ocean–Lower Atmosphere Study (Arctic SOLAS) program. CJM was supported by a postdoctoral fellowship from the Fonds québécois de la recherche sur la nature et les technologies (FQRNT). The CFL and Arctic SOLAS programs are under the overall directions of D. Barber and M. Levasseur, respectively. This is a contribution to the research programs of CFL, Arctic SOLAS, ISMER, and Québec-Océan.

CHAPITRE 3
PHOTOPRODUCTION DE MONOXYDE DE CARBONE À PARTIR DE
MATIÈRES ORGANIQUES PARTICULAIRE ET DISSOUTE DANS LES
CULTURES D'ALGUES DE GLACE

CARBON MONOXIDE PHOTOPRODUCTION FROM PARTICULATE AND
DISSOLVED ORGANIC MATTER IN ICE ALGAL CULTURES

To be submitted to Limnology and Oceanography

with the following authors: G. Song and H. Xie.

RÉSUMÉ

Des données récentes ont démontré que le monoxyde de carbone (CO) est enrichi dans la couche inférieure de la glace de mer de première année pendant la période de prolifération des algues de glace, mais les processus responsables de cet enrichissement ne sont pas bien compris. La présente étude examine pour la première fois l'efficacité de photoproduction de CO (c.-à-d., le rendement quantique apparent, AQY) à partir de CDOM et des particules récoltées sur les cultures d'algues de glace. Une forte photoproduction de CO a été observée à partir de particules aux longueurs d'onde (λ) > 600 nm alors que le CO n'a pas été photochimiquement produit à partir de CDOM aux λ > 500 nm. Les spectres AQY CO des particules provenant de cultures d'algues de glace en phases de croissance exponentielles et sénescentes ont été plus élevés que ceux du CDOM des cultures, en particulier aux longues longueurs d'onde. La modélisation basée sur l'AQY suggère que la photoproduction de CO à partir de CDOM dans la couche inférieure de la glace de mer (10 cm) a été principalement réalisée par le rayonnement UVA pendant la période de prolifération des algues de glace tandis que la lumière visible a été le principal contributeur de la photoproduction de CO à partir de particules. Les particules ont joué un rôle beaucoup plus important que le CDOM dans la photoproduction de CO à la base de la glace de mer. En outre, le rayonnement UVA est devenu de plus en plus important dans la photoproduction de CO à partir de CDOM et des particules, et la contribution du CDOM à la photoproduction totale de CO a augmenté lorsque le couvert de neige et de glace a commencé à fondre. Cette étude a fourni des preuves importantes que la photochimie des particules dans la glace de mer pourrait dépasser celle du CDOM.

ABSTRACT

Recent evidence demonstrated that carbon monoxide (CO) is enriched in the bottom layer of first-year sea ice during ice algal blooms, but the processes responsible for this

enrichment are not well understood. The present study for the first time investigated the wavelength-dependent efficiencies (i.e. apparent quantum yields, AQY) of CO photoproduction from CDOM and particles harvested from ice algal cultures. Prolific CO photoproduction was observed from particles at $\lambda > 600$ nm while no obvious CO was photochemically produced from CDOM at $\lambda > 500$ nm. The AQY spectra showed that particles collected at the exponential and senescent phases were more efficient at CO photoproduction than the corresponding CDOM samples, particularly at long wavelengths. AQY-based modeling suggests that CO photoproduction from CDOM in bottom sea ice (10 cm) was mainly effected by the UVA regime during ice algal blooms while visible light was the main contributor for particle-driven CO photoproduction. Particles played a far more important role than CDOM in CO photoproduction in bottom sea ice. Moreover, UVA became more and more important to CO photoproduction from both CDOM and particles, and the contribution of CDOM to total CO photoproduction increased when the snow cover and ice started to melt. This study provided important evidence that particle photochemistry in sea ice could exceed CDOM.

3.1 INTRODUCTION

Sea ice is an important and special ecosystem in polar oceans by providing a habitat for a variety of organisms (von Quillfeldt et al., 2003; Poulin et al., 2011). Sea ice cover also reduces the light availability and hence the primary production in the water column. On the other hand, sea ice reduces the ratio of ultraviolet radiation (UVR) to photosynthetically active radiation (PAR, 400-700 nm) (Uusikivi et al., 2010) and thus protects the organisms in and under sea ice against damaging UVR. Moreover, sea ice plays a major role in organic carbon cycling in polar oceans via biological production by ice algae. Ice algae can provide 3-25% of the total primary production in seasonally ice covered Arctic seas and >50% in the central Arctic Ocean (Gosselin et al., 1997). DOC production by ice algae makes up about 40% of the total organic carbon fixation in sea ice

(Gosselin et al., 1997; Smith et al., 1997). During ice algal blooms, the concentration of dissolved organic carbon ([DOC]) is much higher than that in the underlying seawater and is correlated with the ice algal standing stock (chlorophyll *a* (Chl *a*) or particulate organic carbon (POC) in the bottom layer of first-year sea ice (Smith et al., 1997; Riedel et al., 2008; Song et al., 2011).

In addition to its role in carbon cycling, sea ice is also involved in the biogeochemistry of certain photo- or bio-reactive gases. Gosink et al. (1976) demonstrates that, unlike freshwater ice, sea ice is highly permeable at temperatures above -15°C , and hence certain climate-related gases could readily be exchanged between air and sea ice. The main conclusions of gas cycling inside sea ice and between the air-ice-seawater interface from previous studies include 1) gases could be rejected from ice to the air during ice formation in winter (Nomurai et al., 2006; Nagurnyi, 2008; Miller et al., 2011; Randall et al., 2012) while an opposite opinion is that the uptake rate of atmospheric CO_2 into the ocean becomes faster during this period due to the increased solubility in the low-temperature-and-high-salinity brine and the rapid transport of brine to deep water (Anderson et al., 2004); 2) the CO_2 uptake rate is faster during ice algal blooms (Delille et al., 2007); however, significant amounts of O_2 are consumed with CO_2 produced by respiration of bacteria during this period (Deming et al., 2010); 3) dimethylsulfide (DMS) (Levasseur et al., 1994; Turner et al., 1995) is produced by ice algae in bottom sea ice, which makes sea ice an important source of atmospheric sulfur (Zemmelink et al., 2008); 4) sea ice is a medium for photoproducing carbon monoxide (CO) (Xie and Gosselin, 2005; Song et al., 2011) and hydrogen peroxide (H_2O_2) (Kláňová et al., 2003; King et al., 2005) and photo-decomposing chlorine dioxide (OClO) (Pursell et al., 1995, 1996) and DMS (Hellmer et al., 2006).

In spite of attention paid to physical, biological, optical and chemical processes in sea ice, the biogeochemistry of trace gases in sea ice is largely unknown. It has been demonstrated that the CO concentration ([CO]) in the bottom layer of first-year sea ice during ice algal bloom is much higher than that in the upper sea ice and the underlying

seawater (Xie and Gosselin, 2005; Song et al., 2011). Considering the known sources of CO in seawater (i.e. photoproduction from particulate and chromophoric dissolved organic matter (POM and CDOM) (Conrad and Seiler, 1980; Zafiriou et al., 2003; Xie and Zafiriou, 2009; Song et al., 2013) and biological production by marine phytoplankton) (Gros et al., 2009), photodegradation of CDOM and POM could be mainly responsible for the enrichment of CO in bottom sea ice during bloom, along with possible biological production. Furthermore, taking into account of the higher transmittance of sea ice for visible light relative to UV (Ehn et al., 2008) and the relatively higher apparent quantum yield (AQY, symbol: Φ) of CO from marine-derived POM than that of CDOM in the visible regime (Song et al., 2013), POM may be more important in CO photoproduction than CDOM in bottom sea ice during bloom. In this study, the wavelength-dependent Φ_{co} spectra from particles and CDOM collected from 3 dominant diatom ice algal monocultures and a natural ice algal assemblage were carried out to compare the relative efficiencies of CDOM and particles in terms of CO photoproduction. Furthermore, the relative contributions of CDOM and particles to total CO photoproduction in bottom sea ice during ice algal blooms were estimated. This study provides novel results about the importance of particle photochemistry in carbon and trace gas cycling in sea ice.

3.2 METHODS

3.2.1 Ice algal culture incubations

Non-axenic monocultures of *Pauliella taeniata* (*P. taeniata*), *Attheya septentrionalis* (*A. septentrionalis*), *Nitzschia frigida* (*N. frigida*) and a natural ice algal assemblage (*NIAA*) collected from bottom sea ice in Resolute Bay were inoculated in 1 L glass flasks with sterilized *f/2* medium. The selected species are the dominant diatoms in sea ice in Arctic Ocean near Alaska and Canada (von Quillfeldt et al., 2003; Poulin et al., 2011), and the *NIAA* was incubated to investigate potential differences between the monocultures and the

natural assemblage. Duplicates of each culture were incubated at 4°C under illumination of cool white fluorescent light (details see Table 3-1). 1 L f/2 medium was stored in a glass flask under the same light and temperature conditions to assess potential alterations of the photoreactivity of the organic matter in the medium (G. Li et al., unpublished data). Chl *a* was monitored at a several-day interval to assess the growth stage of the cultures, and the results suggested, for each culture, the biomass and growth rates in the parallel flasks were highly consistent (< 10% for [Chl *a*]).

Table 3-1 Information of selected ice algae and the incubation conditions

| Ice algae | CCMP strain | Taxon | Cell size ^a (μm) | | Light | | Incubation duration (d) |
|--|-------------|-----------------|--|-------|--|------------|-------------------------|
| | | | Length | Width | Intensity ($\mu\text{mol m}^{-2} \text{s}^{-1}$) | Cycle | |
| <i>Pauliella taeniata</i> ^b | 1115 | Pennate diatoms | 20-22 | 5-7 | 60-70 | 14:10 | 166 |
| <i>Attheya septentrionalis</i> | 2083 | Centric diatoms | 14-20 | 3-4 | 40 | continuous | 94 |
| <i>Nitzschia frigida</i> | NA | Pennate diatoms | NA | | 40 | continuous | 124 |
| Natural ice algal assemblage | NA | NA | NA | | 40 | continuous | 120 |

^athe cell sizes of *P. taeniata* and *A. septentrionalis* are referenced from the webpage of National Center for Marine Algae and Microbiota (NCMA) (<https://ncma.bigelow.org>). No size data is available for *N. frigida*.

^bthe incubation conditions for *P. taeniata* are the standard conditions at the NCMA lab, while for other species (including *NIAA*) are referred to other labs (C. Lovejoy and A. R. Juhl, personal communication)

3.2.2 Sample collection

The main procedures of sample collection and processing are shown in Fig. 3-1. Briefly, when the cultures were at the exponential or senescent phase, one of the duplicates was gravity filtered through a clean 10- μm Nylon mesh to separate the ice algal cells from the liquid phase and bacteria. Furthermore, 10 mL of the original culture was filtered for determining the absorption spectra of CDOM and particles and [Chl *a*] (details see below). The filtrates, as well as the medium, were sequentially vacuum filtered through GF/F (47 mm) and 0.2- μm polyethersulfone filters (PES, Whatman). The final filtrates were transferred into pre-combusted glass bottles and stored in the refrigerator for CDOM absorption spectra and CO AQY determinations. The particles (i.e. ice algal cells plus detritus) retained on the mesh were gently flushed several times with artificial seawater (ASW) until the absorbance of the filtrates was low ($a_{330} < 0.03 \text{ m}^{-1}$). The flushing was purported to diminish bacteria and DOM retained on ice algal cells, thereby minimizing potential microbial CO consumption and DOM-based CO photoproduction during the irradiation of particle samples (see below). The ASW was composed of Na^+ , K^+ , Ca^{2+} , Mg^{2+} , SO_4^{2-} and Cl^- with a salinity ~ 34 (Berges et al., 2001). NaCl , KCl , and Na_2SO_4 were combusted at 400°C for ca. 4 hours. Before use, the ASW was vacuum filtered with 0.2- μm PES filters and then photobleached for 24 hours under full light spectrum with an XLS+ solar simulator to further reduce its DOC content (final concentration: 0.12 mg L^{-1}) and absorbance of CDOM (a_{330} : 0.004 m^{-1}).

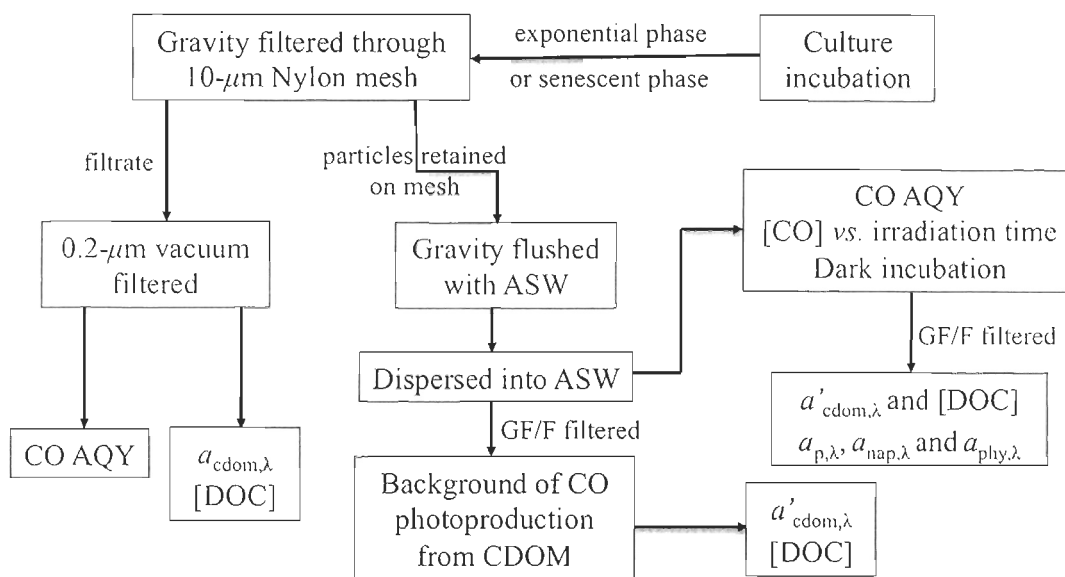


Fig. 3-1 Flow-chart of the main procedures of sample collection and processing. ASW: artificial seawater; $a'_{cdom,\lambda}$: the spectral absorption coefficient of CDOM retained in the ASW plus that if any released from the particles (details see the text).

3.2.3 Irradiation

After flushing with ASW, the ice algal cells were immediately dispersed into ca. 2.5 L photobleached ASW, gently stirred with a Teflon skinned magnetic bar to make the solution homogenous and bubbled with air to minimize background [CO]. After about 30 minutes, part of the sample was transferred into a series of 44 mL quartz cells (OD: 20 mm, Length: 140 mm). Some of the irradiation cells were vertically placed in a temperature-controlled (4°C) water bath and irradiated with a CPS solar simulator. A series of successive Schott long-band cutoff filters (WG280, WG295, WG305, WG320, WG345, GG395, GG435, GG495 and OG570) were employed to conduct the wavelength-dependent CO photoproduction, along with two parallel dark controls. The numeric value in each model number signifies the nominal 50% transmittance cutoff wavelength in nanometers. The sidewalls of the cells were wrapped with black electric tape to prevent lateral light interference between the cells. Irradiation was < 40 min for samples under cutoff filters WG280, WG295, WG305, WG320, and <1.5 h for samples under the other cutoff filters. The samples were shaken gently before irradiation and every 30 min thereafter to minimize particle settlement. Other cells were irradiated in the same manner to determine [CO] with time under full spectrum. The remaining part of the samples was filtered through pre-combusted GF/F (47 mm) filters with low vacuum (< 50 kPa). The filtrate was irradiated in the same manner to determine CO photoproduction from DOM remaining in the ASW plus that released from the particles, if any. After irradiation, [CO] was determined using the headspace method reported by Xie et al. (2002). The particle-containing samples were then filtered with low vacuum (< 50 kPa) through 25-mm pre-combusted GF/F (Whatman) filters for determining the absorption spectra of particles and CDOM and [DOC]. Furthermore, part of the dark control sample was filtered through a 25-mm pre-combusted GF/F (Whatman) filter to determine the [Chl *a*]. It is worthwhile to point out that, to investigate the variations of [DOC], the absorption spectra of CDOM (marked as a'_{cdom}) and the proportion of CO photoproduction from CDOM in particle photochemistry

experimental series, the above parameters were determined based on GF/F filtration (particles $> 0.7 \mu\text{m}$) to precisely retrieve the photons absorbed by particles and CO photoproduction from particles. To determine the CO AQY from CDOM in the f/2 medium and 0.2- μm filtered culture samples, the samples were also bubbled and irradiated in the above manner, along with the determinations of CDOM absorption spectra and [DOC]. The OG570 cutoff filter was not used for CDOM samples, considering that previous studies did not observe significant CO photoproduction from marine CDOM at $\lambda > 600 \text{ nm}$ (Xie et al., 2009a; Song et al., 2013).

3.2.4 Sample analyses

After filtration, the GF/F filters were placed in 10 mL of 90% acetone in scintillation vials for at least 18 h in darkness at $\sim 4^\circ\text{C}$. The supernatant was measured for fluorescence, before and after being acidified with 5% HCl, using a Turner Designs fluorometer (model 10-AU) according to the method of Parsons et al. (1984). [Chl *a*] was calculated using the equation of Holm-Hansen et al. (1965).

Particulate matter collected on the filters was analyzed for optical density (*OD*) using a Perkin Elmer Lambda 850 dual beam spectrometer fitted with a 150-mm snap-in integrating sphere accommodating a filter holder (Röttgers and Gehnke, 2012). The spectral optical density of the filter, $OD_{f,\lambda}$, where λ is wavelength in nm, was recorded from 800 to 290 nm at 1-nm increments and a scanning speed of 120 nm min^{-1} . $OD_{f,\lambda}$ was converted to the spectral particulate absorption coefficient, $a_{p,\lambda}$ (m^{-1}), using Eq. (3-1),

$$a_{p,\lambda} = 2.303 \times (A/V) \times (OD_{f,\lambda} - OD_{blank,\lambda}) \times (1/\beta_\lambda) \quad (3-1)$$

where $OD_{blank,\lambda}$ is the optical density of a blank filter, A the clearance area of particles on the filter (m^2), V the volume of sample water filtered (m^3), and β_λ the path length amplification factor. β_λ was nonlinearly correlated with $OD_{f,\lambda}$ (Röttgers and Gehnke, 2012):

$$\beta_{\lambda} = 2.9OD_{f,\lambda}^2 - 4.76OD_{f,\lambda} + 4.5 \quad (3-2)$$

Upon the completion of $a_{p,\lambda}$ determination, the filter was dipped in 10 mL methanol for ~18 h to bleach pigments and the absorption coefficient of non-algal particles, $a_{nap,\lambda}$ (m^{-1}), was determined in the same manner as that for $a_{p,\lambda}$. Subtracting $a_{nap,\lambda}$ from $a_{p,\lambda}$ gave the phytoplankton absorption coefficient, $a_{phy,\lambda}$ (m^{-1}).

The beam attenuation coefficient (symbol: c , m^{-1}) of the particle-containing sample (the same sample as CO AQY from particles) was determined using a Perkin-Elmer Lambda 35 dual beam spectrophotometer coupled with a 10-cm cylindrical quartz cell with the same diameter of the irradiation cells to minimize the difference in c induced by the different geometries of the two kinds of quartz cells. The scattering coefficient (b ; m^{-1}) of particles at each wavelength is calculated by subtracting a_t from c (i.e. $b=c-a_t$). Here a_t is the total absorption coefficient of the sample, i.e. the sum of a_p , a'_{cdom} and the absorption coefficient of pure water (a_w) (Buiteveld et al., 1994; Pope and Fry, 1997).

The spectral optical density of CDOM, $OD_{cdom,\lambda}$, was scanned from 800 to 200 nm at 1-nm intervals with a Perkin Elmer Lambda 35 dual beam spectrometer fitted with 5-cm quartz cuvettes and referenced to MilliQ water. Samples were allowed to warm up to room temperature before analysis. The sample cuvette was rinsed with methanol, pure water, and sample water between individual scans. A baseline correction was applied by subtracting the optical density averaged over 683-687 nm from all $OD_{cdom,\lambda}$ values (Babin et al., 2003). The spectral CDOM absorption coefficient, $a_{cdom,\lambda}$ (m^{-1}), was calculated as 2.303 times $OD_{cdom,\lambda}$ divided by the light path length of the cell in meters (0.05 m).

Eight milliliters of 0.2- μm or 0.7- μm (GF/F) filtered samples were transferred into 9 mL clean glass vials with adding 100 μL 2N HCl, and stored in the refrigerator for DOC determination. [DOC] was analyzed in triplicate using a Shimadzu TOC-5000A Total Carbon Analyzer calibrated with potassium biphthalate. The system was checked, every seven consecutive sample analyses, against Hansell's low-carbon ([DOC]: 1–2 $\mu mol L^{-1}$)

and deep Sargasso Sea ([DOC]: 44–46 $\mu\text{mol L}^{-1}$) reference waters. The mean coefficient of variation of triplicate measurements was 1.3% (0.1% - 13.5%).

3.2.5 Retrieval of CO AQY

The spectral CO AQY, Φ_λ , is defined as the number of moles of CO produced per mole of photons absorbed by a given set of light-absorbing materials at wavelength λ . Here the light-absorbing materials refer to CDOM or particles, corresponding to Φ_λ for CDOM ($\Phi_{cdom,\lambda}$), particles ($\Phi_{p,\lambda}$), respectively. According to Hu et al. (2002), the number of absorbed photons at wavelength λ , $Q_{a,\lambda}$ (mol photons $\text{s}^{-1} \text{nm}^{-1}$), by CDOM in 0.2- μm filtered samples and by particles, were calculated using Eq. (3-3) and (3-4), respectively:

$$Q_{a,\lambda} = Q_\lambda \times S \times (a_\lambda / a_{t,\lambda}) \times [1 - \exp(-a_{t,\lambda} \times L)] \quad (3-3)$$

$$Q_{a,\lambda} = Q_\lambda \times S \times (a_\lambda / a'_{t,\lambda}) \times [1 - \exp(-a'_{t,\lambda} \times L)] \quad (3-4)$$

Q_λ (mol photons $\text{m}^{-2} \text{s}^{-1} \text{nm}^{-1}$) denotes the photon flux just below the frontal quartz window; a_λ (m^{-1}) stands for $a_{cdom,\lambda}$ for 0.2- μm filtered samples or $a_{p,\lambda}$ for particle-containing samples; $a_{t,\lambda}$ (m^{-1}) is the total absorption coefficient, i.e. $a_{cdom,\lambda}$ plus $a_{w,\lambda}$ (Buiteveld et al., 1994; Pope and Fry, 1997) for 0.2- μm filtered samples; $a'_{t,\lambda}$ (m^{-1}) is the modeled total absorption coefficient of the particle-containing sample; S (m^2) and L (m) are, respectively, the cross-section and path length of the irradiation cells. During irradiation for CO photoproduction from particles, particle scattering could deflect photons out of the irradiation cell and change the effective path length of light transmission (Miller and Zepp, 1979; Estapa et al., 2012a). The contribution of particle scattering to light attenuation in the samples was estimated from Monte Carlo simulations using the SimuIO software (Leymarie et al., 2010; details see Annex 1). According to the simulation results, particle scattering enhanced the total absorption coefficient by 0-39% across the wavelength interval of 290-700 nm, with the factors decreasing with increasing wavelength.

A simple exponential model (Eq. (3-5)) was used for modeling the $\Phi_{cdom,\lambda}$ spectra for the medium and cultures while a modified quasi-exponential model (Eq. (3-6)) was employed for $\Phi_{p,\lambda}$ spectra (details see Annex 2).

$$\Phi_{cdom,\lambda} = m_1 \times \exp(m_2 \times (\lambda - 290)) \quad (3-5)$$

$$\Phi_{p,\lambda} = m_1 \times \exp(m_2 / (m_3 + \lambda)) \quad (3-6)$$

where m_1 , m_2 , and m_3 in Eq.(3-5) and (3-6) are fitting parameters. The amount of CO produced in an irradiation cell over the exposure time could then be predicted as the product of the assumed Φ_λ function and the number of absorbed photons integrated over 290–600 nm for 0.2- μm filtered samples and over 290-700 nm for particle samples. Notably, the concordant control experiments showed CO photoproduction from CDOM retained in the ASW plus released from the particles was $3.1\% \pm 2\%$ (0.4%-7.5%) to total CO photoproduction under each cutoff for all the cultures, and the CO photoproduction rate from particles under each cutoff was corrected by subtracting that from CDOM and the mean value of the dark controls from the total value. CO production rates calculated from the retrieved Φ_λ were in good agreement with the measured rates, with R^2 ranging from 0.990 to 0.999 (mean: 0.996) for CDOM samples and from 0.990 to 0.997 (mean: 0.993) for particle samples.

To facilitate comparison of various Φ_λ spectra, a solar irradiance spectrum-weighted mean apparent quantum yield, $\bar{\Phi}$, was computed for each CO AQY spectrum following the procedure of Zhang et al. (2006):

$$\bar{\Phi} = (\int_{290}^{600} Q_{0,\lambda} \times \Phi_\lambda \times d\lambda) / (\int_{290}^{600} Q_{0,\lambda} \times d\lambda) \quad (3-7)$$

$\bar{\Phi}$ denotes $\bar{\Phi}_{cdom}$ for CDOM and $\bar{\Phi}_p$ for particles, respectively. $Q_{0,\lambda}$ (mol photons $\text{m}^{-2} \text{h}^{-1} \text{nm}^{-1}$) is the surface spectral solar photon fluxes at 70°N, 133°W at 14:00 local time on 01 July, simulated using the SMARTS model (Simple Model of the Atmospheric Radiative Transfer of Sunshine; Gueymard, 2001) under mid-summer Arctic atmospheric and

cloudless conditions with an ozone column burden of 330 Dobson Units. This normalization reduced the AQY spectrum to a single value of CO production in the entire water column, in which all solar radiation was absorbed by a specific group of light-absorbing material, i.e. CDOM or particles (Bélanger et al., 2006). Note that $\bar{\Phi}_p$ is also integrated from 290 nm to 600 nm to facilitate comparison with $\bar{\Phi}_{cdom}$ and with $\bar{\Phi}_p$ published in a previous study (Song et al., 2013), though the $\Phi_{p,\lambda}$ spectra were modeled to 700 nm in this study.

3.3 RESULTS

3.3.1 General chemical, biological and optical properties

The cultures reached their exponential growth phases, which lasted for about 2 months, in 1-2 weeks after inoculation. The maximum [Chl *a*] was 723 $\mu\text{g L}^{-1}$ for *P. taeniata*, 233 $\mu\text{g L}^{-1}$ for *A. septentrionalis*, 131 $\mu\text{g L}^{-1}$ for *N. frigida* and 379 $\mu\text{g L}^{-1}$ for *NIAA*, respectively. The cultures were incubated from 120 to 166 days (Table 3-1), until [Chl *a*]s were much lower than the maximum values.

[Chl *a*]s at the exponential phase were ca. 3 to 50 times higher than their counterparts at the senescent phase (Table 3-2). Like [Chl *a*], at the exponential phase, $a_{p,443}$ was also higher than that at the senescent phase. During the exponential phase, the a_p spectra showed significant pigment absorption peak around 676 nm and the wide band shoulder between the interval of 380-500 nm, with the center around 443 nm. However, during the senescent phase, most cells were dead and the particles became detritus, leading to the characteristic peak and shoulder of pigment smaller or disappeared (Fig. 3-2A, B) and the ratio of $a_{phy,443}:a_{p,443}$ lower relative to that at the exponential phase (Table 3-2).

Both [DOC] and $a_{cdom,330}$ (a_{cdom} at 330 nm) in the cultures were higher than those in the medium (Table 3-3). Furthermore, [DOC] and $a_{cdom,330}$ increased from the exponential phase

to the senescent phase, and the net production of DOC was 0.47-3.04 mg L⁻¹ at the exponential phase and 1.87-16.3 mg L⁻¹ at the senescent phase. [DOC] and the absorption spectra of the medium were not determined at the senescent phase, however, significant variations of DOC and CDOM are not expected to occur in the medium (Li et al., unpublished data). Generally, a_{cdom} in the cultures was higher than that in the medium at all wavelengths (Fig. 3-2D), but in some cases, a_{cdom} in the cultures at the exponential phase was lower than that in the medium at long wavelengths (Fig. 3-2C), due probably to DOM consumption by bacteria. Here we use the spectral slope coefficient over the wavelength interval of 275-295 nm ($S_{275-295}$), which is calculated with an exponential decay model (Helms et al., 2008), to indicate the origin of CDOM (Fichot and Benner, 2012). Owing to the net production of CDOM by ice algae, $S_{275-295}$, like DOC and $a_{cdom,330}$, was higher in the cultures than in the medium, and consistently increased from the exponential phase to the senescent phase. The result agreed with higher $S_{275-295}$ indicating more proportion of marine-derived CDOM (Helms et al., 2008; Fichot and Benner, 2012).

Table 3-2 Biological and optical properties of the particle samples. Note that [Chl *a*], $a_{p,443}$, and $a_{phy,443}:a_{p,443}$ presented here were measured for the irradiation samples, but not in the initial incubation cultures. [Chl *a*] was the mean values of the two dark controls; $a_{p,443}$ and $a_{phy,443}:a_{p,443}$ were the mean values of the dark controls and in the corresponding irradiated samples (after irradiation). [Chl *a*]s and $a_{p,443}$ in the initial incubation cultures (data not shown) were about 3 times of their counterparts in the corresponding irradiation solutions. EP: exponential phase; SP: senescent phase; NA: no data is available.

| | <i>P. taeniata</i> | <i>A. septentrionalis</i> | <i>N. frigida</i> | NIAA |
|---------------------------------------|--------------------|---------------------------|-------------------|------|
| Chl <i>a</i> ($\mu\text{g L}^{-1}$) | | | | |
| EP | 73.7 | 60.6 | 15.0 | 92.7 |
| SP | 22.6 | 13.0 | NA | 2.0 |
| $a_{p,443}$ (m^{-1}) | | | | |
| EP | 0.93 | 1.10 | 0.29 | 1.33 |
| SP | 0.85 | 0.68 | NA | 0.13 |
| $a_{phy,443}:a_{p,443}$ | | | | |
| EP | 0.92 | 0.92 | 0.89 | 0.85 |
| SP | 0.84 | 0.86 | NA | 0.7 |

Table 3-3 Chemical and optical properties of the 0.2- μm filtered samples. EP: exponential phase; SP: senescent phase; [DOC] and the absorption spectra of the medium were not determined at the senescent phase, and we assume there would be no significant difference between those at the exponential phase, since the medium was autoclaved.

| | f/2 medium | <i>P. taeniata</i> | <i>A. septentrionalis</i> | <i>N. frigida</i> | NIAA |
|--|------------|--------------------|---------------------------|-------------------|-------|
| DOC (mg C L ⁻¹) | | | | | |
| EP | 3.40 | 4.92 | 3.87 | 4.08 | 6.44 |
| SP | 3.40 | 18.5 | 7.24 | 5.27 | 19.7 |
| $a_{\text{cdom},330}$ (m ⁻¹) | | | | | |
| EP | 1.45 | 1.67 | 1.67 | 1.70 | 3.02 |
| SP | 1.45 | 7.57 | 2.94 | 2.17 | 6.09 |
| $S_{275-295}$ | | | | | |
| EP | 0.0075 | 0.016 | 0.012 | 0.012 | 0.015 |
| SP | 0.0075 | 0.021 | 0.020 | 0.017 | 0.023 |

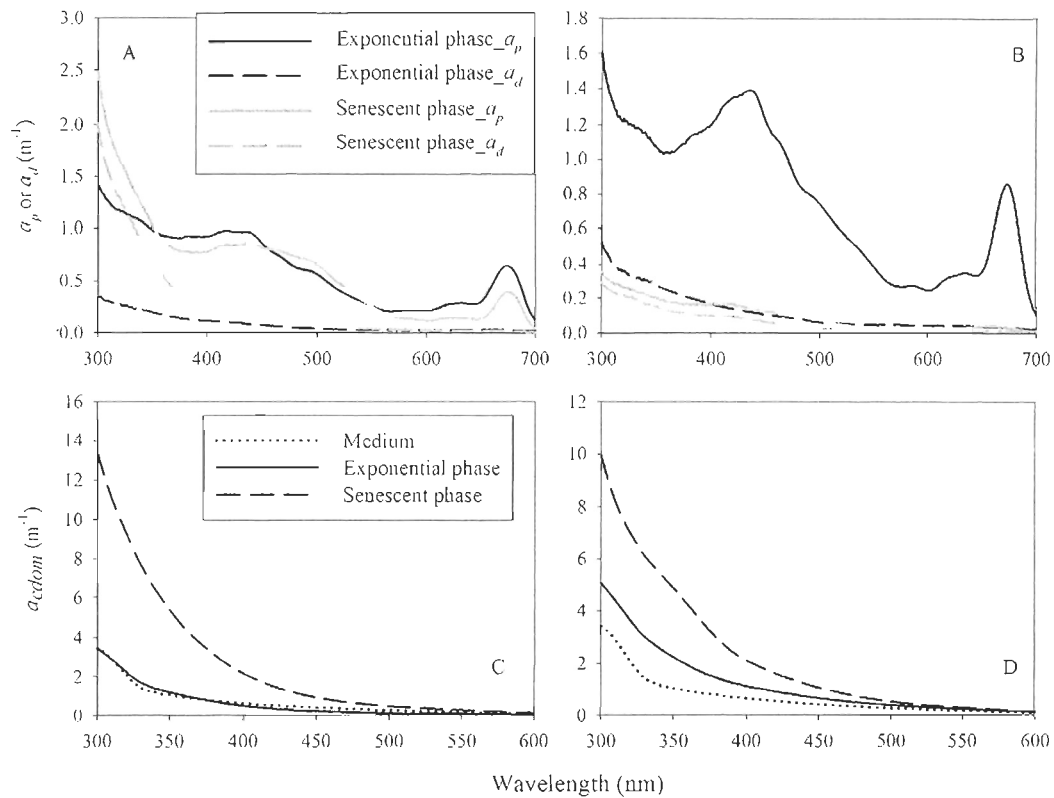


Fig. 3-2 Examples of absorption spectra of particles and CDOM. a_p and a_d spectra presented here were measured for the irradiation samples, but not in the initial cultures, in which they should be 3 times of those for the irradiation samples. Left panel: *P. taeniata*; right panel: *NIAA*.

3.3.2 Controls and linearity of CO photoproduction from particles

Compared with the dark controls, $a_{p,\lambda}$ did not significantly decrease after irradiation under all cutoffs while [DOC] and a'_{cdom} did not substantially increased (Annex 2 Table A2-1). Hence, CO should be photoproduced primarily from particles during irradiation not from POM-derived DOM. In addition, [DOC] and $a_{cdom,\lambda}$ did not change significantly for the 0.2- μm filtered samples before and after irradiation (<3%). A time-course irradiation suggested [CO] increased linearly within 1.5 h (the maxima irradiation duration for CO AQY) under full spectrum (Fig. 3-3A). Concordant dark incubation at 4°C showed [CO] linearly increased or kept constant during incubation (Fig. 3-3B), demonstrating slow dark CO production (thermal and/or biological production) from particles and no significant microbial CO consumption. The result also verified that the filtration and flushing procedure essentially eliminated bacteria, at least CO-oxidizing microbes.

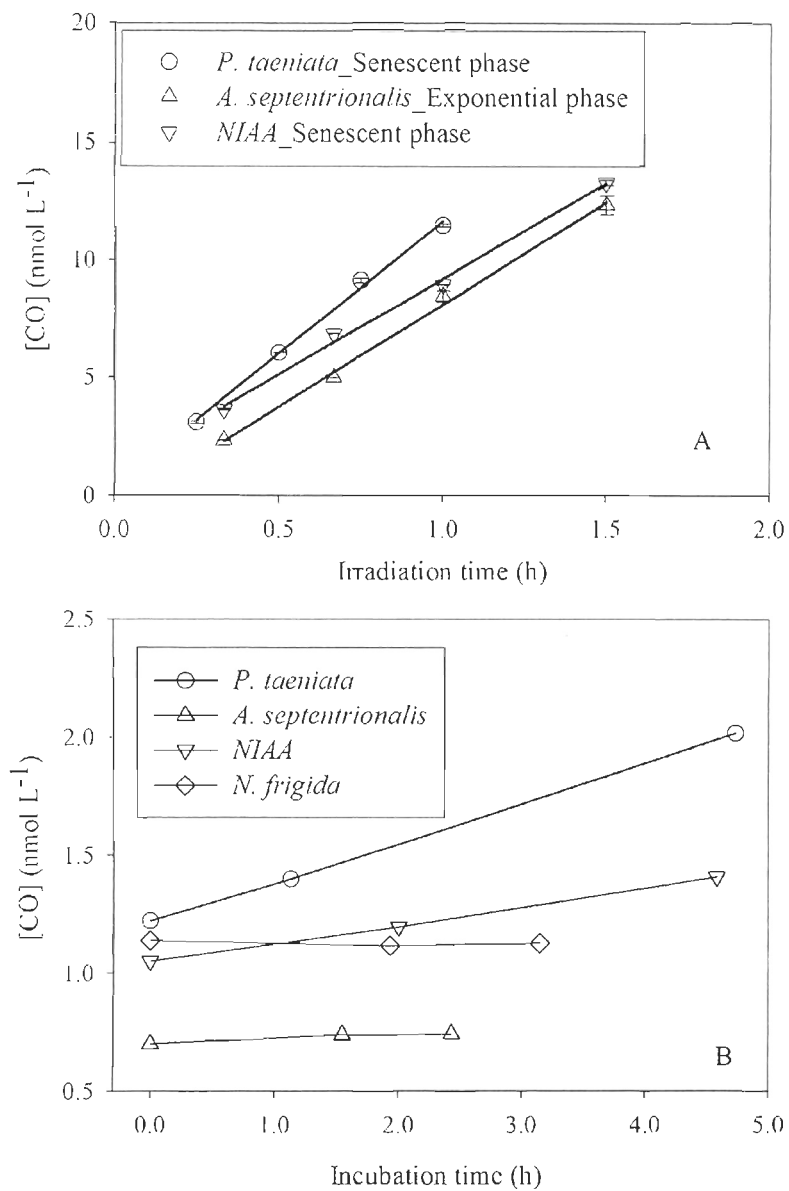


Fig. 3-3 Examples of [CO] along with irradiation time under full spectrum (A) and with dark incubation time (B). Panel A: CO concentration was also linearly increased for other particle samples (not shown in the plot); error bar in panel A is the average deviation of duplicates; dark incubation data shown in panel B were only for the exponential phase, the results for the senescent phase were in the same pattern, with slow dark production.

3.3.3 CO AQY spectra

CO photoproduction rates from CDOM and particles as a function of the nominal 50% cutoff wavelength are shown in Fig. 3-4. CO photoproduction rate from CDOM decreased more rapidly with increasing cutoff wavelength than that from particles. Moreover, there was a significant amount of CO produced from particles under OG570 cutoff filter, and CO production rate from particles under GG495 cutoff filter was higher than that from CDOM. Previous study suggested that CO could also be produced by phytoplankton via biological processes (Gros et al., 2009). To test if there was significant biological production by ice algae during irradiation, CO photoproduction rate from KCN (final concentration: 0.43 mg L⁻¹) poisoned *N. frigida* cells at the exponential phase was investigated, which was slightly lower than that from the parallel unpoisoned sample (<7% under long wavelength cutoff filters and < 4% under short wavelength cutoff filters). The upper limit of CO biological production during the short irradiation duration (< 1.5 h) was < 7%, given that cyanide inhibits CO photoproduction (Song et al., 2013). Hence, CO production from particle samples during irradiation predominantly originated from particle photodegradation.

The fitted parameters for Φ_{co} , along with Φ_{330} and $\bar{\Phi}$, of CDOM and particles are shown in Table 3-4, and Fig. 3-5 displays Φ_{co} spectra from CDOM and particles at the two growth phases, along with that of the medium in each panel. $\Phi_{p,\lambda}$ was higher than its corresponding $\Phi_{cdom,\lambda}$ for each culture, with the differences widening with increasing wavelength and up to several orders in the interval of 500-600 nm. This would be due mainly to the relatively higher CO photoproduction rates under long wavelength cutoff filters from particles (Fig. 3-4). $\Phi_{cdom,\lambda}$ of the cultures were higher than that of the medium (Fig. 3-5). An exception is *N. frigida*, whose $\Phi_{cdom,\lambda}$ spectra at both growth phases were almost the same as that of the medium (Fig. 3-5C), because the biomass of *N. frigida* was very low during incubation (Table 3-2) and thus the production of DOM by *N. frigida* was low. Another possible reason was, unlike the other three cultures, the CO production

efficiency of DOM produced by *N. frigida* was similar to that in the medium. $\Phi_{cdom,\lambda}$ at the senescent phase was almost the same as or slightly lower than that at the exponential phase.

In each culture, CDOM was composed of that brought by the medium but after microbial uptake plus that produced by ice algae. So, $\Phi_{cdom,\lambda}$ for the cultures were the overall results of CDOM and represented the lower limit of that freshly produced by ice algae during incubation. Whereas, the actual absorption spectra of the CDOM produced by ice algae could not be determined, and consequentially $\Phi_{cdom,\lambda}$ of this term could not be retrieved. However, the upper limit of $\Phi_{ca,\lambda}$ of CDOM produced by ice algae could be retrieved using the method of Song et al. (2013), assuming the composition, concentrations and optical properties of the nutrients and DOM in the medium did not change during incubation. Fig. 3-6 displays the lower and upper limits of $\Phi_{cdom,\lambda}$ of each culture at the exponential and senescent phases. The upper limit of $\Phi_{cdom,\lambda}$ was within 5-times that of the lower limit along the wavelength interval, and hence it was still much lower than the corresponding $\Phi_{p,\lambda}$, particularly in the visible wavelengths.

3.3.4 $\bar{\Phi}$ and photoreactivity

$\bar{\Phi}_{cdom}$ (lower limit herein) of the cultures were almost the same between the two growth phases, except *N. frigida*, for which, $\bar{\Phi}_{cdom}$ at the exponential phase was ca. twice of that at the senescent phase (Table 3-4). The upper limit of $\bar{\Phi}_{cdom}$ was similar to its lower limit at the exponential phase, but ca. 2 times at the senescent phase. Hence, the averaged upper limit of $\bar{\Phi}_{cdom}$ at the senescent phase was ca. 2 times that at the exponential phase. The results again demonstrated CDOM freshly produced by ice algae was more photoreactive than that in the medium. The relationships of $\bar{\Phi}_p$ between the two growth phases were more complicated: $\bar{\Phi}_p$ of *P. taeniata*, was higher at the exponential phase than that at the senescent phase while for another two species, the relationships were reversed, especially for *NIAA*, with $\bar{\Phi}_p$ at the senescent phase being ca. 3 times that at the exponential

phase (Table. 3-4). Notably, if $\bar{\Phi}_p$ was integrated from 290 nm to 700 nm, the correlation between different growth phases for each culture was the same as above (data not shown). Moreover, $\bar{\Phi}_p$ was consistently higher than its corresponding value of $\bar{\Phi}_{cdom}$ for each culture and at each growth phase, with the mean value of $\bar{\Phi}_p$ being ca. 4 times that of $\bar{\Phi}_{cdom}$ at the exponential phase and 6 times at the senescent phase, respectively. Furthermore, the mean value of $\bar{\Phi}_p$ was ca. 3.5 times that of the upper limit of $\bar{\Phi}_{cdom}$ at the exponential phase and 3 times at the senescent phase. The relationship suggested particles synthesized by ice algae were far more efficient in CO photoproduction than ice algae-derived CDOM, agreed with particles were more photoreactive than CDOM in open ocean seawater (Song et al., 2013).

Table 3-4 Fitted parameters of Eq. (3-4) for CDOM and Eq. (3-5) for particle samples, along with Φ_{330} and $\bar{\Phi}$. nd: no data available.

| Ice algae | CDOM | | | | | | | | | |
|---------------------------|---------------------------|--------|-------------------------------|-------------------------------|-------------------------------|---------------------------|-------------------------------|-------------------------------|-------------------------------|-------------------------------|
| | Exponential phase | | | | Senescent phase | | | | | |
| | m_1 $\times 10^6$ | m_2 | Φ_{330} $\times 10^6$ | $\bar{\Phi}$ $\times 10^6$ | m_1 $\times 10^6$ | m_2 | Φ_{330} $\times 10^6$ | $\bar{\Phi}$ $\times 10^6$ | | |
| medium | 104.4 | -0.058 | 10.2 | 0.42 | | | nd | | | |
| <i>P. taeniata</i> | 238.6 | -0.044 | 41.5 | 1.99 | 221.9 | -0.043 | 39.0 | 1.88 | | |
| <i>A. septentrionalis</i> | 105.5 | -0.033 | 28.7 | 1.79 | 227.8 | -0.047 | 42.4 | 1.94 | | |
| <i>N. frigida</i> | 306.3 | -0.063 | 24.0 | 0.96 | 137.8 | -0.060 | 12.3 | 0.50 | | |
| NIAA | 136.7 | -0.044 | 23.6 | 1.13 | 159.2 | -0.049 | 22.8 | 1.02 | | |
| | Particles | | | | | | | | | |
| | Exponential phase | | | | | Senescent phase | | | | |
| | m_1 $\times 10^{10}$ | m_2 | m_3 | Φ_{330} $\times 10^6$ | $\bar{\Phi}$ $\times 10^6$ | m_1 $\times 10^{10}$ | m_2 | m_3 | Φ_{330} $\times 10^6$ | $\bar{\Phi}$ $\times 10^6$ |
| <i>P. taeniata</i> | 1883 | 805.1 | -209.4 | 149.5 | 10.6 | 0.92 | 3965 | 45.8 | 104.9 | 5.75 |
| <i>A. septentrionalis</i> | 38.1 | 2024.2 | -116.6 | 50.1 | 3.40 | 3.04 | 3611 | 43.2 | 89.4 | 5.51 |
| <i>N. frigida</i> | 291.1 | 987.8 | -193.9 | 41.2 | 2.83 | | | nd | | |
| NIAA | 2249 | 641.6 | -222.3 | 87.1 | 6.74 | 181.1 | 2271 | -91.2 | 243.9 | 18.2 |

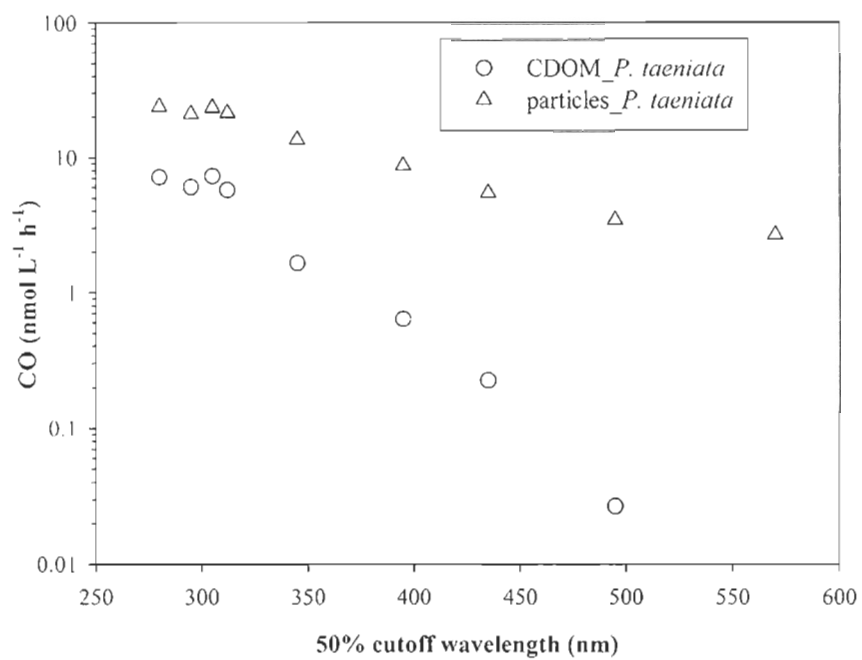


Fig. 3-4 Example of CO photoproduction from CDOM and particles as a function of the nominal 50% cutoff wavelength (*P. taeniata* at the senescent phase).

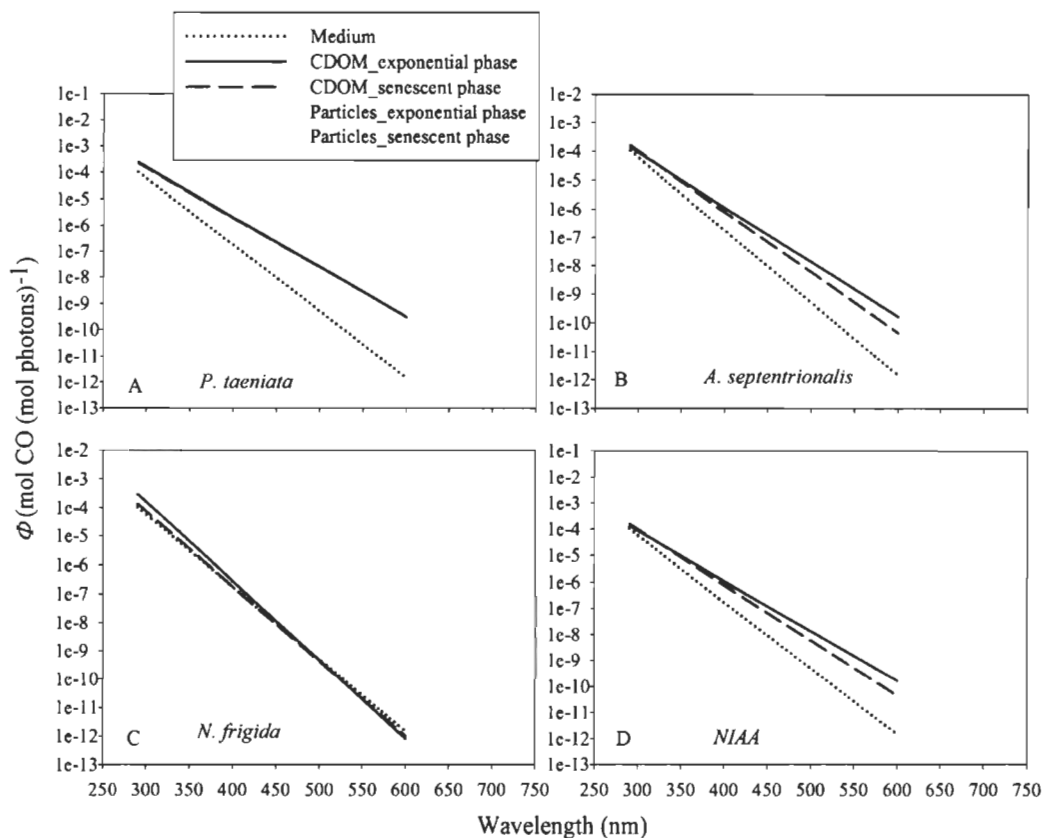


Fig. 3-5 Spectra of $\Phi_{cdom,\lambda}$ and $\Phi_{p,\lambda}$ as a function of wavelength. $\Phi_{cdom,\lambda}$ of the medium was also presented in each panel to directly exhibit $\Phi_{cdom,\lambda}$ of the medium was lower than that of the cultures, excluding *N.frigida*. Note that in panel A, the lines for CDOM at the exponential and senescent phases are overlapped. No data are available for $\Phi_{p,\lambda}$ at the senescent phase for *N.frigida*.

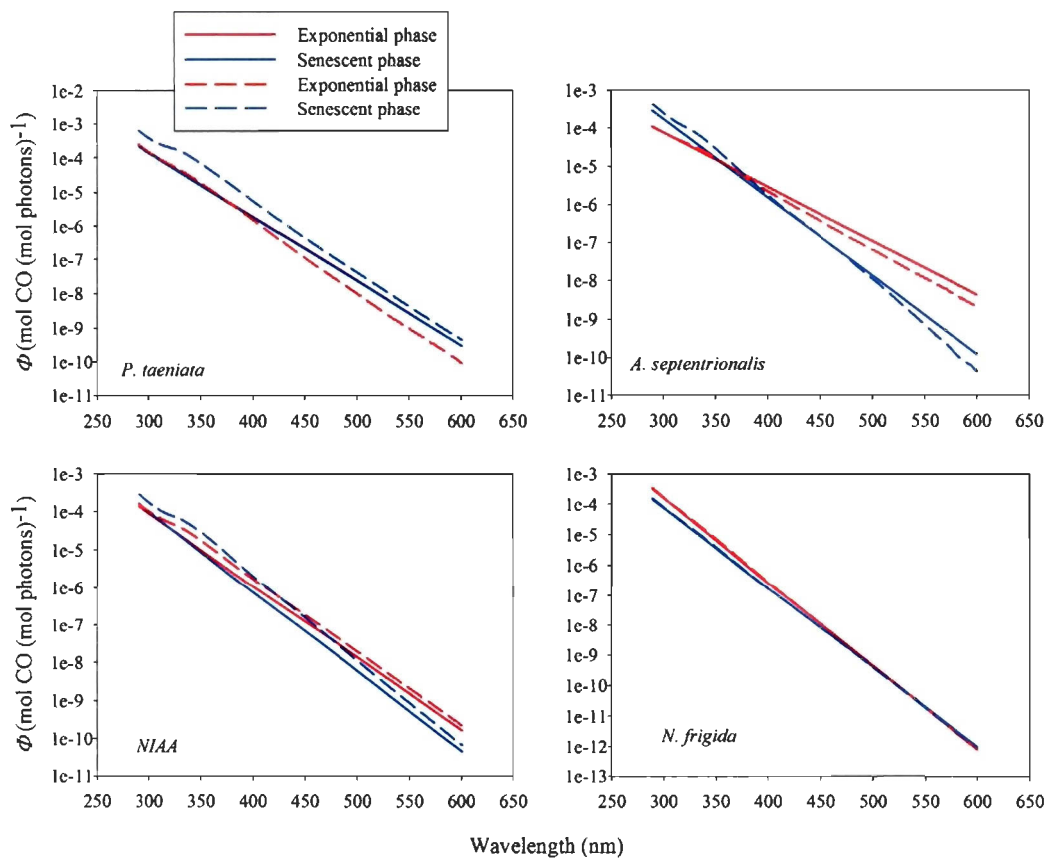


Fig. 3-6 Lower and upper limits of $\Phi_{cdom,\lambda}$ of each culture. Solid line: lower limit; dashed line: upper limit.

3.4 DISCUSSION

3.4.1 Compare Φ_λ with previous studies

Fig. 3-7 displays the spectra of $\Phi_{cdom,\lambda}$ in bulk sea ice (station D43) and the mean values of $\Phi_{cdom,\lambda}$ and $\Phi_{p,\lambda}$ in both the surface and deep chlorophyll maxima (DCM) in Canada Basin (Song et al., 2013), along with the highest and lowest spectra of $\Phi_{cdom,\lambda}$ and $\Phi_{p,\lambda}$ obtained in this study. The CDOM sample in bulk ice at station D43 was collected during the ice algal bloom in the southeastern Beaufort Sea in 2008, during the 2007–2008 International Polar Year–Circumpolar Flaw Lead (IPY–CFL) system study (details see Song et al., 2011), and irradiated at 1°C (H. Xie, unpublished data). $\Phi_{cdom,\lambda}$ spectra obtained in this study were similar to or lower than that in bottom bulk ice and surface and DCM waters in Canada Basin at long wavelengths (Fig. 3-7A). Sea ice and seawater in Canada Basin could contain terrigenous CDOM, which is considered more efficient in CO photoproduction than marine CDOM, especially in visible regime (Valentine and Zepp, 1993; Zafiriou et al., 2003; Xie et al., 2009a). $\Phi_{p,\lambda}$ decreases from the cultures to that in DCM water and then in surface water in Canada Basin (Fig. 3-7B). The ratio of $a_{phy,443}:a_{p,443}$ is highest in the ice algae samples (0.82 ± 0.16), and decreases from DCM (0.81 ± 0.10) to the surface (0.40 ± 0.17) (Song et al., 2013), which suggests fresher cells with higher organic contents are more efficient in CO photoproduction. Moreover, in surface seawater, particles underwent stronger photobleaching, which reduces the photoreactivity of particles.

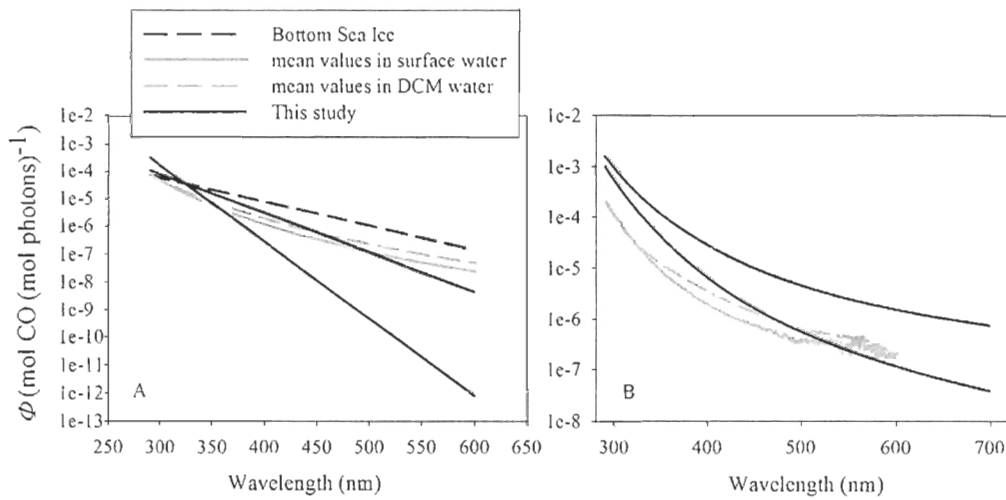


Fig. 3-7 Comparison of Φ_{λ} obtained in this study with previous studies. Panel A: CDOM; panel B: particles. To make the chart clear, only the highest and lowest $\Phi_{cdom,\lambda}$ and $\Phi_{p,\lambda}$ (based on long wavelengths) of the cultures are shown in the charts. Sample details see the text.

3.4.2 Action spectra of CO photoproduction in bottom sea ice

During ice algal blooms, [CO] in the bottom 10-cm layer is enriched in late spring and early summer in Arctic first-year sea ice (Xie and Gosselin, 2005; Song et al., 2011). To evaluate the relative contributions of particles and CDOM to the enrichment, CO photoproduction from particles and CDOM in bottom sea ice was modeled based on the CO AQY spectra of the ice algae cultures and the following assumptions: 1) the selected ice algal species is the dominant species during bloom in Arctic first-year sea ice; and 2) the organic matter produced in lab cultures is quantitatively and qualitatively representative of that produced by ice algae in the field.

The surface action spectra of CO photoproduction at the interface of 10 cm to the bottom, $A_{0,\lambda}$ (mol CO m⁻³ h⁻¹ nm⁻¹), and the depth-integrated (i.e. ice column) action spectra in the bottom 10-cm layer, $A_{col,\lambda}$ (mol CO m⁻² h⁻¹ nm⁻¹) are calculated using Eq. (3-8) and (3-9), respectively:

$$A_{0,\lambda} = Q'_{0,\lambda} \times a_{\lambda} \times \Phi_{\lambda} \quad (3-8)$$

$$A_{col,\lambda} = Q'_{0,\lambda} \times (a_{\lambda}/a_t) \times (1 - \exp(-a_t \times L)) \times \Phi_{\lambda} \quad (3-9)$$

where $Q'_{0,\lambda}$ (mol photons m⁻² h⁻¹) denotes the spectral solar photon fluxes at the depth of 10 cm from the bottom of the sea ice, which is the mean surface spectral solar irradiance at 70°N, 126°W during 25 April to 5 May, multiplying the transmittance of sea ice (T) at the corresponding depth (Ehn et al., 2008). The surface spectral solar photon fluxes are simulated using the SMARTS model under the same conditions mentioned above (section 2.4) (Gueymard, 2001). a_{λ} and Φ_{λ} denote $a_{cdom,\lambda}$ and $\Phi_{cdom,\lambda}$ for CDOM, and $a_{p,\lambda}$ (in the initial cultures) and $\Phi_{p,\lambda}$ for particles at the exponential phase, respectively. $a_{i,\lambda}$ is the total absorption coefficient, i.e. the sum of $a_{cdom,\lambda}$, $a_{p,\lambda}$ and the absorption coefficient of pure ice, $a_{i,\lambda}$ (Grenfell and Perovich, 1981; Perovich and Govoni, 1991). L is the light path-length in the bottom sea ice (0.1 m). The transmittance of landfast sea ice located at the Franklin Bay was determined from 350 nm to 700 nm with the ice thickness ca. 1.8 m and under thin

snow cover (<10 cm) or partially removed during an ice algal bloom (Ehn et al., 2008) and were extrapolated to 320 nm with a Gaussian regression model (Fig. 3-8A). The modeled results of CO photoproduction only apply to the same conditions as those under which the transmittances were determined.

Unlike in natural seawater, both $A_{0,\lambda}$ and $A_{col,\lambda}$ of CDOM and particles in bottom sea ice decrease with increasing wavelength (Fig. 3-8C, D), which is mainly induced by the pattern of the solar spectrum in bottom sea ice (Fig. 3-8B). Furthermore, when the snow cover is partially removed, the transmittance of sea ice increases by about 2 orders as compared to their counterparts with snow cover within the entire wavelength interval, and the ratio of UV to visible light is enhanced (Fig. 3-8A). Hence, the solar spectrum, $A_{0,\lambda}$ and $A_{col,\lambda}$ are sequentially enhanced with the same pattern (Fig. 3-8B, C, D). Overall, averaged on the action spectra of all four cultures, UVA (320-400 nm) and visible light (400-700 nm) contribute $91\% \pm 6\%$ and $9\% \pm 6\%$ to the wavelength-integrated CDOM's A_0 ($A_{cdom,0}$) with snow cover, while visible light is the major contributor to the wavelength-integrated particles' A_0 ($A_{p,0}$), with the value of $66\% \pm 4\%$. When the snow cover is partially removed, the contribution of UVA is enhanced by 4% to $A_{cdom,0}$ and 14% to $A_{p,0}$, respectively. The wavelength-integrated A_{col} of CDOM ($A_{cdom,col}$) and particles ($A_{p,col}$) exhibit the same trend as their counterparts at the surface: UVA is still the main contributor to $A_{cdom,col}$, accounting for $92\% \pm 5\%$, while visible light accounts for more to $A_{p,col}$ ($67\% \pm 3\%$); furthermore, the importance of UVA is enhanced for CDOM and particles when the snow cover thins, with the same extents as those at the surface. So, when the snow and ice start to melt in early summer, the importance of UV becomes more and more important to CO photoproduction in sea ice. Moreover, particles are more important to CO photoproduction in sea ice over wavelength interval of 320-700 nm, particularly at long wavelengths (Fig. 3-8C, D).

CO photoproduction rates (P_{co}) ($\mu\text{mol CO m}^{-2} \text{d}^{-1}$) from both particles (P_p) and CDOM (P_{cdom}) in the bottom 10 cm layer could be calculated by integrating Eq. (3-9) from 320 to 700 nm. Modeled total P_{co} in bottom sea ice ranged from 0.01 to 0.05 $\mu\text{mol CO m}^{-2} \text{d}^{-1}$ with thin snow cover, which was enhanced by more than 100 times (1.34-11.5 $\mu\text{mol CO}$

$\text{m}^{-2} \text{d}^{-1}$) when the snow cover was partially removed. The modeled total P_{co} was comparable with the estimated net accumulation rate ($0.44 \pm 0.2 \mu\text{mol CO m}^{-2} \text{d}^{-1}$, $n=4$) based on the field measurement during bloom in bottom landfast ice (mean ice thickness 1.5 m, snow cover 5 cm) in the southeastern Beaufort Sea (Song et al., 2011). The modeled results also suggest that particles contribute more than 90% to total CO photoproduction at the bottom sea ice (Fig. 3-9) during ice algal blooms. However, CDOM becomes progressively more important when the snow cover reduces or disappears. Note that during the post-bloom period (i.e. stationary and senescent phases), the ratio of $a_{cdom}:a_p$ in sea ice should gradually becomes higher, since the main processes in controlling particle load during this period are bacteria respiration and photodegradation, while CDOM is still produced via these processes. The increased $a_{cdom}:a_p$ ratio at the post-bloom period, relative to that at the exponential phase, can also be proven by the values obtained in this study based on lab-incubation (Table 3-2, 3). So, during the ice melting season, CDOM may accounts for more to total CO photoproduction.

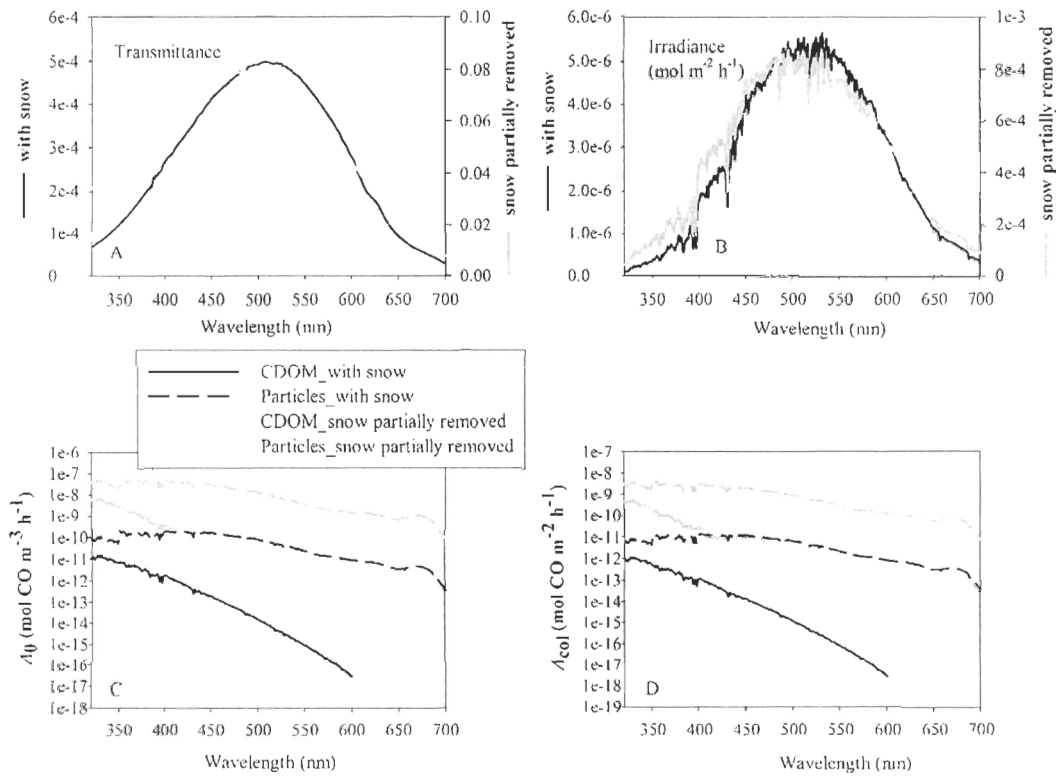


Fig. 3-8 Transmittance of landfast sea ice measured at the depth of 10 cm from the ice-water interface in Franklin Bay (southeastern Beaufort Sea)(Ehn et al., 2008) (A), the calculated solar irradiance (mol m⁻² h⁻¹) at this depth (see the text) (B) and the action spectra of CO photoproduction (mol CO m⁻² h⁻¹) from CDOM and particles for *P. taeniata* at the 10-cm interface from the bottom (surface action spectra) (C) and in the bottom 10 cm layer (depth-integrated action spectra) (D).

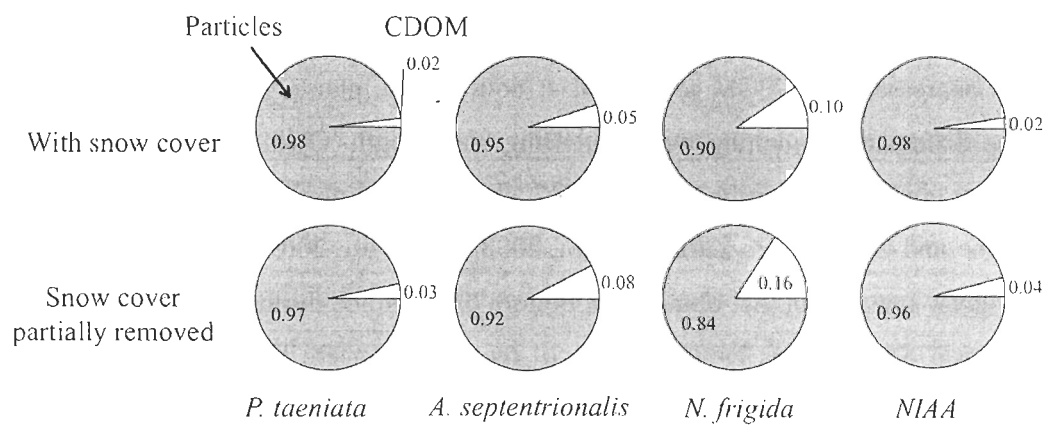


Fig. 3-9 Relative contributions of particles and CDOM to total CO photoproduction in the bottom 10 cm first-year sea ice under different snow cover conditions.

3.5 SUMMARY

Ice algae produced significant amounts of DOM, which was characterized as marine origin with relatively high $S_{275-295}$, along with POM during incubation. Unlike CDOM, there were significant amounts of CO photoproducted from particles at $\lambda > 600$ nm. Φ_{co} of the cultures decreased from POM to CDOM at both growth phases and then to the medium, with the differences widening with increasing wavelength. Owing to terrigenous CDOM being more photoreactive with respect to CO photoproduction than marine-derived CDOM (Valentine and Zepp, 1993; Zafiriou et al., 2003; Xie et al., 2009a), $\Phi_{cdom,\lambda}$ of the cultures were slightly lower than that obtained in bottom bulk sea ice during ice algal bloom and in natural open ocean water. However, $\Phi_{p,\lambda}$ of the cultures were higher than that in natural seawater. Relative organic content, reflected by the ratio of $a_{phy,443}:a_{p,443}$, and photobleaching may be mainly responsible for the differences.

Modeled $A_{0,\lambda}$ and $A_{col,\lambda}$ of CDOM and particles in bottom sea ice during ice algal bloom demonstrated that P_{co} decreased with increasing wavelength. CO was mainly photoproducted in the UVA regime from CDOM in bottom sea ice, while visible light was the main contributor of CO photoproduction from particles. Both $A_{p,0}$ and $A_{p,col}$ were much higher than their CDOM counterparts at each wavelength, so particles play a far more important role in CO photoproduction in bottom sea ice and could contribute more than 90% of total CO photoproduction in the bottom 10 cm layer. Moreover, when the snow cover thinned or disappeared, the importance of UVA was gradually enhanced for CO photoproduction from both CDOM and particles, and the relative contribution of CDOM to total CO photoproduction in sea ice also became higher. Though the modeled results can only be applied to the conditions used in the model, this study revealed that particle photochemistry might exceed its CDOM counterpart in bottom sea ice.

ACKNOWLEDGMENTS

We are grateful to Conie Lovejoy (University Laval), Andrew R. Juhl (Columbia University) and Michel Gosselin (Université du Québec à Rimouski) for providing ice algal cultures. We also thank Mélanie Simard (Université du Québec à Rimouski) for DOC analysis and Jens K. Ehn (University of Manitoba) for providing the ice transmittance data. This study was supported by NSERC (Natural Sciences and Engineering Research Council). GS was supported by graduate scholarships from ISMER (Institut des sciences de la mer de Rimouski) and FRQNT (Fonds de recherche du Québec – Nature et technologies). This is a contribution to the research programs of ISMER, and Québec-Océan.

CHAPITRE 4

L'EFFICACITÉ SPECTRALE DE LA PHOTOPRODUCTION DE MONOXYDE DE CARBONE (CO) DANS L'ARCTIQUE CANADIEN DE L'OUEST: PARTICULES CONTRE SOLUTÉS

SPECTRALLY RESOLVED EFFICIENCIES OF CARBON MONOXIDE (CO) PHOTOPRODUCTION IN THE WESTERN CANADIAN ARCTIC: PARTICLES VERSUS SOLUTES

Article Publié dans Biogeosciences

Song, G., H. Xie, S. Bélanger, E. Leymarie, and M. Babin, 2013. Spectrally resolved efficiencies of carbon monoxide (CO) photoproduction in the western Canadian Arctic: particles versus solutes, *Biogeosciences*, 10, 3731-3748, doi:10.5194/bg-10-3731-2013.

RÉSUMÉ

L'efficacité spectrale (c'est-à-dire le rendement quantique apparent, AQY) dans la photo-production de monoxyde de carbone (CO) est un bon indicateur de la photo-réactivité du substrat et un paramètre crucial pour modéliser les taux de photo-production de CO dans la colonne d'eau. Des données récentes ont suggéré que la photo-production de CO à partir de particules dans les eaux marines est significative par rapport à la production bien connue de CO à partir de la photo-dégradation de la matière organique chromophore dissoute (CDOM). Bien que les spectres AQY de CO basés sur le CDOM aient été largement documentés dans la littérature, on a peu d'information sur la phase particulaire. En utilisant des échantillons d'eau prélevés dans l'estuaire et le plateau continental du McKenzie, et dans le bassin canadien dans le sud-est de la mer de Beaufort, la présente étude quantifie, pour la première fois, les spectres AQY de photo-production de CO associés aux particules. Ces spectres ont été comparés avec ceux associés au CDOM déterminé simultanément. Les AQYs de CO des particules et du CDOM diminuent exponentiellement avec la longueur d'onde, mais la forme spectrale du AQY de la matière particulaire était plus plate dans le régime visible. Cette caractéristique a donné lieu à une production de CO disproportionnellement plus élevée à partir des particules causé par la lumière visible, augmentant ainsi la proportion de CO produit par la photooxydation des particules par rapport au CDOM avec la profondeur dans la zone euphotique. En termes de production intégrée sur toute la zone euphotique, la formation de CO à partir de CDOM était dominée par le rayonnement ultraviolet (UV, 290-400 nm), alors que les rayons UV et la lumière visible jouaient un rôle à peu près égal dans la production de CO à partir des particules. Spatialement, l'AQY du CO de la matière particulaire totale (c'est-à-dire la somme des substances organiques et inorganiques) a augmenté de l'estuaire et du plateau jusqu'au bassin, tandis que la tendance

s'inversait dans le cas du AQY de CO à partir du CDOM. L'eau provenant du maximum profond de chlorophylle a révélé un AQY de CO plus élevé que dans les eaux de surface, autant pour les particules que pour le CDOM. Le AQY de CO de la matière particulaire totale a dépassé celui du CDOM sur le plateau continental et dans le bassin, mais la séquence s'est inversée dans l'estuaire. Considérant le fait que la fraction minérale des particules dans l'estuaire contribue significativement à l'absorption de la lumière UV et visible, l'AQY du CO de la matière organique particulaire pourrait cependant surpasser sa contrepartie en CDOM dans les trois sous-régions. En termes de photo-production de CO, le POM est donc plus photo-réactif que le CDOM, indépendamment des origines de la matière organique (c'est-à-dire terrigènes ou marines). Le CDOM terrigène a montré une photo-réactivité supérieure à celle du CDOM marin, alors que le POM terrigène est apparu moins photo-réactif que le POM marin. La modélisation basée sur l'AQY indique que la photo-production de CO dans la zone d'étude est sous-estimée de 12% à 32% si on ignore par production par les particules.

ABSTRACT

Spectrally resolved efficiency (i.e. apparent quantum yield, AQY) of carbon monoxide (CO) photoproduction is a useful indicator of substrate photoreactivity and a crucial parameter for modeling CO photoproduction rates in the water column. Recent evidence has suggested that CO photoproduction from particles in marine waters is significant compared to the well-known CO production from chromophoric dissolved organic matter (CDOM) photodegradation. Although CDOM-based CO AQY spectra have been extensively determined, little is known of this information on the particulate phase. Using water samples collected from the Mackenzie

estuary, shelf, and Canada Basin in the southeastern Beaufort Sea, the present study for the first time quantified the AQY spectra of particle-based CO photoproduction and compared them with the concomitantly determined CDOM-based CO AQY spectra. CO AQYs of both particles and CDOM decreased with wavelength but the spectral shape of the particulate AQY was flatter in the visible regime. This feature resulted in a disproportionally higher visible light-driven CO production by particles, thereby increasing the ratio of particle- to CDOM-based CO photoproduction with depth in the euphotic zone. In terms of depth-integrated production in the euphotic zone, CO formation from CDOM was dominated by the ultraviolet (UV, 290-400 nm) radiation whereas UV and visible light played roughly equal roles in CO production from particles. Spatially, CO AQY of bulk particulate matter (i.e. the sum of organics and inorganics) augmented from the estuary and shelf to the basin while CO AQY of CDOM trended inversely. Water from the deep chlorophyll maximum layer revealed higher CO AQYs than did surface water for both particles and CDOM. CO AQY of bulk particulate matter exceeded that of CDOM on the shelf and in the basin but the sequence reversed in the estuary. Without consideration of the potential role of metal oxides (e.g. iron oxides) in particle photochemistry, mineral absorption-corrected CO AQY of particulate organic matter (POM) could, however, surpass its CDOM counterpart in all three sub-regions and displayed magnitudes in the estuary that overtook those in shelf and offshore waters. In terms of CO photoproduction, POM was thus more photoreactive than CDOM, irrespective of the organic matter's origins (i.e. terrigenous or marine). Riverine CDOM exhibited higher photoreactivity than marine CDOM and land-derived POM appeared more photoreactive than marine POM. AQY-based modeling indicates that CO photoproduction in the study area is underestimated by 12-32% if the particulate term is ignored.

4.1 INTRODUCTION

The absorption of solar ultra-violet (UV) and visible radiation by chromophoric dissolved organic matter (CDOM) initiates a myriad of chemical reactions that significantly impact marine biogeochemical cycles. CDOM photooxidation plays a critical role in controlling the transformation and fate of dissolved organic carbon (DOC) by mineralizing DOC to carbon dioxide (CO₂) and carbon monoxide (CO) (Miller and Zepp, 1995) and by altering the microbial degradability of DOC (Benner and Biddanda, 1998). CDOM photoprocesses also produce labile nitrogen (Bushaw et al., 1996) and oxidize dimethyl sulfide (Brimblecombe, 2003), thereby influencing marine nitrogen and sulfur cycling in the ocean. While colossal efforts and progress have been made in CDOM photochemistry during the last several decades (see reviews by Mopper and Kieber, 2002; Zafiriou, 2002; Zepp, 2003), much less attention has been paid to photochemical processes involving particulate organic matter (POM). The similarity in the absorption spectrum between POM and CDOM (Kirk, 1980), however, implies that POM may undergo photochemical transformations analogous to those of CDOM. Besides, POM photochemistry could be more efficient due to enrichment of organic substrates and/or photoreactive metals (e.g. Fe, Cu, Mn) in localized microenvironments on or within particles (Zafiriou, 2002), as suggested by studies on photodegradation of chlorophylls and unsaturated lipids of phytoplankton (e.g. SooHoo and Kiefer, 1982; Nelson, 1993; Rontani, 2001). Early surveys have demonstrated that irradiation of detritus of certain vascular plants produces CO (Tarr et al., 1995) and CO₂ (Anesio et al., 1999a) and releases DOC (Anesio et al., 1999b). More recently, a few groups have reported significant losses of particulate organic carbon (POC) and productions of DOC, CO₂, DON, and CDOM from controlled irradiation of resuspensions of river and coastal sediments (Kieber et al., 2006; Mayer et al., 2006; Riggsbee et al., 2008; Pisani

et al., 2011; Shank et al., 2011). Similar results have been found for phytoplankton detritus, with an added finding of ammonium production (Mayer et al., 2009; Estapa and Mayer, 2010).

Although laboratory irradiation experiments suggest potentially significant biogeochemical cycling rates resulting from POM photodegradation, extrapolating these results to real environments often entails potentially large uncertainties due partly to limited sample coverage and the inability of controlled incubations to adequately simulate the more complex optical, chemical, and hydrological conditions occurring in natural waters (Mayer et al., 2009; Estapa and Mayer, 2010). A widely adopted approach for estimating CDOM photochemical fluxes is coupled optical-photochemical modeling based on measured efficiency spectra of the photoprocess in question (e.g. Zafiriou et al., 2003; Xie et al., 2009a; Fichot and Miller, 2010), which in principle can also be applied to POM photochemistry. However, efficiency (also termed apparent quantum yield, AQY) spectra of POM photoreactions have rarely been determined. Estapa et al. (2012a) reported the AQY spectra of DOC photoproduction from coastal Louisiana suspended sediments, which, to the best of our knowledge, are the only published AQY spectra of a POM photoproduct. Apparently, AQY data covering more photoproducts and geographic areas are needed to elucidate whether POM photodegradation in marine ecosystems can effectively impact organic matter and elemental cycles and how important this process is in comparison with CDOM photochemistry.

Here we report the measurement of AQY spectra of CO photoproduction from suspended particulate matter (SPM) in the western Canadian Arctic and a direct comparison between the particle- and CDOM-based CO efficiencies. We model CO photoproduction using the AQY spectra obtained and discussed the implication of POM photooxidation for the CO budget. CO was targeted for a number of reasons. First, a preliminary study evaluating CO photoproduction

from particles suggested a significant POM-based term (up to 40% of the CDOM-based component) in both coastal and oligotrophic marine waters (Xie and Zafiriou, 2009). Second, thanks to its low background concentrations and high analytical sensitivity, CO can be relatively easily and precisely ($\pm 2\%$) quantified (Xie et al., 2002). Thus, even small signal changes due to POM photodegradation should be detectable. Third, the role of CO as a proxy species for other major but more-difficult-to-measure CDOM photoproducts (e.g. CO₂, biolabile carbon) (Miller and Zepp, 1995; Miller et al., 2002; White et al., 2010) could also hold for POM photochemistry. Finally, an assessment of the POM-based CO source helps better understand the physical and biogeochemical functions of this species, since CO is a useful tracer for modeling upper-ocean mixing dynamics (Kettle, 2005), an atmospherically active trace gas emitting from the ocean (Conrad et al., 1982; Stubbins et al., 2006a), and an energy source for bacteria oxidizing it (King and Weber, 2007; Moran and Miller, 2007).

4.2 METHODS

4.2.1 Study area

The study area encompassed the Mackenzie River estuary (MRE), Mackenzie Shelf (MS), and Canada Basin (CB) in the southeastern (SE) Beaufort Sea (Fig. 4-1). The area's most prominent hydrographic feature is the Mackenzie River, the only North American analogue to the immense Arctic rivers on the Siberian continent. The Mackenzie River possesses a watershed area of 1680 km² and delivers to the Arctic Ocean the largest POC ($1.8\text{--}2.1 \times 10^{12}$ g C yr⁻¹), sixth largest DOC (1.3 g C yr⁻¹), and fourth largest freshwater (249-333 km³ yr⁻¹) fluxes among all major Arctic rivers (Dittmar and Kattner, 2003). The river flows into the Beaufort Sea through

two major passages: the western and eastern channels. The river flow, subject to the Coriolis effect, bends to the right toward the Amundsen Gulf under calm conditions but can extend across the shelf into the interior ocean under strong easterly winds (Macdonald et al., 1999). CDOM in surface water is of primarily terrigenous origin on the shelf but has a strong autochthonous signature in the CB (Stedmon et al., 2011). Terrigenous particles dominate within the water column of the river plume, while particles of marine origin prevail outside the plume (Goñi et al., 2005; Forest et al., 2007; Magen et al., 2010). Water column primary production in the SE Beaufort Sea is limited by light availability prior to ice break in early spring but by nitrogen depletion subsequent to the spring phytoplankton bloom in water masses away from direct riverine and upwelling influences (Tremblay et al., 2008). The exhaustion of surface-water nitrogen typically leads to the formation of deep chlorophyll maxima (DCM) near the nutricline having Pacific summer water characteristics (Tremblay et al., 2008; Matsuoka et al., 2012).

The Western Canadian Arctic is one of the most sensitive regions on Earth to climate warming (Flato et al., 2000). Rising temperatures in this region over the last several decades have supposedly shortened sea ice-cover timespan and reduced sea ice extent (Stroeve et al., 2008), allowing more solar radiation to penetrate into the water column. Interests have since intensified concerning the fate and transformation of the terrigenous organic matter exported to the Arctic Ocean (Opsahl et al., 1999; Hansell et al., 2004; Benner et al., 2005). Photooxidation, a well-known CDOM sink in mid- and low-latitude oceans, has recently been proposed as a potentially significant cycling term of terrigenous CDOM in the western Canadian Arctic seas (e.g. Bélanger et al., 2006; Osburn et al., 2009; Xie et al., 2009a), since declining ice cover, combined with increasing solar UV radiation over the high north (Fioletov et al., 2004; see also

website: <http://onlinelibrary.wiley.com/doi/10.1002/wea.700/pdf>), enhances the photooxidation potential in the water column.

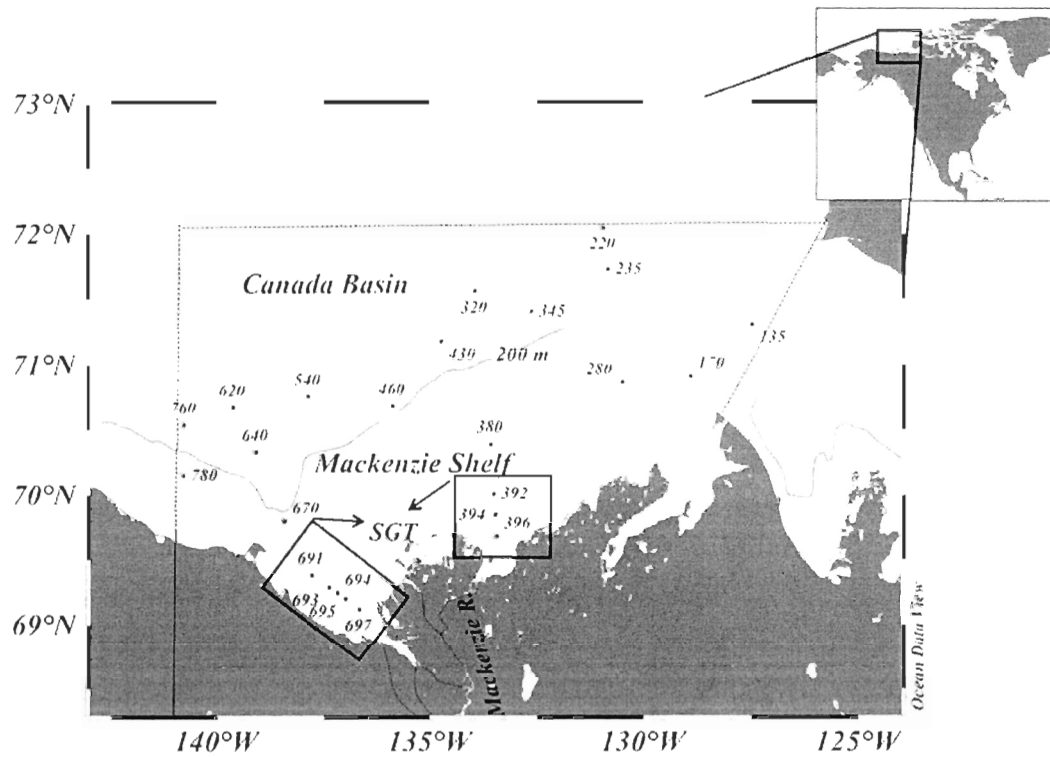


Fig. 4-1 Sampling map. See Table 4-1 for detailed sampling information for each station. Solid line is the 200-m isobath. Dashed line designates the area for which CO photoproduction rates were modeled. This map was constructed using the online software of Ocean Data View (R. Schlitzer, 2010, unpublished data, <http://odv.awi.de>).

4.2.2 Sampling

Sampling was conducted during the Mackenzie Light and Carbon (Malina) Program in August 2009 aboard the icebreaker *CCGS Amundsen*, covering the MS (<200 m deep) and CB (>200 m deep) (Fig. 4-1). A Zodiac boat released from the *CCGS Amundsen* visited two salinity gradient transects (SGTs) characterized by shallow waters, each in the east (SGT-E) and west (SGT-W) channel of the MRE. SGT samples were collected using a clean high-density polyethylene bucket, transferred into 20-L acid-washed, collapsible polyethylene carboys, and then brought back to the *CCGS Amundsen*. Shelf and open ocean samples were taken at the surface (~3 m deep) and DCM (mostly 60-75 m deep) using 12-L Niskin bottles mounted onto a standard conductivity-temperature-depth (CTD) rosette. Detailed sampling information is compiled in Table 4-1. Niskin and bucket samples were gravity-filtered through Whatman Polycap 75 AS filtration capsules sequentially containing 0.2- μm glass microfiber and nylon membrane filters. The filtrates were collected into half-gallon clear glass bottles (Qorpak) for irradiation experiments (see below) and 60-mL clear glass bottles (Qorpak) for CDOM absorbance measurements. The capsules were thoroughly flushed with Nanopure water and then sample water prior to filtration. Unfiltered samples were directly transferred into half-gallon glass bottles for irradiation experiments and 2-L plastic bottles (Nalgene) for chlorophyll *a* (Chl *a*) and particle absorbance determinations. All bottles were protected against light during sample transfer by wrapping them with aluminum foil or black plastic bags. They were all sequentially acid-cleaned with 10% HCl, profusely washed with Nanopure water, and rinsed with sample water before use. Irradiation experiments and particle optical density (i.e. absorbance) and Chl *a* concentration ([Chl *a*]) measurements were performed aboard the ship immediately after sample

collection. CDOM samples, stored under refrigeration and darkness, were transported to Rimouski at the end of the cruise and analyzed immediately thereafter.

Table 4-1 Sampling information along with salinity and water temperature.

| Sub-region ^a | Station ^b | Date of Aug. 2009 | Coordinate | | Total water depth (m) | Sampling depth (m) ^c | Salinity | Temp. (°C) |
|-------------------------|----------------------|----------------------|------------|-----------|--------------------------|------------------------------------|----------|------------|
| | | | Lat., °N | Long., °W | | | | |
| SGT-E | 392-S | 16 | 70.012 | 133.522 | 27 | 0 | 27.902 | 3.2 |
| | 394-S1 | 3 | 69.847 | 133.492 | 14 | 3.5 | 25.311 | 7.1 |
| | 394-S2 | 16 | 69.846 | 133.490 | 12 | 0 | 21.455 | 7.8 |
| | 396-S | 16 | 69.680 | 133.458 | 6.3 | 0 | 17.267 | 8.2 |
| SGT-W | 691-S | 13 | 69.387 | 137.792 | 44 | 0 | 23.612 | 5.2 |
| | 692-S | 13 | 69.342 | 137.594 | 39 | 0 | 22.184 | 5.9 |
| | 693-S | 13 | 69.296 | 137.398 | 32 | 0 | 15.003 | 8.8 |
| | 694-S | 13 | 69.251 | 137.202 | 9.0 | 0 | 9.426 | 9.3 |
| | 695-S | 13 | 69.204 | 137.006 | 5.0 | 0 | 7.042 | 9.3 |
| | 697-S | 13 | 69.125 | 136.681 | 1.7 | 0 | 0.154 | 10.3 |
| MS | 170-S | 7 | 70.917 | 128.919 | 35 | 3.0 | 29.009 | 3.8 |
| | 280-S | 4 | 70.869 | 130.507 | 38 | 3.3 | 27.558 | 4.8 |
| | 280-D | 4 | 70.869 | 130.507 | 38 | 24 | 31.931 | -0.0 |
| | 380-S | 8 | 70.393 | 133.595 | 62 | 6.0 | 27.611 | 4.1 |
| | 380-D | 8 | 70.393 | 133.595 | 62 | 48 | 31.924 | -1.1 |
| | 670-S | 10 | 69.797 | 138.428 | 173 | 3.0 | 23.500 | 4.0 |
| | 780-S | 12 | 70.154 | 140.801 | 50 | 3.0 | 22.845 | 3.6 |
| | 780-D | 12 | 70.154 | 140.801 | 50 | 30 | 31.685 | -1.1 |
| CB | 135-D | 20 | 71.312 | 127.489 | 230 | 60 | 31.505 | -1.3 |
| | 220-S | 5 | 70.050 | 130.945 | 225 | 3.0 | 27.137 | -0.8 |
| | 220-D | 5 | 70.050 | 130.945 | 225 | 70 | 31.534 | -1.4 |
| | 235-D | 23 | 71.728 | 130.842 | 611 | 75 | 31.965 | -1.1 |
| | 320-S | 9 | 71.562 | 133.958 | 1115 | 2.8 | 26.462 | -0.7 |
| | 320-D | 9 | 71.562 | 133.958 | 1115 | 70 | 31.546 | -1.2 |
| | 345-D | 15 | 71.410 | 132.638 | 580 | 60 | 31.276 | -1.0 |
| | 430-S | 18 | 71.184 | 134.748 | 1300 | 3.0 | 26.002 | -0.8 |
| | 430-D | 18 | 71.184 | 134.748 | 1300 | 65 | 31.779 | -1.1 |
| | 460-S | 19 | 70.682 | 135.891 | 362 | 3.0 | 24.731 | -0.1 |
| | 460-D | 19 | 70.682 | 135.891 | 362 | 56 | 31.261 | -1.0 |
| | 540-S | 17 | 70.756 | 137.871 | 1522 | 3.0 | 25.292 | -0.5 |
| | 540-D | 17 | 70.756 | 137.871 | 1522 | 70 | 31.808 | -1.1 |
| | 620-S | 11 | 70.674 | 139.634 | 1538 | 3.0 | 20.751 | 2.9 |
| | 640-S | 11 | 70.334 | 139.099 | 550 | 3.3 | 21.428 | 3.3 |
| | 760-S | 12 | 70.540 | 140.785 | 566 | 3.1 | 22.173 | 0.4 |
| 760-D | 12 | 70.540 | 140.785 | 566 | 70 | 31.475 | -1.1 | |

^a SGT-E (W) = salinity gradient transect-east (west) channel; MS = Mackenzie Shelf; CB = Canada Basin (see text and Fig. 1 for definitions).

^b S = surface; D = DCM (deep chlorophyll maximum).

^c 0 m indicates bucket samples; all other depths indicate Niskin bottle samples.

4.2.3 Irradiation

The irradiation procedure and setup were similar to those reported by Zhang et al. (2006). Unfiltered water samples were poisoned with KCN ($4.3 \mu\text{mol L}^{-1}$) to eliminate microbial CO uptake and filtered samples were amended with the same amount of KCN for uniformity of sample treatment. Samples were purged with CO-free air to minimize background CO concentrations, transferred into pre-combusted, quartz-windowed cylindrical cells having an inner diameter of 3.4 cm and a length of 11.4 cm. The quartz cells were closed without headspace and placed vertically in a temperature-controlled (4°C) incubator, and irradiated using a SUNSET XLS+ solar simulator equipped with a 1.5 kW xenon lamp. The sidewalls of the cells were wrapped with black electric tape to prevent lateral light interference between the cells. Radiation reaching the sample was essentially collimated and perpendicular to the irradiation surface (see Supporting Information in the study by Zhang et al. (2006)). Parallel dark controls served to evaluate any thermal effects on CO production. A series of successive Schott long-band cutoff filters, with model numbers of WG280, WG295, WG320, WG345, GG395, GG435, and GG495, were employed to evaluate the wavelength dependence of CO photoproduction. The numeric value in each model number signifies the nominal 50% transmittance cutoff wavelength in nanometers. Spectral photon fluxes impinging onto the window of each quartz cell were measured at 1 nm intervals using an OL-754 spectroradiometer fitted with a 2-inch OL IS-270 integrating sphere. The variability of the lamp output across the UV and visible regimes was within 4% throughout the entire cruise. Irradiation lasted from 10 min to 3.0 h (mostly <2.0 h) for samples under cutoff filters WG280, WG295, and WG320 and from 10 min to 12.0 h for samples under the remaining longer cutoff filters. Estuarine and coastal samples were subject to shorter durations of exposure compared to open-ocean samples. Because of short irradiations and lack of significant photobleaching (Annex 1, Fig. A1), CO production rate was assumed to be constant within the irradiation times. For the same reasons, the effect of self-shading (Hu et al., 2002) in the two UV-optically thick samples

(Sta. 697 and Sta. 695) was considered negligible. To minimize particle settling during irradiation, the cells were adequately shaken just before irradiation. Few particles were seen on the bottom of the cell after irradiation even for those stations with high particle loads (e.g. Sta. 697 and Sta. 695) due again to the very short irradiation durations (10 min for Sta. 697 and 15 min for Sta. 695).

4.2.4 Analyses

CO concentrations were measured using the headspace method reported by Xie et al. (2002). Briefly, post-irradiation samples were transferred to a 50-ml glass syringe, into which 5-ml CO-free air was introduced to obtain a 1:6 gas:water ratio. The syringe was vigorously shaken for 3 min and the equilibrated headspace gas was injected into a TA3000 Reduction Gas Analyzer (Trace Analytical) for CO quantification. The analyzer was standardized by frequent injections of a National Institute of Standards and Technology (NIST)-traceable gaseous CO standard of 1.23 parts per million by volume (Praxair). To be consistent with the samples' relative humidity (100%), the dry CO standard was drawn into a wetted 10-mL glass before injection. The amount of CO photochemically produced was calculated as the difference in CO concentration between the irradiated sample and the parallel dark control. The uncertainty of CO measurement is within $\pm 2\%$ (Xie et al., 2002).

For Chl *a* quantification, water samples (250-1000 mL) were filtered through pre-combusted 25-mm GF/F filters (Whatman) under low vacuum (<50 kPa). The particles-retained filters were placed in 10 ml of 90% acetone in scintillation vials for at least 18 h in the dark at 4°C. The supernatants were analyzed for fluorescence before and after being acidified with 100 μ L of 5% HCl, using a Turner Designs fluorometer (model 10-AU) according to the method of Parsons et al. (1984). [Chl *a*]s were calculated using the equation of Holm-Hansen et al. (1965).

Water samples (5.0-2735 ml) for particle optical density measurement were subjected to the same filtration procedure as that for Chl *a* determination. Particulate matter collected on the filters was analyzed for optical density using a Perkin Elmer Lambda 19 dual beam spectrometer fitted with a 150-mm integrating sphere (Labsphere) accommodating a homemade filter holder (Röttgers and Gehnke, 2012). The spectral optical density of the filter, $OD_{f,\lambda}$, where λ is wavelength in nanometers, was recorded from 800 to 300 nm at 1-nm increments and a scanning speed of 120 nm min⁻¹. $OD_{f,\lambda}$ was converted to the spectral particulate absorption coefficient, $a_{p,\lambda}$ (m⁻¹), using Eq. (4-1),

$$a_{p,\lambda} = 2.303 \times (A/V) \times (OD_{f,\lambda} - OD_{blank,\lambda}) \times (1/\beta_{\lambda}) \quad (4-1)$$

where $OD_{blank,\lambda}$ is the optical density of a blank filter, A the clearance area of particles on the filter (m²), V the volume of sample water filtered (m³), and β_{λ} the path length amplification factor. Here we fitted β_{λ} nonlinearly to $OD_{f,\lambda}$ (Röttgers and Gehnke, 2012):

$$\beta_{\lambda} = 2.9OD_{f,\lambda}^2 - 4.76OD_{f,\lambda} + 4.5 \quad (4-2)$$

Upon the completion of $a_{p,\lambda}$ determination, the filter was dipped in 10 ml methanol for ~18 h to bleach pigments and the absorption coefficient of non-algal particles, $a_{nap,\lambda}$ (m⁻¹), was determined in the same manner as that for $a_{p,\lambda}$. Data of $a_{p,\lambda}$ and $a_{nap,\lambda}$ between 250 and 299 nm were extrapolated from the exponential fits of $a_{p,\lambda}$ and $a_{nap,\lambda}$ to wavelength over the range from 300-420 nm. Subtracting $a_{nap,\lambda}$ from $a_{p,\lambda}$ gave the phytoplankton absorption coefficient, $a_{phy,\lambda}$ (m⁻¹). More details of particulate absorption measurement can be found in the study of Doxaran et al. (2012).

The spectral optical density of CDOM, $OD_{cdom,\lambda}$, was scanned from 800 to 200 nm at 1-nm intervals using a Perkin-Elmer Lambda 35 dual beam spectrophotometer fitted with a 5-cm quartz flow cell and referenced to high-performance-liquid-chromatography (HPLC) grade pure water (Ricca Chemical). Samples were allowed to warm up to room temperature before analysis. The flow cell was rinsed with methanol, pure water, and sample water between individual scans. A baseline correction was applied by subtracting the optical density averaged over 683–687 nm from all $OD_{cdom,\lambda}$ values (Babin et al., 2003). The

spectral CDOM absorption coefficient, $a_{cdom,\lambda}$ (m^{-1}), was calculated as 2.303 times $OD_{cdom,\lambda}$ divided by the light path length of the cell in meters (0.05 m). The lower detection limit of $a_{cdom,\lambda}$ determination, defined as three times the standard deviation of five replicate analyses of pure water, was $0.02 \pm 0.01 m^{-1}$ over 250–700 nm.

4.2.5 Retrieval of CO AQY

The spectral CO AQY, Φ_λ , is defined as the number of moles of CO produced per mole of photons absorbed by a given set of light-absorbing materials at wavelength λ . Here the light-absorbing materials refer to CDOM, particles, and CDOM plus particles, corresponding to Φ_λ for CDOM ($\Phi_{cdom,\lambda}$), particles ($\Phi_{p,\lambda}$), and total dissolved and particulate matter ($\Phi_{t,\lambda}$), respectively. According to Hu et al. (2002), the number of absorbed photons at wavelength λ , $Q_{a,\lambda}$ (mol photons $s^{-1} nm^{-1}$), was calculated using Eq. (4-3) :

$$Q_{a,\lambda} = Q_\lambda \times S \times (a_\lambda / a_{t,\lambda}) \times [1 - \exp(-a_{t,\lambda} \times L)] \quad (4-3)$$

Q_λ (mol photons $m^{-2} s^{-1} nm^{-1}$) denotes the photon flux just below the frontal quartz window; a_λ (m^{-1}) stands for $a_{cdom,\lambda}$ for filtered samples or $a_{cdom,\lambda}$ plus $a_{p,\lambda}$ for unfiltered samples; $a_{t,\lambda}$ (m^{-1}) is the total absorption coefficient, i.e. $a_{cdom,\lambda}$ plus the absorption coefficient of pure water, $a_{w,\lambda}$ (m^{-1}) (Buiteveld et al., 1994; Pope and Fry, 1997), for filtered samples or the sum of $a_{cdom,\lambda}$, $a_{p,\lambda}$, and $a_{w,\lambda}$ for unfiltered seawater; S (m^2) and L (m) are, respectively, the cross-section and path length of the irradiation cells. In unfiltered samples, particle scattering could deflect photons out of the irradiation cell and change the effective path length of light transmission (Miller and Zepp, 1979; Estapa et al., 2012a). The contribution of particle scattering to light attenuation in unfiltered samples was estimated from Monte Carlo simulations using the SimulO software (Leymarie et al., 2010; see Annex 1). The results indicated that the effect of particle scattering across the 280–600 nm wavelength range was $\leq 0.3\%$ in the CB and $\leq 1.9\%$ on the MS, including two outermost stations along the SGTs (Sta. 392 and 691). Samples from the remaining SGT stations had

larger a_t values (1.00–10.45 m^{-1} at 412 nm) and higher scattering to absorption ratios (2.8–9.8 at 412 nm). The effect of particle scattering for these stations ranged from 2.0% to 27.8%, depending on sampling location and wavelength (Annex 1, Fig. A4). Positive values indicate an overestimate of light absorption by Eq. (4-3) due to photons being scattered out of the cell. Scattering effects of $\geq 2\%$ were accounted for in the calculation of absorbed photons.

$\Phi_{cdom,\lambda}$ and $\Phi_{t,\lambda}$ were obtained with an iterative curve-fit protocol developed by Johannessen and Miller (2001) and modified by Zhang et al. (2006). Briefly, this method assigned a quasi-exponential form with unknown parameters to express the change of Φ_λ ($\Phi_{cdom,\lambda}$ or $\Phi_{t,\lambda}$) as a function of wavelength (Zhang et al., 2006; Xie et al., 2009a):

$$\Phi_\lambda = m_1 \times \exp [m_2 / (\lambda + m_3)] \quad (4-4)$$

where m_1 , m_2 , and m_3 are fitting parameters. The amount of CO produced in an irradiation cell over the exposure time could then be predicted as the product of the assumed Φ_λ function and the number of absorbed photons integrated over 250–600 nm. The optimum values of the unknown parameters in Eq. (4) were computed by varying these parameters from initial estimates until the minimum difference between the measured and predicted production is achieved. CO production rates calculated from the retrieved Φ_λ were in good agreement with the measured rates, with R^2 ranging from 0.969 to 0.998 (mean: 0.991) for filtered samples and from 0.982 to 0.998 (mean: 0.992) for unfiltered samples. Ziolkowski and Miller (2007) validated the multispectral curve fitting approach as adopted here against the conventional monochromatic method for CO photoproduction. Note that our experiment could not resolve fine Φ_λ features for unfiltered samples in the long visible, where Chl *a* presents an absorption peak at ca. 675 nm, since our longest cutoff wavelength was 495 nm (see Sect. 4.2.3). Any potential CO production at >600 nm was ascribed to the visible wavelengths < 600 nm.

$\Phi_{p,\lambda}$ can be derived from $\Phi_{cdom,\lambda}$ and $\Phi_{t,\lambda}$ per the following mathematical manipulations. The spectral CO photoproduction rate in an unfiltered sample, $P_{t,\lambda}$ (mol CO s⁻¹ nm⁻¹), can be expressed as

$$P_{t,\lambda} = \Phi_{t,\lambda} \times Q_{t,a,\lambda} \quad (4-5)$$

$P_{t,\lambda}$ is the sum of CO photoproduction from CDOM, $P_{cdom,\lambda}$ (mol CO s⁻¹ nm⁻¹), and that from particles, $P_{p,\lambda}$ (mol CO s⁻¹ nm⁻¹), i.e.,

$$P_{t,\lambda} = P_{cdom,\lambda} + P_{p,\lambda} \quad (4-6)$$

$P_{cdom,\lambda}$ and $P_{p,\lambda}$ are given by

$$P_{cdom,\lambda} = \Phi_{cdom,\lambda} \times Q_{cdom,a,\lambda} \quad (4-7)$$

and

$$P_{p,\lambda} = \Phi_{p,\lambda} \times Q_{p,a,\lambda} \quad (4-8)$$

Substituting Eqs. (4-5), (4-7) and (4-8) into Eq. (4-6) and rearranging it give

$$\Phi_{p,\lambda} = \Phi_{t,\lambda} + (\Phi_{t,\lambda} - \Phi_{cdom,\lambda}) \times (a_{cdom,\lambda} / a_{p,\lambda}) \quad (4-9)$$

$Q_{t,a,\lambda}$, $Q_{cdom,a,\lambda}$ and $Q_{p,a,\lambda}$ in Eqs. (4-5), (4-7) and (4-8) denote the number of photons absorbed by CDOM plus particles, CDOM, and particles, respectively, in an unfiltered sample as defined by Eq. (4-3).

To facilitate comparison of various Φ_{λ} spectra, a solar irradiance spectrum-weighted mean apparent quantum yield, $\bar{\Phi}$, was computed for each CO AQY spectrum following the procedure of Xie et al. (2009a):

$$\bar{\Phi} = (\int_{290}^{600} Q_{0,\lambda} \times \Phi_{\lambda} \times d\lambda) / (\int_{290}^{600} Q_{0,\lambda} \times d\lambda) \quad (4-10)$$

$\bar{\Phi}$ denotes $\bar{\Phi}_{cdom}$ for CDOM, $\bar{\Phi}_p$ for particles, and $\bar{\Phi}_t$ for CDOM plus particles. $Q_{0,\lambda}$ (mol photons m⁻² h⁻¹ nm⁻¹) is the surface spectral solar photon fluxes at 70°N, 133°W at 14:00 local time on 01 July, simulated using the SMARTS model (Simple Model of the Atmospheric Radiative Transfer of Sunshine; Gueymard, 2001) under mid-summer Arctic atmospheric and cloudless conditions with an ozone column burden of 330 Dobson Units.

This normalization reduced the AQY spectrum to a single value of CO production in the entire water column, in which all solar radiation over 290-600 nm was absorbed by a specific group of light-absorbing material, i.e. CDOM, particles, or the sum of the two (Bélanger et al., 2006).

4.3 RESULTS AND DISCUSSION

4.3.1 General physical, biological, and chemical settings

Salinity, temperature, [Chl *a*], and absorption coefficients of various constituents are shown in Table 4-2. Surface salinity along the SGT-W monotonically increased seaward from 0.15 at Sta. 697 to 23.61 at Sta. 691. The SGT-E covered a much narrower salinity range from 17.27 at Sta. 396 to 27.90 at Sta. 392. The lower mean surface salinity in the CB than that on the MS suggests a stronger influence of sea ice melting in the CB. Surface temperature along the SGTs displayed a trend inverse to salinity, decreasing seaward from 10.3°C to 5.2°C along the SGT-W and from 8.2°C to 3.2°C across the SGT-E; temperature further decreased from the MS to CB. Mean salinity and temperature of the DCM samples were 31.64 and -1.0°C, respectively, typical of Pacific summer water origin (McLaughlin, 1996; Matsouka et al., 2012).

[Chl *a*] generally decreased from nearshore to offshore at both the surface and DCM. The highest value (7.6 $\mu\text{g L}^{-1}$) in the surface occurred at Sta. 170 located within the upwelling zone off Cape Bathurst (Williams and Carmack, 2008). Mean [Chl *a*]s at the DCM were 3.8 $\mu\text{g L}^{-1}$ on the MS and 0.42 $\mu\text{g L}^{-1}$ in the CB, being 2.4 and 5.2 times their surface values.

The absorption coefficients of CDOM and particles at the surface, as exemplified by $a_{cdom,412}$ and $a_{p,412}$, diminished rapidly from the estuary to the MS and CB, indicating a strong influence of the riverine input of dissolved and particulate materials. The highest $a_{cdom,412}$

and $a_{p,412}$ both occurred at Sta. 697 ($a_{cdom,412}$: 2.04 m^{-1} ; $a_{p,412}$: 8.40 m^{-1}) and the lowest in the ice melt-influenced water at Sta. 430 ($a_{cdom,412}$: 0.07 m^{-1} ; $a_{p,412}$: 0.004 m^{-1}). Relatively high $a_{cdom,412}$ (0.20 m^{-1}) and $a_{p,412}$ (0.26 m^{-1}) values were observed in the upwelling zone (Sta. 170). At the DCM, $a_{cdom,412}$ was fairly constant throughout the MS and CB; $a_{p,412}$ was more variable with the mean value for the MS being 9 times that for the CB. The $a_{phy,412}:a_{p,412}$ ratio increased from nearshore to offshore, with the lowest occurring at Sta. 697 (0.06) and the highest at Sta. 430 (0.66). The mean $a_{phy,412}:a_{p,412}$ at the DCM was ~ 2 times that at the surface in both the MS and CB.

Table 4-2 Means and ranges (in the parentheses) of salinity, temperature, [Chl *a*], $a_{cdom,412}$, $a_{p,412}$, and $a_{phy,412}$: $a_{p,412}$. Keys in the sub-region column are the same as those in Table 4-1.

| Sub-region | Salinity | Temp. (°C) | [Chl <i>a</i>] ($\mu\text{g L}^{-1}$) | $a_{cdom,412}$ (m^{-1}) | $a_{p,412}$ (m^{-1}) | $a_{phy,412}$: $a_{p,412}$ |
|------------|------------------------|------------------------|--|------------------------------------|---------------------------------|-----------------------------|
| SGT-E | 22.98 (17.27–27.90) | 6.4 (3.2–8.2) | 1.4 (0.65–2.5) | 0.69 (0.12–1.11) | 0.22 (0.038–0.36) | 0.13 (0.07–0.18) |
| SGT-W | 12.90 (0.15–23.61) | 8.6 (5.2–10.3) | 1.9 (0.17–3.2) | 1.30 (0.39–2.04) | 2.65 (0.053–8.40) | 0.16 (0.06–0.28) |
| MS-surface | 26.10 (22.85–29.10) | 4.1 (3.6–4.8) | 2.0 (0.08–7.6) | 0.22 (0.13–0.33) | 0.076 (0.017–0.26) | 0.25 (0.13–0.41) |
| MS-DCM | 31.85 (31.68–31.93) | -0.7 (-0.006– -1.1) | 3.8 (1.3–8.0) | 0.17 (0.14–0.22) | 0.14 (0.085–0.25) | 0.46 (0.22–0.66) |
| CB-surface | 24.25 (20.75–27.14) | 0.5 (-0.8–3.3) | 0.08 (0.05–0.13) | 0.13 (0.07–0.24) | 0.012 (0.004–0.026) | 0.40 (0.21–0.66) |
| CB-DCM | 31.57 (31.26–31.96) | -1.2 (-1.0– -1.4) | 0.42 (0.12–0.71) | 0.14 (0.10–0.23) | 0.016 (0.009–0.025) | 0.81 (0.56–0.88) |

4.3.2 CO AQY spectra

Fitted parameters for Eq. (4-3) are shown in Table 4-3 and typical $\Phi_{cdom,\lambda}$ and $\Phi_{p,\lambda}$ spectra are displayed in Fig. 4-2. $\Phi_{p,\lambda}$ at the innermost Sta. 697 on the SGT-W was lower than $\Phi_{cdom,\lambda}$, the difference being pronounced in the UV-A wavelengths. At Sta. 280 on the MS and Sta. 430 in the CB, surface water $\Phi_{p,\lambda}$ was higher than $\Phi_{cdom,\lambda}$ at $\lambda > 330$ nm, with the difference increasing with wavelength. Similarly, $\Phi_{p,\lambda}$ at the DCM both on the MS (Sta. 280) and in the CB (Sta. 345) exceeded $\Phi_{cdom,\lambda}$ by large extents over most spectral regimes (Fig. 4-2). Unlike the rather smooth spectral shape of $\Phi_{p,\lambda}$ for the estuarine sample (Sta. 697), the spectral patterns of $\Phi_{p,\lambda}$ for the more marine samples, particularly those from the DCM, were characterized by conspicuous shoulders over the 500–600 nm band. This attribute might be linked to specific compounds with high photoreactivity in the DCM samples. However, as the spectral pattern of $\Phi_{p,\lambda}$ determined in the present study was primarily defined by the assumed spectral shapes of $\Phi_{cdom,\lambda}$ and $\Phi_{t,\lambda}$ (Eqs. (4-4)), more studies using monochromatic irradiations are needed to confirm or further resolve these fine spectral features.

Fig. 4-3 compares $\bar{\Phi}$ among the three sub-regions and between the surface and DCM. Mean surface water $\bar{\Phi}_{cdom}$ dropped by ~40% from the estuary to the MS but only slightly decreased from the MS to the CB (6%). On the contrary, mean surface water $\bar{\Phi}_p$ in the estuary (0.93×10^{-6}) was comparable to that on the shelf (0.98×10^{-6}) but it increased to 1.46×10^{-6} in the CB. At the DCM, the mean $\bar{\Phi}_{cdom}$ on the MS (1.14×10^{-6}) was marginally higher than the mean $\bar{\Phi}_{cdom}$ in the CB (1.04×10^{-6}) while an opposing trend was observed for the mean $\bar{\Phi}_p$ (MS: 1.51×10^{-6} vs. CB: 2.21×10^{-6}). $\bar{\Phi}_{cdom}$ and $\bar{\Phi}_p$ at the DCM were higher than their surface counterparts. The ratio of $\bar{\Phi}_p$ to $\bar{\Phi}_{cdom}$ was <1 in the estuary (0.6) but >1 in shelf and offshore waters at both the surface and DCM (range: 1.3–2.1). Surface and DCM samples exhibited comparable $\bar{\Phi}_p:\bar{\Phi}_{cdom}$ with the highest values seen in the CB.

Table 4-3 Fitted parameters for equation $\Phi_\lambda = m_1 \times \exp(m_2/(\lambda + m_3))$ (Eq. 4-4 in the text) for filtered (CDOM) and unfiltered (CDOM plus particles) samples, along with Φ_{330} and $\bar{\Phi}$ for CDOM, CDOM plus particles, and particles. n.d. = not determined. The uncertainty for Φ_{330} and $\bar{\Phi}$ was estimated to be $\pm 4.5\%$ based on the combined variability of CO and light intensity measurements.

| Station | Filtered sample (CDOM) | | | Unfiltered sample (CDOM plus particles) | | | | | Particles | | | |
|---------|--------------------------------|--------|-------|---|--------------------------------------|--------------------------------|--------|--------|--------------------------------------|--------------------------------------|--------------------------------------|--------------------------------------|
| | m_1 ($\times 10^{-11}$) | m_2 | m_3 | Φ_{330} ($\times 10^{-6}$) | $\bar{\Phi}$ ($\times 10^{-6}$) | m^1 ($\times 10^{-11}$) | m_2 | m_3 | Φ_{330} ($\times 10^{-6}$) | $\bar{\Phi}$ ($\times 10^{-6}$) | Φ_{330} ($\times 10^{-6}$) | $\bar{\Phi}$ ($\times 10^{-6}$) |
| 392-S | 0.82 | 5048.7 | 21.3 | 14.3 | 0.91 | 78.7 | 2768.5 | -47.0 | 14.0 | 1.18 | 12.9 | 1.85 |
| 394-S1 | 3.29 | 4371.8 | 7.48 | 13.9 | 0.96 | 7.11 | 3950.0 | -3.17 | 12.6 | 0.92 | 7.67 | 0.76 |
| 394-S2 | 4.02 | 4573.6 | 28.1 | 14.2 | 1.05 | 8.29 | 3806.9 | -13.0 | 13.6 | 0.98 | 7.05 | 0.46 |
| 396-S | 6.74 | 4282.3 | 13.1 | 17.8 | 1.31 | 11.5 | 3761.8 | -13.0 | 16.4 | 1.19 | 4.01 | 0.51 |
| 691-S | 2.25 | 4410.4 | 0.67 | 14.0 | 0.91 | 2.18 | 4641.0 | 19.6 | 12.7 | 0.88 | 8.69 | 0.81 |
| 692-S | 3.64 | 4362.1 | 6.90 | 15.3 | 1.05 | n.d. | n.d. | n.d. | n.d. | n.d. | n.d. | n.d. |
| 693-S | 6.77 | 4390.5 | 23.2 | 17.0 | 1.29 | 12.8 | 3803.7 | -6.33 | 16.3 | 1.23 | 13.9 | 1.08 |
| 694-S | 22.2 | 4346.7 | 51.1 | 20.4 | 1.89 | 17.2 | 3872.4 | 1.44 | 20.4 | 1.58 | 20.1 | 1.20 |
| 695-S | 12.9 | 4814.8 | 70.3 | 21.7 | 1.97 | 15.8 | 3896.2 | 5.52 | 17.5 | 1.38 | 11.1 | 0.90 |
| 697-S | 13.7 | 4861.1 | 72.5 | 24.1 | 2.19 | 233 | 1900 | -123.4 | 15.0 | 1.14 | 10.0 | 0.81 |
| 170-S | 1.34 | 5300.2 | 50.3 | 15.1 | 1.07 | 5.17 | 3604.5 | -41.5 | 13.8 | 0.86 | 11.2 | 0.65 |
| 280-S | 0.72 | 4754.1 | 3.93 | 10.9 | 0.67 | 6.98 | 3946.8 | -0.002 | 10.9 | 0.82 | 10.7 | 1.21 |
| 280-D | 0.91 | 6378.6 | 112.5 | 16.5 | 1.30 | n.d. | n.d. | n.d. | n.d. | n.d. | n.d. | n.d. |
| 380-S | 0.47 | 5967.6 | 81.1 | 9.46 | 0.69 | 64.5 | 2277.4 | -83.3 | 6.59 | 0.53 | 3.73 | 0.37 |
| 380-D | 1.00 | 6109.1 | 93.4 | 18.5 | 1.39 | 1.35 | 5425.3 | 63.2 | 13.2 | 0.98 | 7.38 | 0.63 |
| 670-S | 1.57 | 4395.3 | -5.80 | 12.1 | 0.76 | 1.64 | 4645.0 | 13.1 | 12.4 | 0.82 | 14.3 | 1.33 |
| 780-S | 1.57 | 4782.9 | 19.8 | 13.7 | 0.91 | 1.66 | 5078.7 | 42.7 | 13.7 | 0.98 | 14.1 | 1.34 |
| 780-D | 0.86 | 4988.9 | 19.0 | 13.8 | 0.87 | 1.57 | 5073.5 | 39.7 | 14.4 | 1.01 | 15.2 | 1.23 |
| 135-D | 0.52 | 6039.2 | 82.9 | 11.7 | 0.84 | 0.59 | 6496.5 | 117.5 | 11.8 | 0.94 | 12.3 | 1.47 |

| | | | | | | | | | | | | |
|-------|------|--------|-------|------|------|------|--------|-------|------|------|------|------|
| 220-S | 0.35 | 4566.3 | -19.1 | 8.33 | 0.46 | 0.30 | 4720.0 | -7.50 | 6.91 | 0.40 | 5.49 | 0.33 |
| 220-D | 0.57 | 4751.3 | 5.79 | 8.02 | 0.50 | 0.64 | 5004.4 | 24.8 | 8.56 | 0.56 | 12.3 | 1.28 |
| 235-D | 0.63 | 6445.5 | 110.2 | 14.3 | 1.10 | 0.84 | 7057.4 | 155.8 | 17.1 | 1.48 | 25.3 | 3.38 |
| 320-S | 0.56 | 4535.7 | -11.9 | 8.70 | 0.51 | 0.35 | 4914.5 | 0.82 | 9.75 | 0.56 | 74.2 | 3.57 |
| 320-D | 0.58 | 6210.1 | 89.2 | 15.8 | 1.14 | 0.80 | 5710.3 | 63.5 | 16.0 | 1.11 | 16.2 | 1.08 |
| 345-D | 0.66 | 5328.9 | 39.4 | 12.1 | 0.80 | 34.8 | 2991.0 | -45.9 | 13.0 | 1.00 | 40.1 | 3.34 |
| 430-S | 0.33 | 5719.3 | 48.2 | 12.0 | 0.76 | 0.34 | 6224.4 | 83.5 | 11.7 | 0.82 | 12.4 | 1.34 |
| 430-D | 0.82 | 7489.0 | 182.1 | 18.3 | 1.67 | 0.97 | 6297.7 | 103.0 | 20.2 | 1.54 | 11.4 | 1.41 |
| 460-S | 1.00 | 5892.0 | 83.4 | 16.0 | 1.19 | 0.45 | 5520.2 | 39.2 | 14.0 | 0.89 | n.d. | n.d |
| 460-D | 0.81 | 5582.4 | 54.1 | 16.6 | 1.12 | 0.97 | 6071.7 | 91.2 | 17.6 | 1.32 | 19.2 | 1.91 |
| 540-S | 0.35 | 5761.6 | 52.5 | 12.3 | 0.79 | 39.4 | 2880.1 | -50.2 | 11.6 | 0.91 | 8.29 | 1.90 |
| 540-D | 0.88 | 6218.1 | 98.2 | 17.9 | 1.35 | 4.45 | 4713.2 | 34.7 | 18.2 | 1.36 | 31.4 | 1.85 |
| 620-S | 1.41 | 4816.2 | 19.5 | 13.6 | 0.90 | 1.45 | 4872.2 | 25.0 | 13.2 | 0.89 | 9.80 | 0.79 |
| 640-S | 1.51 | 4770.5 | 18.3 | 13.4 | 0.89 | 1.53 | 4756.6 | 18.6 | 12.9 | 0.86 | 12.4 | 0.83 |
| 760-S | 0.86 | 4396.6 | -16.8 | 10.7 | 0.63 | 0.93 | 4442.3 | -12.5 | 10.5 | 0.61 | n.d. | n.d |
| 760-D | 0.65 | 6240.1 | 91.8 | 17.2 | 1.25 | 0.80 | 6505.6 | 112.8 | 19.2 | 1.48 | 27.0 | 2.65 |

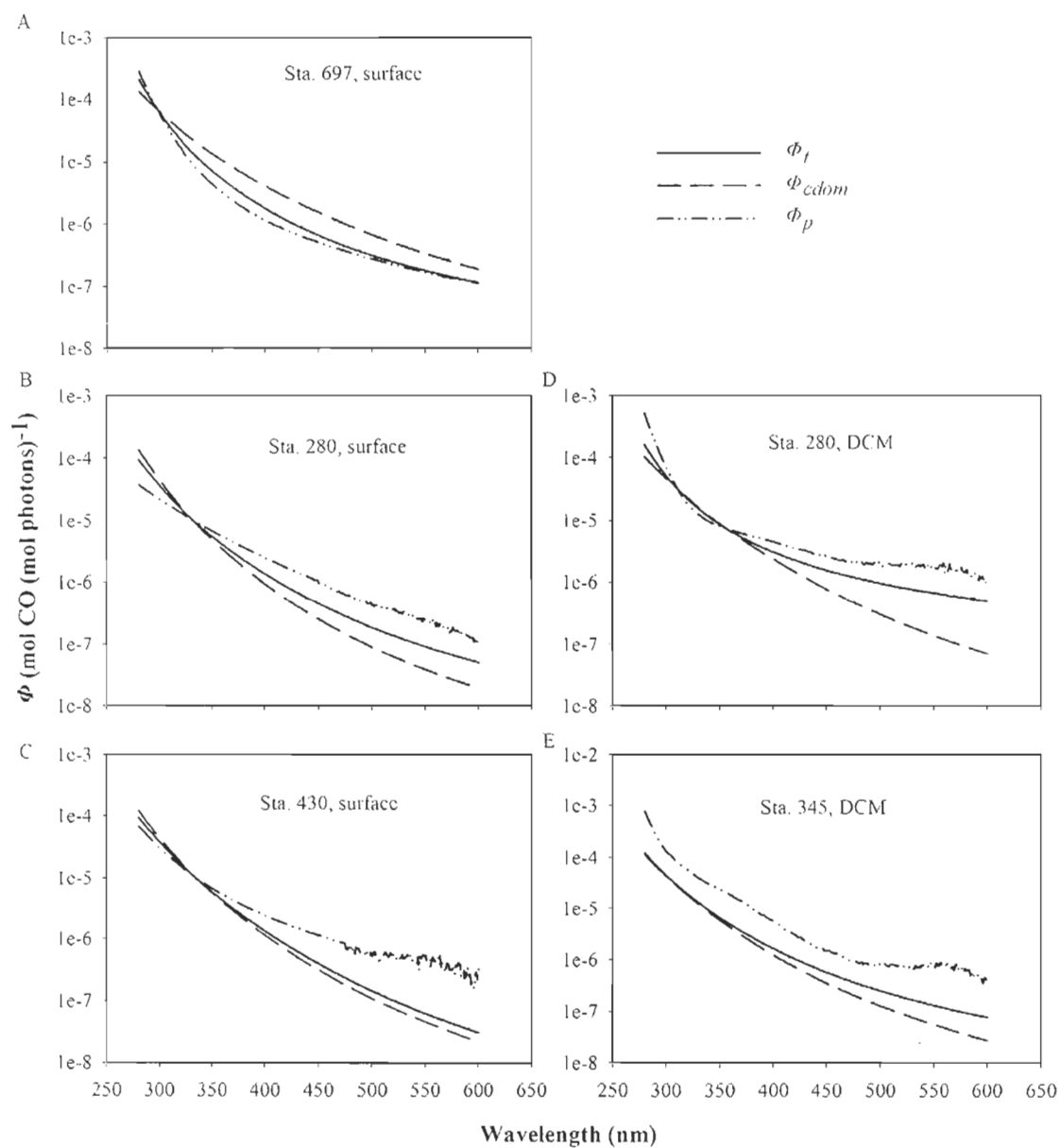


Fig. 4-2 Typical $\Phi_{cdom,\lambda}$, $\Phi_{p,\lambda}$, and $\Phi_{f,\lambda}$ spectra from the Mackenzie River estuary (Sta. 697), Mackenzie Shelf (Sta. 280), and Canada Basin (Sta. 345 and 430).

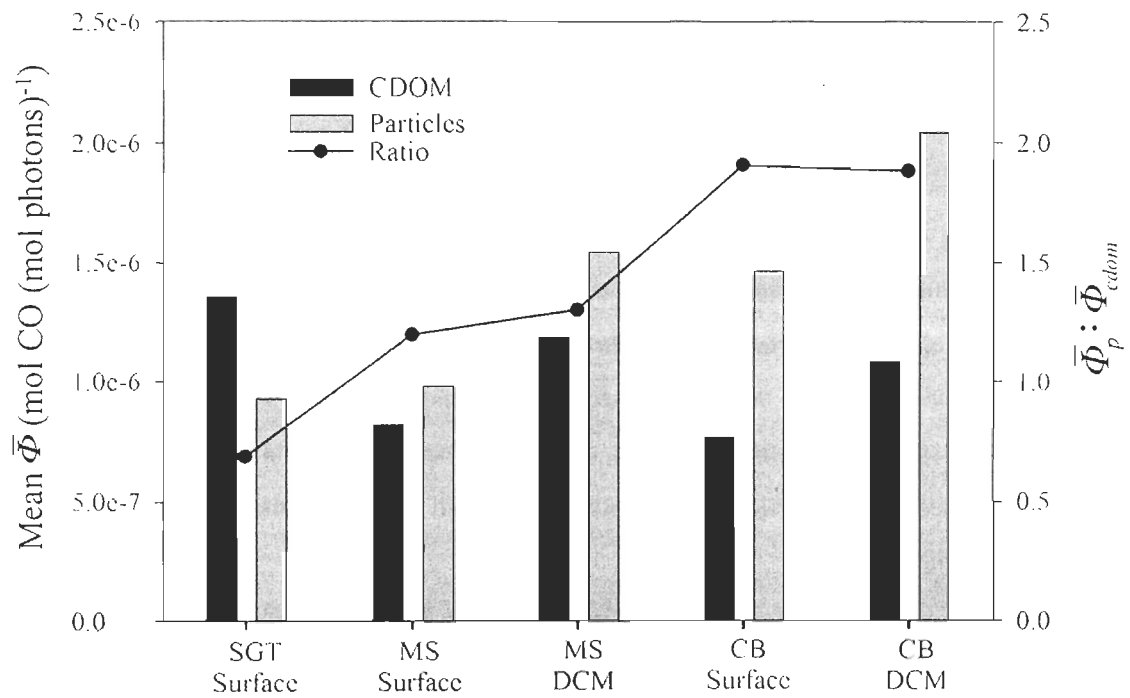


Fig. 4-3 Comparison of mean $\bar{\Phi}$ of particles and CDOM and the ratio of the two among the three sub-regions.

$\bar{\Phi}_{cdom}$ along the SGTs was positively and linearly correlated with a_{cdom} (Fig. 4-4A), consistent with previous findings (Xie et al., 2009a; Stubbins et al., 2011). $\bar{\Phi}_{cdom}$ data from the MS and CB corresponded to a narrow a_{cdom} range (0.07–0.33 m^{-1} at 412 nm) and were scattered with respect to a_{cdom} . The mean of the surface water $\bar{\Phi}_{cdom}$ data essentially followed the SGTs' regression line while at the DCM mean $\bar{\Phi}_{cdom}$ was well (61%) above it. Unlike $\bar{\Phi}_{cdom}$, $\bar{\Phi}_p$ showed no significant relationships with particulate optical properties such as a_p (Fig. 4-4B), a_{phy} , and $a_{phy}:a_p$ (data not shown), neither did it correlate to the mass ratio of particulate organic carbon (POC) to SPM ($R^2 = 0.056$, $p = 0.23$, $n = 26$) as obtained by Doxaran et al. (2012) from the same cruise. Hence, particle-based CO photoproduction appeared to be controlled by more complex mechanisms implicating various factors such as the origin and diagenetic state of POM, the abundance and speciation of photoreactive metals contained in the particles (see Sect. 4.3.3), and environmental variables (e.g. pH, salinity and temperature).

It should be pointed out that KCN used for poisoning samples (see Sect. 4.2.3), though transparent to UV and visible light, suppresses CO photoproduction (Xie and Zafiriou, 2009). Previous tests indicated that addition of 43.0 $\mu\text{mol L}^{-1}$ KCN to filtered seawater samples from a wide range of latitudes decreased CO photoproduction by 25%–36% (H. Xie and O. C. Zafiriou unpublished data). In the present study, we reduced the KCN dose to 4.3 $\mu\text{mol L}^{-1}$, which greatly mitigated the KCN effect on CO photoproduction while was still sufficient to eradicate microbial CO uptake over the irradiation periods adopted. The KCN inhibition of CO production in filtered samples was on average 6.5% (range: 3.5%–16.0%, $n = 20$) in the UV domain and negligible in the visible domain. A limited number of tests on unfiltered samples, in which microbial CO consumption was negligible without poisoning, showed a similar suppression of CO production by KCN. No correction was made for the KCN effect since it was generally small and not all samples were evaluated.

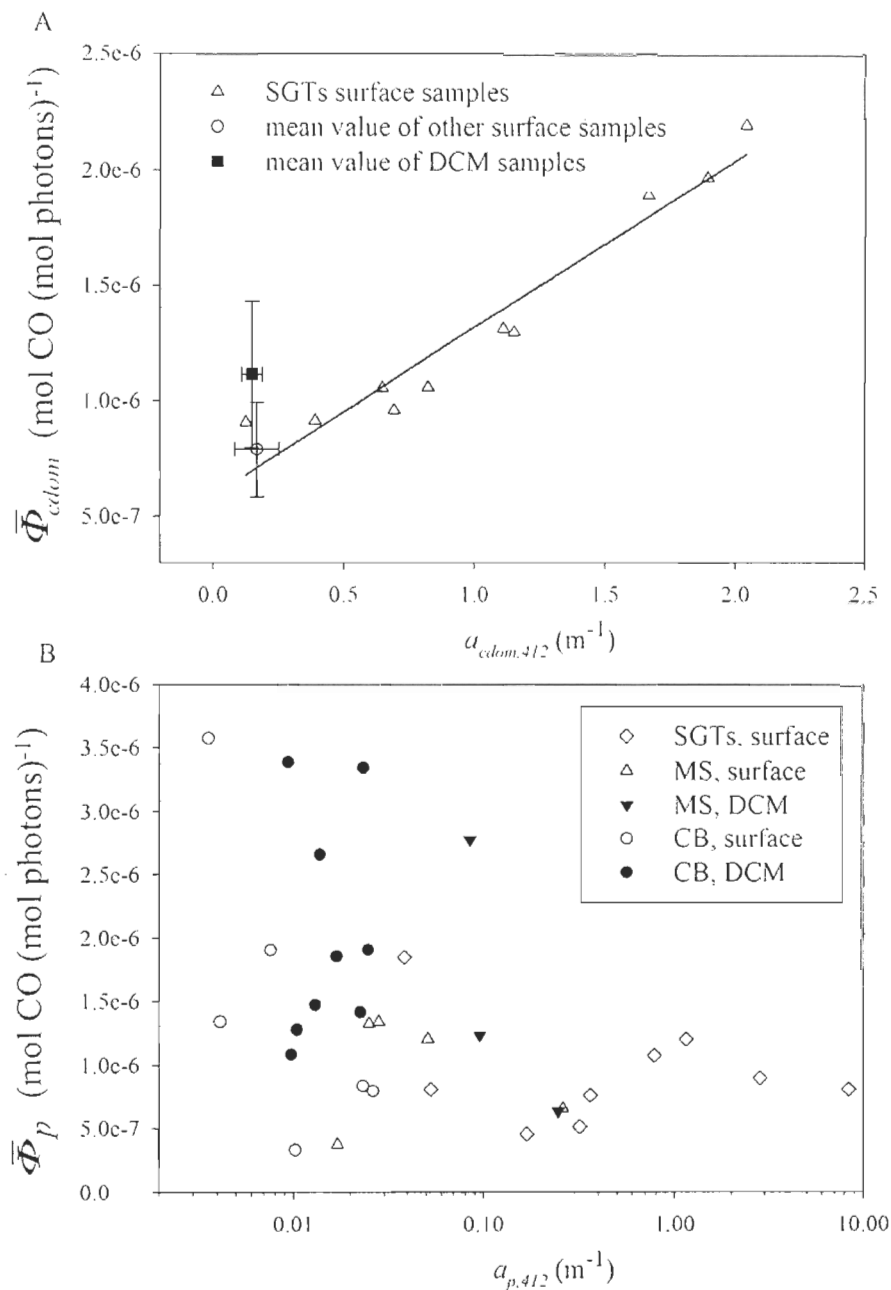


Fig. 4-4 Relationships between $\bar{\Phi}_{cdom}$ and $a_{cdom,412}$ (A) and between $\bar{\Phi}_p$ and $a_{p,412}$ (B). Error bars in panel A are one standard deviation. Solid line in panel A is the best fit to the SGT data and the regression equation is $y = 7.27 \times 10^{-7}x + 5.87 \times 10^{-7}$ ($R^2 = 0.93$, $p < 0.0001$). Note that the x -axis in panel B is on the logarithmic scale.

4.3.3 Photoreactivity of CDOM and particles

The decrease in surface water $\bar{\Phi}_{cdom}$ from the estuary to open ocean (Fig. 4-3) suggests that CDOM photoreactivity with respect to CO photoproduction declined seaward. Such a decay of CDOM photoreactivity could be attributed to a progressively increasing proportion of marine CDOM with distance from land and/or structural modifications associated with photobleaching when CDOM was transported across the MS. Marine CDOM is generally less photoreactive than its terrigenous counterpart (Zepp, 2003) and photobleaching reduces CDOM's CO photoproduction efficiency (Zhang et al., 2006). The photoreactivity of particles in surface water, in terms of $\bar{\Phi}_p$, augmented from the estuary to offshore, displaying an inverse tendency to the CDOM photoreactivity (Figs. 4-3). Hence, marine particles appeared more photoreactive than riverine particulates. Notably, CDOM and particles both exhibited higher photoreactivities at the DCM than at the surface (Fig. 4-3). The higher CDOM photoreactivity at the DCM might be linked to the fact that the DCM layer carried CDOM characteristic of the Pacific summer water (Matsuoka et al., 2011, 2012) and that underwater CDOM was shielded from photobleaching. Concerning the particulate phase, fresher cells and/or higher organic contents within the DCM could make the particles there be more photoreactive. The particulate photoreactivity was far below the CDOM photoreactivity in the estuary but the sequence reversed on the MS and in the CB (Fig. 4-3). This observation of higher particulate photoreactivity for the Arctic shelf and offshore waters is consistent with the results of a previous study using mid-latitude coastal and open waters (Xie and Zafiriou, 2009).

Note that the particulate photoreactivity discussed above refers to the bulk particulate matter without differentiating the organics from inorganics. Doxaran et al. (2012) reported that the mean POC:SPM obtained from the same cruise increased from 2% in the inner part of the MRE to 11% in the transitional river plume to 25% in the open ocean. Based on a POM:POC of 2.6 (Copin-Montégut, 1980; Martin et al., 1993), the parallel POM:SPM was 5.2%, 29% and 65%, demonstrating that minerals were the dominant mass component of

SPM in the estuary and river plume. Accordingly, minerals on average contributed ~75% to $a_{p,412}$ along the estuarine transects (Annex 1) while this percentage in the CB decreased to <60% at the surface and <19% at the DCM based on the $a_{phy,412}:a_{p,412}$ ratios in Table 4-2. We estimated that excluding mineral absorption would increase $\bar{\Phi}_p$ by a factor of ~6 for the estuary but only by <1.3 times for the shelf and offshore waters. This correction led to $\bar{\Phi}_p$ for the SGT stations surpassing its CDOM counterpart and being greater than $\bar{\Phi}_p$ for the MS and CB. Hence, terrigenous POM discharged from the Mackenzie River could be more photoreactive with respect to CO photoproduction as compared to the largely algae-derived marine POM produced in the open Beaufort Sea. However, it should be noted that iron oxides, which often are a primary pigmenting agent for mineral-rich terrigenous particles (Stramski et al., 2007; Estapa et al., 2012b), may play a catalytic role in POM photochemistry, similar to the role that dissolved iron plays in CDOM photochemistry (Gao and Zepp, 1998). Hence, the increase in the particulate photoreactivity for the estuarine samples after correcting for the mineral absorption could partly result from the exclusion of the absorption by iron oxides, which might be involved in CO photoproduction. Clearly, a mechanistic study is needed to elucidate the role of iron and other metals (e.g. Cu and Mn) in particle photochemistry.

Several studies have reported that POM can be photochemically transformed to DOM, including CDOM (Anesio et al., 1999b; Mayer et al., 2009; Pisani et al., 2011). POM-based CO photoproduction could thus arise directly from POM itself or indirectly from POM-derived CDOM. The current study does not aim to distinguish between the two pathways. We, however, did monitor the effect of irradiation on CDOM in certain particle-containing samples and found no substantial production of new CDOM over the relatively short periods of light exposure adopted in our experiments (mostly <2 h) (Annex 1, Fig. A1). CO photoproduction from newly produced CDOM, if any, should therefore not be the primary process responsible for the particle-driven CO photoproduction observed in this study.

4.3.4 Action spectra of CO photoproduction

The action spectrum of CO photoproduction at the sea surface, $\Lambda_{0,\lambda}$ (mol CO m⁻³ h⁻¹ nm⁻¹), was calculated using Eq. (4-11),

$$\Lambda_{0,\lambda} = Q_{0,\lambda} \times a_{\lambda} \times \Phi_{\lambda} \quad (4-11)$$

where $Q_{0,\lambda}$ is defined in Eq. (4-10) and a_{λ} and Φ_{λ} denote $a_{cdom,\lambda}$ and $\Phi_{cdom,\lambda}$ for CDOM and $a_{p,\lambda}$ and $\Phi_{p,\lambda}$ for particles (Fig. 4-5A, B). Both CDOM and particle action spectra were characterized by a non-Gaussian style with the peak response located at 330 nm and a long tail in the visible (Fig. 5C, D). While the particle action spectra were far below the CDOM's in the UV range (290-400 nm), the former were conspicuously above the latter across most of the visible section (>400 nm), leading to a flatter transition from the UV to visible in the particle action spectra. Averaged on action spectra of all surface water samples, UV-B (290-320 nm) contributed 22% (range: 16%-28%), UV-A (320-400 nm) 71% (range: 67%-74%), and the visible (400-600 nm) 7% (range: 4%-13%) to Λ_0 of CDOM integrated over 290-600 nm. The spectral contributions to the wavelength-integrated Λ_0 of particles were: 12% (range: 4%-31%) from UVB, 60% (range: 45%-70%) from UVA and 27% (range: 5%-52%) from the visible. The mean percent contribution from the visible displayed little variations across the three sub-regions but was higher for DCM samples (36%) than for surface samples (23%). The visible component in the particle action spectra was on average four times that in the CDOM action spectra.

Depth-integrated action spectra in the photic zone, $\Lambda_{col,\lambda}$ (mol CO m⁻² h⁻¹ nm⁻¹), were computed using Eq. (4-12),

$$\Lambda_{col,\lambda} = Q_{0,\lambda} \times (a_{\lambda} / a_{t,\lambda}) \times \Phi_{\lambda} \quad (4-12)$$

Here $a_{i,\lambda}$ is the total absorption coefficient in the water column, i.e. the sum of $a_{cdom,\lambda}$, $a_{p,\lambda}$, and $a_{w,\lambda}$ in the euphotic zone. Surface water AQY and absorption values were assumed for the entire euphotic zone, which is a reasonable postulation since the euphotic zone was generally shallower than the surface mixed layer. Like the surface action spectra, the peak-

response wavelengths of the water column action spectra also occurred at 330 nm but their patterns substantially shifted to the visible, particularly for the particle spectra (Fig. 4-5E, F). Particle action spectra for DCM samples were an exception which lacked the typical, sharp response peak and was characterized by a broad elevation, instead (Fig. 4-5F). This pattern is consistent with the presence of perceptible shoulders in the Φ_p spectra over the visible band for DCM samples (Fig. 4-2D, E). Averaged on action spectra of all surface water samples, UV-B, UV-A, and the visible accounted for, respectively, 12% (range: 8%-16%), 67% (range: 62%-70%), and 21% (range: 15%-30%) of CDOM's A_{col} integrated from 290-600 nm and 5% (range: 1%-15%), 41% (range: 26%-71%), and 55% (range: 15%-73%) of particles' A_{col} . Compared to the surface action spectra, the percent contributions from the visible in the water column action spectra increased for CDOM and especially for particles. The difference in the spectral contributions between the surface and water column action spectra arose from the fact that the UV radiation was more rapidly attenuated than the visible light during their transmission in the water column (Fig. 4-6A).

To examine the effect of varying spectral light propagation on the depth dependence of CO photoproduction in the water column, we modeled the vertical distribution of spectral solar photon fluxes using Eq. (4-13),

$$Q_{z,\lambda} = Q_{0,\lambda} \times \exp(-k_{d,\lambda} \times z) \quad (4-13)$$

where $Q_{z,\lambda}$ is the spectral photon flux at depth z (m) and $k_{d,\lambda}$ the diffuse attenuation coefficient (m^{-1}) (Doxaran et al., 2012). The action spectrum at depth z , $A_{z,\lambda}$ ($mol\ CO\ m^{-3}\ h^{-1}\ nm^{-1}$), is given by

$$A_{z,\lambda} = Q_{z,\lambda} \times a_{\lambda} \times \Phi_{\lambda} \quad (4-14)$$

$Q_{z,\lambda}$ and $A_{z,\lambda}$ for the UV-B, UV-A and visible bands were calculated by integration over the relevant wavelength ranges. Clearly, the visible light and visible-driven CO production penetrated much deeper than their UV-B and UV-A counterparts (Fig. 4-6A-C). Consequently, the relative contribution of the visible to full-spectrum (290-600 nm) CO production increased with depth for both CDOM and particles (Fig. 4-6D). Concerning the full spectrum-integrated A_z , the ratio of particles to CDOM rose from 4% at the surface to

38% at the base of the euphotic zone (Fig. 4-6E), due evidently to the dominance of $\Phi_{p,\lambda}$ over $\Phi_{cdom,\lambda}$ at the visible wavelengths (Fig. 4-2).

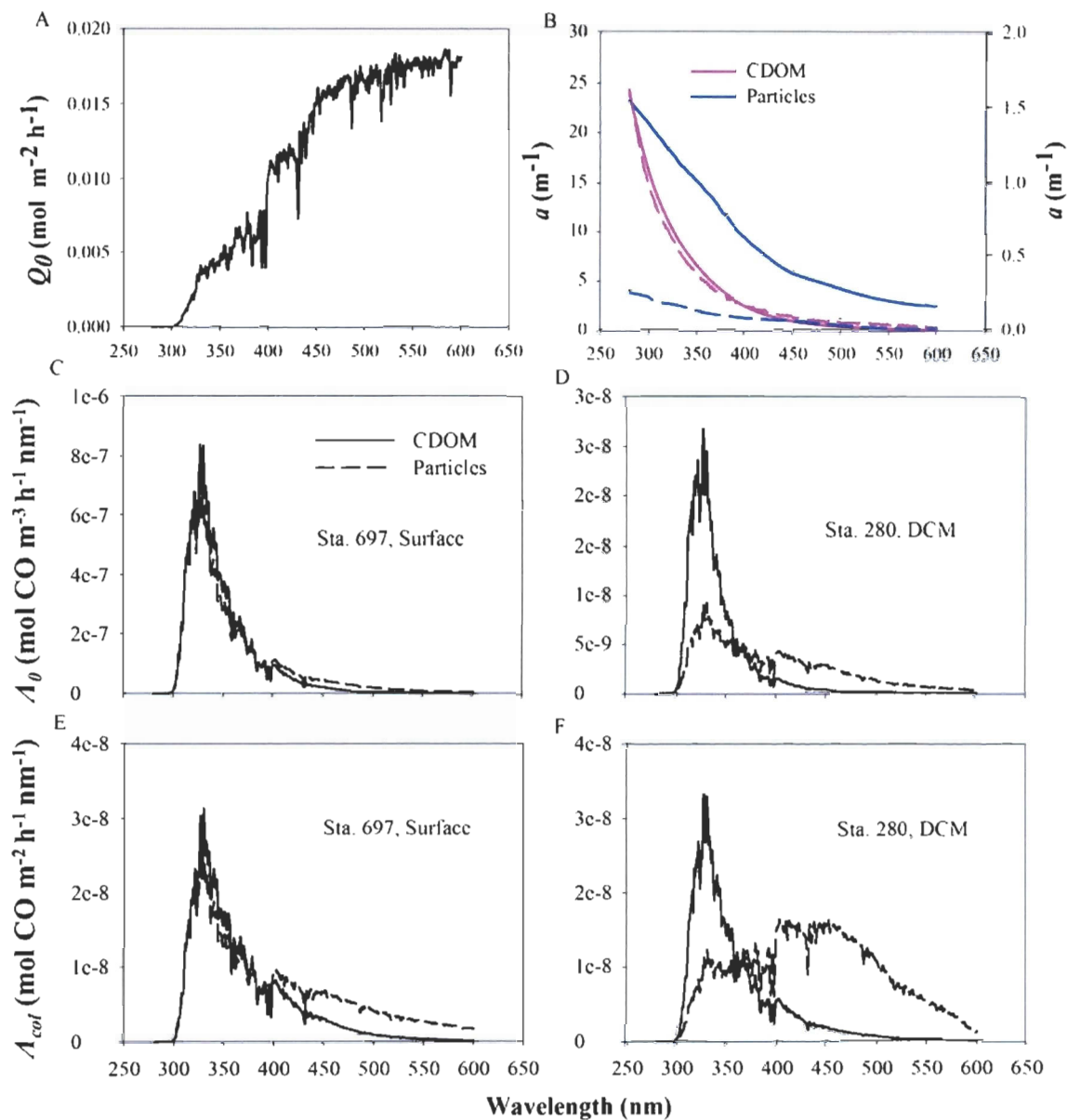


Fig. 4-5. Modeled surface spectral solar irradiance (A), a_{cdom} and a_p (B), surface CO action spectra (C and D) and depth-integrated CO action spectra (E and F). In panel B, left y-axis is for Sta. 697 (solid line) and right y-axis for Sta. 280-DCM (dashed line).

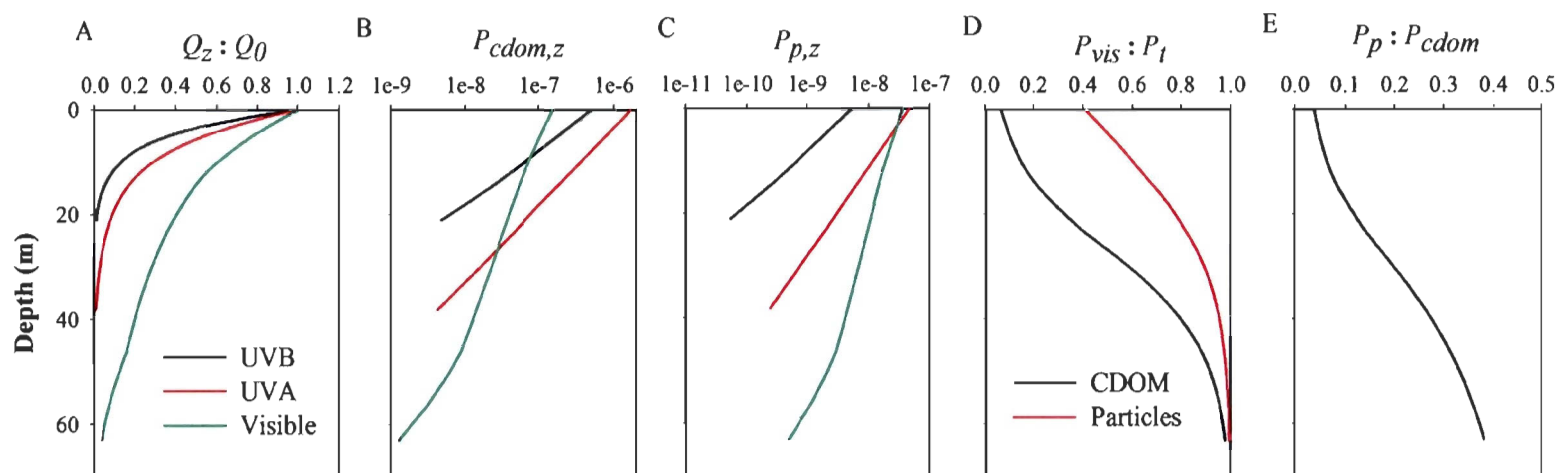


Fig. 4-6. Modeled vertical profiles of normalized solar irradiance (A), CO photoproduction rate ($\text{mol CO m}^{-3} \text{h}^{-1}$) from CDOM (B) and particles (C), the contribution of visible to full-spectrum CO photoproduction (D), and the ratio of full-spectrum particle-based to CDOM-based CO photoproduction (E) at Sta. 430.

4.3.5 Modeling CO photoproduction

CO photoproduction rates from CDOM and particles were modeled at each station for the sampling season of August 2009. The production rates at the surface (0 m), P_0 ($\mu\text{mol CO m}^{-3} \text{ d}^{-1}$), and in the euphotic zone (depth-integrated), P_{col} ($\mu\text{mol CO m}^{-2} \text{ d}^{-1}$), were calculated using Eqs. (4-15) and (4-16), respectively,

$$P_0 = \int_{290}^{600} Q_{0-\lambda} \times a_\lambda \times \Phi_\lambda \times d\lambda \quad (4-15)$$

$$P_{col} = \int_{290}^{600} Q_{d0-\lambda} \times (a_\lambda / a_{t,\lambda}) \times \Phi_\lambda \times d\lambda \quad (4-16)$$

P_0 , P_{col} , a_λ , and Φ_λ denote $P_{cdom,0}$ and $P_{p,0}$, $P_{cdom,col}$ and $P_{p,col}$, $a_{cdom,\lambda}$ and $a_{p,\lambda}$, and $\Phi_{cdom,\lambda}$ and $\Phi_{p,\lambda}$ for CDOM and particles, respectively. $Q_{0-\lambda}$ is the scalar photon flux just beneath the surface ($\text{mol photons m}^{-2} \text{ d}^{-1} \text{ nm}^{-1}$) and $a_{t,\lambda}$ the sum of $a_{cdom,\lambda}$, $a_{p,\lambda}$, and $a_{w,\lambda}$ in the water column. $Q_{0-\lambda}$ was estimated as 1.3 times the downwelling photon flux ($Q_{d0-\lambda}$) (Gordon 1989). $Q_{d0-\lambda}$ was simulated using the Santa Barbara DISORT Atmospheric Radiative Transfer (SBDART) software developed by Ricchiazzi et al. (1998) at 3 h intervals, taking into account of the cloud cover and ozone conditions. Major factors influencing solar incident irradiance, such as cloud fraction, cloud optical thickness, and ozone abundance, were obtained from the International Satellite Cloud Climatology Project (ISCCP, <http://isccp.giss.nasa.gov/products/browsed2.html>). Eqs. (4-15) and (4-16) employed surface water a_λ and Φ_λ and assumed vertical uniformity of the two parameters in the euphotic zone. Areal CO photoproduction in ice-free water, $\sum P_{col}$, was calculated separately for the MRE, MS, and CB by multiplying the mean P_{col} by the open water area for each sub-region. Demarcation of the three sub-regions is described in Fig. 4-1. Daily sea ice cover data were provided by the U.S. National Snow and Ice Data Center (NSIDC, <http://nsidc.org/>).

Both $P_{cdom,0}$ and $P_{p,0}$ reached maxima, $214 \mu\text{mol CO m}^{-3} \text{ d}^{-1}$ and $212 \mu\text{mol CO m}^{-3} \text{ d}^{-1}$, at the most nearshore Sta. 697, in line with the highest a_{cdom} and a_p observed at this locality (see Sect. 3.1). The minimum $P_{cdom,0}$ ($2.0 \mu\text{mol CO m}^{-3} \text{ d}^{-1}$) and $P_{p,0}$ ($0.09 \mu\text{mol CO m}^{-3} \text{ d}^{-1}$)

occurred, respectively, at the offshore Sta. 430 and Sta. 220 having low CDOM and particle abundances. $P_{p,0}:P_{cdom,0}$ was highest at Sta. 697 (0.99) and lowest (0.02) at Sta. 220, conforming to the parallel high (4.1) and low (0.10) $a_p:a_{cdom}$. The maximum $P_{cdom,col}$ (18.8 $\mu\text{mol CO m}^{-2} \text{d}^{-1}$) and $P_{p,col}$ (10.2 $\mu\text{mol CO m}^{-2} \text{d}^{-1}$) were found, respectively, at Sta. 170 in the upwelling zone and at Sta. 697 in the innermost area of the estuary while the minimum $P_{cdom,col}$ (6.9 $\mu\text{mol CO m}^{-2} \text{d}^{-1}$) and $P_{p,col}$ (0.3 $\mu\text{mol CO m}^{-2} \text{d}^{-1}$) were present, respectively, at Sta. 320 and Sta. 220 in offshore waters, respectively. Like $P_{p,0}:P_{cdom,0}$, $P_{p,col}:P_{cdom,col}$ was also highest at Sta. 697 (1.2) and lowest at Sta. 220 (0.02). Note that $P_{p,col}$ surpassed $P_{cdom,col}$ at Sta. 697, which had the highest $a_{p,412}:a_{cdom,412}$ (4.1). This result suggests that the significance of particle photochemistry can overtake that of CDOM photochemistry in highly turbid waters, consistent with the finding of Estapa et al. (2012a) for DOC photoproduction.

Table 4-4 summarizes the means of modeled CO production rates and other related parameters for each sub-region. $P_{cdom,0}$, $P_{p,0}$, and $P_{p,0}:P_{cdom,0}$ all decreased from the estuary to the shelf to the basin, which evolved in the same manner as a_{cdom} , a_p , and $a_p:a_{cdom}$, respectively (Table 4-2). $P_{cdom,col}$ exhibited little regional variations while $P_{p,col}$ declined by 54% from the estuary to the shelf and by 57% from the shelf to the basin. $P_{p,col}:P_{cdom,col}$ thus decreased seaward by roughly the same extents as those for $P_{p,col}$. Because of widening open water area seaward, $\sum P_{cdom,col}$ augmented from the estuary to the shelf to the basin, contrary to the $P_{cdom,col}$ tendency. The combination of relatively high particle abundance and large open water area rendered the MS to possess the highest $\sum P_{p,col}$. The total CO photoproduction in the entire study area in August 2009 amounted to 67×10^6 moles, of which 14% was produced by POM photodegradation.

Note that the estimates in Table 4-4 were based on CO AQY data determined at 4°C while surface water temperature in the sampling area spanned from -0.8°C to 10.3°C (Table 1) and decreased seaward (Section 4.4.1). Using water samples from the St. Lawrence estuarine system, Zhang et al. (2006) observed a 30%–70% (depending on salinity) increase in CO photoproduction from CDOM with a 20°C increase in temperature.

Although little is known about the temperature dependence of particulate CO photoproduction, particle photoprocesses (e.g. DOC photoproduction) appear to be more strongly affected by temperature than many dissolved-phase photoreactions (Mayer et al., 2006; Espapa et al., 2012a). Therefore, the effect of temperature variation on CO photoproduction in the present study could be significant for both CDOM and particles. Here we tentatively assessed this effect based on the results of Zhang et al. (2006), assuming roughly equal extents of temperature dependence for the two pathways. The temperature correction increased $\sum P_{cdom,col}$ and $\sum P_{p,col}$ by 22% in the estuary and 7% on the shelf but decreased them by 2% in the basin. The total CO production in August 2009 increased from 67×10^6 moles to 71×10^6 moles.

It should also be pointed out that the particulate to CDOM CO photoproduction ratios reported in Table 4 were arithmetic averages of these ratios for individual stations within each sub-region. The individual CO production ratios were based on the corresponding individual $a_p:a_{cdom}$ measured. Because of limited spatial coverage by the sampling stations, snapshots of $a_p:a_{cdom}$ might not be representative of the entire sub-region in question. We therefore also evaluated $P_{p,col}$ and $P_{cdom,col}$ using monthly averaged remote sensing-derived a_t (Bélanger, 2006) and $a_{cdom}:a_t$ (Bélanger et al., 2008), from which a_p and a_{cdom} (hence $a_p:a_{cdom}$) can be calculated since $a_t = a_p + a_{cdom} + a_w$ and a_w is known (Buiteveld et al., 1994; Pope and Fry, 1997). The a_p , a_{cdom} and $a_p:a_{cdom}$ in the present study were obtained from the remote sensing-based a_{cdom} and $a_{cdom}:a_t$ published by Xie et al. (2012, their Table 4-3). The $P_{p,col}$, $P_{cdom,col}$, and $P_{p,col}:P_{cdom,col}$ derived from ocean color imaging are shown in Table 4-5. In addition to the sampling month (August), estimates were also made for other months, assuming seasonally constant $\Phi_p:\Phi_{cdom}$ (Table 4-5). The satellite-derived $P_{p,col}:P_{cdom,col}$ in August was similar to the individual stations-based ratio for the MS (including MRE) but the former was nearly twice the latter for the CB due to the much higher $a_p:a_{cdom}$ ratio from remote sensing. $P_{p,col}:P_{cdom,col}$ generally decreased from April (MS: 0.44; CB: 0.47) to September (MS: 0.18; CB: 0.13) and followed a similar pattern for $a_p:a_{cdom}$, underscoring the importance of the POM versus CDOM absorption seasonality in controlling the POM-versus CDOM-based CO photoproduction dynamics. The open water area-normalized

annual $P_{p,col}; P_{cdom,col}$ reached 0.27 on the MS and 0.17 in the CB. These values are within the range reported by Xie and Zafiriou (2009) for mid-latitude coastal and open ocean waters.

Table 4-4. Arithmetic means (\pm s.d.) of P_0 , P_{col} , ΣP_{col} , and $a_{p,412}:a_{cdom,412}$ in August 2009 based on individual stations within each sub-region. Keys for MS and CB are the same as those in Table 4-1.

| | MRE ^a | MS | CB |
|--|------------------|---------------|---------------|
| $a_{p,412}:a_{cdom,412}$ | 0.94 | 0.39 | 0.09 |
| P_0 ($\mu\text{mol m}^{-3} \text{d}^{-1}$) | | | |
| P_{cdom^*0} | 90 ± 72 | 13 ± 7 | 6.7 ± 5 |
| P_{p^*0} | 42 ± 69 | 1.8 ± 2 | 0.4 ± 0.2 |
| $P_{p^*0}:P_{cdom^*0}$ | 0.47 | 0.14 | 0.05 |
| P_{col} ($\mu\text{mol m}^{-2} \text{d}^{-1}$) | | | |
| P_{cdom^*col} | 14 ± 3 | 13 ± 4 | 12 ± 3 |
| P_{p^*col} | 5.0 ± 3 | 2.3 ± 2 | 1.0 ± 0.6 |
| $P_{p^*col}:P_{cdom^*c}$ | 0.37 | 0.18 | 0.08 |
| ΣP_{col} ($10^3 \text{ mol CO d}^{-1}$) | | | |
| $\Sigma P_{cdom,col}$ | 302 ± 62 | 681 ± 188 | 866 ± 244 |
| $\Sigma P_{p,col}$ | 111 ± 72 | 120 ± 87 | 73 ± 44 |
| Total | 413 ± 57 | 800 ± 272 | 930 ± 301 |
| Total CO photoproduction in August (10^6 mol CO) | | | 67 ± 20 |

^a MRE = Mackenzie River estuary.

Table 4-5. $P_{cdom,col}$, $P_{p,col}$ ($\mu\text{mol m}^{-2} \text{d}^{-1}$), and $P_{p,col}:P_{cdom,col}$ based on ocean color data from remote sensing. Also included are $a_p:a_{cdom}$ at 412 nm and open water area ($\times 10^3 \text{ km}^2$) (Xie et al., 2012). Keys for MRE, MS and CB are the same as those in Table4- 4.

| | | Apr. | May | Jun. | Jul. | Aug. | Sep. | Annual |
|------|--------------------------|------|------|------|------|------|------|--------|
| MRE | $a_p:a_{cdom}$ | 0.74 | 0.76 | 0.67 | 0.65 | 0.33 | 0.42 | 0.50 |
| | Area | 2.2 | 12.3 | 43.1 | 63.5 | 74.5 | 74.4 | 74.5 |
| + MS | $P_{cdom,col}$ | 6.6 | 10.4 | 15.8 | 16.7 | 12.2 | 6.6 | 9.6 |
| | $P_{p,col}$ | 2.9 | 4.5 | 6.5 | 4.5 | 2.4 | 1.2 | 2.6 |
| | $P_{p,col}:P_{cdom,col}$ | 0.44 | 0.43 | 0.41 | 0.27 | 0.20 | 0.18 | 0.27 |
| CB | $a_p:a_{cdom}$ | 0.76 | 0.49 | 0.42 | 0.31 | 0.28 | 0.27 | 0.30 |
| | Area | 0.25 | 12.5 | 43.9 | 58.9 | 74.0 | 79.0 | 79.0 |
| | $P_{cdom,col}$ | 6.9 | 10.9 | 16.5 | 18.2 | 10.2 | 5.3 | 9.8 |
| | $P_{p,col}$ | 3.3 | 2.9 | 3.6 | 2.7 | 1.5 | 0.7 | 1.6 |
| | $P_{p,col}:P_{cdom,col}$ | 0.47 | 0.27 | 0.22 | 0.15 | 0.14 | 0.13 | 0.17 |

4.4 SUMMARY

AQY spectra of CO photoproduction from CDOM and particles were determined using water samples from the Mackenzie estuary, shelf, and Canada Basin. Bulk particulate matter-based CO AQY increased from the estuary and shelf to the basin, opposite to the trend of CDOM-based CO AQY. Samples from the deep chlorophyll maximum layer displayed higher CO AQY for both particles and CDOM than did surface water samples. CO AQY of bulk particulate matter in shelf and offshore waters exceeded that of CDOM but the reverse held for estuarine water. Excluding the contribution of minerals to the absorption coefficient of the bulk particles, POM-based CO AQY in estuarine water could surpass its CDOM counterpart and the POM-based CO AQY in offshore waters. While CDOM's CO AQY generally increased linearly with the CDOM's absorption coefficient, particulate matter's CO AQY did not show consistent relationships with its optical properties. The spectral shape of particle-based CO AQY was flatter than that of CDOM-based CO AQY in the visible wavelengths, leading to a continuously increasing proportion of CO produced from particles with depth in the water column. Although depth-integrated CO photoproduction from CDOM was primarily driven by the UV radiation, the visible domain contributed roughly as much as the UV to CO photoproduction from particles. AQY-based coupled optical-photochemical modeling indicates that CO photoproduction from particles in the study area was equivalent to 13-47% of that from CDOM. Future studies are needed to elucidate the roles of metals (e.g. iron oxides) and chlorophylls in POM-based CO photoproduction.

ACKNOWLEDGMENTS

We thank D. Doxaran and J. Ehn for providing the POC, SPM, and backscattering data. We are grateful to M. Babin, the chief scientist of the *CCGS Amundsen* cruise and the principal investigator of the Malina program. This study was supported by grants from

NSERC (Natural Sciences and Engineering Research Council) and conducted as part of the Malina Scientific Program funded by ANR (Agence nationale de la recherche), INSU-CNRS (Institut national des sciences de l'univers – Centre national de la recherche scientifique), CNES (Centre national d'études spatiales) and ESA (European Space Agency). GS received graduate scholarships from ISMER (Institut des sciences de la mer de Rimouski) and FRQNT (Fonds de recherche du Québec – Nature et technologies).

CHAPITRE 5
PHOTOPRODUCTION DE MONOXYDE DE CARBONE (CO) À PARTIR DE
DIFFÉRENTES CLASSES DE TAILLE DE MATIÈRE ORGANIQUE DANS
L'ESTUAIRE DU DELAWARE SOUS DES CONDITIONS HYDRO-
BIOLOGIQUES CONTRASTÉES

CARBON MONOXIDE (CO) PHOTOPRODUCTION FROM SIZE-
FRACTIONATED ORGANIC MATTER IN THE DELAWARE ESTUARY UNDER
CONTRASTING HYDRO-BIOLOGICAL CONDITIONS

RÉSUMÉ

La photochimie de la matière organique (MO) est un terme important du cycle du carbone dans l'eau turbide estuarienne et côtière. Les rendements quantiques apparents spectraux (AQYs) de la photoproduction de monoxyde de carbone (CO) ont été déterminés à partir de OM dans les échantillons d'eau prélevés dans l'estuaire du Delaware pendant les saisons sèche (Août) et humide (Novembre) en 2012. La OM a été fractionnée selon trois classes de taille: $< 0,2 \text{ mm}$ (c.-à-d. dissous OM, DOM), $< 10 \text{ }\mu\text{m}$ (c.-à-d. DOM plus les particules $< 10 \text{ }\mu\text{m}$) et $< 20 \text{ }\mu\text{m}$ (c.-à-d. DOM plus les particules $< 20 \text{ }\mu\text{m}$). Les spectres de CO AQY à partir de la DOM et de DOM plus les particules ont été plus plats que ceux précédemment publiés, conduisant à une photoproduction de CO plus importante due à la lumière visible dans l'estuaire du Delaware. En Août, le spectre AQY de la DOM était plus élevé que ceux des échantillons contenant des particules, tandis que les spectres AQY des deux fractions contenant des particules étaient similaires. En Novembre, les spectres AQY CO des trois composantes fractionnées par classe de taille se recoupaient les uns les autres, avec la OM plus de petite taille étant la plus efficace dans le régime UV, alors que la OM de plus grande taille étant plus efficace dans le régime visible. Saisonnièrement, les trois fractions de taille de l'OM étaient plus efficaces à photoproduction de CO en Novembre, en raison principalement de la forte proportion de DOM d'origine terrestre le long de l'estuaire après la crue de l'ouragan Sandy. Cependant, aucune différence significative dans la photoréactivité des particules, en termes de la production de CO, a été trouvée entre les deux fractions de taille des particules le long de l'estuaire. La photoproduction de CO modélisée indique que les particules pourraient contribuer jusqu'à 29% -55 % et 48% -77 % de la photoproduction totale de CO dans la colonne d'eau en Août et en Novembre, respectivement. En outre, les particules $< 10 \text{ }\mu\text{m}$ ont plus contribué à la photoproduction totale de CO attribuée aux particules, puisque les particules de plus petite taille étaient dominantes de la matière particulaire colorée pendant les deux campagnes. Les résultats suggèrent que les particules pourraient être le principal contributeur à la photoproduction de CO dans les eaux estuariennes très turbides.

ABSTRACT

Photochemistry of organic matter (OM) is an important term of carbon cycling in turbid estuarine and coastal waters. This study determined the spectrally resolved apparent quantum yields (AQYs) of carbon monoxide (CO) photoproduction from OM in water samples collected from the Delaware estuary during the dry (August) and flood (November) seasons of 2012; the OM was size-fractionated into three components: $< 0.2\text{-}\mu\text{m}$ (i.e. dissolved OM, DOM), $< 10\text{-}\mu\text{m}$ (i.e. DOM plus particles $< 10\ \mu\text{m}$), and $< 20\ \mu\text{m}$ (i.e. DOM plus particles $< 20\ \mu\text{m}$). The CO AQY spectra of both DOM and DOM plus particles were flatter than those previously reported, leading to visible light being the main contributor to CO photoproduction in the water column of the Delaware estuary. In August, DOM AQY spectrum lay far above those of particle-containing samples, while the AQY spectra of the two particle-containing fractions were similar. In November, CO AQY spectra of the three size-fractionated components intersected each other, with the smaller sized OM more efficient in the UV regime and the larger sized OM more efficient in the visible regime. Seasonally, all three size fractions of OM were more efficient in CO photoproduction in November, due mainly to the relative higher proportion of terrestrial DOM along the estuary after the freshet of Super-storm Sandy. However, no significant difference in particle photoreactivity in terms of CO production was found between the two size fractions of particles along the estuary. Modeled CO photoproduction indicated that particles could contribute 29%-55% and 48%-77% to total CO photoproduction in the water column in August and November, respectively. Furthermore, particles $< 10\ \mu\text{m}$ contributed more to the total particle-based CO photoproduction than did particles of between 10 and 20 μm , since smaller-sized particles were the dominant component of the colored particulate matter during the two cruises. The results suggested particles could be the main contributor to CO photoproduction in highly turbid estuarine waters.

5.1 INTRODUCTION

Carbon monoxide (CO) is the dominant sink of hydroxyl radicals in the troposphere and hence affects the oxidizing capacity of the atmosphere (Thompson, 1992) and serves as an indirect greenhouse gas (Zepp et al., 2011). The surface waters of open oceans (Bates et al., 1995; Zafiriou et al., 2003; Stubbins et al., 2006a), coastal seas (Day and Faloon, 2009; Xie et al., 2009a), and estuaries (Law et al., 2002; Zhang and Xie, 2012) are supersaturated with CO, thereby acting as a source of CO to the atmosphere. CO is a potential energy and perhaps a carbon source as well for marine microbes oxidizing it (King and Weber, 2007; Moran and Miller, 2007). The short turnover times of CO in seawater (usually < 1 day), due mainly to rapid microbial consumption (Conrad et al., 1982; Zafiriou et al., 2003; Xie et al., 2009b), makes it an excellent tracer for tuning models of upper-ocean mixing dynamics (Kettle, 2005).

In the ocean, CO has long been thought to be mainly produced via photolysis of chromophoric dissolved organic matter (CDOM) (e.g., Conrad and Seiler, 1980; Valentine and Zepp, 1993; Zafiriou et al., 2003; Stubbins et al., 2006b), with little attention paid to the role of particulate organic matter (POM). Xie and Zafiriou (2009) assessed the relative importance of CO photoproduction from CDOM and POM in a limited number of samples collected from mid-latitude coastal and open-ocean areas in the NW Atlantic. Stubbins et al. (2011) estimated the relative contribution of particles to total CO photoproduction in the Tyne estuary, based on the assumption that the wavelength-dependent efficiency of particles to CO photoproduction was equal to that of CDOM. More recently, Song et al. (2013) published spectrally resolved apparent quantum yield (AQY) spectra of particle-based CO photoproduction in the southeastern Beaufort Sea and modeled the contribution of particles to the total CO photoproduction in this part of the Arctic Ocean based on the obtained AQYs. The studies of Xie and Zafiriou (2009) and Song et al. (2013) both demonstrate that the POM-based CO term is significant for their sampled areas, accounting for 11%-47% of the CDOM-based quantity. If these results are representative of other ocean regions, POM photochemistry may provide an important, new source of CO, tipping

the balance of its sources and sinks reported by Zafiriou et al. (2003) and requiring faster microbial oxidation, outgassing or new sinks to re-balance its budget. Furthermore, AQY spectra obtained by Song et al. (2013) suggest that particles are more efficient at CO photoproduction in the visible regime than CDOM, and in contrast with CDOM, terrestrial particles are less efficient at CO photoproduction than marine-derived particles. POM may thus differ substantially from CDOM in contributing to the spatial variability of CO concentrations in seawater.

This paper reports results of CO photoproduction from CDOM and POM in the Delaware Estuary, a mid-latitude estuarine system enriched with organic materials. The objectives of this study are 1) to expand the limited spatial coverage of the previous surveys on particle-based CO photoproduction, 2) to explore the potential impacts of the seasonal hydro-biological cycle on these two photoprocesses, and 3) to evaluate the effect of particle size distribution on POM-derived CO production. AQY spectra of CO photoproduction from 3 different size-fractionated organic matters ($<0.2 \mu\text{m}$, $<10 \mu\text{m}$ and $<20 \mu\text{m}$) were determined and used to model the wavelength-dependence of CO production in the water column and to estimate the relative contributions of the targeted organic matter fractions to total CO photoproduction. As CO is a key organic matter photoproduct that arguably can be most reliably determined (Mopper and Kieber, 2000; Zafiriou et al., 2008), results from this study may have broader implications for other major photoproducts as well (e.g. CO_2).

5.2 METHODS

5.2.1 Study site

The Delaware estuary, including the Delaware Bay, is the second largest estuarine system on the mid-Atlantic coast in the United States with a monthly mean freshwater flux of $650 \text{ m}^3 \text{ s}^{-1}$ (Garvine et al., 1992). The monthly mean discharge usually peaks in April and is at the trough in September (Cook et al., 2007). The water column in the Delaware

estuary is generally well mixed for most of the year due mainly to strong tidal flows but is highly stratified during the spring freshet (Sharp et al., 1986). The river is significantly influenced by anthropogenic inputs, resulting in high concentrations of macronutrients (e.g. inorganic nitrogen and phosphate) in the water column. However, owing to the limitations of light and multiple trace nutrients, primary production in the estuary is generally low (Pennock, 1985; Sharp et al., 2009) with relatively higher primary production located in the lower estuary (i.e. the bay area), where the water is less turbid (Mannino and Harvey, 2000; Harvey and Mannino, 2001). Different from most other major estuaries, peculiar tidal resuspension of sediments and flocculation create two turbidity maxima zones (TMZs) in the upper and middle estuary, respectively (Biggs et al., 1983).

The concentrations of dissolved and particulate organic carbon (DOC and POC) in the Delaware estuary ranges from 144-330 $\mu\text{mol C L}^{-1}$ and 44-320 $\mu\text{mol C L}^{-1}$, respectively (Mannino and Harvey, 2000; Sharp et al. 2009). DOC concentration decreases approximately linearly with distance from the upstream TMZ to the mouth of the bay (Sharp et al., 2009). Seasonally, DOC concentration in the surface water is higher in summer and fall than that in winter and early spring throughout the estuary (Sharp et al., 2009). Unlike DOC, POC is lower in the lower bay and higher in the TMZs and mid-bay regions due respectively to sediment resuspension and autochthonous phytoplankton production (Sharp et al., 2009). POC only contributes less than 5% to the total suspended particulate matter (SPM) in the TMZs (Sharp et al., 2009) because of a much higher concentration of resuspended inorganic sediments there. Terrigenous POM dominates during most of the year, and compared with other seasons, autochthonous biological production contributes relatively more in summer to POM, due to the low discharge and higher primary production in summer (Sharp et al., 2009). The mean size of particles increases and the components vary from the upper to lower estuary: the upstream TMZ is dominated by individual mineral grains with the mean size of 3 μm , while the downstream TMZ is loaded mainly with composite particles with the mean size of 12 μm ; further seaward at salinity > 10, large-sized (10-20 μm) individual particles prevail (Biggs et al.,

1983). Such characteristic particle distributional and compositional patterns make the Delaware estuary ideal for studying size-based particle photochemistry.

5.2.2 Sampling

The field study was carried out during the Photochemistry and Photoheterotroph Interactions (PAPI) Program aboard the *R.V. Sharp* along the main axis of the Delaware Estuary in August and November 2012. The designation of sampling stations starts with letter “A” for August and letter “N” for November (Table 5-1 and Fig. 5-1). Surface water samples were collected at 0.5-m or 1-m depth using 12-L Niskin bottles mounted onto a conductivity-temperature-depth (CTD) rosette. The well-mixed water column (Sharp et al., 1986) assured no significant differences in the concentration, composition, and optical properties of organic matter between the two depths. Each water sample was gravity-filtered through a Whatman Polycap filtration capsule sequentially containing 0.8- μm glass fiber and 0.2- μm Nylon membranes into a 60-mL clear glass bottle (Qorpak) for the measurement of CDOM absorption spectra. At some stations (Table 1), the samples were divided into three portions: the first portion was gravity-filtered with the above procedure into a 60-mL clear glass bottle (Qorpak) for the measurement of CDOM absorption spectra and into a 1-L clear glass bottle for irradiation experiment; the second and third portions of the sample were gravity-filtered through, respectively, 20- μm and 10- μm Nylon meshes into half-gallon clear glass bottles or 2-L Teflon bottles for the determination of particle absorption spectra and CO photoproduction. The 20- μm filtration was purported to remove large inorganic particles and hence to eliminate their effects on light scattering and absorbing during irradiation. Notably some organic particles, such as large-sized zooplankton, phytoplankton, and flocculated terrigenous organic particles, were also removed by this procedure. All bottles were protected against light during sampling by wrapping them with aluminum foil. All glass bottles were muffled and Teflon bottles were acid cleaned. They were all thoroughly rinsed with Milli-Q water and then sample water

before use. For the determination of particulate matter absorption spectra, particles in 20 to 150 mL of the 10- and 20- μm filtered water were collected onto pre-combusted (450°C) 25-mm GF/F (Whatman) filters under low vacuum (< 50 kPa). The filters were then stored at -20°C in petri dishes covered with aluminum foil. CDOM absorption samples were kept in the dark at room temperature. Both the CDOM and particle samples were brought to the land-based labs in Syracuse, New York or Rimouski, Quebec for analysis. CO photoproduction experiments were conducted aboard the ship immediately after sampling. At each station, the attenuation coefficient of photosynthetically active radiation (PAR, 400-700 nm) in the water column, $k_d(\text{m}^{-1})$, was measured using a Biospherical Instruments PNF 2102P probe.

Table 5-1 Station coordinates, sampling dates along with salinity, temperature, total water depth, Chl *a* and attenuation coefficient (k_d). NA: no data. Chl *a* was filtered with GF/F filter.

| Station | Sampling date | Coordinate | | Salinity | Temperature (°C) | Chl <i>a</i> ^a (μg L ⁻¹) | k_d (m ⁻¹) |
|------------------|---------------|------------|----------|----------|------------------|---|--------------------------|
| | | Lat., N | Long., W | | | | |
| August | | | | | | | |
| A1 ^b | 9 | 39.800 | 75.418 | 0.50 | 28.5 | 8.58 | 2.41 |
| A2 | 10 | 39.802 | 75.418 | 0.70 | 28.5 | 8.12 | 2.74 |
| A3 ^b | 13 | 39.779 | 75.460 | 0.88 | 29.0 | 6.89 | nd |
| A4 | 12 | 39.715 | 75.500 | 1.8 | 28.3 | 7.17 | 3.72 |
| A5 | 11 | 39.699 | 75.511 | 2.3 | 28.7 | 8.30 | 3.32 |
| A6 | 12 | 39.611 | 75.541 | 3.0 | 28.4 | nd | 2.65 |
| A7 ^b | 12 | 39.661 | 75.541 | 3.1 | 28.4 | 4.20 | nd |
| A8 | 12 | 39.634 | 75.566 | 4.6 | 28.5 | 7.15 | 2.48 |
| A9 | 9 | 39.622 | 75.580 | 4.6 | 28.5 | 10.3 | nd |
| A10 ^b | 10 | 39.504 | 75.556 | 6.5 | 28.7 | 10.0 | 2.04 |
| A11 ^b | 9 | 39.425 | 75.529 | 7.2 | 29.0 | 13.2 | 2.03 |
| A12 ^b | 13 | 39.397 | 75.498 | 11.7 | 28.2 | 5.32 | nd |
| A13 ^b | 12 | 39.382 | 75.481 | 10.2 | 28.4 | 6.31 | 1.43 |
| A14 | 10 | 39.380 | 75.466 | 10.2 | 28.5 | 9.95 | 1.99 |
| A15 | 11 | 39.290 | 75.374 | 12.0 | 28.8 | 9.08 | 1.14 |
| A16 ^b | 9 | 39.279 | 75.363 | 16.0 | 29.5 | 11.6 | 1.38 |
| A17 ^b | 10 | 39.162 | 75.262 | 20.4 | 27.8 | 7.15 | 1.18 |
| A18 | 11 | 39.162 | 75.251 | 18.3 | 27.9 | 5.63 | 1.02 |
| A19 | 12 | 39.149 | 75.251 | 19.6 | 27.7 | 8.45 | 1.02 |
| A20 ^b | 13 | 39.147 | 75.252 | 18.5 | 27.7 | 13.5 | NA |
| A21 ^b | 10 | 39.112 | 75.220 | 25.6 | 27.8 | 9.22 | 0.92 |
| A22 | 9 | 39.086 | 75.179 | 27.5 | 27.3 | 5.93 | 0.80 |
| A23 ^b | 11 | 39.072 | 75.175 | 23.1 | 27.6 | 8.50 | 0.81 |
| A24 | 12 | 39.055 | 75.174 | 27.8 | 27.1 | 5.70 | 0.64 |
| A25 | 13 | 39.040 | 75.167 | 25.8 | 28.2 | 6.96 | 0.84 |
| A26 | 10 | 38.871 | 75.087 | 30.3 | 24.3 | nd | 0.42 |
| A27 | 11 | 38.848 | 75.107 | 29.8 | 25.3 | 3.67 | 0.54 |
| A28 ^b | 11 | 38.784 | 74.921 | 31.2 | 22.7 | 4.62 | 0.47 |

| November | | | | | | | |
|------------------|----|--------|--------|------|------|------|------|
| N1 | 13 | 39.851 | 75.325 | 0.10 | 9.6 | 1.98 | 5.96 |
| N2 ^b | 13 | 39.775 | 75.464 | 0.20 | 10.1 | 2.64 | 9.26 |
| N3 | 14 | 39.703 | 75.511 | 0.80 | 10.4 | 4.25 | nd |
| N4 | 15 | 39.669 | 75.526 | 2.0 | 9.6 | 2.33 | 5.87 |
| N5 ^b | 15 | 39.546 | 75.540 | 4.1 | 9.8 | 2.15 | 10.1 |
| N6 ^b | 15 | 39.480 | 75.563 | 10.6 | 9.6 | 1.91 | 3.16 |
| N7 | 14 | 39.470 | 75.557 | 8.6 | 10.5 | 2.33 | 5.37 |
| N8 | 12 | 39.463 | 75.538 | 6.4 | 10.6 | 1.89 | nd |
| N9 | 15 | 39.407 | 75.498 | 13.0 | 9.8 | 1.66 | 2.34 |
| N10 | 12 | 39.365 | 75.446 | 11.4 | 10.8 | 1.86 | nd |
| N11 ^b | 13 | 39.319 | 75.415 | 14.7 | 10.4 | 3.54 | 6.50 |
| N12 | 14 | 39.311 | 75.394 | 16.5 | 10.1 | 1.66 | 1.83 |
| N13 ^b | 14 | 39.268 | 75.505 | 19.9 | 10.2 | 2.13 | 1.54 |
| N14b | 12 | 39.207 | 75.283 | 25.4 | 10.1 | 1.82 | 1.97 |
| N15 ^b | 16 | 39.188 | 75.276 | 19.5 | 9.4 | 1.94 | 1.68 |
| N16 | 16 | 39.174 | 75.264 | 21.7 | 9.7 | 2.28 | 1.07 |
| N17 | 13 | 39.168 | 75.258 | 20.0 | 10.5 | 2.07 | 2.18 |
| N18 | 15 | 39.137 | 75.229 | 23.0 | 9.9 | 1.92 | 1.65 |
| N19 | 16 | 39.083 | 75.177 | 27.0 | 10.3 | 3.40 | 1.74 |
| N20 | 13 | 39.082 | 75.188 | 23.4 | 10.6 | 1.71 | nd |
| N21 | 15 | 38.918 | 75.105 | 28.0 | 10.1 | 2.26 | nd |
| N22 ^b | 12 | 38.849 | 75.107 | 28.6 | 11.6 | 3.25 | 1.30 |
| N23 | 13 | 38.845 | 75.075 | 30.0 | 11.5 | 2.61 | nd |

^a[Chl *a*] is provided by David L. Kirchman (unpublished data);

^bCO photoproduction was also conducted at these stations.

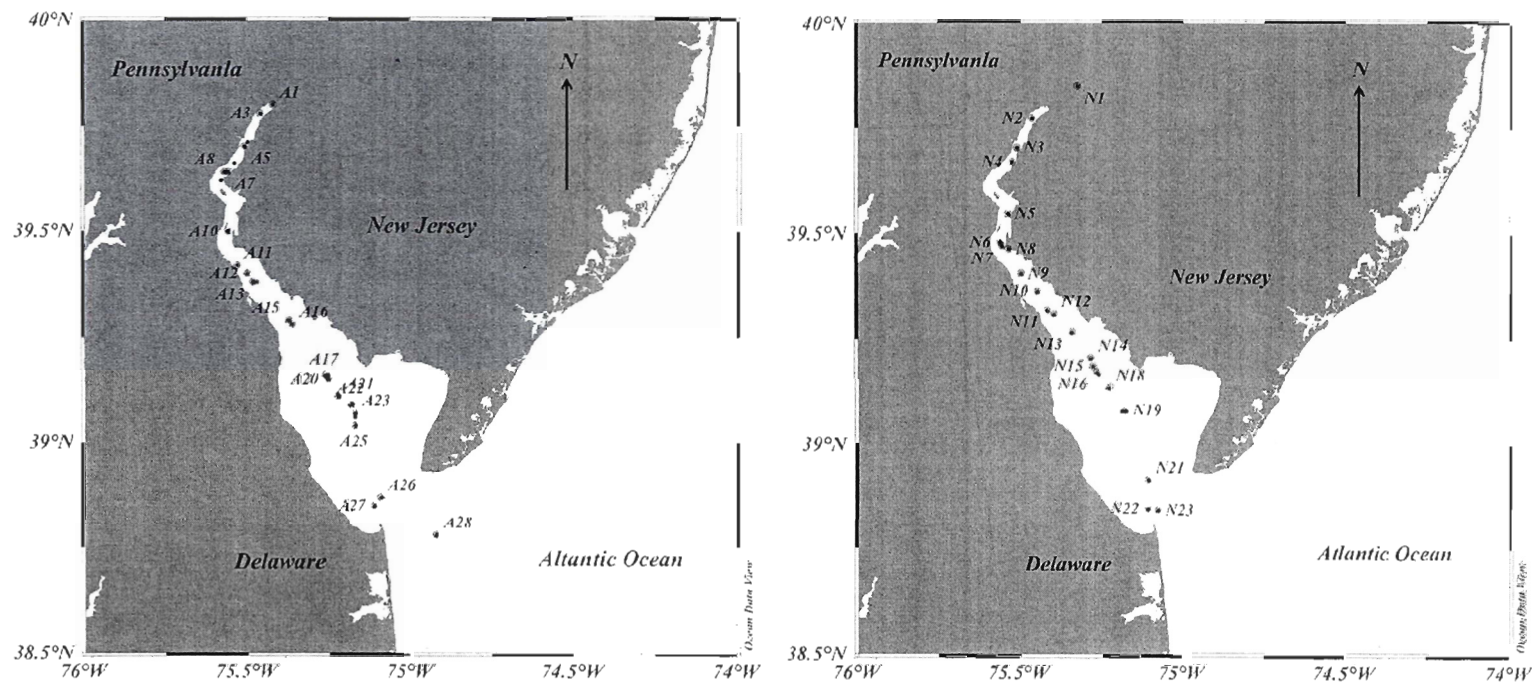


Fig. 5-1 Map of sampling stations for the two cruises. Station details see Table 5-1.

5.2.3 Irradiation

The 10- μm and 20- μm filtered water samples were poisoned with KCN (final concentrations: 2.7 mg L⁻¹ in August and 0.27 mg L⁻¹ in November) to prevent microbial consumption of CO (Xie and Zafiriou, 2009; Song et al., 2013). The same amounts of KCN were added to the corresponding 0.2- μm filtered samples to minimize systematic biases caused by the negative effect of cyanide on CO photoproduction (Song et al., 2013). The samples were then gently shaken for 5 minutes with ambient air as headspace to diminish the initial concentration of CO ([CO]) and then poured into a series of 40-mL borosilicate glass vials having an inner diameter of 2.5 cm. The glass vials were nearly transparent to solar radiation with the 1% and 50% transmittance cutoff wavelengths located at 205 nm and 285 nm, respectively. After the vials were sufficiently overflowed by sample water, they were closed without headspace with Teflon-lined, threaded screw caps. Duplicate vials, horizontally immersed in an on-deck water bath that was temperature-buffered with continuously flowing ambient surface water, were irradiated with three light treatments: full-spectrum sunlight, sunlight screened by a Mylar-D film to remove ultra-violet B radiation (UVB, 290-330 nm) and sunlight screened by a UF3 Plexiglas filter to eliminate both UVB and UVA radiations (290-400 nm). Parallel dark controls were incubated to account for potential CO production from thermal reactions. Poisoning vs. non-poisoning tests showed that cyanide depressed CO photoproduction from CDOM by 20% and 10% under the full-spectrum and Mylar-D treatments, respectively, for the August cruise and by 10% and 5% for the November expedition. These effects were taken into account in the calculation of CO photoproduction rates. The cyanide effect under the UF3 treatment (i.e. predominantly visible radiation) was negligible in both seasons. In particle-containing samples, the cyanide effect could not be reliably assessed due to fast microbial CO oxidation in non-poisoned samples (J. Richardson et al., unpublished data). Based on the result of Song et al. (2013), the inhibitory effect of cyanide on CO photoproduction from particles was assumed to be similar to that on CO photoproduction from CDOM for each light treatment. Nitrate actinometry solutions, concordantly exposed to full-spectrum solar

radiation, were employed to quantify the UVB photon fluxes entering the irradiation vials (Jankowski et al., 2000). The temperature in the water bath was recorded at the beginning, middle, and end of each irradiation. The temperature varied within 0.5°C during each irradiation and the mean value of the three measurements was used for actinometry calculations. Spectral photon fluxes of solar radiation on the ship's deck were monitored at 1 nm intervals from 290 to 600 nm using an OL-754 spectroradiometer fitted with a 2-inch OL IS-270 integrating sphere from 7 a.m. to 7 p.m. in August and from 8 a.m. to 5 p.m. in November. The spectral photon fluxes impinging onto the upper surface of the irradiation vials were obtained from the OL-754 data which were corrected for the transmittances of the vials, the Mylar-D film and the UF3 filter and normalized to UVB photon fluxes determined with the nitrate actinometry.

After irradiation, the samples were analyzed using a headspace method for CO extraction (Xie et al., 2002) and a modified Peak Performer 1 reduction gas analyzer (Peak Laboratories) for CO quantification. The analyzer had a linear response of up to 2.0 parts per million by volume (ppmv) and was periodically calibrated with a 1.0 ppmv National Institute of Standards and Technology (NIST)-traceable gaseous CO standard (Praxair). The lower detection limit and analytical precision were similar to those reported by Xie et al. (2002).

5.2.4 Determination of absorption spectra of CDOM and particles

The spectral optical density of CDOM, $OD_{cdom,\lambda}$, where λ is wavelength in nanometers, was scanned from 800 to 200 nm at 1-nm intervals with an Agilent 8453 spectrophotometer fitted with a 5-cm quartz flow cell and referenced to Milli-Q water. Samples were allowed to warm up to room temperature before analysis. The flow cell was rinsed with methanol, pure water, and sample water between individual scans. A baseline correction was applied by subtracting the optical density averaged over 683-687 nm from all $OD_{cdom,\lambda}$ values (Babin et al., 2003). The spectral CDOM absorption coefficient, $a_{cdom,\lambda}$

(m^{-1}), was calculated as 2.303 times $OD_{cdom,\lambda}$ divided by the light pathlength of the cell in meters (0.05 m).

The frozen particles retained on the GF/F filters were hydrated with 2 droplets of the corresponding 0.2- μm filtered sample waters to minimize phytoplankton cell lysis. The filters were warmed up to room temperature and analyzed for optical density using a Perkin Elmer Lambda 850 dual beam spectrometer fitted with a 150-mm snap-in integrating sphere accommodating a filter holder (Röttgers and Gehnke, 2012). The spectral optical density of the particles, $OD_{f,\lambda}$, was recorded from 800 to 290 nm at 1-nm increments and a scanning speed of 120 nm min^{-1} . $OD_{f,\lambda}$ was converted to the spectral particulate absorption coefficient, $a_{p,\lambda}$ (m^{-1}), using Eq. (5-1),

$$a_{p,\lambda} = 2.303 \times (A/V) \times (OD_{f,\lambda} - OD_{blank,\lambda}) \times (1/\beta_\lambda) \quad (5-1)$$

where $OD_{blank,\lambda}$ is the optical density of a blank filter, A the clearance area of particles on the filter (m^2), V the volume of sample water filtered (m^3), and β_λ the pathlength amplification factor. β_λ was nonlinearly correlated with $OD_{f,\lambda}$ (Röttgers and Gehnke, 2012):

$$\beta_\lambda = 2.9OD_{f,\lambda}^2 - 4.76OD_{f,\lambda} + 4.5 \quad (5-2)$$

Upon the completion of $a_{p,\lambda}$ determination, the filter was dipped in 10 mL methanol for ~18 h to bleach pigments and the spectral absorption coefficient of non-algal particles, $a_{nap,\lambda}$ (m^{-1}), was determined in the same manner as that for $a_{p,\lambda}$. Here $a_{p,\lambda}$ and $a_{nap,\lambda}$ of particles with the sizes of 10-20 μm were retrieved by subtracting the corresponding values for the size fraction of <10 μm from those for the size fraction of <20 μm . Subtracting $a_{nap,\lambda}$ from $a_{p,\lambda}$ gave the phytoplankton absorption coefficient, $a_{phy,\lambda}$ (m^{-1}).

5.2.5 Retrieval of CO AQY spectra

The spectral CO AQY, Φ_λ , is defined as the number of moles of CO produced per mole of photons absorbed by a given set of light-absorbing materials at wavelength λ . Here the light-absorbing materials refer to CDOM in 0.2 μm filtered samples, and CDOM plus particles in 10 μm or 20 μm filtered samples, corresponding to Φ_λ for CDOM ($\Phi_{cdom,\lambda}$), 10 μm filtered samples ($\Phi_{<10,\lambda}$) and 20 μm filtered samples ($\Phi_{<20,\lambda}$), respectively. The amount of photons absorbed by CDOM or CDOM plus particles was calculated as follows:

$$Q_{a,\lambda} = Q_\lambda \times S \times (a_\lambda / a_{t,\lambda}) \times (1 - \exp(-a_{t,\lambda} \times L)) \quad (5-3)$$

where Q_λ denotes the photon flux just below the upper surface of the glass vial ($\text{mol photons m}^{-2} \text{ s}^{-2} \text{ nm}^{-1}$), S the cross section of the vial (m^2), a_λ the absorption coefficient of CDOM or CDOM plus particles, $a_{t,\lambda}$ the sum of $a_{cdom,\lambda}$ and the absorption coefficient of pure water ($a_{w,\lambda}$) (Buiteveld et al., 1994; Pope and Fry, 1997) in 0.2- μm filtered samples and the sum of $a_{cdom,\lambda}$, $a_{p,\lambda}$, and $a_{w,\lambda}$ in 10- or 20- μm filtered samples, and L the light pathlength (m) of the vials. L was estimated to be 0.022 m according to the protocol of Vähätalo and Zepp (2005). Based on previous CDOM photochemistry studies (e.g. Johannessen and Miller, 2001; Vähätalo and Zepp, 2005), $\Phi_{cdom,\lambda}$, $\Phi_{<10,\lambda}$ and $\Phi_{<20,\lambda}$ were modeled using the simple exponential decay formula:

$$\Phi_\lambda = m_1 \times \exp(m_2 \times (\lambda - 290)) \quad (5-4)$$

where m_1 and m_2 are fitting parameters. The amount of CO produced in an irradiation vial over the exposure time could then be predicted as the product of the assumed Φ_λ function and the number of absorbed photons integrated over 290–600 nm. The optimum values of m_1 and m_2 were obtained from iterative curve fitting by varying these parameters from initial estimates until the minimum difference between the measured and predicted production is achieved. CO production rates calculated from the retrieved Φ_λ were in good agreement with the measured rates, with R^2 ranging from 0.973 to 1.000 (mean: $0.994 \pm$

0.007) for the 0.2- μm filtered samples, from 0.977 to 1.000 (mean: 0.994 ± 0.007) for the 10- μm filtered samples and from 0.978 to 1.000 (mean: 0.993 ± 0.007) for the 20- μm filtered samples.

In principle, the scattering effect of particles should be taken into account for quantifying the amount of photons absorbed in each vial. However, because particles were present both inside and outside the vials, the amounts of light scattered out of and into the vials should roughly cancel out. Although the size spectra of particles inside the vials somewhat differed from that in the water bath, this argument is tenable on a first-order approximation, since particles with a size of $<10 \mu\text{m}$ dominated over other size fractions (see section 3.2). Furthermore, the mean ratio of UVB photon fluxes obtained from the nitrate actinometer to those recorded with the spectroradiometer on the deck was 0.98 for both cruises after taking into account the transmittance of the vials. This result suggested that the effect of particle scattering on the UVB photon fluxes entering the vials was negligible. As the particle scattering effect generally increases with decreasing wavelength in highly colored, particle-rich waters (Song et al., 2013), it is expected that light scattering in the UVA and visible wavelengths can also be ignored for the present study.

To facilitate comparison of various Φ_λ spectra, a solar irradiance spectrum-weighted mean apparent quantum yield, $\bar{\Phi}$, was computed for each CO AQY spectrum following the procedure of Xie et al. (2009a):

$$\bar{\Phi} = (\int_{290}^{600} Q_{0,\lambda} \times \Phi_\lambda \times d\lambda) / (\int_{290}^{600} Q_{0,\lambda} \times d\lambda) \quad (5-5)$$

$\bar{\Phi}$ denotes $\bar{\Phi}_{cdom}$ for CDOM, and $\bar{\Phi}_{<10}$ and $\bar{\Phi}_{<20}$ for CDOM plus particles in 10- μm and 20- μm filtered samples, respectively. $Q_{0,\lambda}$ ($\text{mol photons m}^{-2} \text{ h}^{-1} \text{ nm}^{-1}$) is the mean surface spectral solar photon fluxes measured during the August cruise. This normalization reduced the AQY spectrum to a single value equivalent to CO production in the entire water column in which all solar radiation over 290-600 nm is absorbed by the light-absorbing materials,

i.e. CDOM or CDOM plus particles. $\bar{\Phi}$ thus reflects the overall photoreactivity of the chromophoric group or groups in question across the entire wavelength range of interest.

5.3 RESULTS

5.3.1 General hydrological, biological and meteorological conditions

In 2012, the catchment area of the Delaware estuary experienced an unusual dry summer, especially in July and August, whereas it received historically high rainfall at the end of October brought by storm Sandy. The monthly mean freshwater discharge in August 2012 was $119 \text{ m}^3 \text{ s}^{-1}$, 39% lower than the August mean discharge averaged from 2007-2012. On the contrary, the freshet occurred from 28th October to 5th November, with the daily mean freshwater runoff of $600 \text{ m}^3 \text{ s}^{-1}$ and 74% above the 5-year-averaged monthly mean discharge in November (USGS, <http://www.usgs.gov>). The August and November cruises took place shortly after these prominent climatic events in the respective month, providing a marked contrast in hydrology, particularly on a basis of freshwater runoff and organic matter discharge.

Salinity, temperature, Chl *a* concentration ([Chl *a*]), and k_d are shown in Table 1. Salinity varied from 0.50 to 31.2 in August and from 0.10 to 30.0 in November. The surface water temperature along the estuary remained relatively constant in both August (range: 27.6-29.5°C, excluding Sta. A26-28) and November (range: 9.4-11.6°C). Sta. A26, A27 and A28 were exceptions having lower temperature (22.7-25.3°C) amongst all August stations; these three stations were located at or outside the mouth of the estuary and hence strongly impacted by the Atlantic seawater. The mean surface water temperature in August ($27.9 \pm 1.1^\circ\text{C}$, excluding Sta. A28) was nearly three times that in November ($10.2 \pm 0.7^\circ\text{C}$). [Chl *a*] ranged from 3.67 to $13.50 \mu\text{g L}^{-1}$ in August and from 1.66 to $4.25 \mu\text{g L}^{-1}$ in November. The mean [Chl *a*] in August was about 3.5 times that in November ($7.90 \mu\text{g L}^{-1}$ vs. $2.33 \mu\text{g L}^{-1}$), consistent with a previous study (Sharp et al., 2009). k_d in August generally

decreased seaward, ranging from 0.42 m^{-1} to 3.72 m^{-1} with the maximum and minimum located at Sta. A4 and Sta. A26, respectively. In November, k_d followed a similar trend but was much higher (Table 1) due to a higher abundance of particles and CDOM (see section 3.2 and 3.3). The TMZ, as characterized by k_d occurred around Sta. A4 in August and around Sta. N2-N5 in November (upper-TMZ herein), respectively. In both August and November, a weak TMZ occurred in the middle estuary (around Sta. A14-16 and Sta. N11) (mid-TMZ herein), with relative higher k_d . The measured cruise-mean solar radiation (290-600 nm) (7:30-17:00) in August was about twice that in November (1126 W m^{-2} vs. 460 W m^{-2}).

5.3.2 Absorption coefficient of CDOM

The absorption coefficient of CDOM at 412 nm ($a_{cdom,412}$) ranged from 0.27 m^{-1} to 1.31 m^{-1} during the August cruise with the maximum located at Sta. A11 and the minimum at the outermost station A28 (Fig. 5-2A). Notably, the maximum $a_{cdom,412}$ occurred downstream of the upper-TMZ. This could be attributed to the adsorption of CDOM onto the surface of particles during mixing and flocculation in the upper-TMZ and then partial release of the adsorbed CDOM seaward of the upper-TMZ. In November, $a_{cdom,412}$ generally decreased from land to sea, ranging from 0.37 m^{-1} to 3.24 m^{-1} with the maximum and minimum observed at the innermost and outermost stations, N1 and N23, respectively (Fig. 5-2B). Compared with the conservative mixing line, the $a_{cdom,412}$ versus salinity relationship was characterized by a convex curve in August but a concave one in November (Fig. 5-2). The different distribution patterns suggested that there was a net input of CDOM within the freshwater-saltwater transitional zone in August but a net loss of CDOM in November. The linear correlation between $a_{cdom,412}$ and salinity seaward from Sta. A16 in August ($R^2 = 0.97$, $p < 0.0001$, $n = 13$) (Fig. 5-2A) suggested the main factor controlling the behavior of CDOM in this region was dilution by seawater during estuarine mixing and the net input of CDOM mainly took place in the upper estuary, especially in the upper-TMZ. At salinity <

5, $a_{cdom,412}$ in November was almost twice that in August, concurring with the very low runoff in the summer and the extraordinarily high freshwater discharge linked to storm Sandy in the fall (see Section 5.3.1). At salinity > 10 , the abundance of CDOM was comparable for the two cruises, which was consistent with the net addition of CDOM in August and the net removal in November during estuarine mixing.

The spectral slope coefficient over the wavelength interval of 275-295 nm, $S_{275-295}$, has been demonstrated to be a good indicator of the origin of CDOM in estuarine and coastal waters. Small $S_{275-295}$ values generally imply the dominance of terrigenous CDOM while large $S_{275-295}$ values are often associated with CDOM of marine origin (Helms et al., 2008; Fichot and Benner, 2012). In the present study, $S_{275-295}$ ranged from 0.0174 to 0.0225 nm^{-1} in August and from 0.0134 to 0.0210 nm^{-1} in November. The $S_{275-295}$ in November was relatively lower than that in August at the same salinity, suggesting a higher fraction of terrigenous CDOM in the fall likely associated with the freshet of storm Sandy. In both seasons, $S_{275-295}$ increased with salinity; the estuarine mixing behavior of $S_{275-295}$, however, differed between the two seasons. The measured $S_{275-295}$ in August was generally slightly lower than that expected from the conservative mixing line (dashed line) (Fig. 5-3A), whereas the measured $S_{275-295}$ in November was typically well above the mixing line (Fig. 5-3B). Hence, there was a small net addition of terrigenous CDOM in August and a relatively large net loss of the land-derived CDOM in November across the freshwater-saltwater transitional zone. However, $S_{275-295}$ in August seaward from Sta. A16 generally followed the conservative mixing line with Sta. A16 and Sta. A28 as the low-salinity and high-salinity end members, respectively (solid line) (Fig. 5-3A). Therefore, the addition could arise primarily from CDOM leached from particles around the upper-TMZ. The loss in November could mainly be ascribed to adsorption of terrigenous CDOM onto particles, given the high turbidity (see Section 5.3.3).

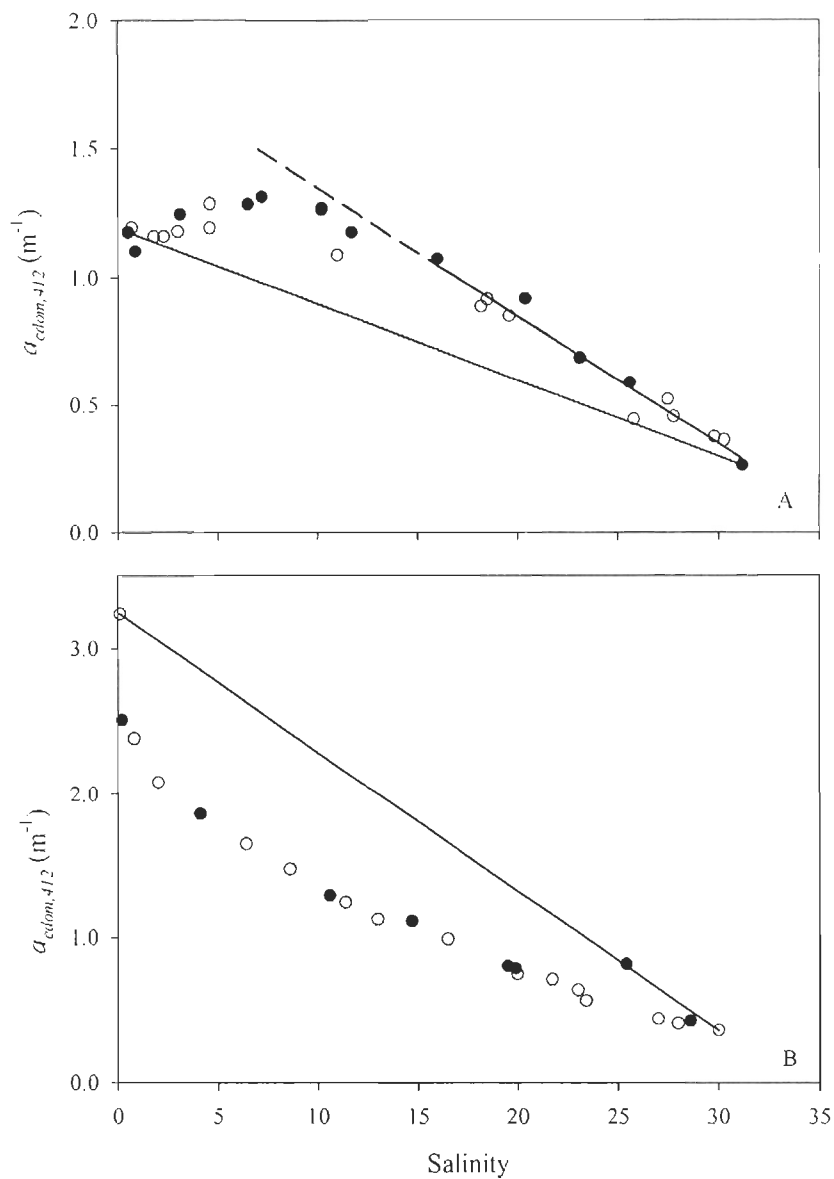


Fig. 5-2 Measured $a_{cdom,412}$ and ideal two end-member conservative mixing lines of August cruise (A) and November cruise (B). Filled points: CO photoproduction was also conducted with these samples; empty points: other CDOM samples; straight line from salinity ~ 0 : conservative mixing model line. In panel A, the straight line from salinity 16.0 to 31.2 is the linearly regressed line and the dashed line is extrapolated according to the regressed function.

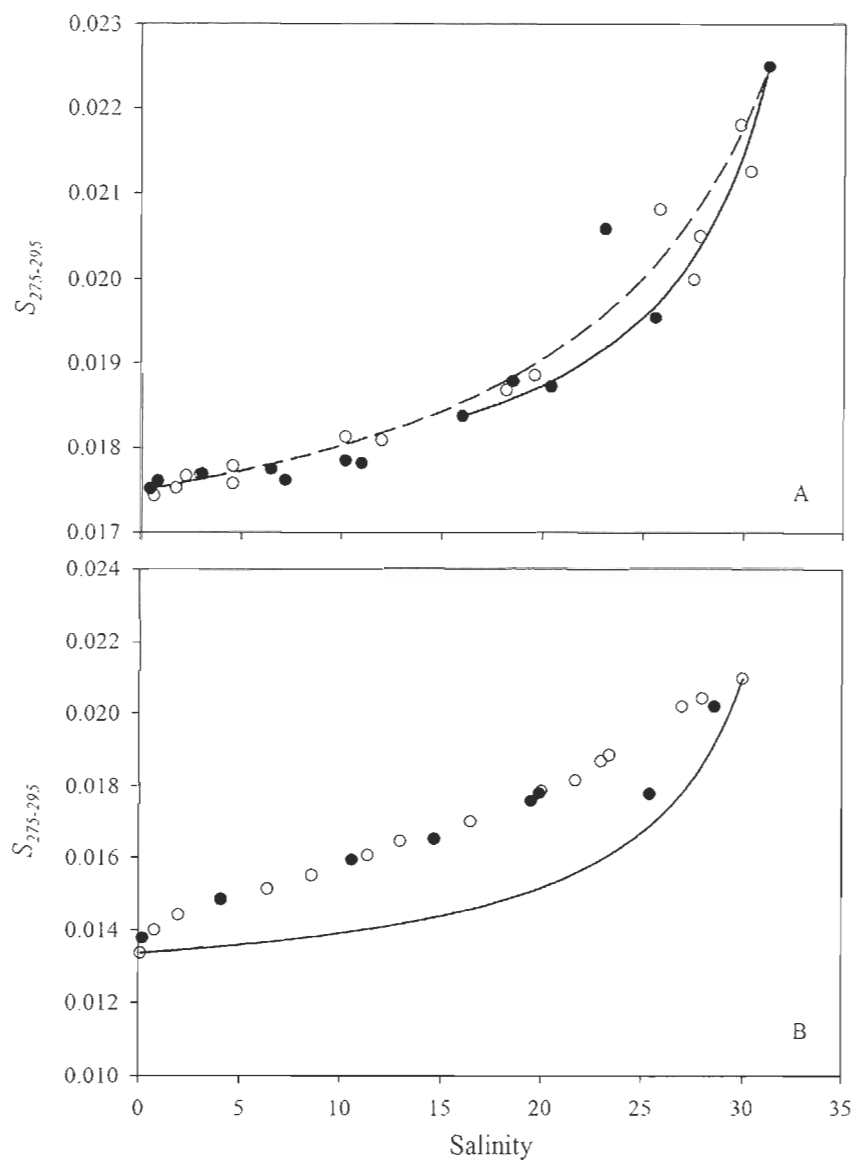


Fig. 5-3 Actual $S_{275-295}$ and ideal two end-member conservative mixing lines of August cruise (A) and November cruise (B). Filled points: CO photoproduction was also conducted with these samples; empty points: other CDOM samples; line: conservative mixing model line. In panel A: the dashed line is the mixing model line for all samples and the solid line is the mixing model line for samples from Sta. A16 to Sta. A28 (salinity 16.0-31.2).

5.3.3 Absorption coefficient of particles

Herein the particulate absorption coefficients (412 nm) of the fractions of $<20 \mu\text{m}$, $10\text{-}20 \mu\text{m}$ and $<10 \mu\text{m}$ are designated as $a_{p<20,412}$, $a_{p,10-20,412}$ and $a_{p<10,412}$, respectively. In August, the overall trend of decreasing $a_{p<20,412}$ with salinity were overlaid with two maxima of $a_{p<20,412}$, one at Sta. A7 and the other at Sta. A16 (Fig. 5-4A). The patterns of $a_{p,10-20,412}$ and $a_{p<10,412}$ vs. salinity were similar to that of $a_{p<20,412}$; some features observed for $a_{p<20,412}$, including the maximum at Sta. A16, were difficult to assess for $a_{p,10-20,412}$ and $a_{p<10,412}$ due to the lack of sampling for $a_{p<10,412}$ at certain locations (Fig. 5-4A). In November, both $a_{p<20,412}$ and $a_{p<10,412}$ decreased from land to sea, excepting a pronounced peak at Sta. N11 where the relative higher k_d was found; the mid-estuary peak was, however, absent for $a_{p,10-20,412}$ (Fig. 5-4B). The high particulate absorption coefficients in the upper- and mid-TMZ should mainly result from sediment resuspension and flocculation of particles during mixing of freshwater with seawater. Along the other sections of the estuary, sedimentation and biological and photochemical degradation of particulate matter could be the overarching factors controlling a_p . The ratio of $a_{p<10,412}$ to $a_{p<20,412}$ ranged from 0.63 to 0.80 in August and from 0.62 to 0.93 in November, indicating that the colored particulate matter was dominated by the $<10\text{-}\mu\text{m}$ fraction during both cruises. The ratio of a_{phy} at 412 nm ($a_{phy,412}$) to $a_{p,412}$ ($a_{phy,412}:a_{p,412}$) for the $<20\text{-}\mu\text{m}$ fraction generally increased seaward, ranging from 0.08 to 0.56 (mean: 0.30) in August and from 0.03 to 0.29 (mean: 0.11) in November. The size fractions of $<10 \mu\text{m}$ and $10\text{-}20 \mu\text{m}$ exhibited $a_{phy,412}:a_{p,412}$ ratios comparable to those for the $<20\text{-}\mu\text{m}$ fraction. The ratio of a_{cdom} to $a_{p<20}$ at 412 nm ranged from 0.5 to 2.2 (mean: 1.2) in August and from 0.4 to 1.2 (mean: 0.8) in November. However, a_{cdom} was often higher than $a_{p<20}$ at shorter wavelengths, particularly in the UV-B band. Therefore, particulate absorption prevailed over CDOM absorption in the visible regime while the dominance inverted at the UV wavelengths.

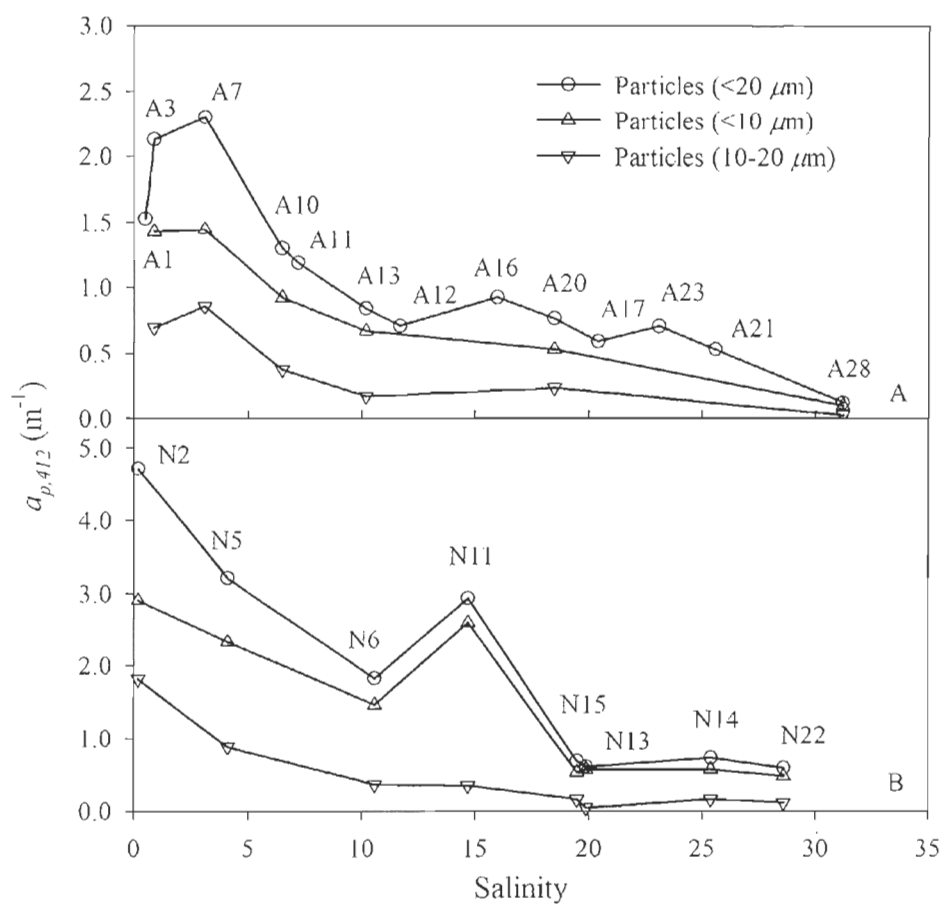


Fig. 5-4 The distributions of $a_{p,412}$ of different size ($<20 \mu\text{m}$, $<10 \mu\text{m}$ and $10-20 \mu\text{m}$) along with salinity for August cruise (A) and November cruise (B).

5.3.4 Absorption coefficient of particles

The fitted parameters, m_1 and m_2 , in Eq. 5-4 are shown in Table 5-2. The shapes of CO AQY spectra are dictated by m_2 with smaller values giving flatter AQY spectra and hence slower decreases in AQY with increasing wavelength. The m_2 value varied considerably among different stations for all three size fractions (Table 5-2). In August, m_2 for Φ_{cdom} showed a negative correlation with salinity ($R^2 = 0.57$, $p = 0.003$), indicating that the AQY spectrum became flatter seaward. This trend opposes those observed in the St. Lawrence estuary (Zhang et al., 2006), the Mackenzie estuary (Xie et al., 2009), and the Delaware estuary by a previous study (White et al., 2010). CDOM in these earlier studies all behaved conservatively, which contrasts with the non-conservative behavior found in the present study. The newly added CDOM, which was of primarily terrigenous origin, during estuarine mixing in August (see Section 5.3.2) likely contained CO precursors that were relatively more photoreactive at the visible wavelengths than those in the CDOM transported down from upstream. In November, m_2 for Φ_{cdom} was positively, albeit weakly, correlated to salinity ($R^2 = 0.41$, $p = 0.089$), consistent with the removal of the photoreactive terrigenous CDOM across the estuarine mixing zone. The m_2 values for $\Phi_{<10,\lambda}$ and $\Phi_{<20,\lambda}$ were not significantly correlated to salinity in both seasons, suggestive of more complicated mechanisms that controlled CO photoproduction from particles (Song et al., 2013). The mean value of m_2 for Φ_{cdom} (0.0082 nm^{-1}) in August was only marginally higher than those for $\Phi_{<10}$ (0.0073 nm^{-1}) and $\Phi_{<20}$ (0.0078 nm^{-1}). In November, the mean value of m_2 for Φ_{cdom} (0.0102 nm^{-1}) was, however, 31% higher than that for $\Phi_{<10}$ (0.0078 nm^{-1}) and 65% higher than that for $\Phi_{<20}$ (0.0062 nm^{-1}). Between the $<10\text{-}\mu\text{m}$ and $<20\text{-}\mu\text{m}$ fractions, the mean value of m_2 for $\Phi_{<10}$ was comparable to that for $\Phi_{<20}$ in August, whereas the former was 26% larger than the latter in November. Seasonally, the mean value of m_2 for $\Phi_{<10}$ in August was similar to that in November while the m_2 values for Φ_{cdom} and $\Phi_{<20}$ in August were on average 19% smaller and 26% larger than the respective counterparts in November.

These m_2 distributional patterns, combined with m_1 in Eq. 5-4 (Table 5-2), gave rise to several notable features in the relationships between the three size fractions in terms of the cruise-mean CO AQY spectra. In August, the Φ_{cdom} spectrum lay far above those of $\Phi_{<10}$ and $\Phi_{<20}$ throughout the wavelengths of interest (290-600 nm) (Fig. 5-5A); Φ_{cdom} in November, however, intersected $\Phi_{<10}$ and $\Phi_{<20}$ at the short visible wavelengths (< 480 nm), leading to the former being superior to the latter in the UV but inferior in the main domain of the visible (Fig. 5-5B). In November, $\Phi_{<10}$ and $\Phi_{<20}$ crossed each other as well, whereas in August the difference between the two was much smaller (Fig. 5-5A). Seasonally, Φ_{cdom} in November surpassed that in August across most of the UV and visible regimes but the two progressively converged with increasing wavelength (Fig. 5-5C). Both $\Phi_{<10}$ and $\Phi_{<20}$ were substantially larger in November than in August but the $\Phi_{<20}$ spectra diverged from short to long wavelengths (Fig. 5-5D).

Comparison of CO AQY spectra from this study with those in the literature is shown in Fig. 5-6. Referenced to salinity, our Φ_{cdom} spectra are the flattest ever reported, including the spectra of two brackish samples from the Delaware estuary determined by White et al. (2010) (Fig. 5-6A). The exceptions are the spectrum for a previous Delaware estuary sample having a salinity of 0.1 (White et al., 2010) and the mean spectra published by Valentine and Zepp (1993), which display increasing AQY with wavelength in the visible. The unusually flat Φ_{cdom} spectra observed in the present study was likely linked to the addition of new CDOM during estuarine mixing in August and to the large amounts of fresh terrigenous CDOM brought into the estuary by storm Sandy in November. If the dry weather condition in August proves to be the primary cause of the non-conservative behavior of CDOM, our results provide a good example of how extreme weather events could affect the photochemical property of CDOM and its biogeochemical significance. Because of the scarcity of CO AQY spectra of particle-containing samples, comparison with prior studies is possible only for the Mackenzie estuary in the western Canadian Arctic (Song et al., 2013). The $\Phi_{<20}$ spectra for the Delaware estuary are much flatter than the spectra of whole water samples from the Mackenzie estuary; quantitatively, the former also well exceed the latter at the UV-A and visible wavelengths (Fig. 5-6B). Hence, POM in the

Delaware estuary appears more photoreactive and/or photoreactive metals (e.g. Fe, Cu, Mn) on minerals in the Delaware estuary are richer and/or in more reactive forms such as MnO_2 and Fe (III) (Sunda et al., 1983; Barbeau et al, 2001).

Table 5-2 Fitted parameters for function $\Phi_\lambda = m_1 \times \exp(m_2 \times (\lambda - 290))$ for 0.2-, 10- and 20- μm filtered water samples and the values of Φ_{330} and $\bar{\Phi}$. nd means no data.

| Station | 0.2- μm filtered samples | | | | 10- μm filtered samples | | | | 20- μm filtered samples | | | |
|---------|-------------------------------------|--------|-----------------------------------|-----------------------------------|------------------------------------|--------|-----------------------------------|-----------------------------------|------------------------------------|--------|-----------------------------------|-----------------------------------|
| | m_1 ($\times 10^6$) | $-m_2$ | Φ_{330} ($\times 10^6$) | $\bar{\Phi}$ ($\times 10^6$) | m_1 ($\times 10^6$) | $-m_2$ | Φ_{330} ($\times 10^6$) | $\bar{\Phi}$ ($\times 10^6$) | m_1 ($\times 10^6$) | $-m_2$ | Φ_{330} ($\times 10^6$) | $\bar{\Phi}$ ($\times 10^6$) |
| | August | | | | | | | | | | | |
| A1 | 44.1 | 0.0124 | 26.9 | 5.68 | | nd | | | 27.0 | 0.0112 | 17.3 | 4.08 |
| A3 | 32.6 | 0.0104 | 21.5 | 5.48 | 15.7 | 0.0078 | 11.5 | 3.91 | 12.7 | 0.0073 | 9.49 | 3.45 |
| A7 | 25.7 | 0.0087 | 18.1 | 5.56 | 17.3 | 0.0102 | 11.5 | 3.02 | 13.4 | 0.0068 | 10.2 | 3.93 |
| A10 | 26.0 | 0.0115 | 16.5 | 3.78 | 19.1 | 0.0110 | 12.3 | 2.95 | 17.8 | 0.0106 | 11.6 | 2.91 |
| A11 | 33.1 | 0.0111 | 21.3 | 5.10 | | nd | | | 23.7 | 0.0095 | 16.2 | 4.54 |
| A12 | 16.3 | 0.0062 | 12.7 | 5.28 | | nd | | | 15.6 | 0.0084 | 11.2 | 3.57 |
| A13 | 17.2 | 0.0067 | 13.1 | 5.12 | 12.7 | 0.0059 | 10.0 | 4.32 | 11.2 | 0.0051 | 9.15 | 4.38 |
| A16 | 25.9 | 0.0052 | 21.1 | 9.97 | | nd | | | 24.2 | 0.0074 | 18.0 | 6.46 |
| A17 | 36.8 | 0.0091 | 25.6 | 7.50 | | nd | | | 28.1 | 0.0082 | 20.3 | 6.62 |
| A20 | 32.6 | 0.0084 | 23.3 | 7.39 | 27.4 | 0.0089 | 19.2 | 5.81 | 23.9 | 0.0083 | 17.1 | 5.49 |
| A21 | 21.8 | 0.0054 | 17.5 | 8.00 | | nd | | | 20.5 | 0.0072 | 15.3 | 5.62 |
| A23 | 16.6 | 0.0070 | 12.6 | 4.73 | | nd | | | 14.4 | 0.0088 | 10.2 | 3.09 |
| A28 | 17.2 | 0.0044 | 14.5 | 7.64 | 9.92 | 0.0001 | 9.86 | 9.64 | 12.3 | 0.0022 | 11.2 | 7.98 |
| mean | 26.6 | 0.0082 | 18.8 | 6.24 | 17.0 | 0.0073 | 12.4 | 4.94 | 18.8 | 0.0078 | 13.6 | 4.78 |
| s.d. | 8.8 | 0.0026 | 4.9 | 1.7 | 6.0 | 0.0040 | 3.5 | 2.5 | 6.0 | 0.0023 | 3.8 | 1.6 |

| Station | 0.2- μm filtered samples | | | | 10- μm filtered samples | | | | 20- μm filtered samples | | | |
|---------|-------------------------------------|--------|-----------------------------------|-----------------------------------|------------------------------------|--------|-----------------------------------|-----------------------------------|------------------------------------|--------|-----------------------------------|-----------------------------------|
| | m_1 ($\times 10^6$) | $-m_2$ | Φ_{330} ($\times 10^6$) | $\bar{\Phi}$ ($\times 10_6$) | m_1 ($\times 10^6$) | $-m_2$ | Φ_{330} ($\times 10^6$) | $\bar{\Phi}$ ($\times 10_6$) | m_1 ($\times 10^6$) | $-m_2$ | Φ_{330} ($\times 10^6$) | $\bar{\Phi}$ ($\times 10_6$) |
| | November | | | | | | | | | | | |
| N2 | 35.6 | 0.0079 | 25.9 | 8.72 | 20.7 | 0.0067 | 15.8 | 6.10 | 14.2 | 0.0046 | 11.9 | 6.11 |
| N5 | 46.4 | 0.0097 | 31.4 | 8.62 | 24.2 | 0.0073 | 18.1 | 6.54 | 18.1 | 0.0062 | 14.2 | 5.88 |
| N6 | 36.4 | 0.0077 | 26.8 | 9.24 | 33.4 | 0.0092 | 23.2 | 6.77 | 28.7 | 0.0076 | 21.3 | 7.41 |
| N11 | 73.7 | 0.0098 | 49.9 | 13.6 | 41.8 | 0.0064 | 32.2 | 12.9 | 38.4 | 0.0046 | 31.9 | 16.2 |
| N13 | 53.6 | 0.0134 | 31.3 | 6.00 | 29.1 | 0.0085 | 20.7 | 6.53 | 25.7 | 0.0069 | 19.5 | 7.34 |
| N14 | 34.0 | 0.0110 | 21.9 | 5.29 | 30.3 | 0.0096 | 20.6 | 5.70 | 26.0 | 0.0084 | 18.6 | 5.92 |
| N15 | 45.2 | 0.0115 | 28.4 | 6.49 | 33.9 | 0.0090 | 23.6 | 6.98 | 28.8 | 0.0078 | 21.3 | 7.24 |
| N22 | 34.7 | 0.0104 | 22.9 | 5.84 | 15.5 | 0.0054 | 12.5 | 5.75 | 12.8 | 0.0031 | 11.2 | 7.01 |
| mean | 45.0 | 0.0102 | 29.8 | 7.98 | 28.6 | 0.0078 | 20.8 | 7.16 | 24.1 | 0.0062 | 18.7 | 7.89 |
| s.d. | 13.6 | 0.0019 | 8.8 | 2.7 | 8.3 | 0.0015 | 5.9 | 2.4 | 8.6 | 0.0019 | 6.7 | 3.4 |

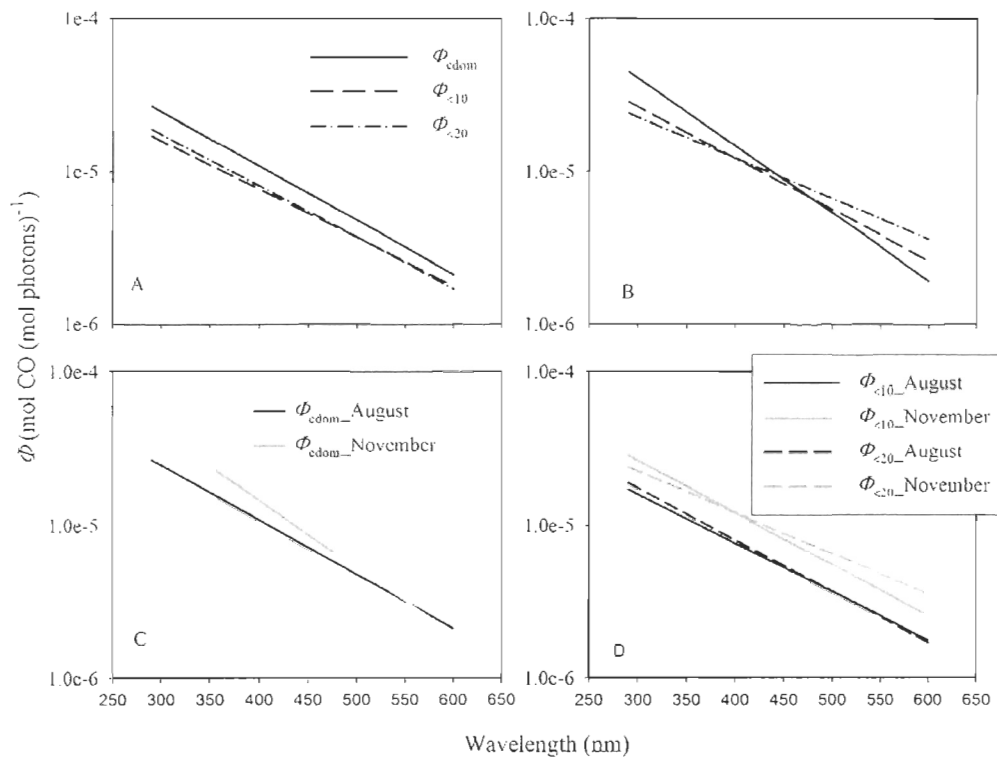


Fig.5-5 $\phi_{\text{cdom},\lambda}$, $\phi_{<10,\lambda}$ and $\phi_{<20,\lambda}$ spectra for August cruise (A) and November cruise (B) and seasonal comparison of $\phi_{\text{cdom},\lambda}$ (C), $\phi_{<10,\lambda}$ and $\phi_{<20,\lambda}$ (D).

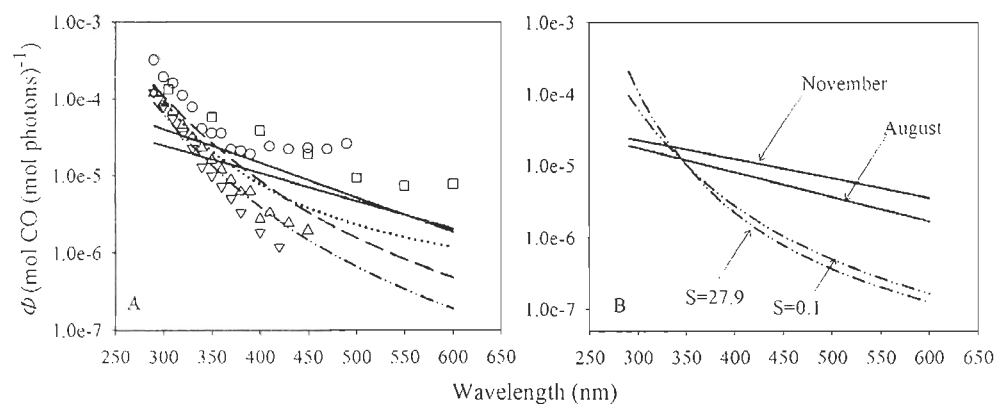


Fig. 5-6 Comparison of typical $\Phi_{\text{cdom},\lambda}$ (A) and $\Phi_{<20,\lambda}$ (B) spectra in this study with $\Phi_{\text{cdom},\lambda}$ and $\Phi_{i,\lambda}$ spectra published in other studies. Solid lines denote the spectra obtained in this study. In panel A: open square denotes the mean spectra published by Valentine and Zepp (1993); open circle (S=0.1), up triangle (S=13), down triangle (S=21), Delaware Estuary (White et al., 2010); dashed line: St. Lawrence Estuary, S=0 (Zhang et al., 2006), dotted line: Mackenzie Estuary, S=0.1 (Xie et al., 2009); dashed-dotted line: Mackenzie Estuary, S=27.9 (Song et al., 2013). For the data in the St. Lawrence Estuary and Mackenzie Estuary mentioned in panel A are the highest values at long wavelengths in the studies of Zhang et al. (2006), Xie et al. (2009) and Song et al. (2013). In panel B, $\Phi_{i,\lambda}$ with the lowest and highest salinities (0.1 vs. 27.9) are mentioned.

5.3.5 $\bar{\Phi}$ and photoreactivity

The eye-catching feature of the along-estuary distribution of $\bar{\Phi}$ was the highly elevated $\bar{\Phi}_{\text{cdom}}$, $\bar{\Phi}_{<10}$ and $\bar{\Phi}_{<20}$ in the mid estuary (salinity ~ 15 , $\bar{\Phi}_{\text{cdom}}$ only in August) (Fig. 5-7). Zhang et al. (2006) reported a similar enhancement of CDOM-based CO AQY in the TMZ of the St. Lawrence estuary. The mechanisms behind this type of enhancement are unclear but were likely related to intense mixing dynamics and elevated particulate loads in the TMZ. Leaching of DOM from POM, which is accelerated by mixing, is well known (Shank et al., 2010). Production of DOM from photodissolution of POM is also quantitatively significant, particularly in particle-laden waters (Estepa et al., 2012a). The “new” CDOM generated from these processes could be more photoreactive compared to CDOM either upstream or downstream of the TMZs. Alternatively, various physicochemical processes such as salinity and pH shifts, coupled with strong turbulence, might increase the concentrations of dissolved photoreactive metals and/or changed them into more reactive species. Resuspended particles could be more photoreactive and/or flocculation and coagulation, often prevalent in TMZs, might enrich photoreactive metals in coatings on particles (Robert et al., 2004), leading to the spiked $\bar{\Phi}_{<10}$ and $\bar{\Phi}_{<20}$ in the November mid-TMZ.

In August, $\bar{\Phi}_{\text{cdom}}$ was higher than $\bar{\Phi}_{<10}$ and $\bar{\Phi}_{<20}$ along the estuary, except at Sta. A28 (Fig. 5-7A), while $\bar{\Phi}_{<10}$ was generally similar to its corresponding $\bar{\Phi}_{<20}$. $\bar{\Phi}_{\text{cdom}}$, $\bar{\Phi}_{<10}$ and $\bar{\Phi}_{<20}$ were fairly constant in the upper estuary, however, they fluctuated in the lower estuary, which was consistent with the discrete S275-295 in this region (Fig. 5-3A). The interrelations among $\bar{\Phi}_{\text{cdom}}$, $\bar{\Phi}_{<10}$ and $\bar{\Phi}_{<20}$ in the upper estuary in November were the same as those in August, whereas, in the lower estuary, $\bar{\Phi}_{\text{cdom}}$ was lower than $\bar{\Phi}_{<10}$ and $\bar{\Phi}_{<20}$, and $\bar{\Phi}_{<20}$ was marginally higher than the corresponding $\bar{\Phi}_{<10}$ (<10%). Seasonally, the overall results suggested $\bar{\Phi}_{\text{cdom}}$, $\bar{\Phi}_{<10}$ and $\bar{\Phi}_{<20}$ were higher in November than their counterparts in August, which was consistent with the relatively higher abundance of terrestrial CDOM along the estuary in November (see section 5.3.2). Furthermore, after the freshet of storm Sandy, the

concentrations of trace metals might be higher and the particles could be more photoreactive than in August.

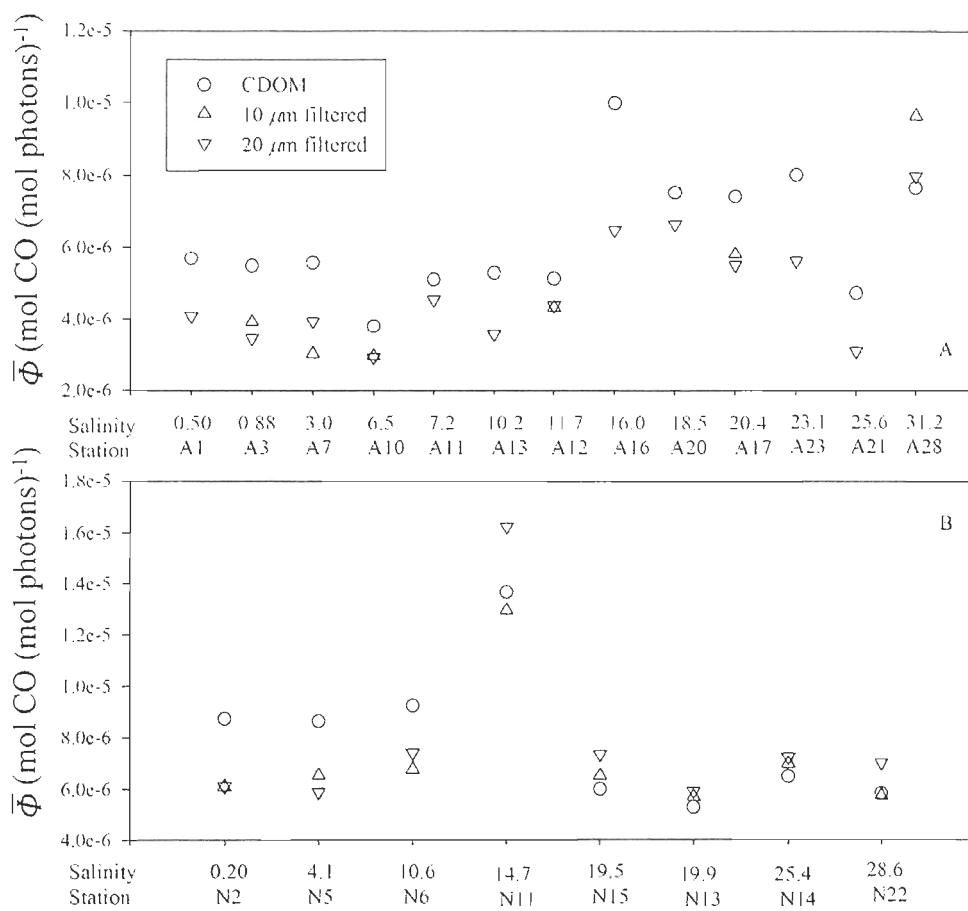


Fig. 5-7 $\bar{\Phi}_{cdom}$, $\bar{\Phi}_{<10}$ and $\bar{\Phi}_{<20}$ at each station for August cruise (A) and November cruise (B). Note that no $\bar{\Phi}_{<10}$ data are available for some stations for August cruise.

5.3.6 Action spectra of CO photoproduction

The action spectrum of CO photoproduction at the surface, $A_{0,\lambda}$ (mol CO m⁻³ h⁻¹ nm⁻¹), was calculated using Eq. (5-6),

$$A_{0,\lambda} = Q_{0,\lambda} \times a_{\lambda} \times \Phi_{\lambda} \quad (5-6)$$

where $Q_{0,\lambda}$ is the cruise mean of the daily averaged values of the measured spectral solar irradiance (7 am. to 7 pm. in August and 8 am. to 5 pm. in November) and a_{λ} and Φ_{λ} denote $a_{cdom,\lambda}$ and $\Phi_{cdom,\lambda}$ for CDOM, $a_{cdom,\lambda}$ plus $a_{p<10,\lambda}$ and $\Phi_{<10,\lambda}$ for 10 μm filtered samples and $a_{cdom,\lambda}$ plus $a_{p<20,\lambda}$ and $\Phi_{<20,\lambda}$ for 20 μm filtered samples. Consistent with the study of Song et al. (2013), the action spectra were characterized by a non-Gaussian style with the peak value at ~ 330 nm and a long tail in the visible (Fig. 5-8A, B). Averaged on all samples for both the August and November cruises, UVB (290-320 nm), UVA (320-400 nm) and the visible (400-600 nm) were, respectively, responsible for 6% (4% - 8%), 68% (62% - 74%) and 26% (19% - 33%) of CDOM's A_0 integrated over 290-600 nm. The contributions of UVB, UVA and visible light to the wavelength-integrated A_0 of the 10 μm filtered samples were 4% (3% - 6%), 59% (46% - 66%) and 36% (28% - 51%). For the 20 μm filtered samples, the contribution of each light regime was almost the same as that for the 10 μm filtered samples. The results suggested that UVA was mainly responsible for CO photoproduction, for both CDOM only and particle-containing samples, and moreover, for particle-containing samples, the relative contributions of UVB and UVA decreased while that of the visible to CO photoproduction increased during both cruises. No substantial inter-cruise differences were found in the contributions of UVB, UVA and visible to CO photoproduction for the 0.2 μm (i.e. CDOM only) and 10 μm filtered samples, whereas the importance of the visible was slightly higher for 20 μm filtered samples ($36\% \pm 5\%$ vs. $42\% \pm 7\%$) in November than that in August.

The depth-integrated action spectra of CO photoproduction in the photic layer, $A_{col,\lambda}$ (mol CO m⁻² h⁻¹ nm⁻¹), was computed using Eq. (5-7),

$$A_{col,\lambda} = Q_{0,\lambda} \times (a_{\lambda}/a_{t,\lambda}) \times \Phi_{\lambda} \quad (5-7)$$

where $a_{t,\lambda}$ is the total absorption coefficient. However, the absorption spectra of the particles removed by the 20 μm Nylon mesh (i.e., $> 20 \mu\text{m}$) were unknown. Thus this part was ignored and $a_{t,\lambda}$ was the sum of $a_{w,\lambda}$, $a_{cdom,\lambda}$ and $a_{p<20,\lambda}$. So the $A_{col,\lambda}$ spectra of CDOM and 10- and 20- μm filtered samples were overestimated at all wavelengths, with unknown uncertainties for the relative contributions of UVB, UVA and visible to CO photoproduction. Similar to the surface action spectra, the peak-response wavelength of the depth-integrated action spectra of CDOM also presented at 330 nm, but with a wide band in UVA regime. Furthermore, the tails in the long wavelengths were relatively higher (Fig. 5-8C, D). Different from $A_{col,\lambda}$ of CDOM, the $A_{col,\lambda}$ spectra of the 10 μm and 20 μm filtered samples were characterized by two joined shoulders over the 400-450 nm and 450-500 nm wavelength ranges, echoing the two broad elevations in the solar irradiance spectra within the same wavelength bands. This features was also present in the $A_{col,\lambda}$ spectra of particles in the deep chlorophyll maximum in Mackenzie Shelf and Canada Basin (Song et al., 2013). UVB, UVA and visible contributed, averaged for the two cruises, 2% (1% - 3%), 42% (34% - 50%) and 56% (47% - 65%) to the integrated A_{col} of CDOM, respectively. Like surface action spectra, the relative contributions of UVB, UVA and visible to CO photoproduction for 10 μm and 20 μm filtered samples were almost the same, with the values of 1% (1% - 2%), 29% (19% - 38%) and 70% (69% - 81%), respectively. Compared to the surface action spectra, visible was more important on a depth-integrated basis, especially for particle-containing samples. Furthermore, visible light was the main contributor to the depth-integrated CO photoproduction, which differed from the results in the Mackenzie Estuary and Shelf (Song et al., 2013).

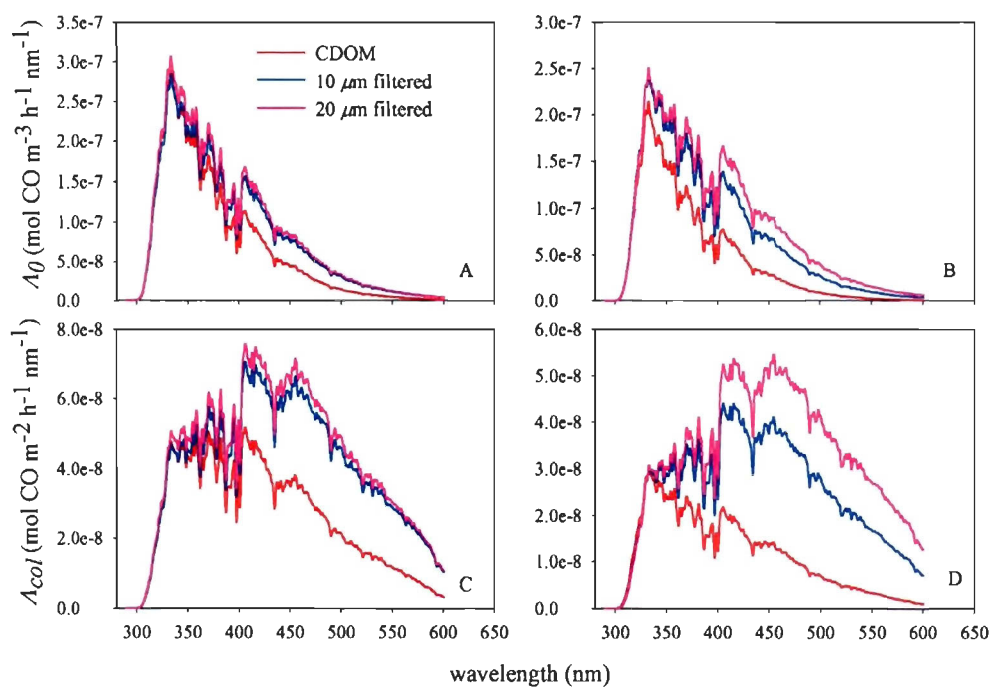


Fig. 5-8 Surface CO action spectra for August (A) and November (B), and depth-integrated CO action spectra for August (C) and November (D).

5.3.7 Modeling CO photoproduction

CO photoproduction rates at the surface (0 m), P_0 ($\mu\text{mol CO m}^{-3} \text{ d}^{-1}$), and in the euphotic zone (depth-integrated), P_{col} ($\mu\text{mol CO m}^{-2} \text{ d}^{-1}$), were calculated using Eqs. (5-8) and (5-9), respectively,

$$P_0 = \int_{290}^{600} Q_{0-\lambda} \times a_{\lambda} \times \Phi_{\lambda} \times d\lambda \quad (5-8)$$

$$P_{col} = \int_{290}^{600} Q_{d0-\lambda} \times (a_{\lambda}/a_{t,\lambda}) \times \Phi_{\lambda} \times d\lambda \quad (5-9)$$

P_0 stands for $P_{cdom,0}$, $P_{<10,0}$ and $P_{<20,0}$, P_{col} for $P_{cdom,col}$, $P_{<10,col}$ and $P_{<20,col}$, a_{λ} for $a_{cdom,\lambda}$ and $a_{cdom,\lambda}$ plus $a_{p<10,\lambda}$, and $a_{cdom,\lambda}$ plus $a_{p<20,\lambda}$ and Φ_{λ} for $\Phi_{cdom,\lambda}$, $\Phi_{<10,\lambda}$ and $\Phi_{<20,\lambda}$ for CDOM only and 10 μm filtered samples and 20 μm filtered samples, respectively. $Q_{0-\lambda}$ is the scalar photon flux just beneath the surface ($\text{mol photons m}^{-2} \text{ d}^{-1} \text{ nm}^{-1}$) and $a_{t,\lambda}$ the sum of $a_{cdom,\lambda}$, $a_{p,\lambda}$, and $a_{w,\lambda}$ (particles $> 20 \mu\text{m}$ are ignored). $Q_{0-\lambda}$ was estimated as 1.3 times the downwelling photon flux ($Q_{d0-\lambda}$) (Gordon 1989). $Q_{d0-\lambda}$ was simulated using the Santa Barbara DISORT Atmospheric Radiative Transfer (SBDART) software developed by Ricchiuzzi et al. (1998) at 3 h intervals, taking into account of the cloud cover and ozone conditions, which were obtained from the International Satellite Cloud Climatology Project (ISCCP, <http://isccp.giss.nasa.gov/products/browsed2.html>). More details were published in Song et al. (2013).

P_0 and P_{col} for each treatment of the samples in August and November were shown in Table 4-3. In August, the mean values of $P_{cdom,0}$, $P_{<10,0}$ and $P_{<20,0}$ were $264 \pm 94.8 \mu\text{mol m}^{-3} \text{ d}^{-1}$, $285 \pm 107 \mu\text{mol m}^{-3} \text{ d}^{-1}$ and $337 \pm 129 \mu\text{mol m}^{-3} \text{ d}^{-1}$, respectively. The maxima of $P_{cdom,0}$, $P_{<10,0}$ and $P_{<20,0}$ located at the innermost station (Sta. A1) (no data was available for $P_{<10,0}$ at Sta. A1) and the minima at the outermost station (Sta. A28), respectively. The contribution of particles $< 20 \mu\text{m}$ to total CO photoproduction at the surface ranged from 14% to 36% (Table 5-4), with the minima occurring at Sta. A13 and Sta. A20 and the maximum at Sta. A7. Smaller-sized particles ($< 10 \mu\text{m}$) contributed 8% to 15% to CO total photoproduction,

while the larger-sized particles (10-20 μm) contributed 3% - 28%. In most cases, smaller-sized particles accounted for more CO photoproduction than larger-sized (mean: 13% vs. 5%), except at Sta. A7, where the contribution of the larger-sized particles far exceeded that of the smaller-sized particles (28% vs. 8%). This might be attributed to the higher CO photoproduction efficiency of the larger-sized particles (i.e. $\bar{\Phi}_{<20} > \bar{\Phi}_{<10}$) and the largest $a_{p<20,412}$: $a_{p<10,412}$ at this station. $P_{cdom,col}$, $P_{<10,col}$ and $P_{<20,col}$ fluctuated along the estuary in August, with the mean values of $139 \pm 44.8 \mu\text{mol m}^{-2} \text{d}^{-1}$, $181 \pm 71.7 \mu\text{mol m}^{-2} \text{d}^{-1}$ and $220 \pm 60.7 \mu\text{mol m}^{-2} \text{d}^{-1}$, respectively. The contributions of particles to total depth-integrated CO photoproduction ranged from 29%-55% (Table 5-4), higher than those at the surface. Furthermore, smaller-sized particles were relative more important than larger-sized particles, except at Sta. A7, similar to that of P_0 . At the outermost station, Sta. A28, smaller-sized particles accounted for 39% of total CO photoproduction, while the contribution of larger-sized particles was negligible (2%), consistent with the dominance 80% of the smaller-sized particles in the particle absorption with the size of $< 20 \mu\text{m}$.

In November, the averaged $P_{cdom,0}$, $P_{<10,0}$ and $P_{<20,0}$ were $150 \pm 91 \mu\text{mol m}^{-3} \text{d}^{-1}$, $226 \pm 155 \mu\text{mol m}^{-3} \text{d}^{-1}$ and $254 \pm 187 \mu\text{mol m}^{-3} \text{d}^{-1}$, respectively. The maximum and minimum $P_{cdom,0}$ were also located at the innermost and outermost stations (i.e., Sta. N1 and Sta. N22), respectively. And the minima of $P_{<10,0}$ and $P_{<20,0}$ were both located at Sta. N22. Different from the results in August, the maxima of $P_{<10,0}$ and $P_{<20,0}$ in November, presented at Sta. N11 in the mid-TMZ where the particle absorption also peaked. The mean values of $P_{cdom,col}$, $P_{<10,col}$ and $P_{<20,col}$ were $49.1 \pm 7.3 \mu\text{mol m}^{-2} \text{d}^{-1}$, $96.3 \pm 36.9 \mu\text{mol m}^{-2} \text{d}^{-1}$ and $120 \pm 53.1 \mu\text{mol m}^{-2} \text{d}^{-1}$, with the maxima all located at Sta. N11 in the mid-TMZ and the minima located at Sta. N22, N1 and N14. Particles ($<20 \mu\text{m}$) contributed 24% - 62% to total CO photoproduction at the surface, and 48% - 77% in the water column (Table 5-4). The results suggest that in this highly turbid estuary, the importance of particles photochemistry can exceed that of the dissolved phase, agreeing with the result of Estapa et al. (2012a), which concluded DOC photoproduction from particles in highly turbid estuarine and coastal waters could surpass the photolysis of DOC. At all the stations, the smaller-sized particles produced more CO than did larger-sized particles both at the surface and in the water

column, except at Sta. N1, where the CO production rates from the two fractions of particles were similar in the water column. Due to the lower solar irradiance and shorter solar duration in November, the mean values of both P_0 and P_{col} were lower than those in August, especially for CDOM and the depth-integrated term. The higher abundance of particles in November, however, led to a higher percent contribution of particles to total CO photoproduction.

The contributions of particles to total CO photoproduction obtained by this and earlier studies are compiled in Table 4. Both the $P_{p,0}:P_{t,0}$ and $P_{p,col}:P_{t,col}$ in this study were in the ranges of previous studies (Xie and Zafiriou, 2009; Stubbins et al., 2011; Song et al., 2013). The results reported in the above references were collected in different seasons and carried out with different methods. Specially, CO photoproduction from particles in the Tyne Estuary was estimated based on the assumption that $\Phi_{p,\lambda}$ was the same as $\Phi_{cdom,\lambda}$. However, terrigenous particles are less photoreactive in terms of CO photoproduction than terrigenous CDOM (Song et al., 2013). Hence, the ratio of $P_{p,col}:P_{t,col}$ could be somewhat overestimated in the Tyne Estuary. Therefore, the relative contributions of particles to total CO photoproduction on a depth-integrated basis are comparable between the Delaware Estuary (this study), the Mackenzie Estuary (Song et al., 2013) and the Tyne Estuary (Stubbins et al., 2011) (Table 5-4). These results elucidated that particles may play a more important role in CO photoproduction in highly turbid estuarine waters.

Table 5-3 Modeled CO photoproduction rates at the surface (P_{θ}) and in the water column (P_{col}) at each station in August and November. nd: no data is available.

| Station | P_{θ} ($\mu\text{mol m}^{-3} \text{d}^{-1}$) | | | P_{col} ($\mu\text{mol m}^{-2} \text{d}^{-1}$) | | |
|----------|---|-----------------|-----------------|--|--------------|--------------|
| | $P_{cdom,\theta}$ | $P_{10,\theta}$ | $P_{20,\theta}$ | $P_{cdom,col}$ | $P_{10,col}$ | $P_{20,col}$ |
| August | | | | | | |
| A1 | 379 | nd | 492 | 121 | nd | 197 |
| A3 | 314 | 375 | 396 | 89.6 | 145 | 166 |
| A7 | 298 | 338 | 470 | 85.9 | 109 | 189 |
| A10 | 259 | 298 | 328 | 90.7 | 122 | 141 |
| A11 | 346 | nd | 469 | 127 | nd | 218 |
| A12 | 219 | nd | 257 | 127 | nd | 167 |
| A13 | 250 | 283 | 293 | 135 | 182 | 205 |
| A16 | 375 | nd | 471 | 215 | nd | 305 |
| A17 | 318 | nd | 383 | 206 | nd | 309 |
| A20 | 301 | 339 | 349 | 180 | 231 | 259 |
| A21 | 172 | nd | 226 | 161 | nd | 256 |
| A23 | 133 | nd | 166 | 96.9 | nd | 144 |
| A28 | 64.7 | 75.9 | 79.2 | 178 | 296 | 303 |
| November | | | | | | |
| N2 | 285 | 361 | 415 | 45.6 | 69.8 | 96.0 |
| N5 | 236 | 310 | 316 | 47.3 | 83.1 | 91.9 |
| N6 | 157 | 242 | 269 | 55.8 | 93.0 | 115 |
| N11 | 230 | 501 | 608 | 59.0 | 184 | 251 |
| N13 | 89.2 | 113 | 118 | 52.5 | 95.1 | 109 |
| N14 | 69.9 | 107 | 113 | 41.8 | 77.2 | 89.6 |
| N15 | 90.1 | 125 | 131 | 53.1 | 93.8 | 109 |
| N22 | 39.5 | 52.6 | 62.2 | 37.6 | 73.9 | 100 |

Table 5-4 Comparison of the contributions of particles to total CO photoproduction at the surface and in the water column with the values in other regions

| Study site ^a | Sampling time | $P_{p,0}:P_{t,0}$ | $P_{p,col}:P_{t,col}$ | Reference |
|-------------------------|-------------------|-------------------|-----------------------|------------------------|
| DE ^b | Aug. 2012 | 0.14-0.36 | 0.29-0.55 | this study |
| DE | Nov. 2012 | 0.24-0.62 | 0.48-0.77 | this study |
| BATs | Jun. 2007 | 0.19 | ndc | Xie and Zafiriou, 2009 |
| VS | Sep. 2007 | 0.26 | nd | Xie and Zafiriou, 2009 |
| PAP | Sep. 2007 | 0.10 | nd | Xie and Zafiriou, 2009 |
| TE | Apr. and May 2001 | nd | 0.61 | Stubbins et al., 2011 |
| ME | Aug. 2009 | 0.04-0.50 | 0.06-0.55 | Song et al., 2013 |
| MS | Aug. 2009 | 0.03-0.19 | 0.05-0.21 | Song et al., 2013 |
| CB | Aug. 2009 | 0.02-0.13 | 0.02-0.13 | Song et al., 2013 |

a: DE: Delaware Estuary; BATs: Bermuda Atlantic Time-series Study site; VS: Vineyard Sound, Massachusetts; PAP: Pointe-au-Père, Rimouski, Québec; TE: Tyne Estuary; ME: Mackenzie Estuary; MS: Mackenzie Shelf; CB: Canada Basin.

b: $P_{p,0}:P_{t,0}$ and $P_{p,col}:P_{t,col}$ in DE were $P_{p,0}$ and $P_{p,col}$ from particles (0.2-20 μm) to $P_{t,0}$ and $P_{t,col}$ (i.e. from 20 μm filtered water), respectively.

c: nd: no data.

5.4 SUMMARY

Along the main axis of the Delaware Estuary, CO AQY spectra from size-fractionated OM ($< 0.2 \mu\text{m}$ (i.e. CDOM), $< 10 \mu\text{m}$ and $< 20 \mu\text{m}$) were determined to evaluate the relative photoreactivity of CDOM and particles after two extreme weather events in August (dry) and November (flood) 2012.

The spectra of CO AQY were much flatter than those published in previous studies (Zhang et al., 2006; Xie et al., 2009a; White et al., 2010, Song et al., 2013), due likely to the distinct properties of CDOM and particles in the Delaware Estuary after the two extreme weather events. The photoreactivity of both CDOM and particles in the mid-TMZ were much higher than their counterparts carried by freshwater from land. However, no significant difference of the CO photoproduction efficiency was found between the smaller-sized ($< 10 \mu\text{m}$) and larger-sized ($10\text{-}20 \mu\text{m}$) particles along the estuary. Modeled total CO photoproduction, at the surface, ranged from 79.2 to 492 $\mu\text{mol m}^{-3} \text{d}^{-1}$ (mean: 337 $\mu\text{mol m}^{-3} \text{d}^{-1}$) in August and from 62.2 to 608 $\mu\text{mol m}^{-3} \text{d}^{-1}$ (mean: 254 $\mu\text{mol m}^{-3} \text{d}^{-1}$) in November, respectively. On a depth-integration basis, total CO photoproduction ranged from 141 to 309 $\mu\text{mol m}^{-2} \text{d}^{-1}$ in August, and from 89.6 to 251 $\mu\text{mol m}^{-2} \text{d}^{-1}$ in November. Due to the lower solar irradiance and shorter solar duration in November, the averaged total CO photoproduction rates at the surface and in the water column in November were ca. 3/4 and half of those in August. UVA was mainly responsible for CO photoproduction at the surface from both CDOM and particles, while visible light acted as the most important factor in the water column. Particles ($< 20 \mu\text{m}$) contributed 14%-36% to total CO photoproduction at the surface in August, and 24%-62% in November. In the water column, particles accounted for more of total CO photoproduction for both cruises, suggesting photochemistry of particles was more important with increasing depth. Moreover, smaller-sized particles were the main contributor of particle-based CO photoproduction during both cruises, because the smaller-size fraction was the dominant component of the colored particulate matter.

ACKNOWLEDGMENTS

We thank D. L. Kirchman for providing the chlorophyll *a* and diffuse attenuation coefficient data. We also appreciate the cooperation of the chief scientist (D. L. Kirchman), captains, and crews of *R.V. Sharp* during the study cruises. This study was supported by grants from NSF (Natural Science Foundation, US) and NSERC (Natural Sciences and Engineering Research Council, CA). GS was supported by graduate scholarships from ISMER (Institut des sciences de la mer de Rimouski) and FRQNT (Fonds de recherche du Québec – Nature et technologies). This is a contribution to the research programs of PAPI, ISMER, and Québec-Océan.

CHAPITRE 6

SOMMAIRE ET CONCLUSIONS

Cette étude a été principalement axée sur la quantification de l'efficacité (c.-à-d. AQY) et la contribution de la photochimie des particules comme une source de CO dans divers écosystèmes aquatiques, y compris les estuaires, les mers côtières et ouvertes, et la glace de mer. Elle a également caractérisé les variations spatiotemporelles de la concentration de CO ([CO]) dans la glace de mer de première année en Arctique.

La [CO] à la base de la glace de mer de première année dans le SE de la mer de Beaufort a suivi la progression de la concentration de chlorophylle *a*. Les profils verticaux de CO ont décrit une baisse du CO en profondeur dans la glace de mer au début du printemps, une élévation très haute de [CO] dans la couche inférieure au cours de la prolifération des algues de glace et des structures verticales variables lors de la fonte des glaces. Il a été prouvé que la photodégradation de la matière organique (c.-à-d. CDOM et particules), en particulier les particules dérivées d'algues de glace, est principalement responsable de l'enrichissement de CO fonda la base de la glace de mer pendant la floraison.

En terme de rendement quantique, les particules collectées à partir à la fois de cultures d'algues de glace et d'eau de mer naturelle sont généralement plus efficaces que le CDOM pour la photoproduction de CO, en particulier dans les longueurs d'onde visibles. Cette caractéristique a conduit à une production disproportionnellement plus haute de CO à partir des particules causée par la lumière visible. Par conséquent, le ratio entre la photoproduction de CO à partir de particules et du CDOM tend à augmenter avec la profondeur dans la zone euphotique et dans la glace de mer. Dans le SE de la mer de

Beaufort, le rayonnement UVA (330-400 nm) a été le principal moteur de la photoproduction de CO à partir de CDOM, à la fois en surface et pour la production intégrée avec profondeur dans la glace de mer et dans les eaux ouvertes. En revanche, la lumière visible (400-600 nm) a dominé la photoproduction de CO à partir des particules intégrée sur toute la colonne d'eau et dans la glace de mer au cours de la prolifération d'algues de glace. Dans l'estuaire du Delaware, la photoproduction de CO intégrée à partir à la fois du CDOM et des particules était surtout causé par la lumière visible, probablement à cause des propriétés uniques de la matière organique caractérisée par des AQY spectralement beaucoup plus plat.

L'étude dans le SE de la mer de Beaufort a démontré que la photoréactivité du CDOM, en termes de photoproduction de CO, a diminué de la côte vers le large (c.-à-d. CDOM terrestre > CDOM marin) alors que la tendance s'est inversée pour les particules (c.-à-d. particules terrestres < particules marines). De plus, les particules marines étaient plus efficaces pour la photoproduction de CO que le CDOM marin tandis que les particules terrestres étaient moins photoréactives que leurs homologues terrestres dissoutes. Dans l'estuaire du Delaware, aussi bien le CDOM et que les particules dans la zone de turbidité maximale (TMZ) au milieu de l'estuaire étaient plus efficaces à photoproduire du CO que leurs homologues recueillies en amont ou en aval de la zone de TMZ. Ce résultat suggère que la floculation, l'adsorption/désorption et la suspension des sédiments dans la TMZ ont peut-être amélioré la photoréactivité de la CDOM et des particules et/ou les concentrations de métaux traces photoréactifs plus élevées (par exemple : Fe, Cu, Mn). En outre, peu de différence a été observée dans l'efficacité de la photoproduction de CO entre les fractions de particules <10 μm et 10-20 μm à la fois en août et en novembre.

La modélisation couplée optique-photochimique a révélé que les particules pourraient contribuer jusqu'à 84% de la photoproduction totale de CO à la base de la glace de mer au cours de la prolifération d'algues de glace, entre 12% et 32% dans l'eau libre de glace dans le SE de la mer de Beaufort et entre 29% et 77% dans l'estuaire du Delaware. Par ailleurs, les particules de petite taille (<10 μm) ont dominé la photoproduction de CO à

partir de particules dans l'estuaire du Delaware car les a_p dominaient largement l'absorption de la lumière par les particules.

Les résultats de cette étude démontrent clairement que la photochimie des particules est importante ou peut même être un élément prépondérant dans la photoproduction de CO. Comme le CO est un photoproduit clé de la matière organique, cette étude implique un rôle potentiellement important de la photochimie des particules dans le carbone organique marin et les cycles des gaz en trace, en particulier dans les eaux ayant des charges élevées en particules, telles que la base de la glace de mer chargé d'algues de glace et les eaux estuariennes et côtières relativement turbides.

Contributions à la science et perspectives :

Ce projet a, pour la première fois, permis de déterminer les AQYs de CO spectraux des particules dans différents écosystèmes aquatiques et d'estimer leur contribution à la photoproduction totale de CO. Il fournit de nouveaux résultats sur l'importance de la photochimie des particules en carbone organique marin et le cycle des gaz trace dans l'eau de mer libre ainsi que dans la glace de mer. Comme la photochimie des particules est encore à ses balbutiements, il reste beaucoup à faire. Ci-dessous voici plusieurs aspects prioritaires pour l'étude future de la photoproduction de CO lésa partir des particules :

1) Mieux résoudre la forme spectrale de AQY du CO à partir des particules, en particulier le rôle des pigments dans la photoproduction de CO, en employant un rayonnement monochromatique ;

2) Élucider les effets des concentrations de métaux (par exemple, Fe, Mn, Cu) et de la spéciation, ceux de la propriété de la POM (par exemple, $a_{pom}:a_p$), de la température, du pH, de la salinité, etc., sur la photoproduction de CO particulaire;

3) Quantifier les flux d'autres procédés photochimiques particuliers, comme tels que la photoproduction d'espèces réactives à l'oxygène, de CO₂ et d'ammonium.

CONCLUSIONS

This study was mainly focused on quantifying the efficiency (i.e. AQY) and contribution of particle photochemistry as a source of CO in various aquatic ecosystems, including estuaries, coastal and open seas, and sea ice. It also characterized the spatiotemporal variations in CO concentration ([CO]) in Arctic first-year sea ice.

The bottom [CO] in the SE Beaufort Sea first-year sea ice followed the progression of chlorophyll *a* concentration. CO vertical profiles in sea ice depicted decreasing [CO] with depth in early spring, extremely elevated [CO] in the bottom layer during ice algal blooms, and inconsistent patterns in the ice melting season. Photodegradation of organic matter (i.e. CDOM and particles), especially ice algae-derived particles, was demonstrated to be mainly responsible for the enrichment of CO in bottom sea ice during bloom.

On an absorbed-photon basis, particles collected from both ice algae cultures and natural seawater were generally more efficient than CDOM at CO photoproduction, particularly in visible wavelengths. This feature led to a disproportionately higher visible light-driven CO production by particles, thereby increasing the ratio of particle- to CDOM-based CO photoproduction with depth in the euphotic zone and in sea ice. In the SE Beaufort Sea, UVA radiation (330-400 nm) was the primary driver of both surface and depth-integrated CO photoproduction from CDOM in both sea ice and open seawater. In contrast, visible light (400-600 nm) dominated the depth-integrated CO photoproduction from particles in the water column and in bottom sea ice during ice algal blooms. In the Delaware estuary, the depth-integrated CO photoproduction from both CDOM and particles

was primarily visible light-driven due likely to unique properties of organic matter that led to much flatter AQY spectra.

The SE Beaufort Sea study demonstrated that the photoreactivity of CDOM in terms of CO photoproduction decreased from inshore to offshore (i.e. terrestrial CDOM > marine CDOM) while the trend for particles was reversed (i.e. terrestrial particles < marine particles). Moreover, marine particles were more efficient at CO photoproduction than marine CDOM whereas terrestrial particles were less photoreactive than its terrestrial counterpart. In the Delaware estuary, both CDOM and particles in the mid-estuary turbidity maximum zone (TMZ) were more efficient at CO photoproduction than their counterparts collected from either upstream or downstream of the TMZ. This result suggests flocculation, adsorption/desorption and sediment suspension in the TMZ may have enhanced the photoreactivity of CDOM and particles and/or the concentrations of photoreactive trace metals (e.g. Fe, Cu, Mn). Furthermore, little difference was found in CO photoproduction efficiency between the particle fractions of <10 μm and 10-20 μm in both August and November.

Coupled optical-photochemical modeling revealed that particles could contribute more than 84% to total CO photoproduction in bottom sea ice during ice algal blooms, 12-32% in ice-free water in the SE Beaufort Sea and 29%-77% in the Delaware estuary. Furthermore, the small-sized particles (< 10 μm) accounted for more particle-based CO photoproduction in the Delaware estuary because of the dominance of this fraction in the colored particulate matter.

Results from this study clearly demonstrate that particle photochemistry is an important or even can be a dominant term in CO photoproduction. As CO is a key photoproduct of organic matter, this study implies a potentially significant role of particle photochemistry in marine organic carbon and trace gas cycling, especially in waters with high loads of particles, such as ice algae-laden bottom sea ice and estuarine and coastal waters.

Contributions to science and perspectives:

This project for the first time determined the spectrally resolved CO AQYs of particles in various aquatic ecosystems and estimated the relative contributions of particles and solutes to total CO photoproduction. It provides novel results about the importance of particle photochemistry in marine organic carbon and trace gas cycling in open seawater as well as in sea ice. As particle photochemistry is still in its infancy, much remains to be done. Listed below are several suggested priorities for study of particle-based CO photoproduction in the future:

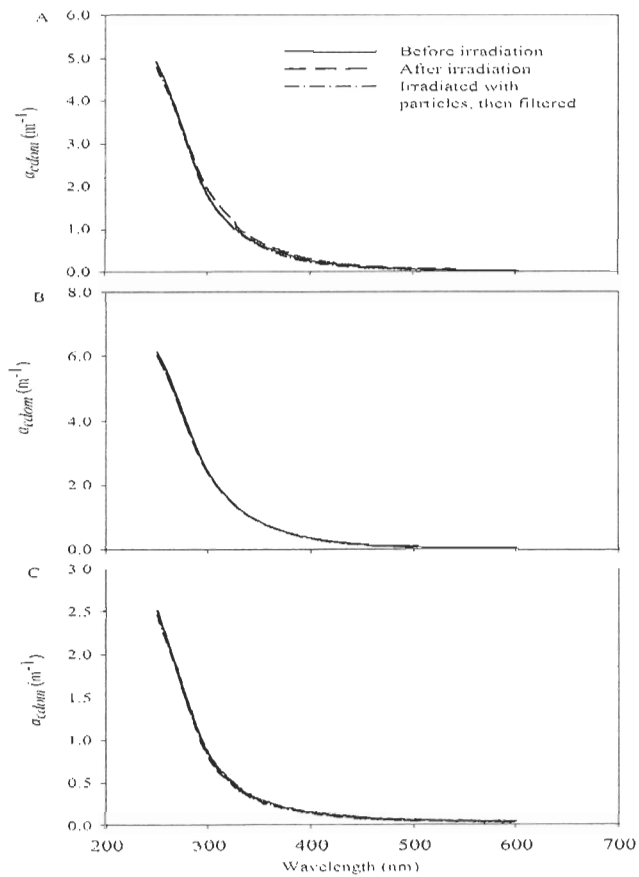
1) To better resolve the spectral shape of particulate CO AQY, particularly the role of pigments in CO photoproduction, employing monochromatic radiation;

2) To elucidate the effects of metal concentrations (e.g. Fe, Mn, Cu) and speciation, POM property (e.g. the $a_{pom}:a_p$ ratio), temperature, pH, salinity, etc., on particle-based CO photoproduction;

3) To quantify the fluxes of other particulate photochemical processes, such as photoproduction of reactive oxygen species, CO₂, and ammonium.

ANNEX 1

Fig. A1. Comparison of CDOM absorption spectra before and after irradiation. A): Sta. 170, surface (1-h irradiation); B): Sta. 670, surface (1.5-h irradiation); C): Sta. 135, DCM (3-h irradiation, the longest irradiation in this study for short cutoff filters). For unfiltered samples, they were filtered with 0.2- μm Nylon syringe filters after irradiation. Note some lines are almost completely overlapped.



Monte Carlo Simulation. The quantum absorbed (Q_a) by an optically significant constituent inside a quartz cell irradiated from above by a collimated light beam³ can be estimated using Eq. (4-3) in the paper (abbreviated as Eq. (4-3) herein), as long as the light scattering is negligible relative to the absorption. Filtered seawater with dissolved organic matter (DOM) meets this requirement, since both seawater and DOM have low scattering and CDOM absorption coefficient in short wavelengths is large (i.e. $b:a \sim 0$; b : scattering coefficient and a : absorption coefficient). Unfiltered seawater, however, may not meet this requirement, since scattering by particles can increase the path-length of some photons (i.e. path-length amplification, PA herein) but deflect some other photons out of the quartz cell in all directions (i.e. scattering loss, SL herein). Under this circumstance, Eq. (4-3) overestimates Q_a if $SL > PA$ or underestimates Q_a if $PA > SL$. Here we assessed the effect of particle scattering on the quantity of photons absorbed using Monte Carlo (MC) simulations (SimuIO software; Leymarie et al. 2010) and proposed a modification to Eq. (3) to account for the scattering effect.

MC was used to simulate the trajectories of collimated photons hitting a vertically placed cylindrical quartz cell (length: 114 mm, o.d.: 34 mm, wall thickness: 1.5mm, refractive index: 1.48) from above. The refractive index of pure seawater was set to be 1.34 and its inherent optical properties were taken from Morel (1974) and Buitelveld (1994). All photons scattered out of the cell's side wall were assumed to be totally absorbed by the black electric tape that wrapped the cell. The reflection from the bottom quartz window was ignored since it was in contact with a black plastic block. The particle phase function was given by the Fournier-Forand model (Fournier and Forand, 1994; Mobley et al., 2002) with a backscattering ratio of 2.2%. This backscattering ratio is within the range observed by Doxaran et al. (2012) in the study area.

³ Justification of collimated light reaching the sample's surface in the quartz cell can be found in the Support Information of the study by Zhang et al. (2006). This is also confirmed by a direct comparison between the multispectral irradiation system as adopted in our study and a monochromatic system in the measurement of CO AQY (Ziolkowski and Miller, 2007).

Absorption and scattering coefficient values used in our simulations cover the large ranges encountered during the Malina cruise (a_t : 0.045–47.2 m^{-1} ; b : 0.056–241.5 m^{-1} ; b/a_t : 0.12–20.4). The total absorption (a_t , m^{-1}) coefficient is the sum of pure seawater, CDOM and particle absorption coefficients, whereas scattering coefficient (b , m^{-1}) is only the particle scattering coefficient. Scattering by pure water was neglected as it was several orders of magnitude lower than a_t or b . For each simulation (i.e. a given set of b and a_t). The SimulO software computed the number of photons absorbed within the water body, taking into account all scattering and reflection processes. Then, this number was compared to the number of absorbed photons calculated from Eq. (4-3) without accounting for the scattering effect.

For a given a_t , the ratio (R) of the number of absorbed photons calculated using Eq. (4-3) to that from the MC simulation is found to be linearly correlated to b/a_t , within the range of 0 to 25 (Fig. A2):

$$R = S \times \left(\frac{b}{a_t} \right) + 1 \quad (\text{A1})$$

where S is the regressed slope. S increases with a_t in a manner of exponential rise to maximum (Fig. S3) as expressed by Eq. (A2):

$$S = 0.0539(1 - e^{-0.191a_t}) \quad (\text{A2})$$

R for our Malina samples can thus be calculated from Eqs. (A1) and (A2) with known values of a_t and b ; a_t is from our own study while b is from the study of Doxaran et al. (2012). Fig. A4 shows R as a function of wavelength. The scattering effect (i.e. $R-1$) was $\leq 0.3\%$ in the CB and $\leq 1.9\%$ on the MS, including two outermost stations along the SGTs (Sta. 392 and 691). Samples from the remaining SGT stations had larger a_t values (1.00–10.45 m^{-1} at 412 nm) and higher scattering to absorption ratios (2.8–9.8 at 412 nm). The scattering effect for these stations ranged from 2.0% to 27.8%, depending on sampling location and wavelength. The effect was positive, indicating SL was larger than PA.

Fig. A2. Ratio (R) of the number of absorbed photons calculated using Eq. (4-3) to that from the MC simulation at various $b:a_l$ and a_l values.

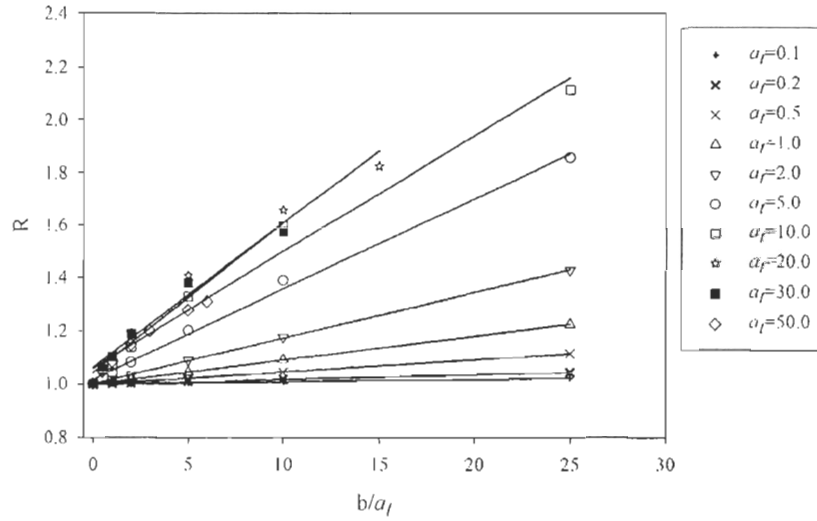


Fig. A3 Regressed slope (S) in Fig. S2 as a function of a_l .

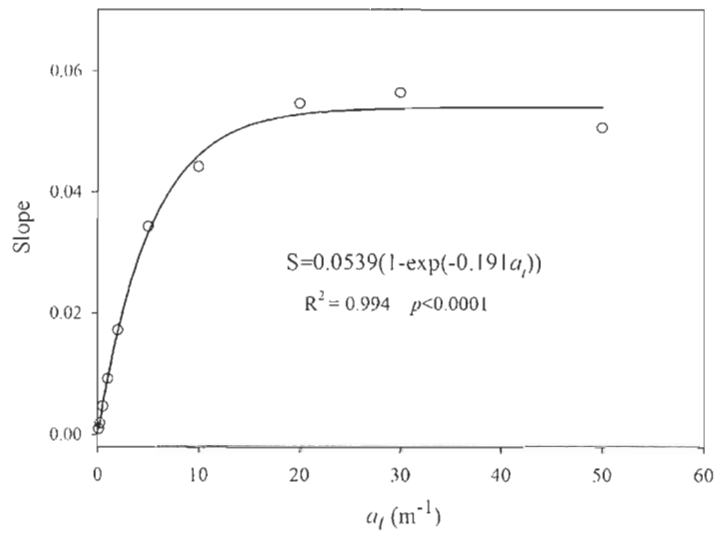
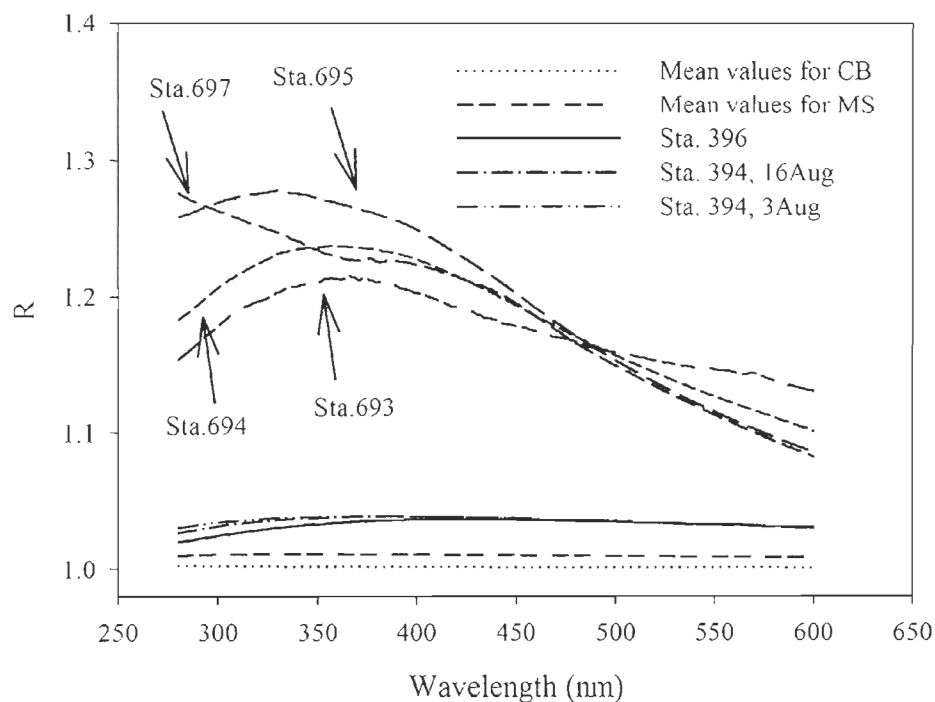


Fig. A4 ($R-1$) as a function of wavelength for Malina samples. Stations with $(R-1) \geq 2\%$ are presented individually while stations with $(R-1) < 2\%$ are presented by mean values. Mean value for the MS include two outermost stations (Sta. 392 and 691) along the salinity gradient transects.

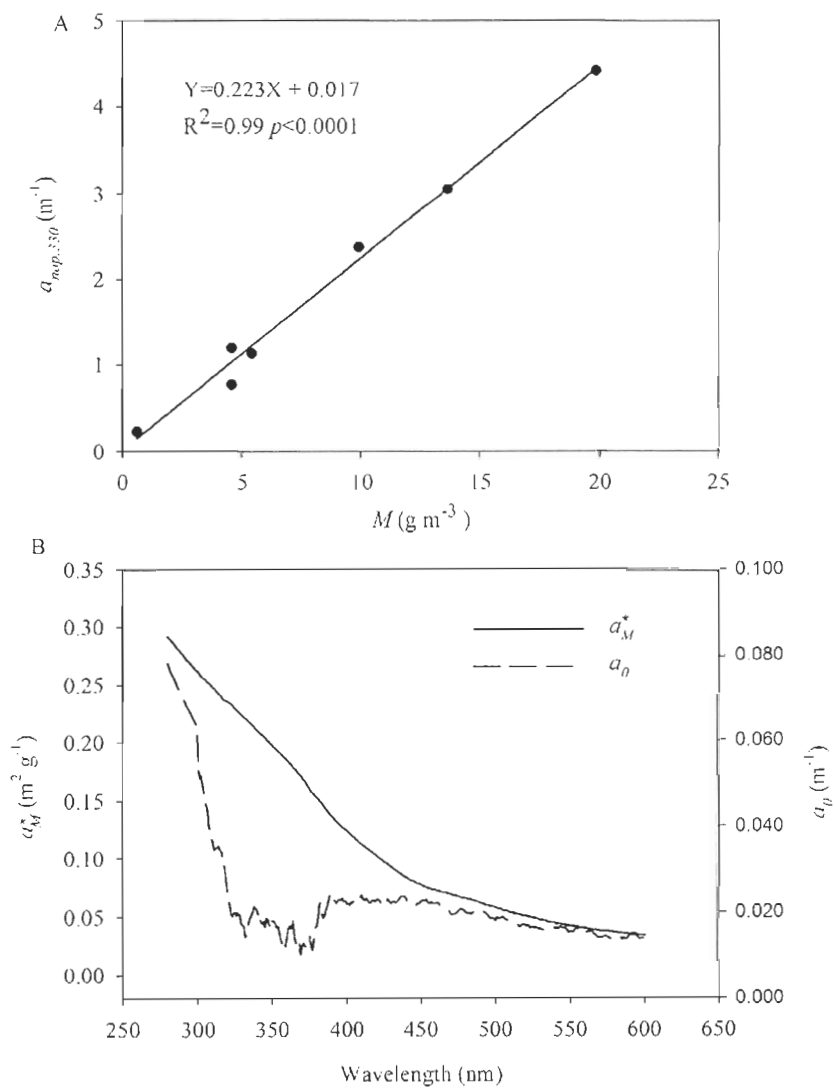


Derivation of the absorption coefficient of minerals. Following the method of Moate et al. (2012), the mass-specific absorption coefficient of suspended minerals, a_M^* ($\text{m}^2 \text{g}^{-1}$), for the estuarine transect samples was derived by the regression of the non-algal particulate absorption coefficient (a_{nap}) against the concentration of suspended minerals, M (g m^{-3}), in the form of

$$a_{nap,\lambda} = a_{0,\lambda} + a_M^* \times M \quad (\text{A3})$$

where a_0 (m^{-1}) represents the organic particle absorption not removed by the methanol treatment. M was calculated as the difference between the total suspended particulate matter (SPM) and the particulate organic matter (POM). POM was estimated as 2.6 times the particulate organic carbon (POC) (Copin-Montégut, 1980; Martin et al., 1993). The a_{nap} , SPM, and POC data, separately collected by Doxaran et al. (2012) from the SGTs during the same cruise, were used to perform the regression of a_{nap} on M (since our own study did not measure SPM and POC). The regression result for wavelength at 330 nm is shown in Fig. A5A and the derived a_M^* (and a_0) as a function of wavelength are shown in Fig. S5B. The mineral absorption coefficients for the salinity transect samples can thus be calculated as $a_M^* \times M$. The spectral shape and values of a_M^* obtained in the present study are comparable to those in the Conwy and Mersey estuaries of the Irish Sea (Moate et al., 2012). They also mimic the a_M^* spectra of Saharan dusts in red rain collected at the Mediterranean coast in France (Babin and Stramski, 2004). Because a_{nap} showed no significant relationship to the mineral concentration in the shelf and offshore water samples (data not shown), it was not possible to obtain the a_M^* of these samples from the regression method described above. The upper limits of their mineral absorption coefficients can, however, be estimated as the difference between the total particle absorption coefficient (a_p) and phytoplankton absorption coefficient (a_{phy}).

Fig. A5. Regression of a_{nap} at 330 nm against the mineral concentration (A) and the derived a_M^* and a_ρ (B).



ANNEX 2

According to the previous studies, simple exponential ($\Phi_{\lambda} = m_1 \times \exp(m_2 \times (\lambda - 290))$) and quasi-exponential ($\Phi_{\lambda} = m_1 \times \exp(m_2 / (m_3 + \lambda))$) models are more popular in modeling the CO AQY spectra from CDOM and particles in natural waters (Zhang et al., 2006; Xie et al., 2009; Song et al., 2013). To our knowledge, the simple exponential model works better for open ocean CDOM samples (marine-derived), while the quasi-exponential model is more suitable for estuarine and coastal CDOM samples and particles samples collected from both the open ocean and estuarine and coastal waters. To verify if the model can reflect the actual CO AQY spectra of the sample, the following factors should be taken into consideration and the model work better when:

- 1) the residues (i.e. the measured CO photoproduction - the predicted CO photoproduction) are much closer to 0, especially for long wavelength cutoff filters;
- 2) the squared correlation coefficient (R^2) of the least-squares linear regression ($y=a*x+b$) between the measured and predicted CO photoproduction rates is high (i.e. closer to 1);
- 3) the slope (a) and intercept (b) of the least-squares linear regression ($y=a*x+b$) between the measured and predicted CO photoproduction rates are much closer to 1 and 0, respectively.

In this study, no data were output when the simple exponential was run for modeling the particle AQY of the ice algal samples, but the quasi-exponential model did well for these samples. However, for CDOM samples, no data were output when the quasi-exponential function to model CO AQY, except two cases (*P. taeniata* at senescent phase and *N. frigida* at exponential phase), while the simple exponential model could work well. For that two CDOM samples (*P. taeniata* at senescent phase and *N. frigida* at exponential phase), the two models worked well, but the residues obtained from the quasi-exponential

phase), the two models worked well, but the residues obtained from the quasi-exponential model, in most cases, were larger and thereafter with worse fits between the measured and predicted CO photoproduction rates (smaller R^2 , or the a value was not good enough) (Fig. A2-1 and A2-2). So, in this study, all CDOM samples (including medium) were modeled using the simple exponential model, while the quasi-exponential model was used for particle samples.

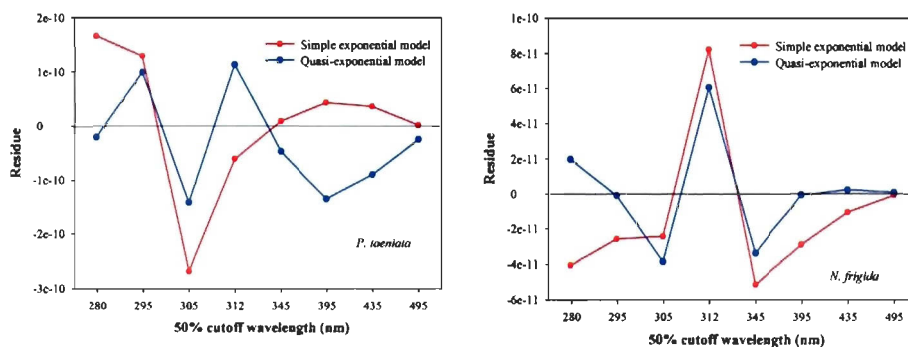


Fig. A2-1 Residue ($\text{mol CO m}^{-3} \text{s}^{-1}$) obtained from two models for CDOM samples collected from *P. taeniata* at the senescent phase (left panel) and *N. frigida* at the exponential phase (right panel) vs. the nominal 50% cutoff wavelength.

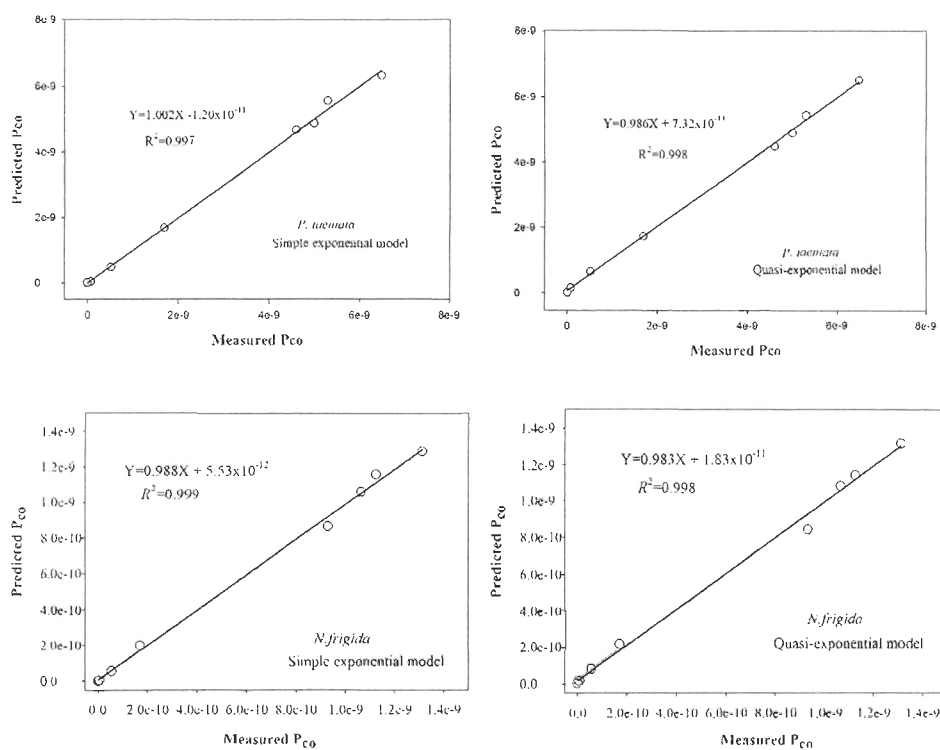


Fig. A2-2 Linear regressions between measured and predicted CO photoproduction rates (P_{CO} , mol CO $m^{-3} s^{-1}$) using two models for CDOM samples collected from *P. taeniata* at the senescent phase (upper panels) and *N. frigida* at the exponential phase (lower panels).

Table A2-1 Variations of $a_{p,443}$, $a'_{cdom,330}$ and [DOC] during irradiation for CO photoproduction from particles. Dark means the dark controls; Irrad. means after irradiation under full spectrum (i.e. under cutoff WG 280); EP denotes exponential phase, SP denotes senescent phase; NA denotes no data are available.

| | <i>P. taeniata</i> | | <i>A. septentrionalis</i> | | <i>N. frigida</i> | | <i>NIAA</i> | |
|---------------------------------|--------------------|--------|---------------------------|--------|-------------------|--------|-------------|--------|
| | Dark | Irrad. | Dark | Irrad. | Dark | Irrad. | Dark | Irrad. |
| $a_{p,443} (\text{m}^{-1})$ | | | | | | | | |
| EP | 0.93 | 0.94 | 1.10 | 1.08 | 0.29 | 0.29 | 1.33 | 1.32 |
| SP | 0.85 | 0.84 | 0.68 | 0.68 | NA | NA | 0.13 | 0.13 |
| $a'_{cdom,330} (\text{m}^{-1})$ | | | | | | | | |
| EP | 0.11 | 0.11 | 0.08 | 0.08 | 0.06 | 0.06 | 0.22 | 0.23 |
| SP | 0.08 | 0.10 | 0.09 | 0.09 | NA | NA | 0.07 | 0.08 |
| [DOC] (mg C L^{-1}) | | | | | | | | |
| EP | 0.32 | 0.29 | 0.20 | 0.16 | 0.27 | 0.25 | 0.44 | 0.44 |
| SP | 0.64 | 0.62 | 0.52 | 0.53 | NA | NA | 0.30 | 0.32 |

RÉFÉRENCES BIBLIOGRAPHIQUES

- Amon, R. M. W., 2004. The role of dissolved organic matter for the organic carbon cycle in the Arctic Ocean, in: *The Organic Carbon Cycle in the Arctic Ocean*, edited by R. Stein, and R. W. Macdonald, pp. 83–100, Springer, New York.
- Amon, R. M. W., H.-P. Fitznar, and R. Benner, 2001. Linkages among the bioreactivity, chemical composition, and diagenetic state of marine dissolved organic matter, *Limnol. Oceanogr.*, 46(2), 287–297.
- Anderson, L. G., E. Falck, E. P. Jones, S. Juttertröm, and J. H. Swift, 2004. Enhanced uptake of atmospheric CO₂ during freezing of seawater: A field study in Storfjorden, Svalbard, *J. Geophys. Res.*, 109, C06004, doi:10.1029/2003JC002120.
- Anesio, A. M., L. J. Tranvik, and W. Granéli, 1999a. Production of inorganic carbon from aquatic macrophytes by solar radiation, *Ecology*, 80(6), 1852-1859.
- Anesio, A. M., C. M. T. Denward, L. J. Tranvik, and W. Granéli, 1999b. Decreased bacterial growth on vascular plant detritus due to photochemical modification, *Aquat. Microb. Ecol.*, 17, 159-165.
- Babin, M., and D. Stramski, 2004. Variations in the mass-specific absorption coefficient of mineral particles suspended in water, *Limnol. Oceanogr.*, 49, 756-767.
- Babin, M., D. Stramski, G. M. Ferrari, H. Claustre, A. Bricaud, G. Obolensky, and N. Hoepffner, 2003. Variations in the light absorption coefficients of phytoplankton, nonalgal particles, and dissolved organic matter in coastal waters around Europe, *J. Geophys. Res.*, 108(C7), 3211, doi:10.1029/2001JC000882.
- Barbeau, K., E. L. Rue, K. W. Bruland, and A. Butler, 2001. Photochemical cycling of iron in the surface ocean mediated by microbial iron (III)-binding ligands, *Nature*, 413, 409-413.
- Barber, D. G., M. Asplin, Y. Gratton, J. Lukovich, R. Galley, R. Raddatz, and D. Leitch, 2010. The international polar year (IPY) circumpolar flaw lead (CFL) system

study: Introduction and physical system, Atmos-Ocean, doi:10.3137/OC317.2010.

- Bates, T. S., K. C. Kelly, J. E. Johnson, and R. H. Gammon, 1995. Regional and seasonal variations in the flux of oceanic monoxide to the atmosphere, *J. Geophys. Res.*, 100(D11), 23093–23101, doi:10.1029/95JD02737.
- Bélanger, S., 2006. Response of light-related carbon fluxes in the Arctic Ocean to climate change: Quantification and monitoring of dissolved organic matter photo-oxidation in the Beaufort Sea using satellite remote sensing. Ph.D. thesis, Université Pierre et Marie Curie (UPMC– Paris XI), Paris, France.
- Bélanger, S., H. Xie, N. Krotkov, P. Larouche, W. F. Vincent, and M. Babin, 2006. Photomineralization of terrigenous dissolved organic matter in Arctic coastal waters from 1979 to 2003: Interannual variability and implications of climate change, *Global Biogeochem. Cycles*, 20, GB4005, doi: 10.1029/2006GB002708.
- Bélanger, S., M. Babin, and P. Larouche, 2008. An empirical ocean color algorithm for estimating the contribution of chromophoric dissolved organic matter to total light absorption in optically complex waters, *J. Geophys. Res.*, 113, C04027, doi:10.1029/2007JC004436.
- Belzile, C., S. C. Johannessen, M. Gosselin, S. Demers, and W. L. Miller, 2000. Ultraviolet attenuation by dissolved and particulate constituents of first-year ice during late spring in an Arctic polynya, *Limnol. Oceanogr.*, 45(6), 1265–1273.
- Belzile, C., J. A. E. Gibson, and W.F. Vincent, 2002. Colored dissolved organic matter and dissolved organic carbon exclusion from lake ice: Implications for irradiance transmission and carbon cycling, *Limnol. Oceanogr.*, 47(5), 1283–1293.
- Benner, R., and B. Biddanda, 1998. Photochemical transformations of surface and deep marine dissolved organic matter: Effects on bacterial growth, *Limnol. Oceanogr.*, 43, 1373-1378.
- Benner, R., and K. Kaiser, 2011. Biological and photochemical transformations of amino acids and lignin phenols in riverine dissolved organic matter, *Biogeochem.*, 102, 209-222, doi:10.1007/s10533-010-9435-4.
- Benner, R., P. Louchouart, and R. M. W. Amon, 2005. Terrigenous dissolved organic matter in the Arctic Ocean and its transport to surface and deep waters of the North Atlantic, *Global Biogeochem. Cycles*, 19, GB2025, doi:10.1029/2004GB002398.

- Berges, J. A., D. J. Franklin, and P. J. Harrison, 2001. Evolution of an artificial seawater medium: improvements in enriched seawater, artificial water over the last two decades, *J. Phycol.*, 37, 1138-1145.
- Biggs, R. B., J. H., Sharp, T. M. Church, and J. M., Tramontano, 1983. Optical properties, suspended sediments, and chemistry associated with the turbidity maxima of the Delaware estuary, *Can. J. Fish. Aquat. Sci.*, 40 (Supp: 1), 172-179.
- Blough, N. V., and R.G. Zepp, 1995. Reactive oxygen species in natural waters, in: *Active oxygen in chemistry*, edited by: Foote, C. S., Pacentine, J. S., Greenberg, A., and Liebman, J. F., Chapman & Hall, New York, p280-333.
- Blough, N. V., O. C. Zafiriou, and J. Bonilla, 1993. Optical absorption spectra of waters from the Orinoco River outflow: terrestrial input of colored organic matter to the Caribbean, *J. Geophys. Res.*, 98(2), 2271-2278, doi:10.1029/92JC02763.
- Bourbonniere, R. A., W. L. Miller, and R. G. Zepp, 1997. Distribution, flux, and photochemical production of carbon monoxide in a boreal beaver impoundment, *J. Geophys. Res.*, 102(D24), 29321-29329.
- Brimblecombe, P., 2003. The global sulfur cycle, in: *Biogeochemistry: Treatise on geochemistry*, edited by: Schlesinger, W. H., Elsevier Ltd., p645-682.
- Brown, T. A., S. T. Belt, B. Philippe, C. J. Mundy, G. Massé, M. Poulin, and M. Gosselin, 2010. Temporal and vertical variations of lipid biomarkers during a bottom ice diatom bloom in the Canadian Beaufort Sea: further evidence for the use of the IP₂₅ biomarker as a proxy for spring Arctic sea ice, *Polar Biol.*, doi:10.1007/s00300-010-0942-5.
- Buiteveld, H., J. M. H. Hakvoort, and M. Donze, 1994. The optical properties of pure water, in: *SPIE proceeding on ocean optics XII. The Society of Photo-Optical Instrumentation Engineers*, edited by: Jaffe, J. S., p174-183.
- Bunch, J. N., and R. C. Harland, 1990. Bacterial production in the bottom surface of sea ice in the Canadian subarctic, *Can. J. Fish. Aquat. Sci.*, 47(10), 1986-1995.
- Bushaw, K. L., R. G. Zepp, M. A. Tarr, D. Schulz-Jander, R. A. Bourbonniere, R. E. Hodson, W. L. Miller, D. A. Bronk, and M. A. Moran, 1996. Photochemical release of biologically labile nitrogen from aquatic dissolved organic matter, *Nature*, 381, 404-407.
- Canadian Ice Service (CIS), <http://ice-glaces.ec.gc.ca/IceGraph103/page1.jsf>.

- Conrad, R., and W. Seiler, 1980. Photooxidative production and microbial consumption of carbon monoxide in seawater, *FEMS Microbiol. Lett.*, 9, 61-64.
- Conrad, R., W. Seiler, G. Bunse, and H. Giehl, 1982. Carbon monoxide in seawater (Atlantic Ocean), *J. Geophys. Res.*, 87(C11), 8839–8852.
- Cook, T. L., C. K. Sommerfield, and K.-C. Wong, 2007. Observations of tidal and springtime sediment transport in the upper Delaware Estuary, *Estuarine Coastal Shelf Sci.*, 72, 235-246.
- Copin-Montégut, G., 1980. *Matières en suspension dans les eaux de mer: répartition composition chimique, origine et evolution*, Thèse d'état. Université Pierre et Marie Curie Paris IV, p173.
- Cox, G. F. N., and W. F. Weeks, 1983. Equations for determining the gas and brine volumes in sea-ice samples, *J. Glaciol.*, 29, 306-316.
- Day, D. A., and I. Faloona, 2009. Carbon monoxide and chromophoric dissolved organic matter cycles in the shelf waters of the northern California upwelling system, *J. Geophys. Res.*, 114, C01006, doi:10.1029/2007JC004590.
- Delille, B., B. Jourdain, A. V. Borges, J.-L. Tison, and D. Delille, 2007. Biogas (CO₂, O₂, dimethylsulfide) dynamics in spring Antarctic fast ice, *Limnol. Oceanogr.*, 52(4), 1367–1379.
- Deming, J. W., 2010. Sea ice bacteria and viruses, in: *Sea ice*, edited by D. N. Thomas, and G. S. Dieckmann, p247-282, Wiley-Blackwell, Oxford, UK.
- Dittmar, T., and G. Kattner, 2003. The biogeochemistry of the river and shelf ecosystem of the Arctic Ocean: a review, *Mar. Chem.*, 83, 103-120.
- Doney, S. C., R. G. Najjar, and S. Stewart, 1995. Photochemistry, mixing and diurnal cycles in the upper ocean, *J. Mar. Res.*, 53, 341–369.
- Doxaran, D., J. Ehn, S. Bélanger, A. Matsuoka, S. Hooker, and M. Babin, 2012. Optical characterization of suspended particles in the Mackenzie River plume (Canadian Arctic Ocean) and implications for ocean colour remote sensing, *Biogeosciences*, 9, 3213-3229, doi:10.5194/bg-9-3213-2012.
- Ehn, J. K., C. J. Mundy, and D. G. Barber, 2008. Bio-optical and structural properties inferred from irradiance measurements within the bottommost layers in an Arctic landfast sea ice cover, *J. Geophys. Res.*, 113, C03S03, doi:10.1029/2007JC004194.

- Ehn, J. K., C. J. Mundy, D. G. Barber, H. Hop, A. Rossnagel, and J. Stewart, 2011. Impact of horizontal spreading on light propagation in melt pond covered seasonal sea ice in the Canadian Arctic, *J. Geophys. Res.*, 116, C00G02, doi:10.1029/2010JC006908.
- Eicken, H., 1992. Salinity profiles of Antarctic sea ice: Field data and model results, *J. Geophys. Res.*, 97(C10), 15545–15557.
- Eicken, H., 2003. From the microscopic, to the macroscopic, to the regional scale: Growth, microstructure and properties of sea ice, in *Sea Ice: an Introduction to its Physics, Chemistry, Biology, and Geology*, edited by D. N. Thomas and G. S. Dieckmann, pp. 22–81, Blackwell Science, Oxford, UK.
- Estapa, M. L., and L. M. Mayer, 2010. Photooxidation of particulate organic matter, carbon/oxygen stoichiometry, and related photoreactions, *Mar. Chem.* 122, 138–147.
- Estapa, M. L., L. M. Mayer, and E. Boss, 2012a. Rate and apparent quantum yield of photodissolution of sedimentary organic matter, *Limnol. Oceanogr.* 57, 1743–1756.
- Estapa, M. L., E. Boss, L. M. Mayer, and C. S. Roesler, 2012b. Role of iron and organic carbon in mass-specific light absorption by particulate matter from Louisiana coastal waters, *Limnol. Oceanogr.*, 57, 97–112.
- Fanning, K. A., and L. M. Torres, 1991. ^{222}Rn and ^{226}Ra : Indicators of sea-ice effects on air-sea gas exchange, *Polar Res.*, 10, 51–58.
- Fichot, C. G., and R. Benner, 2012. The spectral slope coefficient of chromophoric dissolved organic matter ($S_{275-295}$) as a tracer of terrigenous dissolved organic carbon in river-influenced ocean margins, *Limnol. Oceanogr.*, 57(5), 1453–1466, doi:10.4319/lo.2012.57.5.1453.
- Fichot, C. G., and W. L. Miller, 2010. An approach to quantify depth-resolved marine photochemical fluxes using remote sensing: Application to carbon monoxide (CO) photoproduction, *Remote Sens. Environ.*, 114, 1363–1377.
- Fioletov, V. E., M. G. Kimlin, N. Krotkov, L. J. B. McArthur, J. B. Kerr, D. I. Wardle, J. R. Herman, R. Meltzer, T. W. Mathews, and J. Kaurola, 2004. UV index climatology over the United States and Canada from ground-based and satellite estimates, *J. Geophys. Res.*, 109, D22308, doi:10.1029/2004JD004820.

- Flato, G. M., G. J. Boer, W. G. Lee, N. A. McFarlane, D. Ramsden, M. C. Reader, and A. J. Weaver, 2000. The Canadian Centre for climate modeling and analysis global coupled model and its climate, *Clim. Dyn.*, 16, 451-467.
- Forest, A., M. Sampei, H. Hattori, R. Makabe, H. Sasaki, M. Fukuchi, P. Wassmann, and L. Fortier, 2007. Particulate organic carbon fluxes on the slope of the Mackenzie Shelf (Beaufort Sea): Physical and biological forcing of shelf-basin exchange, *J. Mar. Syst.*, 68, 39-54.
- Fournier, G., and J. L. Forand, 1994. Analytic phase function for ocean water, *Proc. SPIE*, 2258, 194-201.
- Gao, H., and R. G. Zepp, 1998. Factors influencing photoreactions of dissolved organic matter in a coastal river of the Southeastern United States, *Environ. Sci. Technol.*, 32, 2940-2946.
- Garrison, D. L., and K.R. Buck, 1986. Organism losses during ice melting: a serious bias in sea ice community studies, *Polar Biol.*, 6, 237-239.
- Garvine, R. W., R. K. McCarthy, and K.-C. Wong, 1992. The axial salinity distribution in the Delaware Estuary and its weak response to river discharge. *Estuarine Coastal Shelf Sci.*, 35, 157-165.
- Giannelli, V., D. N. Thomas, C. Hass, G. Kattner, H. Kennedy, G. S. Dieckmann, 2001. Behaviour of dissolved organic matter and inorganic nutrients during experimental sea-ice formation, *Ann. Glaciol.*, 33, 317-321.
- Gleitz, M., M. R. v.d. Loeff, D. N. Thomas, G. S. Dieckmann, and F. J. Millero, 1995. Comparison of summer and winter inorganic carbon, oxygen and nutrient concentrations in Antarctic sea ice brine, *Mar. Chem.*, 51, 81-91.
- Golden, K. M., S. F. Ackley, and V. I. Lytle, 1998. The percolation phase transition in sea ice, *Science*, 282, 2238-2241, doi:10.1126/science.282.5397.2238.
- Goñi, M. A., M. B. Yunker, R. W. Macdonald, T. I. Eglinton, 2005 The supply and preservation of ancient and modern components of organic carbon in the Canadian Beaufort Shelf of the Arctic Ocean, *Mar. Chem.*, 93, 53-73.
- Gordon, H. R., 1989. Can the Lambert-Beer law be applied to the diffuse attenuation coefficient of ocean water, *Limnol. Oceanogr.*, 34, 1389-1409.
- Gosink, T. A., J. G. Pearson, and J. J. Kelley, 1976. Gas movement through sea ice, *Nature*, 263, 41-42.

- Gosselin, M., M. Levasseur, P. A. Wheeler, R. A. Horner, and B. C. Booth, 1997. New measurements of phytoplankton and ice algal production in the Arctic Ocean, *Deep-Sea Res., Part II*, 44(8), 1623–1644.
- Gradinger, R., 2009. Sea-ice algae: Major contributors to primary production and algal biomass in the Chukchi and Beaufort Seas during May/June 2002, *Deep-Sea Res., Part II*, 56, 1201–1212.
- Grannas, A. M., A. R. Bausch, and K. M. Mahanna, 2007. Enhanced aqueous photochemical reaction rates after freezing, *J. Phys. Chem. A*, 111, 11043–11049.
- Grenfell, T. C., and D. K. Perovich, 1981. Radiation absorption coefficients of polycrystalline ice from 400-1400 nm, *J. Geophys. Res.*, 86(C8), 7447-7450.
- Gros, V., I. Peeken, K. Bluhm, E. Zöllner, R. Sarda-Esteve, and B. Bonsang, 2009. Carbon monoxide emissions by phytoplankton: evidence from laboratory experiments, *Environ. Chem.*, 6, 369–379, doi:10.1071/EN09020.
- Gueymard, C. A., 2001. Parameterized transmittance model for direct beam and circumsolar spectral irradiance, *Sol. Energy*, 71, 325-346.
- Hansell, D. A., D. Kadko, and N. R. Bates, 2004. Degradation of terrigenous dissolved organic carbon in the western Arctic Ocean, *Science*, 304, 858-861.
- Harvey, H. R., and A. Mannino, 2001. The chemical composition and cycling of particulate and macromolecular dissolved organic matter in temperate estuaries as revealed by molecular organic tracers, *Org. Geochem.*, 32, 527-542.
- Hedges, J. I., 2002. Why dissolved organic matter, in: *Biogeochemistry of marine dissolved organic matter*, edited by D. A. Hansell, and C. A. Carlson, p1-33, Academic Press, San Diego, USA.
- Hedges, J. I., R. G. Keil, and R. Benner, 1997. What happens to terrestrial organic matter in the ocean? *Org. Geochem.*, 27 (5/6), 195-212.
- Hellmer, H. H., C. Haas, G. S. Dieckmann, and M. Schröder, 2006. Sea ice feedbacks observed in Western Weddell Sea, *Eos Trans. AGU*, 87(18), 173–184.
- Helms, J. R., A. Stubbins, J. D. Ritchie, E. C. Minor, D. J. Kieber, and K. Mopper, 2008. Absorption spectral slopes and slope ratios as indicators of molecular weight, source, and photobleaching of chromophoric dissolved organic matter, *Limnol. Oceanogr.*, 53(2), 955-969.

- Holm-Hansen, O., C. J. Lorenzen, R. W. Holmes, and J. D. Strickland, 1965. Fluorometric determination of chlorophyll, *J. Cons. Int. Explor. Mer*, 30, 3–15.
- Horner, R., 1985. Taxonomy of sea ice microalgae, in: *Sea Ice Biota*, edited by R. A. Horner, pp. 83–103, CRC Press, Boca Raton, Florida.
- Hu, C., F. E. Muller-Karger, and R. G. Zepp, 2002. Absorbance, absorption coefficient, and apparent quantum yield: A comment on common ambiguity in the use of these optical concepts, *Limnol. Oceanogr.*, 47, 1261-1267.
- ISCCP, <http://isccp.giss.nasa.gov/products/browsed2.html>.
- Jankowski, J. J., D. J. Kieber, K. Mopper, and P. J. Neale, 2000. Development and intercalibration of Ultraviolet solar actinometers, *Photochem. Photobiol.*, 71(4), 431-440.
- Johannessen, S. C., and W. L. Miller, 2001. Quantum yield for the photochemical production of dissolved inorganic carbon in seawater, *Mar. Chem.*, 76, 271-283.
- Kettle, A. J., 2005. Diurnal cycling of carbon monoxide (CO) in the upper ocean near Bermuda, *Ocean Modell.*, 8, 337–367, doi:10.1016/j.ocemod.2004.01.003.
- Kieber, D. J., J. A. McDaniel, and K. Mopper, 1989. Photochemical source of biological substrates in seawater: implications for carbon cycling, *Nature* 341, 637-639.
- Kieber, R. J., L. H. Hydro, and P. J. Seaton, 1997. Photooxidation of triglycerides and fatty acids in seawater: implication toward the formation of marine humic substances, *Limnol. Oceanogr.*, 42, 1452-1464.
- Kieber, R. J., R. F. Whitehead, and S.A. Skrabal, 2006. Photochemical production of dissolved organic carbon from resuspended sediment, *Limnol. Oceanogr.*, 51(5), 2187-2195.
- King, G. M., 2001. Aspects of carbon monoxide production and oxidation by marine macroalgae, *Mar. Ecol. Prog. Ser.*, 224, 69-75.
- King, M. D., and C. F. Weber, 2007. Distribution, diversity and ecology of aerobic CO-oxidizing bacteria, *Nature Reviews Microbiol.*, 5, 107–118.
- King, M. D., J. L. France, F. N. Fisher, and H. J. Beine, 2005. Measurement and modeling of UV radiation penetration and photolysis rates of nitrate and hydrogen peroxide in Antarctic sea ice: An estimate of the production rate of

- hydroxyl radicals in first-year sea ice, *J. Photochem. Photobiol. A Chem.*, 176, 39–49, doi:10.1016/j.jphotochem.2005.08.032.
- Kirk, J. T. O., 1980. Spectral adsorption properties of natural waters: contribution of the soluble and particulate fractions to light absorption in some inland waters of south-eastern Australia, *Aust. J. Mar. Freshwater Res.*, 31, 287–296.
- Klánová, J., P. Klán, D. Heger, and I. Holoubek, 2003. Comparison of the effects of UV, H₂O₂/UV and γ -irradiation processes on frozen and liquid water solutions of monochlorophenols, *Photochem. Photobiol. Sci.*, 2, 1023–1031.
- Lavoie, D., R. W. Macdonald, and K. L. Denman, 2009. Primary productivity and export fluxes on the Canadian shelf of the Beaufort Sea: A modeling study, *J. Mar. Syst.*, 75, 17–32, doi:10.1016/j.jmarsys.2008.07.007.
- Law, C. S., T. N. Sjöberg, and R. D. Ling, 2002. Atmospheric emission and cycling of carbon monoxide in the Scheldt Estuary, *Biogeochem.*, 59, 69–94.
- Le Fouest, V., B. Zakardjian, F. J. Saucier, 2010. Plankton ecosystem response to freshwater-associated bulk turbidity in the subarctic Gulf of St. Lawrence (Canada): A modeling study, *J. Mar. Sys.*, 81, 75–85, doi:10.1016/j.jmarsys.2009.12.003.
- Legendre, L., S. F. Ackley, G. S. Dieckmann, B. Gulliksen, R. Horner, T. Hoshiai, I. A. Melnikov, W. S. Reeburgh, M. Spindler, and C. W. Sullivan, 1992. Ecology of sea ice biota. 2. Global significance, *Polar Biol.*, 12, 429–444.
- Levasseur, M., M. Gosselin, and S. Michaud, 1994. A new source of dimethylsulfide (DMS) for the arctic atmosphere: ice diatoms, *Mar. Biol.*, 121, 381–387.
- Leymarie, E., D. Doxaran, and M. Babin, 2010. Uncertainties associated to measurements of inherent optical properties in natural waters, *Applied Optics*, 49, 5415–5436.
- Loose, B., W. R. McGillis, P. Schlosser, D. Perovich, and T. Takahashi, 2009. Effects of freezing, growth, and ice cover on gas transport processes in laboratory seawater experiments, *Geophys. Res. Lett.*, 36, L05603, doi:10.1029/2008GL036318.
- Loose, B., P. Schlosser, D. Perovich, D. Ringelberg, D. T. Ho, T. Takahashi, J. Richter-Menge, C. M. Reynolds, W. R. McGillis, and J.-L. Tison, 2011. Gas diffusion through columnar laboratory sea ice: implications for mixed-layer ventilation of CO₂ in the seasonal ice zone, *Tellus*, 63B, 23–39.

- Macdonald, R. W., E. C. Carmack, F. A. McLaughlin, K. K. Falkner, and J. H. Swift, 1999. Connections among ice, runoff and atmospheric forcing in the Beaufort Gyre, *Geophys. Res. Lett.*, 26, 2223-2226.
- Magen, C., G. Chaillou, S. A. Crowe, A. Mucci, B. Sundby, A. Gao, R. Makabe, H. Sasaki, 2010. Origin and fate of particulate organic matter in the southern Beaufort Sea – Amundsen Gulf region, Canadian Arctic, *Est. Coast. Shelf Sci.*, 86, 31-41.
- Mannino, A., and H. R. Harvey, 2000. Terrigenous dissolved organic matter along an estuarine gradient and its flux to the coastal ocean, *Organic Geochem.*, 31, 1611-1625.
- Martin, J. M., D. M. Guana, F. Elbaz-Poulichet, A. J. Thomas, V. V. Gordeev, 1993. Preliminary assessment of the distributions of some trace elements (As, Cd, Cu, Fe, Ni, Pb and Zn) in a pristine aquatic environment: the Lena River estuary (Russia), *Mar. Chem.*, 43, 185-199.
- Matsuoka, A., V. Hill, Y. Huot, A. Bricaud, and M. Babin, 2011. Seasonal variability in the light absorption properties of western Arctic waters: parameterization of the individual components of absorption for ocean color applications, *J. Geophys. Res.*, 116, doi:10.1029/2009JC005594.
- Matsuoka, A., A. Bricaud, R. Benner, J. Para, R. Sempéré, L. Prieur, S. Bélanger, and M. Babin, 2012. Tracing the transport of colored dissolved organic matter in water masses of the Southern Beaufort Sea: relationship with hydrographic characteristics, *Biogeosciences*, 9, 925-940.
- Mayer, L. M., L. L. Schick, K. Skorko, and E. Boss, 2006. Photodissolution of particulate organic matter from sediments, *Limnol. Oceanogr.*, 51, 1064-1071.
- Mayer, L. M., L. L. Schick, K. R. Hardy, and L. E. Margaret, 2009. Photodissolution and other photochemical changes upon irradiation of algal detritus, *Limnol. Oceanogr.*, 54, 1688-1698.
- McLaughlin, F. A., E. C. Carmack, R. W. Macdonald, and J. K. B. Bishop, 1996. Physical and geochemical properties across the Atlantic/Pacific water mass front in the southern Canadian Basin, *J. Geophys. Res.*, 101, 1183-1197.
- Mei, Z.-P., F. J. Saucier, V. Le Fouest, B. Zakardjian, S. Sennville, H. Xie, M. Starr, 2010. Modeling the timing of spring phytoplankton bloom and biological production of the Gulf of St. Lawrence (Canada): effects of colored dissolved

- organic matter and temperature, *Continental Shelf Res.*, 30, 2027-2024, doi:10.1016/j.csr.2010.10.003.
- Miller, G. C., and R. G. Zepp, 1979. Effects of suspended sediments on photolysis rates of dissolved pollutants, *Water Res.*, 13, 453-459.
- Miller, L. A., T. N. Papakyriakou, R. E. Collins, J. W. Deming, J. K. Ehn, R. W. Macdonald, A. Mucci, W. Owens, M. Raudsepp, and N. Sutherland, 2011. Carbon dynamics in sea ice: A winter flux time series, *J. Geophys. Res.*, 116, C02028, doi:10.1029/2009JC006058.
- Miller, W. L., and R. G. Zepp, 1995. Photochemical production of dissolved inorganic carbon from terrestrial organic-matter – significance to the oceanic organic-carbon cycle, *Geophys. Res. Lett.*, 22, 417-420.
- Miller, W. L., D. W. King, J. Lin, and D. R. Kester, 1995. Photochemical redox cycling of iron in coastal seawater, *Mar. Chem.*, 50, 63-77.
- Miller, W. L., M. A. Moran, W. M. Sheldon, R. G. Zepp, and S. Opsahl, 2002. Determination of apparent quantum yield spectra from the formation of biologically labile photoproducts, *Limnol. Oceanogr.*, 47, 343-352.
- Moate, B. D., D. G. Bowers, and D. N. Thomas, 2012. Measurements of mineral particle optical absorption properties in turbid estuaries: Intercomparison of methods and implications for optical inversions, *Estuarine, Coastal and Shelf Science*, 99, 95-107.
- Mobley, C. D., L. K. Sundman, and E. Boss, 2002. Phase function effects on oceanic light fields, *Appl. Opt.*, 41, 1035–1050.
- Mopper, K., and D. J. Kieber, 2000. Marine photochemistry and its impact on carbon cycling, in: *The effects of UV radiation in the marine environment*, edited by S. de Mora, S. Demers, and M. Vernet, pp. 101-129, Cambridge Univ. Press, New York.
- Mopper, K., and D. J. Kieber, 2002. Photochemistry and the cycling of carbon, sulfur, nitrogen and phosphorus, in: *Biogeochemistry of marine dissolved organic matter*, edited by D. A. Hansell, and C. A. Carlson, p456-508, Academic Press, San Diego, USA.
- Moran, M. A., and W. L. Miller, 2007. Resourceful heterotrophs make the most of light in the coastal ocean, *Nature Reviews Microbiol.*, 5, 1–9.

- Moran, M. A., W. M. Sheldon Jr., and R. G. Zepp, 2000. Carbon loss and optical property changes during long-term photochemical and biological degradation of estuarine dissolved organic matter, *Limnol. Oceanogr.*, 45(6), 1254-1264.
- Morel, A., 1974. Optical properties of pure water and pure seawater, in *Optical Aspects of Oceanography*, edited by Jerlov N. G., and Nielsen, E. S., Academic, p1-24.
- Mundy, C. J., M. Gosselin, J. K. Ehn, C. Belzile, M. Poulin, E. Alou, S. Roy, H. Hop, T. N. Papakyriakou, D. G. Barber, and J. Stewart, 2011. Characteristics of two distinct high-light acclimated microbial communities during advanced stages of sea ice melt, *Polar Biol.*, doi: 10.1007/s00300-011-0998-x.
- Nagurnyi, A. P., 2008. On the role of the Arctic sea ice in seasonal variability of carbon dioxide concentration in northern latitudes, *Russian Meteorol. Hydro.*, 33(1), 43-47.
- Nelson, N. B., D. A. Siegel, and A. F. Michaels, 1998. Seasonal dynamics of colored dissolved material in the Sargasso Sea, *Deep-Sea Res. Part II*, 45, 931-957.
- Nelson, J. R., 1993. Rates and possible mechanism of light-dependent degradation of pigments in detritus derived from phytoplankton, *J. Mar. Res.*, 51, 155-179.
- Nomurai, D., H. Yoshikawa-Inoue, and T. Toyota, 2006. The effect of sea-ice growth on air-sea CO₂ flux in a tank experiment, *Tellus*, 58B, 418-426, doi:10.1111/j.1600-0889.2006.0020.x.
- National Snow and Ice Data Center (NSIDC, <http://nsidc.org/>).
- Opsahl, S., and R. Benner, 1998. Photochemical reactivity of dissolved lignin in river and ocean waters, *Limnol. Oceanogr.*, 43(6), 1297-1304.
- Opsahl, S., R. Benner, and R. M. W. Amon, 1999. Major flux of terrigenous dissolved organic matter through the Arctic Ocean, *Limnol. Oceanogr.*, 44, 2017-2023.
- Osburn, C. L., L. Retamal, and W. F. Vincent, 2009. Photoreactivity of chromophoric dissolved organic matter transported by the Mackenzie River to the Beaufort Sea, *Mar. Chem.*, 115, 10-20.
- Parsons, T. R., Y. Maita, and C. M. Lalli, 1984. *A Manual of Chemical and Biological Methods for Seawater Analysis*, Pergamon, New York.
- Pennock, J. R., 1985. Chlorophyll distributions in the Delaware Estuary: regulation by light-limitation, *Estuarine Coastal Shelf Sci.*, 21, 711-725.

- Perovich, D. K., and J. W. Govoni, 1991. Absorption coefficients of ice from 250 to 400 nm, *Geophys. Res. Lett.*, 18(7), 1233-1235.
- Pisani, O., Y. Yamashita, and R. Jaffé, 2011. Photo-dissolution of flocculent, detrital material in aquatic environments: Contributions to the dissolved organic matter pool, *Water Res.*, 45, 3836-3844.
- Pope, R. M., and E. S. Fry, 1997. Absorption spectrum (380–700 nm) of pure water. 2. Integrating cavity measurements, *Appl. Optics*, 36, 8710–8723.
- Poulin, M., N. Daugbjerg, R. Gradinger, L. Ilyash, T. Ratkova, and C. von Quillfeldt, 2011. The pan-Arctic biodiversity of marine pelagic and sea-ice unicellular eukaryotes: a first-attempt assessment, *Mar. Biodiv.*, 41, 13-28, doi:10.1007/s112526-010-0058-8.
- Pursell, C. J., J. Conyers, P. Alapat, and R. Parveen, 1995. Photochemistry of chlorine dioxide in ice, *J. Phys. Chem.*, 99(26), 10433–10437.
- Pursell, C. J., J. Conyers, and C. Denison, 1996. Photochemistry of chlorine dioxide in polycrystalline ice (T= 140-185K): production of chloryl chloride, Cl-(OCIO), *J. Phys. Chem.*, 100, 15450-15453.
- Rachold, V., H. Eicken, V. V. Gordeev, M. N. Grigoriev, H.-W. Hubberten, A. P. Lisitzin, V. P. Shevchenko, and L. Schirrmeister, 2004. Modern terrigenous organic carbon input to the Arctic Ocean, in: *The Organic Carbon Cycle in the Arctic Ocean*, edited by R. Stein, and R. W. Macdonald, pp. 33–54, Springer, New York.
- Randall, K., M. Scarratt, M. Levasseur, S. Michaud, H. Xie, and M. Gosselin, 2012. First measurements of nitrous oxide in Arctic sea ice, *J. Geophys. Res.*, 117, C00G15, doi:10.1029/2011JC007340.
- Ricchiazzi, P., S. Yang, and C. Gautier, 1998. A Practical Tool for Plane-Parallel Radiative Transfer in the Earth's Atmosphere, available at <http://arm.mrcsb.com/sbdart/html/sbdart-intro.html>.
- Riedel, A., C. Michel, M. Gosselin, and B. LeBlanc, 2008. Winter–spring dynamics in sea-ice carbon cycling in the coastal Arctic Ocean, *J. Mar. Syst.*, 74, 918–932, doi:10.1016/j.jmarsys.2008.01.003.
- Riggsbee, J. A., C. H. Orr, D. M. Leech, M. W. Doyle, and R. G. Wetzel, 2008. Suspended sediments in river ecosystems: photochemical sources of dissolved

organic carbon and adsorptive removal of dissolved iron, *J. Geophys. Res.*, 113, G03019, doi:10.1029/2007JG000654.

Robert, S., G. Blanc, J. Schäfer, G. Lavaux, G. Abril, 2004. Metal mobilization in the Gironde Estuary (France): the role of the soft mud layer in the maximum turbidity zone, *Mar. Chem.*, 87, 1-13, doi:10.1016/S0304-4203(03)00088-4.

Rontani, J.-F., 2001. Visible light-dependent degradation of lipidic phytoplanktonic components during senescence: a review, *Phytochem.*, 58, 187-202.

Röttgers, R., and S. Gehnke, 2012. Measurement of light absorption by aquatic particles: improvement of the quantitative filter technique by use of an integrating sphere approach, *Applied Optics*, 51, 1336-1351.

Rózańska, M., M. Gosselin, M. Poulin, J. M. Wiktor, and C. Michel, 2009. Influence of environmental factors on the development of bottom ice protist communities during the winter-spring transition, *Mar. Ecol. Prog. Ser.*, 386, 43-59.

Schindler, D. W., P. J. Curtis, B. R. Parker, M. P. Stainton, 1996. Consequences of climate warming and lake acidification for UV-B penetration in North American boreal lakes, *Nature*, 379, 705-708, doi:10.1038/379705a0.

Schlitzer, R., 2010. Ocean Data View, <http://odv.awi.de>.

Shank, G. C., R. G. Zepp, A. Vähätalo, R. Lee, and E. Bartels, 2010. Photobleaching kinetics of chromophoric dissolved organic matter derived from mangrove leaf litter and floating Sargassum colonies, *Mar. Chem.*, 119, 162-171, doi:10.1016/j.marchem.2010.01.003.

Shank, G. C., A. Evans, Y. Yamashita, R. Jaffé, 2011. Solar radiation-enhanced dissolution of particulate organic matter from coastal marine sediments, *Limnol. Oceanogr.*, 56, 577-588.

Sharp, J. H., L. A. Cifuentes, R. B. Coffin, J. R. Pennock, and K.-C. Wong, 1986. The influence of river variability on the circulation, chemistry, and microbiology of the Delaware Estuary, *Estuaries*, 9 (4A), 261-269.

Sharp, J. H., K. Yoshiyama, A. E. Parker, M. C. Schwartz, S. E. Curless, A. Y. Beauregard, J. E. Ossolinski, and A. R. Davis, 2009. A biogeochemical view of estuarine eutrophication: seasonal and spatial trends and correlations in the Delaware Estuary, *Estuaries and Coasts*, 32, 1023-1043, doi:10.1007/s12237-009-9210-8.

- Siegel, D. A., S. Maritorena, N. B. Nelson, D. A. Hansell, and M. Lorenzi-Kayser, 2002. Global distribution and dynamics of colored dissolved and detrital organic materials, *J. Geophys. Res.*, 107(C12), doi:10.1029/2001JC000965.
- Smith, E. M., and R. Benner, 2005. Photochemical transformations of riverine dissolved organic matter: effects on estuarine bacterial metabolism and nutrient demand, *Aquat. Microb. Ecol.*, 40, 37-50.
- Smith, R. E. H., M. Gosselin, S. Kudoh, B. Robineau, and S. Taguchi, 1997. DOC and its relationship to algae in bottom ice communities, *J. Mar. Syst.*, 11, 71-80.
- Song, G., H. Xie, C. Aubry, Y. Zhang, M. Gosselin, C. J. Mundy, B. Philippe, and T. N. Papakyriakou, 2011. Spatiotemporal variations of dissolved organic carbon and carbon monoxide in first-year sea ice in the western Canadian Arctic, *J. Geophys. Res.*, 116, C00G05, doi:10.1029/2010JC006867.
- Song, G., H. Xie, S. Bélanger, E. Leymarie, and M. Babin, 2013. Spectrally resolved efficiencies of carbon monoxide (CO) photoproduction in the western Canadian Arctic: particles versus solutes, *Biogeosciences*, 10, 3731-3748, doi:10.5194/bg-10-3731-2013.
- SooHoo, J. B., and D. A. Kiefer, 1982. Vertical distribution of phaeopigments-II. Rates of production and kinetics of photooxidation, *Deep-Sea Res. Part A*, 29, 1553-1563.
- Stedmon, C. A., R. M. W. Amon, A. J. Rinehart, and S. A. Walker, 2011. The supply and characteristics of colored dissolved organic matter (CDOM) in the Arctic Ocean: Pan Arctic trends and differences, *Mar. Chem.*, 124, 108-118.
- Stramski, D., M. Babin, and S. Woźniak, 2007. Variations in the optical properties of terrigenous mineral-rich particulate matter suspended in seawater, *Limnol. Oceanogr.*, 52, 2418-2433.
- Stroeve, J., M. Serreze, S. Drobot, S. Gearheard, M. Holland, J. Maslanik, W. Meier, and T. Scambos, 2008. Arctic sea ice extent plummets in 2007, *Eos Trans., AGU* 89(2), 13-14, doi:10.1029/2008EO020001.
- Stubbins, A., G. Uher, V. Kitidis, C. S. Law, R. C. Upstill-Goddard, and E. M. S. Woodward, 2006a. The open-ocean source of atmospheric carbon monoxide, *Deep-Sea Res. II*, 53, 1685-1694.

- Stubbins, A., G. Uher, C. S. Law, K. Mopper, C. Robinson, and R. C. Upstill-Goddard, 2006b. Open-ocean carbon monoxide photoproduction, *Deep-Sea Res. II*, 53, 1695–1705.
- Stubbins, A., C. S. Law, G. Uher, and R. C. Upstill-Goddard, 2011. Carbon monoxide apparent quantum yields and photoproduction in the Tyne estuary, *Biogeosciences*, 8, 703-713.
- Sunda, W. G., S. A. Huntsman, and G. R. Harvey, 1983. Photoreduction of manganese oxides in seawater and its geochemical and biological implications, *Nature*, 301, 234-236, doi:10.1038/301234a0.
- Swinnerton, J. W., and R. A. Lamontagne, 1974. Carbon monoxide in the South Pacific Ocean, *Tellus*, 26, 136–142.
- Tarr, M. A., W. L. Miller, and R. G. Zepp, 1995. Direct carbon monoxide photoproduction from plant matter, *J. Geophys. Res.*, 100, 11403-11413.
- Thompson, A. M., 1992. The oxidizing capacity of the Earth's atmosphere: Probable past and future changes, *Science*, 256, 1157–1165.
- Tison, J. L., A. Worby, B. Delille, F. Brabant, S. Papadimitriou, D. Thomas, J. de Jong, D. Lannuzel, and C. Haas, 2008. Temporal evolution of decaying summer first-year sea ice in the Western Weddell Sea, Antarctic, *Deep-Sea Res. II*, 55, 975-987.
- Tolli, J. D., and C. D. Taylor, 2005. Biological CO oxidation in the Sargasso Sea and in Vineyard Sound, Massachusetts, *Limnol. Oceanogr.*, 50(4), 1205–1212.
- Toyota, T., S. Takatsuji, K. Tateyama, K. Naoki, and K. I. Ohshima, 2007. Properties of sea ice and overlying snow in the southern Sea of Okhotsk, *J. Oceanogr.*, 63, 393–411.
- Tremblay, J.-É., K. Simpson, J. Martin, L. Miller, Y. Gratton, D. Barber, and N. M. Price, 2008. Vertical stability and the annual dynamics of nutrients and chlorophyll fluorescence in the coastal, southeast Beaufort Sea, *J. Geophys. Res.*, 113, C079S90, doi:10.1029/2007JC004547.
- Turner, S. M., P. D. Nightingale, W. Broadgate, and P. S. Liss, 1995. The distribution of dimethyl sulphide and dimethylsulphoniopropionate in Antarctic waters and sea ice, *Deep-Sea Res. II*, 42(4-5), 1059-1080.

- Uusikivi, J., A. V. Vähätalo, M. A. Granskog, and R. Sommaruga, 2010. Contribution of mycosporine-like amino acids and colored dissolved and particulate matter to sea ice optical properties and ultraviolet attenuation, *Limnol. Oceanogr.*, 55(2), 703-713.
- Vähätalo, A. V., and R. G. Wetzel, 2004. Photochemical and microbial decomposition of chromophoric dissolved organic matter during long (months-years) exposures, *Mar. Chem.*, 89, 313-326, doi:10.1016/j.marchem.2004.03.010.
- Vähätalo, A. V., and R. G. Zepp, 2005. Photochemical mineralization of dissolved organic nitrogen to ammonium in the Baltic Sea, *Environ. Sci. Technol.*, 39, 6985-6992.
- Valentine, R. L., and R. G. Zepp, 1993. Formation of carbon monoxide from the photodegradation of terrestrial dissolved organic carbon in natural waters, *Environ. Sci. Technol.*, 27(2), 409-412.
- Voelker, B. M., and D. L. Sedlak, 1995. Iron reduction by photoproduct superoxide in seawater, *Mar. Chem.*, 50, 93-102.
- Voelker, B. M., D. L. Sedlak, and O. C. Zafiriou, 2000. Chemistry of superoxide radical in seawater: Reactions with organic Cu complexes, *Environ. Sci. Technol.*, 34, 1036-1042.
- von Quillfeldt, C. H., W. G. Ambrose Jr., and L. M. Clough, 2003. High number of diatom species in first-year ice from the Chukchi Sea, *Polar Biol.*, 26, 806-818, doi:10.1007/s00300-003-0549-1.
- Wanninkhof, R., 1992. Relationship between wind speed and gas exchange over the ocean, *J. Geophys. Res.*, 97, 7373-7382.
- Watson, R. T., H. Rodhe, H. Oeschger, and U. Siegenthaler, 1990. Greenhouse gases and aerosols, in: *Climate Change: The IPCC (Intergovernmental Panel on Climate Change) Scientific Assessment*, edited by J. T. Houghton, G. J. Jenkins, and J. J. Ephraums, pp. 1-40, Cambridge Univ. Press, Cambridge.
- White, E. M., D. J. Kieber, J. Sherrard, W. L. Miller, K. Mopper, 2010. Carbon dioxide and carbon monoxide photoproduction quantum yields in the Delaware Estuary, *Mar. Chem.*, 118, 11-21.
- Williams, W. J., and E. C. Carmack, 2008. Combined effect of wind-forcing and isobaths divergence on upwelling at Cape Bathurst, Beaufort Sea, *J. Mar. Res.*, 66, 645-663.

- Williamson, C. E., D. P. Morris, M. L. Pace, and O. G. Olson, 1999. Dissolved organic carbon and nutrients as regulators of lake ecosystems: resurrection of a more integrated paradigm, *Limnol. Oceanogr.*, 44(3, part 2), 795-803.
- Winther, J.-G., K. Edvardsen, S. Gerland, and B. Hamre, 2004. Surface reflectance of sea ice and under-ice irradiance in Kongsfjorden, Svalbard, *Polar Res.*, 23, 115–118.
- Wiscombe, W. J., and S. G. Warren, 1980. A model for the spectral albedo of snow. I: Pure snow, *J. Atmos. Sci.*, 37 (12), 2712–2733.
- Xie, H., and M. Gosselin, 2005. Photoproduction of carbon monoxide in first-year sea ice in Franklin Bay, southeastern Beaufort Sea, *Geophys. Res. Lett.*, 32, L12606, doi:10.1029/2005GL022803.
- Xie, H., and O. C. Zafiriou, 2009. Evidence for significant photochemical production of carbon monoxide by particles in coastal and oligotrophic marine waters, *Geophys. Res. Lett.*, 36, L23606, doi:10.1029/2009GL041158.
- Xie, H., S. S. Andrews, W. R. Martin, J. Miller, L. Ziolkowski, C. D. Taylor, O. C. Zafiriou, 2002. Validated methods for sampling and headspace analysis of carbon monoxide in seawater, *Mar. Chem.*, 77, 93-108.
- Xie, H., O. C. Zafiriou, W.-J. Cai, R. G. Zepp, and Y. Wang, 2004. Photooxidation and its effect on the carboxyl content of dissolved organic matter in two coastal rivers in the Southeastern United States, *Environ. Sci. Technol.*, 38(15), 4113–4119.
- Xie, H., O. C. Zafiriou, T. P. Umile, and D. J. Kieber, 2005. Biological consumption of carbon monoxide in Delaware Bay, NW Atlantic and Beaufort Sea, *Mar. Ecol. Prog. Ser.*, 290, 1–14.
- Xie, H., S. Bélanger, S. Demers, W. F. Vincent, and T. N. Papakytiakou, 2009a. Photobiogeochemical cycling of carbon monoxide in the southeastern Beaufort Sea in spring and autumn, *Limnol. Oceanogr.*, 54, 234-249.
- Xie, H., Y. Zhang, K. Lemarchand, and P. Poulin, 2009b. Microbial carbon monoxide uptake in the St. Lawrence estuarine system, *Mar. Ecol. Prog. Ser.*, 389, 17–29.
- Xie, H., S. Bélanger, G. Song, R. Benner, A. Taalba, M. Blais, V. Le Fouest, J.-É. Tremblay, and M. Babin, 2012. Photoproduction of ammonium in the southeastern Beaufort Sea and its biogeochemical implications, *Biogeosciences*, 9, 3047-3061, doi:10.5194/bg-9-3047-2012.

- Zafiriou, O.C., 2002. Sunburnt organic matter: Biogeochemistry of light-altered substrates, *Limnol. Oceanogr. Bulletin*, 11, 69-74.
- Zafiriou, O.C., J. Jousset-Dubien, R. G. Zepp, and R. G. Zika, 1984. Photochemistry of natural waters, *Environ. Sci. Technol.*, 18, 358A-371A.
- Zafiriou, O. C., S. S. Andrews, and W. Wang, 2003. Concordant estimates of oceanic carbon monoxide source and sink process in the Pacific yield a balanced global "blue-water" CO budget, *Global Biogeochem. Cycles*, 17(1), 1015, doi:10.1029/2001GB001638.
- Zafiriou, O. C., H. Xie, N. B. Nelson, R. Jajjar, and W. Wang, 2008. Diel carbon monoxide cycling in the upper Sargasso Sea near Bermuda at the onset of spring and in mid-summer, *Limnol. Oceanogr.*, 53(2), 835–850.
- Zemmelink, H. J., J. W. H. Dacey, L. Houghton, E. J. Hints, and P. S. Liss, 2008. Dimethylsulfide emissions over the multi-year ice of the western Weddell Sea, *Geophys. Res. Lett.*, 35, L06603, doi:10.1029/2007GL031847.
- Zepp, R. G., 2003. Solar UVR and aquatic carbon, nitrogen, sulfur and metals cycles, in: *UV effects in aquatic organisms and ecosystems*, edited by E. W. Helbling, and H. Zagarese, p137-183, The Royal Society of Chemistry, Cambridge, UK.
- Zepp, R. G., D. J. Erickson III, N. D. Paul, and B. Sulzberger, 2011. Effects of solar UV radiation and climate change on biogeochemical cycling: interactions and feedbacks, *Photochem. Photobiol. Sci.*, 10, 261-279, doi:10.1039/c0pp90037k.
- Zhang, Y., and H. Xie, 2012. The sources and sinks of carbon monoxide in the St. Lawrence estuarine system. *Deep-Sea Res. II.*, 81-84, 114-123, doi:10.1016/j.dsr2.2011.09.003.
- Zhang, Y., H. Xie, and G. Chen, 2006. Factors affecting the efficiency of carbon monoxide photoproduction in the St. Lawrence Estuarine system (Canada), *Environ. Sci. Technol.*, 40, 7771-7777.
- Zhang, Y., H. Xie, C. G. Fichot, and G. Chen, 2008. Dark production of carbon monoxide (CO) from dissolved organic matter in the St. Lawrence estuarine system: Implication for the global coastal and blue water CO budgets, *J. Geophys. Res.*, 113, C12020, doi:10.1029/2008JC004811.
- Zhang, Y., H. Xie, and G. Chen, 2006. Factors affecting the efficiency of carbon monoxide photoproduction in the St. Lawrence Estuarine system (Canada), *Environ. Sci. Technol.*, 40, 7771-7777.

Ziolkowski, L. A., and W. L. Miller, 2007. Variability of the apparent quantum efficiency of CO photoproduction in the Gulf of Maine and Northwest Atlantic, *Mar. Chem.*, 105, 258-270.

